Dynamic modeling and bioinspired control of a walking piezoelectric motor

Dissertation submitted in partial fulfillment
of the requirements for the degree of
Doctor in Engineering

FILIP SZUFNAROWSKI

October 2013

Dynamic modeling and bioinspired control of a walking piezoelectric motor

Dissertation submitted in partial fulfillment
of the requirements for the degree of
Doctor in Engineering

FILIP SZUFNAROWSKI

Supervisors:

PROF. DR. AXEL SCHNEIDER, supervisor
University of Bielefeld, Faculty of Technology

PROF. DR.-ING. RALF MÖLLER, reviewer
University of Bielefeld, Faculty of Technology

DR. WALTER FEDERLE, reviewer
University of Cambridge, Department of Zoology

To my family

ACKNOWLEDGMENTS

> After all manner of professors
> have done their best for us,
> the place we are to get
> knowledge is in books. The
> true university of these days is
> a collection of books.
>
> Albert Camus

I want to thank all people who have been teachers to me. The long list, which I am not able to complete, starts with my parents Krystyna and Paweł and my brothers Krzysztof and Jakub. From the times of my official education, I am grateful to all teachers who were passionate about the subjects they taught. In particular, I am grateful to my elementary school teacher Ms. Alicja Dobrzycka for waking my interest in biology; and to my high school teachers Ms. Barbara Obremska for making me love mathematics as well as Mr. Wojciech Jaśkiewicz for making me understand that "English is not a foreign language". I am most grateful to my informal but actual German teacher Ms. Auguste Upmeier and to Prof. Joachim Frohn with his wife Irmengard as well as to Almuth Bury for letting me gain a foothold in a foreign country.

From the times of my computer science graduate studies in Bielefeld, I am particularly grateful to three professors. First, in a chronological order, I want to thank Prof. Ralf Möller for giving the best lectures at the Faculty of Technology and waking my interests in hardware, robotics and control theory. Second, I want to thank Prof. Holk Cruse for his lectures on biological cybernetics and his kind and open attitude to people from all disciplines. Third, my words of gratitude go to Prof. Axel Schneider. It has been a long time since we started to work on an elastic servo motor and I have gained a lot of practical skills since that time – soldering, routing, reading data sheets, μC programming, using CAD tools and writing papers to name just a few of them.

As far as my postgraduate studies are concerned, I want to thank Axel again. This time for letting me work in a project which was as multidisciplinary as possible. In our project on elastic actuation (ELAN), my interests in mathematics, physics, biology, electronics and mechanics could meet together. My words of gratitude go to all the people who supported me during my postgraduate studies, especially during the difficult periods, either by providing a hint, critical feedback or a word of motivation – they will know. I thank

PUBLICATIONS

This thesis is partly based on the following publications, which are referred to in the text by their Roman numerals.

I - Two-dimensional dynamics of a quasi-static legged piezoelectric actuator
F. Szufnarowski, A. Schneider (2012)
Smart Materials and Structures (vol. 21, no. 5)

II - Force control of a piezoelectric actuator based on a statistical system model and dynamic compensation
F. Szufnarowski, A. Schneider (2011)
Mechanism and Machine Theory (vol. 46, pp. 1507-1521)

III - Muscle-like Force Generation with Piezoelectric Actuators in an Antagonistic Robot Joint
F. Szufnarowski, A. Schneider (2010)
Conference Proceedings of the 1st International Conference on Applied Bionics and Biomechanics ICABB 2010, Venice, Italy, 14-16 October 2010

IV - Compliant piezo-flexdrives for muscle-like, antagonistic actuation of robot joints
F. Szufnarowski, A. Schneider (2010)
Conference Proceedings of the 3rd IEEE RAS and EMBS International Conference on on Biomedical Robotics and Biomechatronics BIOROB 2010, Tokyo, Japan, 26-29 September 2010

SUMMARY

Piezoelectric motors have increasingly extended their field of applications during recent years. Improved material properties and manufacturing techniques have led to a variety of designs which can achieve theoretically unlimited displacements for moderate voltage levels while retaining a relatively high stiffness. In practical terms, this leads to stronger and faster motors which become a viable alternative to electromagnetic drives, especially if compact size and small weight are important. The piezoelectric motor considered in this work consists of four piezoelectric bender elements which can forward a ceramic bar by means of a frictional interaction. The drive elements can be compared to "legs" walking on a movable plane.

The walking motor offers outstanding force generation capabilities for a motor of its size. Despite this fact, this motor has not been used in a force control scenario before and no motor models exist in the literature which can reproduce the effect of load on its performance. In this work, two dynamic motor models are developed to address the latter issue. Both of them faithfully reproduce the non-linear motor velocity decrease under load.

The first model is based on an analytic approach and describes the low-level frictional interactions between the legs and the ceramic bar by means of several physically meaningful assumptions. This analytic model explains several non-linear phenomena in the operation of the walking motor within the full bandwidth of its rated operation. Non-linear influences due to the impact dynamics of the legs, ferroelectric hysteresis and friction are identified in the motor and new insights for an improved motor design as well as an improved motor-drive strategy gained. Moreover, the analytic model finds its application in a theoretical investigation of an alternative motor-drive strategy which is based on findings in insect walking. Specifically, it is shown that the performance of the motor can be improved by a half in terms of its force generation and doubled in terms of its maximal velocity, as compared to classical drive approaches, if the bioinspired drive strategy as proposed in this work is used.

The second model is based on an experimental approach and system identification. Although less general, the second model is well-suited for a practical application in a force-control scenario. In particular, the experimental model is used in this work for the development of a load compensation strategy based on force feedback which restores the linearity of motor operation for moderate levels of loading. Based on the linearized motor model, a force controller is developed whose

performance is evaluated both theoretically and experimentally. The developed force controller is also used in a bioinspired control scenario. Specifically, two walking motors together with their force controllers are employed in a 1-DOF antagonistic joint as force generators. The motors are supposed to partially mimic the functionality of a muscle based on the non-linear force-length relation as derived by Hill. A simple positioning task shows the feasibility of this kind of non-standard application of a piezoelectric motor.

Beside the development of motor models and bioinspired control approaches, this work addresses the issue of drive-signal generation for the walking motor. Specifically, the development of motor-drive electronics is presented which supersedes the commercially available products due to its compactness and the possibility of waveform generation at much higher drive frequencies, above 50 kHz, as compared to the nominal limit of 3 kHz and commercial products. In this context, the possibility of motor operation at ultrasonic frequencies is discussed which would benefit the motor in terms of its speed and the absence of audible noises.

CONTENTS

1 | INTRODUCTION

ABSTRACT

This chapter provides a general motivation for and a short introduction into the topics of bioinspired control and modeling of a walking piezoelectric motor as regarded in detail in further chapters of this thesis. Specifically, the necessity of the derivation of a motor model capable of reproducing the behavior of the real motor under external loading is motivated. Further, an alternative drive strategy in which all driving elements are allowed to move independently is proposed in order to improve the force generation capabilities of the motor. Additionally, the feasibility of a non-standard application in a biologically inspired robot joint is discussed. Finally, the main research objectives of the thesis are defined and the content of the particular chapters sketched.

1.1 MOTIVATION

It is interesting to note that most innovations are material based. Different materials together with the technology of their processing have always had a profound impact on the evolution of human civilization which is reflected in the names given to the past epochs like the *Stone*, *Bronze* or the *Iron Age* [212]. The time after World War II was abundant in a new class of man-designed synthetic materials like plastics or composites which are suited to specific applications and show superior performance over traditional materials. This period of time is sometimes referred to as the *Synthetic Materials Age* [75]. Gandhi [75] sees the beginning of the 21st century as the dawn of yet another class of materials, including piezoelectric materials, which are not only designed to have certain properties but which are also able to actively change their properties in response to some external conditions. He terms this class of materials *Smart Materials*. Piezoelectric materials can change their shape under the influence of an electric field and build up an electric field under the application of a mechanical stress. Since the discovery of piezoelectricity in 19th century and of ferroelectric ceramics in 20th century, piezoelectric materials have been engineered into a variety of products utilizing the above properties and ranging from the sonar and ultrasonographic devices, through buzzers and auto-focus lenses to atomic force microscopes and piezoelectric motors [172]. These products help us now to gain
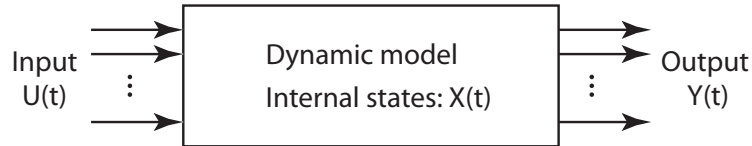
Figure 1: Abstract depiction of a dynamic system model having some time-dependent internal states $X(t)$ and reacting to input $U(t)$ with a response $Y(t)$.

invaluable insights into the process of fetal development or the atomic structure of matter [25, 169].

Recent years have also brought about many interesting developments in the field of piezoelectric actuation – the utilization of piezoelectric materials in order to produce (macroscopic) motion. Newton describes in [155] a linear motor whose actuation principle is inspired by the movement pattern of an inchworm. Uchino [207] enumerates several resonant motors whose working principle can be compared to the movement mechanism of *Euglena*, *Paramecium* or *Ameba*. Bouchilloux [30] presents a miniature tube-shaped motor and Johansson [114] introduces a non-resonant (quasistatic) motor based on the walking principle in which four driving elements ("legs") interact with a movable drive rod. This thesis is concerned with the latter, now commercially available **walking piezoelectric motor**.

The above developments were possible because of a good understanding of piezoelectric properties based on formal models. In more formal terms, the motivation behind creating models of physical systems consists in the wish to predict the behavior of the system in terms of its response $Y(t)$ (e.g. displacement, speed) to a given input $U(t)$ (e.g. voltage, stress) at a certain time t [192, 121]. If the mathematical description accounts for the time-dependent changes in the internal state $X(t)$ of the system, the mathematical model is called a *dynamic model* and the process of its derivation **dynamic modeling**.[1] Fig. 1 illustrates the idea of a dynamic system model. If the formal description is accurate enough, i.e. it faithfully predicts the response of the real system, the model can be used to develop control strategies which let the system generate a desired response [188]. However, since the actual system to be modeled is rarely fully understood, its mathematical model is necessarily a simplified description of the real physical system. In fact, the modeling process can be seen as means to improve one's own understanding of the physical system.[2] In general,

---

[1]This should not be confused with *dynamics* as the branch of physics which studies the effect of forces and torques on motion. However, a *dynamic model* can also describe the *dynamics* of a given system.

[2]Mathematical models are used not only to model physical systems. A vast field of their application is for example economics and sociology, where they are used to predict the development of stocks or the behavior of groups [136].

the better the description is, the better the understanding becomes.[3] In this context, a mathematical model can also be used in order to investigate possible design improvements of or application scenarios for the real system. This kind of model exploration is greatly facilitated by modern computers together with specialized simulation and optimization software [148, 126, 104]. This thesis is concerned with the derivation of dynamic models which can faithfully describe the dynamics of the walking piezoelectric motor.

A successful application of a technical device in general and of a piezoelectric motor in particular depends not only on a good understanding of its behavior but also on finding suitable means of its control. According to the notation from the previous paragraph, the objective of a control task is to make the output Y behave in a desired way by manipulating the input U [188]. In case of a piezoelectric motor the usual control objective is to make the motor move to a certain position or at a given velocity by changing the frequency of the drive signal. A more sophisticated control scenario, as pursued in this work, could involve the adaptive change of the drive signals in order to improve certain characteristics of the motor (e.g. its stall force or maximal speed) or the generation of forces according to the non-linear characteristics of a muscle. These non-standard control scenarios are examples of a **bioinspired control**. Bioinspiration or bioinspired technology refers to the transfer of knowledge about structure and function of biological systems into technological solutions [108]. The motivation behind this process is twofold. First, biological systems have efficiently solved many problems which scientists are interested in like dynamic control of adhesion [78, 66], outdoor locomotion [49, 232, 110] or robust navigation [211, 149]. Second, we are ourselves biological systems, thus the understanding of biological principles is essential in order to develop technical devices like an artificial heart [43, 167] or hand prostheses [131] controlled by means of myoelectric activity [97]. This thesis is concerned with bioinspired control in both of the above senses.

The starting point for this work was a market research on small-sized contemporary actuators carried out by the author in 2008. The objective of this research was to find an actuator which would be able to lift a weight of about 1 kg and be as small and lightweight as possible for an application in a biologically inspired robot joint. Large force generation capability was especially important since the actuator of choice was supposed to mimic a muscle and muscles can be seen as force generators with nonlinear force-position and force-velocity characteristics [102, 101]. In a long-term perspective, such actuator together with biologically inspired control approaches could be used

---

[3]This does not have to hold true for purely data-driven models. However, even this kind of models benefits from prior knowledge and physical insight about the system [187]. Moreover, techniques exist to extract useful information about the system from data-driven models [192].
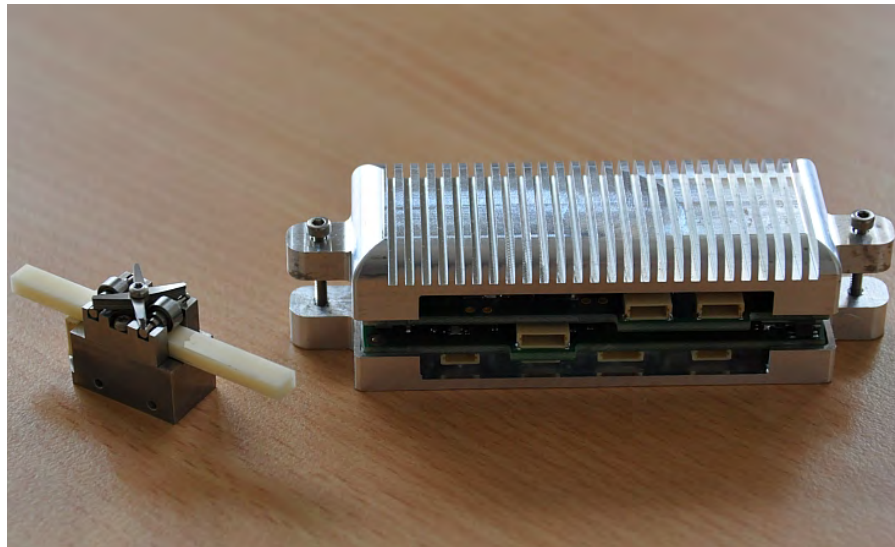
Figure 2: A photograph of the piezoelectric walking motor considered in this work together with the drive electronics developed to control the motor.

for example in robotic prostheses of the hand. As of 2008, the force generation capability of the walking motor was truly exceptional for motors of its size, even if compared to the state-of-art electromagnetic drives. The walking motor weights only 20 g and has the dimensions of 22 x 10.8 x 18 mm. It can develop forces up to 10 N and move at velocities exceeding 1 cm/s over a theoretically unlimited distance defined by the length of the movable drive rod (white ceramic bar having the length of 50 mm in the photograph of Fig. 2) while retaining positional accuracy in the range of tens of nanometers. Furthermore, it can hold its position when powered down which saves energy and does not develop interfering magnetic fields. This combination of features makes it a theoretically perfect candidate for an application in a small-sized joint. However, the motor also comes with certain disadvantages. Beside its noisy operation, the motor requires a relatively complex and large drive electronics [195] and is difficult to model due to its discontinuous and nonlinear dynamics. Before the publication by Merry et al. [145] in 2009, no dynamic models of this motor existed in literature. Still, Merry's modeling approach was purely experimental and delivered a compound model of the motor together with a nanopositioning stage in which the motor was integrated. Additionally, the proposed model neglected the discontinuous dynamics of the interaction between the legs and the drive rod, was focused on low driving velocities and – most importantly – did not consider the effects of external load on motor velocity. The model by Merry et al. [146] from 2011 introduced the discontinuous dynamics but it required a dedicated solver and still did not explain the behavior of the walking motor for large drive velocities and external loading. These limitations

4

in the models by Merry are comprehensible since classical application scenarios for piezoelectric actuation are positioning tasks in which forces and masses play a subordinate role. The focus of the above models was put on precise positioning capabilities and low-velocity operation in an almost load-free condition. Motor models capable of reproducing the nonlinear load-velocity characteristics observed in the walking motor and thus faithfully describing its dynamics were not available. This understanding, however, is necessary for a successful application in any force control scenario. Further, beside the influence of the load, the performance of the motor is affected by the shape of driving signals and their frequency. A deeper understanding of these relations is a foundation for an improved motor-drive strategy. Classically, the walking motor is driven by fixed periodic signals which make the four legs move in pairs. Several signals of different shapes are commonly used [186]. The particular form of these signals has a significant effect on the performance of the motor in terms of its speed or force generation capacity. Merry et al. [146] proposed a waveform optimization strategy based on Fourier series description of the waveforms with 32 parameters. Despite this large number of degrees of freedom, the model-based reduction of velocity errors in their work did not exceed 24 % for low drive frequencies below 20 Hz as compared to one of the classical waveforms. Higher drive frequencies or optimization in terms of maximal motor velocity were not considered. Although flexible in terms of the shape of the waveforms, their approach still relies on the pairwise drive strategy in order not to compromise motor stability. However, motor stability does not have to suffer if the legs are allowed to move independently. The only necessary ingredient for a stable operation is a proper coordination mechanism. In this context, it is natural to look for a bioinspired solution since the task of multi-leg coordination had been efficiently solved by the nature [24]. Specifically, the findings concerning the coordination mechanisms in insects [47, 49] pose a plausible solution approach. From a conceptual point of view, if more than two legs were allowed to have contact to the drive rod, the force generation capacity of the motor could be improved due to improved load sharing among them.

1.2 OBJECTIVES OF THE THESIS

The piezoelectric motor considered in this work is an example of an end product of a highly elaborated engineering process. The details related to this process are internal knowledge of the manufacturing company and not available to the public in other form than a patent [139]. As soon as a non-standard application, like force control or a bioinspired drive strategy, is intended, or if the system shows

a different behavior than expected, this information turns out to be insufficient.

This thesis has several objectives which are listed below in the order in which they are considered. The lack of publicly available data and motor models capable of reproducing the dynamic behavior of the walking motor hinder its application in force control scenarios. Therefore, the main objective of this work is the **development of a motor model** which can faithfully reproduce several non-linear phenomena observed in the behavior of the walking piezoelectric motor which cannot be explained by the published data. In particular, the movement speed of the motor has an approximatively linear dependency on the frequency of the driving signals. However, this dependency varies depending on the particular form of the electrical signals in a way which cannot be explained by the linear assumption about the motion of the driving elements inside the motor. Further, the motor is characterized by a stall force limit of 10 N. However, the actual stall force limit changes not only in dependency of the particular driving signal but also of its drive frequency. And – most importantly for the application in a force control scenario – the speed of the motor changes non-linearly under load. The model to be developed in the scope of this thesis is supposed to identify the non-linear effects in the motor.

With a deeper understanding of the non-linear dependencies and the working principle of the motor, the next objective of this work is to investigate the **feasibility of a bioinspired drive approach** based on the findings on insect walking [49, 61]. There are four driving elements inside the motor which are hard-wired to move in pairs due to stability issues. A theoretical investigation in this work is supposed to answer the question to what degree the performance of the motor could be improved, in terms of its force generating capabilities, if the driving elements were allowed to move independently. At the same time, however, the coordination mechanism between the driving elements has to guarantee a stable operation of the motor.

The starting point for this research was the idea to employ the piezo-electric motor as a force generator in a biologically inspired joint. This is a non-standard application since piezoelectric motors are almost exclusively employed in precise positioning tasks even if they present notable force generating capabilities [72]. A foundation for this is the **development of a force control strategy** suitable for the application in a biologically inspired joint, which is the third objective of this work.

Finally, according to the long-term perspective of an application in a biologically inspired hand-prostheses, the piezoelectric motor together with an appropriate force controller is to be used as a **muscle-like force generator** in a simple 1-DOF joint to test the feasibility of this kind of application. Fig. 3 illustrates the idea. Two motors are ar-
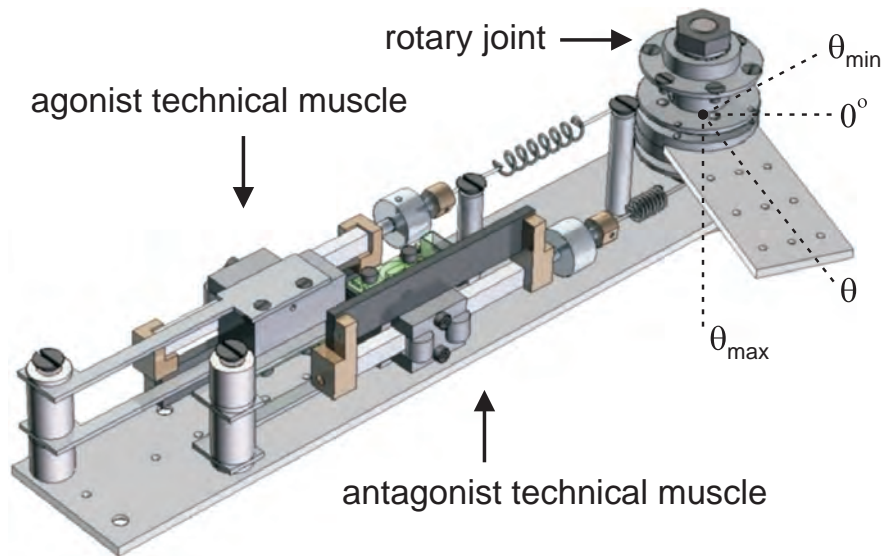
Figure 3: Two piezoelectric motors arranged antagonistically as actuators in a simple 1-DOF rotary joint. The actuators are supposed to mimic the characteristics of muscles and move the joint by exerting pulling forces on tendons connected to a pulley.

ranged in an antagonistic setup and rotate the joint by transmitting pulling forces via tendons connected to the joint. The motors are equipped with position and force sensors in order to act as virtual muscles and generate forces according to the characteristic of a muscle as described by Hill [101, 79].

1.3 OUTLINE OF THE THESIS

The thesis consists of nine chapters including the Introduction in Chapter 1. Each chapter begins with a short abstract summarizing its content. Each chapter except of the Introduction and the final Discussion (Chapter 9) contains an additional chapter-specific introduction with the relevant background also in the context of other works. The main structural division of the thesis consists of three parts. Beside the general Introduction and the final Discussion, the remaining six chapters belong either to the **Modeling**, **Control** or the **Application** part according to their content.

MODELING PART
Chapter 2 – Fundamentals of Piezoelectric Technology – provides the reader with the background knowledge about piezoelectricity including the mathematical foundations used later in the process of motor model derivation. This chapter also presents an overview of

the contemporary piezoelectric motors in general and the construction and drive principle of the walking motor in particular.

Chapter 3 – Physical Model of Motor Dynamics – is concerned with the derivation of a new and physically meaningful model of the dynamics of the walking motor. The difficulty of this process lies in the fact that the motor is fully assembled and only macroscopic measurements related to its operation are available. The physical motor model, however, is meant to explain the nonlinear phenomena observed in motor operation which are based on the microscopic effects within the motor. The model of Chapter 3 is essential for the evaluation of the bioinspired drive strategy in Chapter 5.

Chapter 4 – Gray-box Identification of Semiphysical Motor Dynamics – presents an experimental approach to the derivation of a simplified motor model which is suitable for control-theoretical applications including the design of a force controller in Chapter 7. This chapter additionally contains a discussion of the nonlinearities of the physical motor model and the possible means of their linearization.

CONTROL PART
Chapter 5 – Bioinspired Generation of Optimal Driving Waveforms – proposes a novel motor-drive strategy inspired by the kinematic model of insect walking. The issues related to the novel application of the original biological model, describing the coordination rules between neighboring legs of an insect, are discussed and a solution strategy proposed. The bioinspired drive strategy is also contrasted with other alternative drive approaches and finally evaluated in the simulation.

Chapter 6 – Frequency Matching in Waveform Generation – presents the motor-drive electronics developed in order to overcome several deficits of the commercial products delivered together with the motor. This chapter is also concerned with the technical question of how the motor driving signals or waveforms can be generated at a particular frequency. An algorithmic approach based on the solution to the Bézout's identity and a practical solution to this problem are presented.

Chapter 7 – Dynamic Load Compensation and Force Control – is devoted to the development of a compensation strategy which is supposed to restore the linear operation of the motor under load and to the design of a force controller suitable for the application in a bioinspired robot joint. The chapter is also concerned with the derivation of theoretical limits on the performance of the force controller. The actually designed force controller is subsequently evaluated in simulation and in a real-world experiment.

APPLICATION PART
Chapter 8 – Muscle-like Actuation of a Bioinspired Antagonistic Joint – presents a technical implementation of a 1-DOF robot joint driven by two virtual muscles in an antagonistic arrangement. The piezoelectric motors are equipped with positional and force sensors and generate pulling forces on the joint according to a classical model of the muscle. The whole arrangement is evaluated in a simple joint positioning scenario.

The last Chapter 9 contains the final discussion of the achievements of this thesis and the presentation of further research topics and possible applications of the walking piezoelectric motor.

APPENDICES
Appendix A contains a detailed description of the manufacturing process of the driving elements of the walking piezoelectric motor.

Appendix B contains the mathematical proof of the Bézout's identity and the derivation of the algorithm used in Chapter 6.

Appendix C is a collection of the circuit diagrams and PCB layout images of the motor-drive electronics, which is introduced in Chapter 6.

Appendix D introduces the bound graph notation used in the modeling of mechatronical systems and presents the derivation of state space equations for the force sensor described in Chapter 7.

MODELING PART
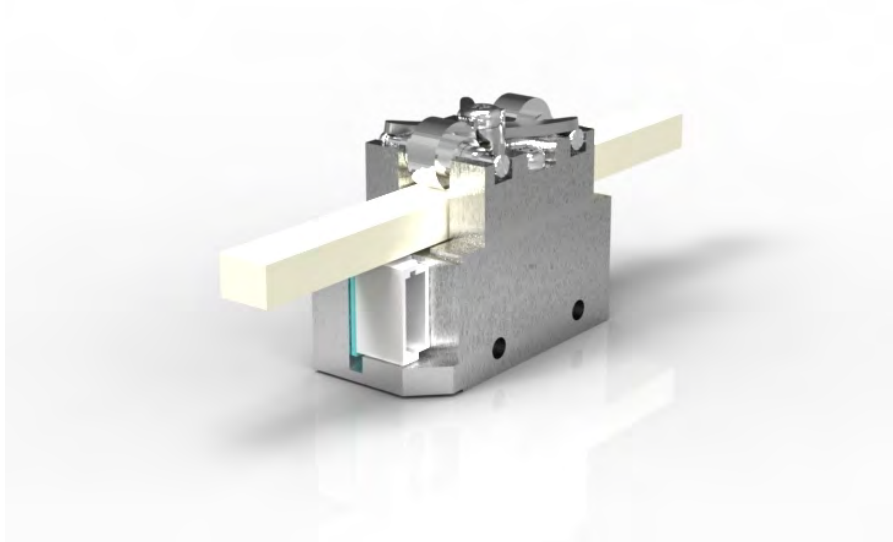
2 | FUNDAMENTALS OF PIEZOELECTRIC TECHNOLOGY

ABSTRACT

Barely noticed by the public, piezoelectric technology has dominated many technological applications during recent years. These include communication, industrial automation, medical diagnostics and consumer electronics. Since its discovery at the end of 19th century, the history of piezoelectricity has been a parade example of material-based innovation. Also in the field of actuation, improved material properties and manufacturing techniques have led to a variety of actuator designs which can achieve large displacements for moderate voltage levels while retaining a relatively high stiffness. Within this trend, modern linear piezoelectric motors have become a viable alternative to electro drives in terms of their size, speed and stall force characteristics. They can generate large displacements, do not require a gear and develop forces of several Newtons at velocities in the range of a few cm/s. This chapter is devoted to sketching the history of the development of piezoelectric technology and lay the foundation for its understanding. The focus is put additionally on presenting the state-of-art piezoelectric linear motors with the final presentation of the walking piezoelectric motor.

2.1 INTRODUCTION

Piezoelectric materials are crystalline materials which become electrically polarized when subjected to mechanical stress and conversely change shape when an electric field is applied [100]. From the technological point of view, this phenomenon only becomes interesting if it provides efficient, stable, reproducible, cost-effective and large enough means to convert electrical to mechanical energy or vice-versa.[1] The many requirements pose serious obstacles for a successful application of an emerging technology which has to compete with already established and profitable solutions. This fact has also influenced the development of piezoelectric technology, whose practical applications have been mostly hampered by the elder and more mature electromagnetic technology, since its discovery in 1880. From this point of view, the actual rise of piezoelectric technology has started only in 1940s with the discovery of modern piezoelectric ceramics. This discovery

---

[1]The change of shape in natural piezoelectric materials is too small for many practical applications. Many applications have only become possible with the emergence of artificial materials which exhibit a much stronger piezoelectric effect.

offered a large enough factor of advantage, i.e. improved properties as compared to other technologies, to succeed in practical applications.

The following sections explain the phenomenon of piezoelectricity and give a brief overview of the history of its discovery and contemporary applications. In particular, sect. 2.2 introduces the piezoelectric effect from the phenomenological point of view and sect. 2.2.1 sketches the history of its discovery. This is followed by sect. 2.2.2 which explains piezoelectricity in modern piezoelectric ceramics and the derivation of linear equations describing piezoelectric phenomena in sect. 2.2.3. This section also discusses the limitations of the linear theory and thus lays the foundation for deriving the physical motor model in the next chapter (chapt. 3) of this work. This chapter closes with the presentation of piezoelectric technology in contemporary linear motors in sect. 2.3 and in the walking piezoelectric motor in particular (sect. 2.4).

2.2 PIEZOELECTRIC EFFECT

The *piezoelectric effect* interrelates mechanical quantities such as stress or strain and electrical quantities such as electric field and displacement. It is exhibited by a number of naturally occurring crystals, e.g. quartz, tourmaline, topaz, cane sugar and Rochelle salt. If a force is applied to a piezoelectric material, electric charge is induced by the dielectric displacement which causes an electric field to build up. This phenomenon is termed *direct piezoelectric effect* and illustrated in Fig. 4(a,b). The effect is direction-dependent. Given the direction of polarization of a piezoelectric material, the measured potential is either positive or negative depending on the direction of the applied force. The piezoelectric effect is also reciprocal. The application of an electric field to a piezoelectric body causes its distortion and by mechanically preventing the distortion/blocking the material, force can be generated. This is known as the *converse piezoelectric effect* (see Fig. 4(c,d)). Finally, the piezoelectric effect is highly linear, i.e. the polarization varies in proportion to the applied stress. The following sections will give the historical background of piezoelectricity (next section) and the physical explanation of its origin in the so called ferroelectric ceramics (sect. 2.2.2). Finally, the mathematical formulation of the linear theory of piezoelectricity will follow in sect. 2.2.3.

2.2.1 History of discovery

The discovery of piezoelectricity dates back to the 19th century. Ballato [13] suggests in his review of literature that the French physicist Charles-Augustin de Coulomb theorized already in the late 18th century that electricity might be produced by the application of pressure.
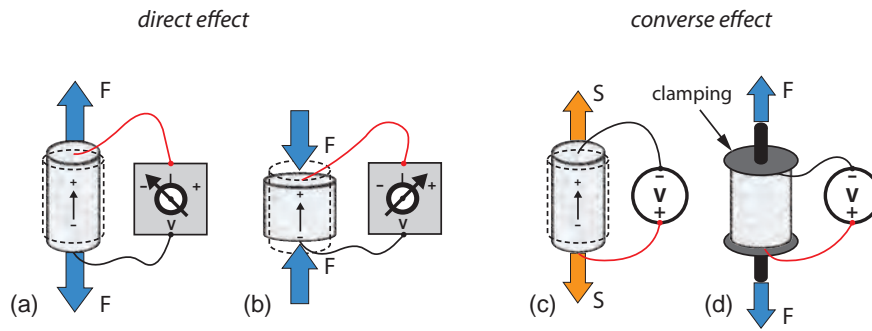
Figure 4: In the direct piezoelectric effect, electric potential builds up on the surface of a piezoelectric material if an external (a) tensile or (b) compressive force is applied. The dipoles indicate the direction of polarization in the material, the voltmeters the polarity of induced potentials. In the converse effect, application of an electric field leads to the induction of strain and distortion of the piezoelectric material – (c). If the material is clamped an elastic tension occurs and force is generated – (d).

However, it was not until 1880 that a first successful experimental demonstration of this phenomenon was conducted by Pierre and Jacques Curie. In a series of consecutive surface charge measurements on different crystals including tourmaline, quartz and Rochelle salt they observed charge variation which was dependent on the amount of applied mechanical stress. They announced their discovery as follows [39]:

> *Those crystals having one or more axes whose ends are unlike, that is to say, hemihedral crystals with oblique faces, have the special physical property of giving rise to two electrical poles of opposite signs at the extremities of these axes when they are subjected to a change in temperature. This is the phenomenon known under the name of pyro-electricity [...] We have found a new method for the development of polar electricity in these same crystals, consisting in subjecting them to variations in pressure along hemihedral axes.*

Thus the Curie brothers are to be attributed the discovery of the *direct piezoelectric effect*. The actual term *"piezoelectricity"* was suggested one year later (1881) by Wilhelm Hankel and it soon found wide acceptance in the scientific circles. The term derives from the Greek words *piezo* (to press) and *electric* (amber). The discovery attracted much attention among scientists. In the same year Gabriel Lippmann deduced from fundamental thermodynamic principles that the reverse effect should exist, i.e. that the imposition of surface charge would induce mechanical deformation. The Curie brothers confirmed the *converse piezoelectric effect* experimentally in 1882. Further milestones in the understanding of piezoelectricity were reached by Franz Ernst
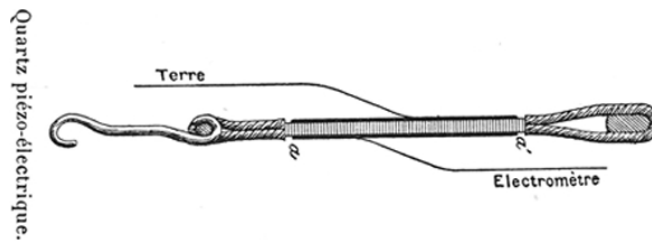
Figure 5: The Curies' *quartz piezo-electrique* consisting of an elongated quartz bar with two metalized surfaces as used in their original instrument from 1882 [50].

Neumann who laid the foundation for understanding the physical properties of crystalline materials, Lord Kelvin who developed in 1893 the first atomic model explaining the direct and converse piezoelectric effects, and by Neumann's student Woldemar Voigt who developed the tensor notation describing the linear behavior of piezoelectric crystals (see sect. 2.2.3). Within 15 years after the discovery the theoretical core of piezoelectric science was established. This core grew steadily and by 1910 – with the publication of *"Lehrbuch der Kristallphysik"* [216] by Voigt – 20 natural crystal classes displaying the piezoelectric effect together with their corresponding macroscopic coefficients were identified. Still, the piezoelectric science remained in the realm of scientific investigation as opposed to electromagnetism which by that time had already taken the step to technological applications. The practical change was brought about by the sinking of the *Titanic* in 1912 and the outbreak of World War I in 1914 which led to an urgent need for submarine detection technology. The challenge was picked up, among others, by Ernest Rutherford and Paul Langevin. Their work resulted in the development of a measuring device by the former and the sonar by the latter. Rutherford's device was based on Pierre and Jacques Curie's instrument for measuring either electric charge or pressure (see Fig. 5). Although the device was a highly sensitive sensor useful for determining the amplitudes of underwater diaphragms, it was inefficient as a generator because it relied on the *transverse mode* of operation in the original crystal cut.[2] Langevin, who knew the Curies

---

[2]The term *transverse* refers to the displacement mode of a piezoelectric material which is perpendicular to the direction of the applied electric field. A *longitudinal*

personally, had a deeper understanding of piezoelectricity and adjusted the design in order to employ a crystal of different dimensions (in *longitudinal mode*) having a much larger surface exposed to changes in water pressure. With his final design he was able to detect submarines from a distance of 3 km but the device did not go into actual service by the end of war [208, 122].

The success of sonar stimulated the development of other piezoelectric devices like crystal oscillators, material testing and pressure measurement devices. In fact, before the outbreak of World War II the foundation for most of the by now classic piezoelectric applications was already laid including microphones, accelerometers, bender actuators, phonograph pick-ups, etc. However, in the first half of 20th century the development, performance and commercial application of these devices were hampered by the fact that only natural piezoelectric materials were known and could be employed. The war was again to be the trigger for innovative developments. During World War II, three independent research groups from the USA in 1942 as well as Japan and the Soviet Union in 1944 working on improved high capacitance materials for radar systems discovered that certain ceramic materials – in particular barium titanate ($BaTiO_3$, BT) – exhibited dielectric constants even 100 times higher than common crystals. Although the original discovery of BT was not directly related to piezoelectric properties, it was soon found out by the engineer Robert B. Gray from Erie Resistor Corp. that the electrically poled BT exhibited piezoelectricity owing to the domain re-alignment (see next section). Gray applied for a patent for his discovery in 1946 and thus is seen as the "father of piezoceramics" [208]. The discovery of easily producible BT triggered an intensive research on these electro-ceramics including other perovskite isomorphic oxides (see next section) and developing of a rationale for doping them with metallic impurities to achieve desired physical properties. This led to the discovery of the present key composition of lead (Latin *plumbum*) zirconate titanate ($Pb(Zr_x,Ti_{1-x})O_3$ with $0 \leq x \leq 1$, PZT) in 1950s and later other (also Pb-free) solid solutions, relaxor ferroelectrics as well as piezoelectric polymers and piezoceramic-polymer composites [208]. A new era for piezoelectric devices began – tailoring materials to specific applications. The next section gives an explanation of how compositional variations with different piezoelectric properties can be realized in case of PZT.

The discovery of modern piezoelectric materials started an avalanche of piezo technology which nowadays covers many markets with turnover of billions of dollars [100]. Table 1 shows a selection of some contemporary piezoelectric applications. They range from research and military, through medical and automotive to telecommunication

---

mode refers to the displacement coincident with the direction of the electric field. In both cases, however, the directions of the electric field and of material polarization coincide. In a *shear mode*, electric field and polling directions are perpendicular to each other.

and consumer electronics. While the selection is far from being complete, its main purpose is to illustrate the wide variety of contemporary piezoelectric applications. Sect. 2.3 will focus on how piezo technology is utilized in piezoelectric motors in general and in the walking piezoelectric motor in particular.

Table 1: Major applications of piezoelectricity as of the beginning of 21st century. No claim for completeness is raised. The division in categories is not strict as many applications overlap several categories. Modified and extended from [100].

| Communications and control	Industrial and automotive	Health and consumer	Research and military	Emerging applications
Signal processing	Ultrasonic cleaning	Noninvasive diagonostics	Radar	MEMS devices
Frequency control	Sonar	Hyperthermia	Electronic warfare	MOMS devices
Correlators	Liquid level sensors	Subcutaneous medication	IFF	Biomimetic devices
Convolvers	Vibration damping	Wristwatches	Guidance systems	Composite and functionally graded devices
Filters	High temperature sensors	Camera focusing	Fuzes	Rainbow devices
Delay lines	Non-destructive testing	Ignition of gases	Atomic clocks	Acousto-photonic-electronic devices
Oscillators	Chemical/biological sensors	Lithotripsy	Sonobuoys	Energy harvesting
Bandpass (SAW) filters	Fuel valves	Braille for the blind	Adaptive control	
Bandpass (BAW) filters	Fine positioning/optics	Microphones/speakers	AF-microscopy	
Navigation/GPS	Acceleration sensors	Inkjet printer heads		

2.2.2 Modern piezoelectric ceramics

The immense success of piezoelectricity in technological applications can to a large degree be attributed to the discovery of modern piezoelectric ceramics. From a technological point of view, there are several important characteristics of piezoelectric materials. Uchino [208] enumerates five of them as the *piezoelectric charge/strain constant d*, the *piezoelectric voltage constant g*, the *electromechanical coupling factor k*, the *mechanical quality factor Q* and the *acoustic impedance Z*. Also the *Curie temperature* (see below) is important from the application and production process point of view. Not all of these characteristics are superior in ceramic materials. For example quartz has a quality factor Q which is several orders of magnitude higher than the one of ceramics. This means a low mechanical loss which together with a (cut-dependent) compensation of temperature and stress effects, elastic linearity and the presence of (relatively weak) piezoelectricity makes it the perfect choice for acoustic (e.g. surface-acoustic-wave (SAW) filters, wireless transceivers) and timekeeping (e.g. clocks, pulse generators) applications [100]. On the contrary, piezoelectric ceramics have a relatively low quality factor but a high electromechanical coupling factor and piezoelectric strain constant which is most important for high-power transducer and actuator applications. Obviously, the latter application is of particular interest to this work.

Another important reason for focusing on piezoelectric ceramics in this section is the understanding of the origins of piezoelectricity in the nowadays most common piezoelectric ceramic – PZT. This understanding is grounded in the internal structure of the ceramic material. Both epoch-making ceramic materials mentioned in the previous section, BT and PZT, are polycrystalline, i.e. they consist of multiple (variously oriented) crystals. Crystals can be classified into 32 point groups according to their crystallographic symmetry [91]. Of the 32 point groups, 21 classes are noncentrosymmetric (a necessary condition for piezoelectricity to exist) and 20 of these are actually piezoelectric,[3] i.e. positive and negative charges appear on their surface when stress is applied. 10 of these 20 groups are polar (exhibit spontaneous polarization) and thus pyroelectric, i.e. electric charge appears on their surface in temperature dependent way. If their polarization is additionally reversible by the application of an external electric field they are called ferroelectric.[4] Both BT and PZT are ferroelectric ceramics which have the so called Perovskite crystalline structure [20] named

---

[3]One class – the point group "432" – is not piezoelectric because of the combined effect of other symmetry elements which eliminates the accumulation of electric charge in this group.

[4]Although most ferroelectric materials do not contain iron (Greek *ferro*) the name *ferro*electricity was chosen because of some principal analogies to ferromagnetism which was already known before the discovery of ferroelectricity in 1920 by Joseph Valasek.
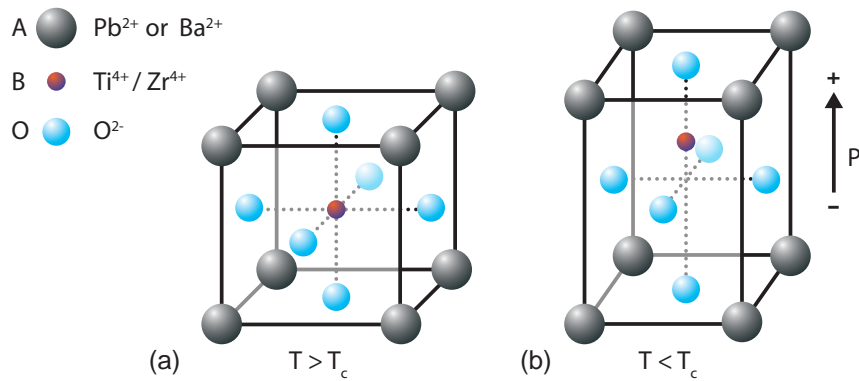
Figure 6: Schematic representation of the Perovskite crystal unit cell structure ABO_3. In case of PZT, the unit cell consists of an oxygen octahedron with the B-site cation around its center occupied by either Ti^{4+} or Zr^{4+} ions and the A-site cations of the surrounding cuboid occupied by Pb^{2+} ions. BT has A-site cations occupied by Ba^{2+} and the B-site cation by Ti^{4+} ions. (a) shows the Cubic phase of the structure above the Curie temperature T_C and (b) the tetragonal phase below T_C exhibiting spontaneous polarization.

after the Russian mineralogist Lev Perovski. Fig. 6 shows the structure represented by the compositional formula ABO_3 which is adopted by both BT and PZT. The following discussion of piezoelectric ceramics focuses on the latter. PZT is a solid solution of $PbZrO_3$ and $PbTiO_3$ adapting the Perovskite structure. The A-site cations are filled with the larger lead ions and form a cuboid box which an oxygen filled octahedron falls within. The B-site cation is randomly filled with the smaller Zr or Ti ions. Above the so-called *Curie temperature* T_C, this structure is symmetric and does not exhibit ferroelectricity. At T_C an asymmetry develops as the oxygen octahedron is shifted off the center of the cuboid box and the B-site ions are shifted off the center of the octahedron. An electrical dipole builds up, the structure starts exhibiting spontaneous polarization and becomes ferroelectric. The understanding of this process has been developed only recently due to first-principles studies. For a detailed discussion the reader is referred to [100] where five key concepts are used to explain the phenomenon of ferroelectricity in oxide materials including hybridization between the B-site cation and its oxygen neighbors, polarization rotation and the prediction of morphotropic phase boundary.[5] At this point only a brief explanation will be given. The Perovskite structure forms several stable lower-symmetry or distorted versions besides the ideal symmetric case as the stability of the cubic structure is strongly dependent on the relative ion sizes and the formation of certain types of bondings. Ferroelectricity comes to be as an overall effect due to the competition between long-range Coulomb forces which favor

---

[5]Hybridization refers to the concept of mixing atomic orbitals and forming new hybrid orbitals with different properties.
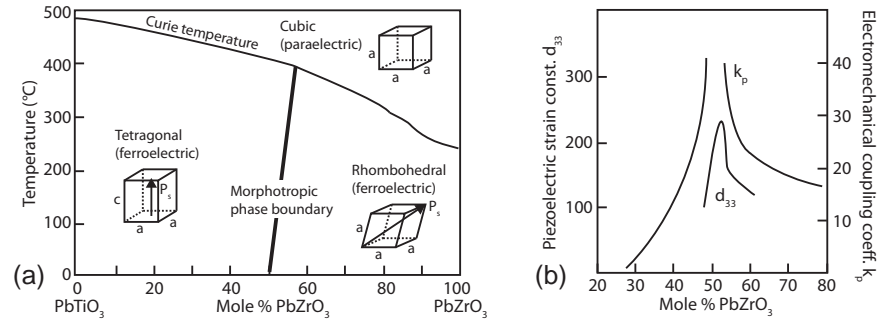
Figure 7: Phase diagram of $PbTiO_3$-$PbZrO_3$ solid solutions adapted from [100]. (a) shows the different lattice structures according to the temperature and Ti/Zr ratio and the morphotropic phase boundary (MPB). One possible direction of polarization is indicated for both the tetragonal and rhombohedral phase. (b) shows the enhancement of piezoelectric properties of PZT at the MPB.

off-centering and short-range repulsive forces which favor the high-symmetry centric phase where the atoms are as far apart as possible. Hybridization or the formation of covalent bondings between the B-side cation and its oxygen neighbors reduces the repulsive forces and allows the atoms to move off-center. This induces large crystalline distortion and the formation of an electric dipole. In case of PZT, this distortion is additionally enhanced due to the hybridization of Pb 6s electrons with the covalent bondings between the Ti and O ions such that its spontaneous polarization is three times larger than of BT. Consequently, PZT is especially suitable for high performance piezoelectric materials. Furthermore, because of the possibility of compositional modification a wide variety of piezoelectric properties can be realized. Kimura et al. [208] describe three typical methods of compositional modifications.

First, the Ti/Zr ratio can be modified which strongly influences the lattice structure and the piezoelectric properties. Fig. 7 illustrates this graphically. The asymmetric structures below the Curie temperature are ferroelectric. In the tetragonal phase, the Ti ions move in the oxygen octahedra in the $< 100 >$ directions, according to the convention of indexing lattice directions in material science, which gives 6 possible directions each passing through each vertex of the oxygen octahedron. In the rhombohedral phase, the Ti ions can move in the $< 111 >$ directions through the centers of each octahedral face. This gives altogether 8 possible dipole moment directions. The phase boundary between the tetragonal and rhombohedral structures is termed morphotropic phase boundary (MPB). This boundary is vertically elongated around the composition with the Ti/Zr ratio of 47/53 and exhibits extraordinary piezoelectric properties. However, to the best knowledge of the author the reason for this enhancement has still not been sufficiently clarified and is the matter of scientific investigations.

It should be noted that if stability of piezoelectric properties against external conditions (e.g. heat, pressure) are especially important for a given application, a composition close to the MPB should be avoided. In such cases, tetragonal PZT composition is usually chosen due its high Curie temperature.

Second, the cation sites of PZT can be doped with donor or acceptor ions. Donor or acceptor-doped PZT is called *soft* or *hard* PZT, respectively. The descriptors correspond to the electrically and mechanically compliant or rigid behavior of PZT. Hard PZT ceramics possess generally more stable piezoelectric properties and have higher quality factors and are thus preferred for applications utilizing resonance, e.g. in ultrasonic actuators (see sect. 2.3), whereas soft PZT is better suited for non-resonant sensors and actuators as the one described in this thesis. Doping affects the piezoelectric properties because it has a strong effect on the ferroelectric domain switching behavior (described in more detail below).

The third compositional modification is a solid solution with other Perovskite compounds. The resulting PZT is called the ternary PZT system. Kimura et al. [208] give the examples of $Pb(Sb_{1/2}Nb_{1/2})O_3$ PZT showing good temperature stability and used in communication circuit components, $Pb(Mn_{1/3}Sb_{2/3})O_3$ PZT with a high mechanical quality factor used for electromechanical transducers and $Pb(Ni_{1/2}Nb_{1/2})O_3$ PZT which exhibits a very large strain constant d and is often used in actuator applications. These three compositional methods mentioned above, especially if combined, result in a great variety of PZT with different piezoelectric properties suitable for a broad range of applications.

So far in the discussion of piezoelectric ceramics in this section, it has been implicitly assumed that the piezoelectric properties of a unit cell of PZT and of a polycrystalline ceramic made of PZT can be treated in the same way. This is of course not true (for a detailed discussion refer to [100]) and becomes obvious at the latest when any compositional variation of PZT is considered. In general, ferroelectric polycrystalline materials consist of ferroelectric domains, i.e. groups of unit cells with the same direction of spontaneous polarization. Because the domains – called *Weiss domains* after the French physicist Pierre-Ernest Weiss who suggested the existence of such magnetic domains in ferromagnets – are randomly oriented after the sintering process (see sect. 2.4.2), the ferroelectric material does not exhibit any piezoelectric properties globally.[6] However, by an application of a strong external electric field, it is possible to force the domains to be oriented or *poled* along the direction of the field. This process is called poling and is schematically depicted in Fig. 8. Depending on the phase of PZT, the external field causes the domains to switch

---

[6]Sintering refers to the process of creation of solid objects from powders.
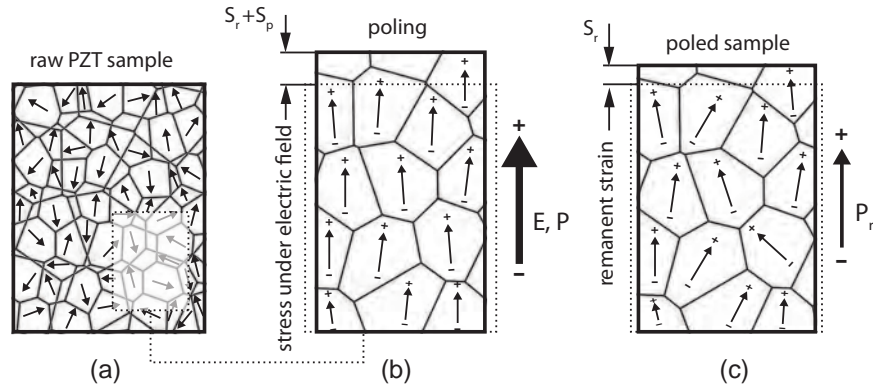
Figure 8: Schematic illustration of the poling process adapted from [100]. (a) shows a raw PZT sample with randomly oriented domains – no net polarization can be observed. In (b) an external electric field is applied to the sample which causes the realignment of dipoles in the domains along the external field and formation of net polarization P together with sample distortion and induction of strain S_r. The overall strain is additionally enhanced by the poling external field component S_p. After removal of the external field in (c) most of the domain retain their new orientation and thus the poled sample exhibits the remanent polarization P_r and the remanent strain S_r.

their orientation to one of 6 (tetragonal) or 8 (rhombohedral phase) possible states. While the domains cannot be perfectly aligned with the external field, except if the compound crystals were by coincidence oriented in field direction, the polarization vectors align with the external field in a way which maximizes the number of components resolved in that direction. Thus by means of poling, a macroscopic asymmetry/distortion and polarization are imprinted in the ceramic sample. After poling, when the external field is removed, a remanent polarization P_r and strain S_r are maintained in the sample. In practice, poling is usually performed at an elevated temperature above the T_C when the crystal structures become centrosymmetric and the electric dipoles vanish. When the material is cooled in the presence of external field, the formation of dipoles in field direction is enhanced [163].

A poled PZT sample has been given artificial anisotropy, i.e. direction dependence, and exhibits piezoelectric properties macroscopically. However, these properties are still strongly influenced by the domain behavior. Depending on the magnitude and direction of an external field, the domains can switch their metastable configurations which results in the change of polarization and strain exhibited by the poled sample. The overall effect is usually described by the polarization hysteresis loop and the butterfly curve, both depicted in Fig. 9. After sintering, the polarization value is zero (point ① in Fig. 9) and increases during poling with the application of an electric field along the dashed curve ①-② until it reaches the maximum level P_m at which it
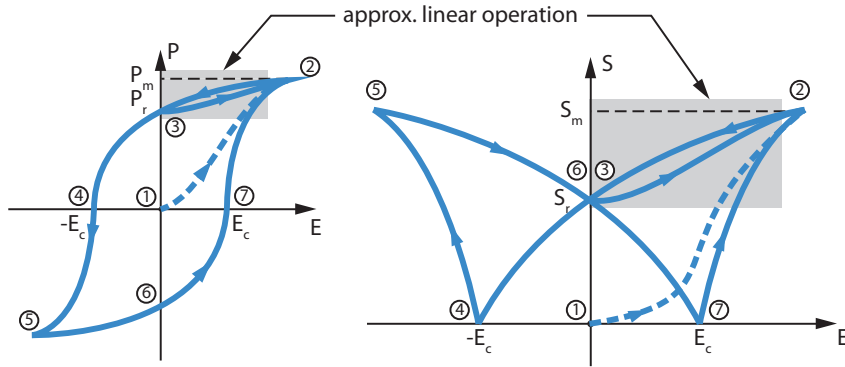
Figure 9: Schematic illustration of (a) the polarization hysteresis and (b) the strain butterfly curve of a typical ferroelectric ceramic. P denotes polarization, S strain and E electric field. The corresponding subscripts denote the remanent (r) and maximal (m) polarization or strain levels. E_c is the coercive field strength. Gray-shaded areas indicate the typical region of operation in which positive electric field is employed and the strain/field dependence is approximately linear. Depiction after [95].

saturates. At this point ②, all domains have aligned with the external field and the maximal positive strain S_m has been reached. If the external field is gradually reduced, the orientations of the domains will also return to their random state. However, due to the induced deformation and mechanical stress within the ceramic, many of them will retain new configurations close to the orientation they took during poling. Even if the external field is completely removed, a remanent polarization P_r and strain S_r are exhibited at point ③. In order to turn the polarization/strain value back to zero, a negative field needs to be applied. The necessary value of this field is called (negative) *coercive field* E_c and is shown at point ④. If the negative field is further increased beyond the E_c value, a polarization reversal arises until it saturates again at point ⑤ where the domains are aligned along the negative field. In the strain butterfly curve this corresponds to the maximum negative strain. By reversing the electric field again, the polarization returns to zero, passing the remanent negative polarization point ⑥ and reaching zero polarization at the (positive) electric field value of E_c. Further increasing the field leads again to saturation at point ②, the curves close and the hysteretic cycle is completed. In addition to the change in polarization due to the application of a strong electric field, the orientation change of the electrical dipoles can also be caused by mechanical stress. If an external stress of sufficiently large magnitude is applied in the direction of the polarization, it can displace the B-site ions to energetically more favorable positions leading to mechanical form change. This change is also hysteretic and can be described with a stress/strain hysteresis loop which crosses regions of zero strain at the coercive stress level, the remanent and

maximal strain in a way similar to the polarization hysteresis loop from Fig. 9(a) [175]. This phenomenon is called ferroelasticity.

As can be seen from the above discussion, most mechanical, electrical and thus piezoelectric properties of PZT exhibit a strong nonlinear behavior if subjected to large electric fields or mechanical stresses. Furthermore, the area of the hysteresis loop enclosed while operating the piezoelectric ceramic in a particular application corresponds to the dissipated energy density [77] and degrades efficiency. For this reason but even more importantly because of the difficulties connected with nonlinear modeling and control, piezoelectric actuators are usually operated in an approximately linear unipolar region of the hysteresis loop as indicated in Fig. 9. In this region, the *linear theory of piezoelectricity* applies.

2.2.3 Linear theory of piezoelectricity

The behavior of piezoelectric materials can be approximated with the linear theory very accurately if non-ferroelectric materials like quartz are considered [212]. In case of ferroelectric materials, the application of linear theory is subjected to several restrictions. First of all, it is limited to the linear range of operation mentioned in the previous section when small or moderate unipolar electric or mechanical field levels are used. Second, there exist important nonlinear effects like electrostriction, resonance, creep, depolarization, etc. which will be discussed at the end of this section and whose influence needs to be taken into account in an application specific way. For interested readers, a detailed treatment of the limitations of the linear theory can be found in [229].

In the linear theory of piezoelectricity, the properties of a piezoelectric material are described by the elastic, dielectric and piezoelectric tensors. A tensor-based description is necessary since a piezoelectric material is inherently asymmetric and its response to given electrical or mechanical stimuli is direction dependent. Furthermore, this response is temperature dependent and consists of both real and imaginary (out-of-phase) components. The interrelation between the mechanical, electrical and thermal components is often depicted by means of the Heckmann diagram [94] shown in Fig. 10. In this diagram, the circles of the outer triangle represent the intensive variables of mechanical stress T, electric field strength E and temperature Θ and the circles of the inner triangle the extensive variables of strain S, dielectric displacement D and entropy σ.[7] The connections between the outer and inner circles represent the major mechanical, electrical and thermal effects. The piezoelectrical, pyroelectrical and thermoelastic

---

[7]Intensive and extensive properties of matter refer to their dependency on size/extend. An intensive property does not depend on size in contrast to an extensive property.
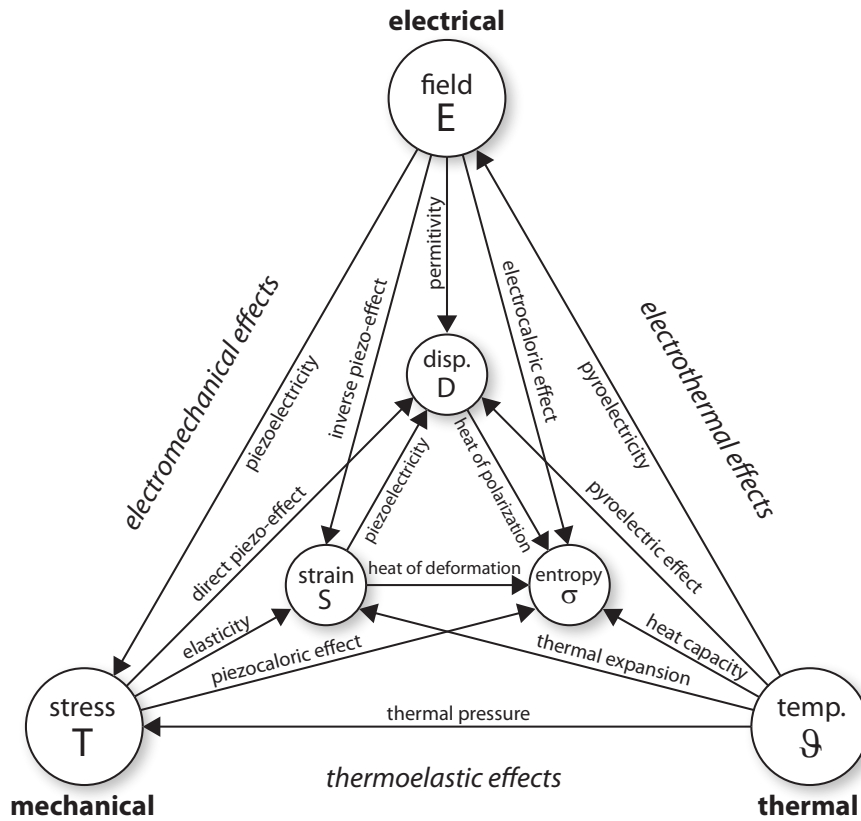
Figure 10: Heckmann diagram illustrating the interrelationship between mechanical, electrical and thermal properties in an inorganic solid. The outer circles represent the intensive variables of mechanical stress, electric field strength and temperature. The inner circles are the extensive variables of strain, dielectric displacement and entropy. The coupling effects between the intensive and extensive variables are represented by arrow-headed lines with labels corresponding to their common naming.

couplings between the intensive variables are the edges of the outer triangle. The remaining couplings represent the interrelations between thermal (scalar), electrical (vector) or mechanical (second-rank tensor) properties of the material. The coupling of different effects in the diagram indicates the difficulty in measuring any of the encircled variables since their change may be due to multiple effects. For example, the mechanical strain in a piezoelectric material may be caused by an external stress through Hooke's law or be induced by an electric field through converse piezoelectric effect or due to temperature change and thermal expansion of the material. In order to accurately describe the response of the material, an energy (thermodynamical) approach is used. In particular, the equations governing the behavior of piezoelectric materials can be formulated from the Gibbs free energy thermodynamical approach [100, 203, 106, 51] by considering

infinitesimal energy changes at a constant temperature and pressure. The derivation of these equations is outlined below.

The first law of thermodynamics (energy conservation law) states that the change in the internal energy of a system U must correspond to the heat q transferred into or out of the system and the work w done on or by the system

$$dU = dq + dw. \tag{1}$$

According to the second law of thermodynamics (entropy change for reversible processes) dq can be expressed as

$$dq = \Theta d\sigma \tag{2}$$

and if work is considered to consist of a mechanical and an electrical part as is the case in piezoelectric materials, then dw can be formulated as

$$dw = \underbrace{T_{ij}dS_{ij}}_{dw_{\text{mech}}} + \underbrace{E_i dD_n}_{dw_{\text{elec}}}, \quad i,j = 1,2,3. \tag{3}$$

Variables with single indices are vector-valued and variables with double indices correspond to second-rank tensors. Reformulating equation (1) in terms of (2) and (3) one arrives at

$$dU = \Theta d\sigma + T_{ij}dS_{ij} + E_i dD_i. \tag{4}$$

This equation is formulated in terms of the extensive independent variables S, D and σ. In order to replace the independent variables with their intensive thermodynamic conjugates (which are usually known from material property tables or experiments), a Legendre transform of U is used resulting in the Gibbs free energy formulation [106, 204]

$$G = U - \Theta\sigma - T_{ij}S_{ij} - E_i D_i, \tag{5}$$

where G is the Gibbs function.[8] The total differential of G together with a substitution from (4) gives

$$dG = -\sigma d\Theta - S_{ij}dT_{ij} - D_i dE_i. \tag{6}$$

By setting two of the now independent (intensive) variables constant at a time, three relations follow for the dependent variables

$$\sigma = -\left.\frac{\partial G}{\partial \Theta}\right|_{T,E}, \quad S_{ij} = -\left.\frac{\partial G}{\partial T_{ij}}\right|_{E,\Theta}, \quad D_n = -\left.\frac{\partial G}{\partial E_i}\right|_{T,\Theta}. \tag{7}$$

For many applications it is sufficient to approximate the relations between the dependent and independent variables with a set of linear

---

[8]There are $\binom{2}{1}^3 = 8$ different ways of choosing a triple of independent variables from the altogether 6 intensive and extensive properties. For each selection, an appropriate thermodynamical potential can be defined and the transition from U to this new potential realized via Legendre transform.

functions [203]. In this case, the total differentials of S, D and σ are computed resulting in the set of so called constitutive equations

$$d\sigma = \underbrace{\left.\frac{\partial\sigma}{\partial\Theta}\right|_{T,E} d\Theta}_{\text{heat capacity}} + \underbrace{\left.\frac{\partial\sigma}{\partial T_{ij}}\right|_{E,\Theta} dT_{ij}}_{\text{piezocaloric effect}} + \underbrace{\left.\frac{\partial\sigma}{\partial E_i}\right|_{T,\Theta} dE_i}_{\text{electrocaloric effect}} \tag{8}$$

$$dS_{ij} = \underbrace{\left.\frac{\partial S_{ij}}{\partial\Theta}\right|_{T,E} d\Theta}_{\text{thermal expansion}} + \underbrace{\left.\frac{\partial S_{ij}}{\partial T_{kl}}\right|_{E,\Theta} dT_{kl}}_{\text{elastic compliance}} + \underbrace{\left.\frac{\partial S_{ij}}{\partial E_k}\right|_{T,\Theta} dE_k}_{\text{converse piezoelectricity}} \tag{9}$$

$$dD_n = \underbrace{\left.\frac{\partial D_i}{\partial\Theta}\right|_{T,E} d\Theta}_{\text{pyroelectric effect}} + \underbrace{\left.\frac{\partial D_i}{\partial T_{jk}}\right|_{E,\Theta} dT_{jk}}_{\text{direct piezoelectricity}} + \underbrace{\left.\frac{\partial D_i}{\partial E_j}\right|_{T,\Theta} dE_j}_{\text{dielectric permittivity}} \,. \tag{10}$$

where dT and dE are assumed to be small deviations from zero initial stress and electric field. The derivatives of the dependent variables with respect to the independent ones in the above set of equations correspond to physical effects from Fig. 10. They also represent material coefficients and can be written as partial second derivatives of the Gibbs function by substituting (7) into the constitutive equations.[9] In this way the direct and converse piezoelectric effects can be shown to be thermodynamically equivalent

$$d^{T,\Theta}_{ijk} = \underbrace{\left.\frac{\partial S_{ij}}{\partial E_k}\right|_{T,\Theta}}_{\text{converse}} = \frac{\partial^2 G}{\partial E_k \partial T_{ij}} = \frac{\partial^2 G}{\partial T_{ij} \partial E_k} = \underbrace{\left.\frac{\partial D_k}{\partial T_{ij}}\right|_{E,\Theta}}_{\text{direct}} = d^{E,\Theta}_{kij}. \tag{11}$$

In the above relationship, $d^{E,\Theta}_{kij}$ and $d^{T,\Theta}_{ijk}$ represent the coefficients in the direct and converse piezoelectric effects, respectively, both defined at a constant temperature (indicated by the superscripts). Since the order of derivatives (indicated by the subscripts) is irrelevant, these coefficients are equal and the superscript indication of constant E or T conditions redundant (cf. simplified notation in (17)). In a similar way other coefficients can be defined. It is common to express the constitutive equations (8)-(10) in an integrated form with material coefficients in place of the equivalent partial derivative expressions

$$\Delta\sigma = \frac{c^{T,E}}{\Theta}\Delta\Theta + \alpha^{E,\Theta}_{ij} T_{ij} + p^{T,\Theta}_i E_i \tag{12}$$

$$S_{ij} = \alpha^{T,E}_{ij}\Delta\Theta + s^{E,\Theta}_{ijkl} T_{kl} + d^{T,\Theta}_{kij} E_k \tag{13}$$

$$D_i = p^{T,E}_i\Delta\Theta + d^{E,\Theta}_{ijk} T_{jk} + \epsilon^{T,\Theta}_{ij} E_j, \tag{14}$$

---

[9]Because of the second derivative formulation these coefficients are called second-order material coefficients.

Table 2: Matrix notation rules according to Voigt's convention.

Tensor notation	Equivalent matrix notation
$ii = 11, 22, 33$	$\alpha = 1, 2, 3$
$ij = 23$ or 32, 13 or 31, 12 or 21	$\alpha = 4, 5, 6$
s_{ijkl}	$s_{\alpha\beta}$, both α and $\beta = 1, 2, 3$
$2s_{ijkl}$	$s_{\alpha\beta}$, α or $\beta = 4, 5, 6$
$4s_{ijkl}$	$s_{\alpha\beta}$, both α and $\beta = 4, 5, 6$
d_{ijk}	$d_{i\alpha}$, $\alpha = 1, 2, 3$
d_{ijk}	$\frac{1}{2}d_{i\alpha}$, $\alpha = 4, 5, 6$

where c, α, p, s, d and ϵ are heat capacity, expansion, pyroelectric, compliance, piezoelectric and permittivity coefficients, respectively, and superscripts indicate variables held constant in the definitions of the coefficients. The Δ in σ and Θ indicates that specific initial conditions need to be taken into account while changes in T and E are considered always with respect to zero initial condition. By assuming adiabatic ($\Delta\sigma = 0$) and isothermal ($\Delta\Theta = 0$) conditions, these equations can be further simplified. Moreover, as in the above equations tensors up to the forth order appear, it is common to simplify the notation by using Voigt's matrix notation[10] together with Einstein's summation convention[11] for repeated subscripts [100]. The notation adapted by Voigt [216] takes advantage of symmetries in the material tensors and is summarized in Table 2. Eventually, the simplified set of matrix equations takes the following form

$$S_\alpha = s^E_{\alpha\beta} T_\beta + d^T_{i\alpha} E_i \tag{15}$$

$$D_i = d^E_{i\alpha} T_\alpha + \epsilon^T_{ij} E_j \tag{16}$$

or by omitting the subscripts altogether and using block matrix notation

$$\begin{bmatrix} S \\ D \end{bmatrix} = \begin{bmatrix} s^E & d^t \\ d & \epsilon^T \end{bmatrix} \begin{bmatrix} T \\ E \end{bmatrix} \tag{17}$$

which is known as the *d-form constitutive equation* because the coupling between mechanical and electrical behavior is realized by the *d* piezoelectric coefficient (strain/charge constant), i.e. for non-piezoelectric material $d = 0$. Depending on the choice of independent variables in the formulation of thermodynamical potential, three other isothermal piezoelectric constitutive equations can be defined – *h*, *g* and *e*-form corresponding to the couplings via piezoelectric stiffness, voltage and stress coefficients, respectively. However, these formulations are of no interest for this work and are not further considered. The *d*-form

---

[10] $i, j = 1, 2, 3$ and $\alpha, \beta = 1, \dots, 6$
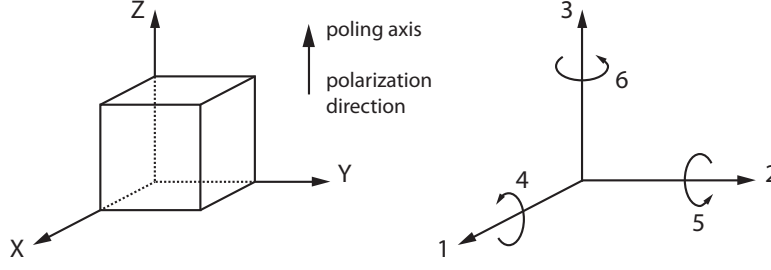[11] $T_\alpha S_\alpha \equiv \sum_\alpha T_\alpha S_\alpha$

Figure 11: Designation of the axes and directions of deformation according to the IEEE Standard on Piezoelectricity.

shown compactly in (17) consists of the *elasto-piezo-dielectric matrix* and is presented below with all direction specific coefficients

$$
\begin{pmatrix} S_1 \\ S_2 \\ S_3 \\ S_4 \\ S_5 \\ S_6 \\ D_1 \\ D_2 \\ D_3 \end{pmatrix} = \begin{pmatrix} s_{11}^E & s_{12}^E & s_{13}^E & s_{14}^E & s_{15}^E & s_{16}^E & d_{11} & d_{12} & d_{13} \\ s_{21}^E & s_{22}^E & s_{23}^E & s_{24}^E & s_{25}^E & s_{26}^E & d_{21} & d_{22} & d_{23} \\ s_{31}^E & s_{32}^E & s_{33}^E & s_{34}^E & s_{35}^E & s_{36}^E & d_{31} & d_{32} & d_{33} \\ s_{41}^E & s_{42}^E & s_{43}^E & s_{44}^E & s_{45}^E & s_{46}^E & d_{41} & d_{42} & d_{43} \\ s_{51}^E & s_{52}^E & s_{53}^E & s_{54}^E & s_{55}^E & s_{56}^E & d_{51} & d_{52} & d_{53} \\ s_{61}^E & s_{62}^E & s_{63}^E & s_{64}^E & s_{65}^E & s_{66}^E & d_{61} & d_{62} & d_{63} \\ d_{11} & d_{12} & d_{13} & d_{14} & d_{15} & d_{16} & \epsilon_{12}^T & \epsilon_{12}^T & \epsilon_{13}^T \\ d_{21} & d_{22} & d_{23} & d_{24} & d_{25} & d_{26} & \epsilon_{22}^T & \epsilon_{22}^T & \epsilon_{23}^T \\ d_{31} & d_{32} & d_{33} & d_{34} & d_{35} & d_{36} & \epsilon_{32}^T & \epsilon_{32}^T & \epsilon_{33}^T \end{pmatrix} \begin{pmatrix} T_1 \\ T_2 \\ T_3 \\ T_4 \\ T_5 \\ T_6 \\ E_1 \\ E_2 \\ E_3 \end{pmatrix}.
$$

(18)

The material coefficients in the above matrix are experimentally determined values for a given piezoelectric material and numbered according to the IEEE Standard on Piezoelectricity [1, 144]. The standard defines the z direction as the polarization direction and numbers the orthogonal axes x, y and z as 1, 2 and 3. The numbers 4, 5, and 6 correspond to rotations about x, y and z (shear stress about these axes). The convention is visualized in Fig. 11. The constants in the matrix are written with subscripts referring to these numbers. For example, s_{26}^E is the compliance for shear stress about axis 6 (z) and accompanying strain in direction 2 (y) under the condition of a constant electric field. In practice, only a few entries in the elasto-piezo-dielectric matrix are of interest for a given application and many are negligibly small and thus assumed zero. In the next chapter [see sect. 3.2.1, eq. (21)] where the physical model of the walking piezoelectric motor (see sect. 2.4) is derived, the set of nine equations in (18) reduces to just two.

The above derivation of the piezoelectric constitutive equations has led to the elasto-piezo-dielectric matrix which describes the global direction-dependent response of a piezoelectric material by coupling its mechanical and electrical behavior in a unified mathematical framework. This idealized response is computed for isothermal conditions and is linear as the piezoelectric coefficients in the matrix are assumed

constant. However, it should be stressed that their values are not invariable. These coefficients describe material properties under small-signal conditions only and vary to some degree with mechanical as well as electrical boundary conditions, environmental conditions like temperature, pressure or humidity, electric field, form factor and time. While the linear approximation is sufficient for many applications and will be used further in this work to model the piezoelectric drive units (legs or bimorphs, see sect. 2.4.1 and 3.2.1), it is important to be aware of the limitations of the linear theory.

Probably the most serious limitation, at least in ferroelectric piezoelectric materials, is the inadequacy in describing material behavior for large signal conditions or signals of varying polarity both electrically and mechanically. This is the consequence of the resistance to domain switching in ferroelectric materials and results in the polarization hysteresis loop, butterfly-shaped strain curve and ferroelastic stress/strain hysteresis loop described in the previous section. Even if operated in the approximately linear unipolar region, ferroelectric materials are still subjected to memory and saturation effects and thus react differently depending on input history and level. These effects are especially important for nano-positioning applications [77, 111, 133] and need to be carefully compensated if absolute accuracy is aimed at. In this work, dielectric hysteresis is assumed to be responsible for nonlinear leg deflection characteristics described in sect. 3.3.3. For low-level hysteresis modeling approaches, the reader is referred to [113, 105, 217, 134] and for hysteresis compensation techniques (e.g. input shaping, dynamic digital linearization etc.) to [178, 21].

Another nonlinear effect not covered by the linear theory is the secondary electromechanical coupling or the *electrostrictive effect*. Electrostriction is a property of all dielectric materials, whether they are crystalline, amorphous, polar or centrosymmetric, which causes them to change shape under the application of an electric field [91]. This relation is quadratic meaning that the induced strain is proportional to the square of applied field; the proportion is described with the electrostrictive coefficient Q. In piezoelectric materials this coefficient is usually lower than the piezoelectric strain coefficient d of the primary linear coupling. However, the electrostrictive effect can become significant if the electric field is gradually increased. Although not further considered in this work, electrostriction plays an important role in a group of so called relaxor ferroelectric ceramics such as $Pb(Mg_{1/3},Nb_{2/3})O_3$ (PMN) in which the electrostrictive effect is much stronger than the piezoelectric and is comparable to piezoelectricity in PZT-based materials. Some advantages of electrostrictive over piezoelectric ceramics are minimal hysteresis, very stable (in terms of aging and creep, see below) deformation and no necessity of poling treatment as these ceramics are operated above their Curie temperature (which is very low compared to typical piezoelectric ceramics). The

disadvantages include a limited usable temperature and frequency range (high temperature and frequency dependence), small deformations at low fields and high drive currents for dynamic operation due to their especially high capacitance [91]. PMN-based actuators have been utilized e.g. in the Hubble Space Telescope to drive the tilt mirrors of its corrector optics [100, 208].

Piezoelectric ceramics exhibit time-dependent non-linear deformation effects under constant mechanical loading known as (mechanical) creep as well as creep effects under constant electrical field [95]. In both cases, the deformation of the material increases/decreases slowly in the direction of the applied loading or field. These effects are important in all application in which stable deformation over time has to be maintained but negligible for dynamic/periodic operation, as in the piezoelectric motor considered in this work, due to their negligible effect on repeatability.

Another class of non-linear influences in piezoelectric ceramics consists of depolarization effects. After poling the ceramic material may be depolarized thermally, electrically or mechanically. Thermal depolarization takes place as soon as the material is heated to its T_C temperature when the domains become disordered and complete depolarization occurs. However, partial depolarization at elevated temperatures can already take place well below T_C [100]. Electrical depolarization occurs whenever the piezoelectric material is exposed to a strong electric field of the opposite polarity to the poling field. The level of depolarization also depends on the time the depolarizing field is applied and the ambient temperature. Finally, mechanical depolarization occurs when the level of mechanical stress on the piezoelectric material becomes high enough to disturb the orientation of ferroelectric domains. Also in this case many factors, e.g. material grade, play an important role. For actuator application, if safety margins given by the manufacturer are respected, the depolarization effects are negligible as re-poling occurs every time a high electric field (high voltage in the periodic drive signal) is applied.

Last but not least, all physical systems have a natural frequency of vibration in whose vicinity they can oscillate with high amplitudes when excited by a periodic driving force at a frequency close to the natural one. This phenomenon is called resonance and the linear theory can only be applied in frequency regions which are not affected by resonance. For some actuators/motors (ultrasonic motors, see sect. 2.3.2) resonance is utilized as the main driving principle and its accurate modeling is naturally of paramount importance for a successful application. In case of quasistatic motors (see sect. 2.3.3), as the one considered in this work, the driving signals are usually far below the resonance regions.

The previous sections were supposed to make the reader acquainted with the phenomenon of piezoelectricity in general and with the
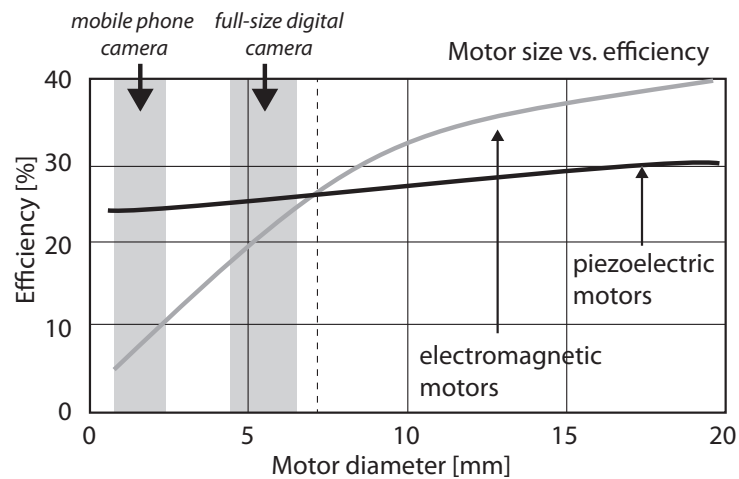
Figure 12: Efficiency vs. motor size. Piezoelectric motors whose efficiency is virtually not affected by size are superior to electromagnetic motors in mini-motor applications. Courtesy of New Scale Technologies, Inc.

workhorse of piezoelectric actuation, the ferroelectric ceramic PZT [209] in particular. The linear theory of piezoelectricity described in this section together with the non-linear effects in ferroelectric ceramics form the foundation for any actuator modeling approach and will show themselves especially useful in sect. 3. The following sections will give an overview of current piezoelectric linear motor technology (sect. 2.3) and describe the construction as well as the working principle of the walking piezoelectric motor (sect. 2.4).

2.3 PIEZOELECTRIC MOTORS

Piezoelectricity plays nowadays the most prominent role in actuator applications next to electromagnetic, hydraulic and pneumatic actuators [209, 207, 95]. While the latter actuation principles dominate the industry whenever large displacements or high force/torque output are relevant, piezoelectric actuation has dominated applications where compact size, fast response and highest positional accuracy are of importance. This area of application is naturally determined by the characteristics of piezoelectric energy conversion which is scalable, direct (no resolution limiting moving parts), fast (acceleration rates over 10000 g possible) and controllable down to sub-nanometer range [209]. Moreover, as new techniques of (unlimited) movement amplification (see next section) are developed and even more importantly the demand for small-sized actuator applications gains momentum, piezoelectric motor technology is likely to gain further on importance. This tendency is explained graphically in Fig. 12. Piezoelectric motors
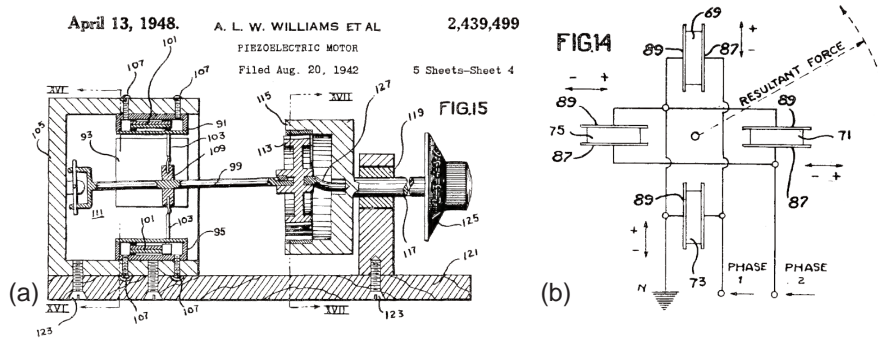
Figure 13: Schematic drawings of the first piezoelectric motor developed by
L.W. Williams and W.J. Brown from the patent application [223]
filled at United States Patent Office in 1942. (a) cross-sectional
view of an embodied motor and (b) diagrammatic view exempli-
fying the mode of operation.

are virtually insensitive to size in terms of efficiency [164]. The com-
mercially available motors maintain a typical efficiency of about 30 %
whereas the efficiency of electromagnetic motors decreases steeply for
motor size below 10 mm – a critical size for many electronic devices.[12]
Uchino [209] compares the piezoelectric and electromagnetic motors
in terms of efficiency as the function of power consumption and es-
timates that the later are inferior to the former in the power range
below 30 W.

Some strong points of piezoelectric motor technology can be already
recognized in the patent application for the invention of the first
"piezoelectric motor" from 1942 [223]:

> [...] Another object is to provide an electric motor that shall
> not require commutators, slip rings or the like for convey-
> ing alternating electric potentials [...] wherein vibratory
> movement of a piezoelectric crystal element is translated
> into rotary motion of a driven part without the interposi-
> tion of gears, ratchet wheels or like [...] and provide speed
> reducing means devoid of gears of conventional type.

The inventors obviously had in mind as simple as possible direct drive.
Two schematic illustrations from this patent application (granted in
1948) can be seen in Fig. 13. The motor consisted of multiple piezo-
electric flexing elements so arranged that their vibrational motion
was converted into rotary motion of a shaft and gear. Besides their
(generally) simple structure, no need of a reduction stage and suit-
ability for miniaturization, piezoelectric motors offer other important

---

[12]The theoretical efficiency of piezoelectric motors is much higher, e.g. 98 % for
standing-wave ultrasonic motors [100] but practically it remains at about 30 % in
commercial products due to losses in the drive circuitry, piezoelectric and elastic
materials and due to friction.

advantages including quick response, wide velocity range, excellent controllability and position resolution, high power/weight ratio and efficiency, no backlash, no power consumption in steady state, very low or no maintenance effort, EMI and vacuum compatibility, operation at cryogenic temperature and high temperature sterilization, non-flammability, etc. The disadvantages include reduced durability due to frictional drive, dropping velocity under load, necessity of high-frequency power supply and high electric fields. For a more complete discussion on this topic, the interested reader is referred to the literature [209, 207, 96, 112].

In the subsequent sections, a selection of contemporary piezoelectric motors will be discussed. The discussion will be constrained to linear motors due to the focus of this thesis starting with a general classification of piezoelectric linear motors (next section), followed by several examples of ultrasonic (sect. 2.3.2) and quasistatic (sect. 2.3.3) linear motors.

2.3.1 Classification

The classification task should start with a clear definition of the term *piezoelectric motor* and how it differs from the term *piezoelectric actuator*. In the literature the terms are often used interchangeably or a vague distinction is made. In this work, the following definitions after [194] are adopted:

- *Piezoelectric actuator* is an electro-mechanical energy transducer which converts electrical energy into motion using the inverse piezoelectric effect.

- *Piezoelectric motor* is an electro-mechanical drive system in which the limited displacement of a piezoelectric element is converted into the unlimited rotary or translatory (in case of linear motors) motion of a rotor or slider.

According to the above definitions every piezoelectric element can be considered an actuator if it is utilized with the objective to produce motion. However, the travel range of a simple actuator is naturally limited by the maximum possible deformation of the material. In more complex actuators the displacement can be amplified in terms of space by using a suitable mechanism. The most common techniques are listed below with the indication of further references for the interested reader:

1. Amplifying longitudinal strain by stacking actuators
   - high-voltage discrete stack actuator [140]
   - low-voltage co-fired multilayer actuator [202]

2. Producing bending motion by internal leverage

- unimorph actuator [209]
- bimorph actuator [209, 58]
- multimorph actuator [129]

3. Coupling longitudinal strain to a rigid strut or shell via flexures

- moonie actuator [154, 209]
- cymbal actuator [209, 59]

4. Monolithic hinge lever mechanism [209]

5. Using a combination of the above techniques

- monomorph/rainbow actuator [90, 210]
- thunder actuator [53, 157]

Strictly speaking, the (functionally) bimorph drive elements of the walking motor (see sect. 2.4) also use a combination of the above techniques (multilayer as well as bimorph actuators, see sect. 3.2.1) in order to increase the displacement of the legs. In addition to the above direct amplification techniques, other forms of amplification in connection with a secondary amplification system (lever mechanism, oil-pressure amplifier, etc.) are employed [209, 172].

In case of piezoelectric motors a further step is taken. They utilize either simple actuators or some of the above-mentioned amplification techniques and additionally accumulate the small displacements by means of intermittent frictional coupling with a movable element. Thus the displacement amplification occurs in terms of time. The resulting macroscopic movement is either rotatory or translatory depending on the constraints imposed on the movable element. In the following sections only the latter type will be considered. A possible classification of piezoelectric linear motors based on their working principle is approached in Fig. 14. The top-level branching in the diagram builds up on the distinction between the resonant (ultrasonic, speed-controlled) and non-resonant (quasistatic, position-controlled) mode of operation. In the following sections these two classes of piezoelectric motors are introduced with the objective of showing the diversity of actual designs and providing the reader with a reference to commercially available products.

2.3.2 Ultrasonic motors

In ultrasonic motors, a piezoelectric actuator is driven by a high-frequency power supply at one of resonant frequencies of the actuator to make it oscillate with an increased amplitude. This oscillation of the actuator produces motion of a movable part (slider) through their smooth frictional contact. The name *ultrasonic* is supposed to reflect the fact that the motors are operated at ultrasonic frequencies (above
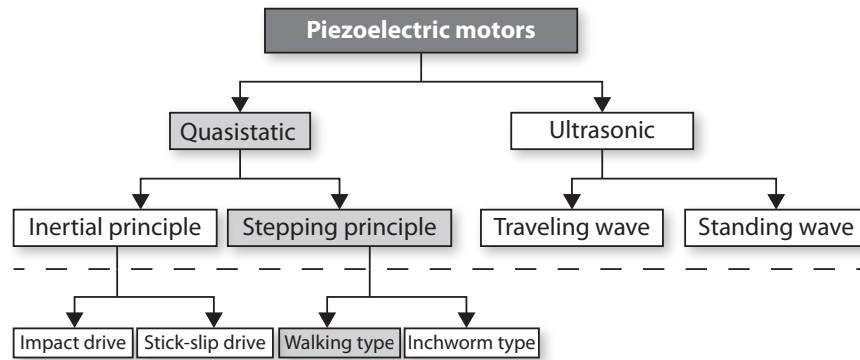
Figure 14: Classification of piezoelectric linear motors according to their working principle. The gray-shaded path illustrates how the classification applies to the walking piezoelectric motor.

20 kHz) and thus their operation is not audible. However, this name may be misleading because the resonance frequency of a particular motor design may lie in the audible range and because there are other non-piezoelectric (solid state, e.g. magnetostrictive) motors which operate in the ultrasonic range. With this side note in mind, the naming convention is so widely accepted that it is also used in this work. From the vibration characteristics point of view two types of ultrasonic motors exist – the standing-wave (or stationary-wave) and the traveling-wave (or propagating-wave) type. By waves mechanical oscillations traveling through the piezoelectric medium and induced through resonance are meant.

The standing-wave type is also called vibratory-coupler type due to the fact that the motion of the vibrating element is transferred to the slider as a series of microscopic pushes. In the simplest possible design, these pushes provide a unidirectional force transmission. While this may be sufficient for many rotary applications, bidirectional motion is usually needed for linear motors. The bidirectional motion can be obtained either by employing at least two separate vibrating elements excited with a phase difference or by superimposing two oscillations in a single resonator (bimodal motor). An example of the former design is the motor by Endo et al. [64] which employs two longitudinal effect piezoelectric elements arranged at right angle to each other which produce an elliptical vibration locus of a common tip. The direction of motion can be reversed by swapping the drive signals between the elements. Another interesting design of this kind is the piezoelectric motor using two orthogonal bending modes of a hollow cylinder developed by Uchino et al. [125]. The original design is a rotary motor. A linear version has been commercialized by New Scale Technologies, Inc. (Victor, NY, USA) in a series of *Squiggle* motors. The smallest version of this motor is shown in Fig. 15. The motor consists of four piezoceramic actuators, a threaded nut and
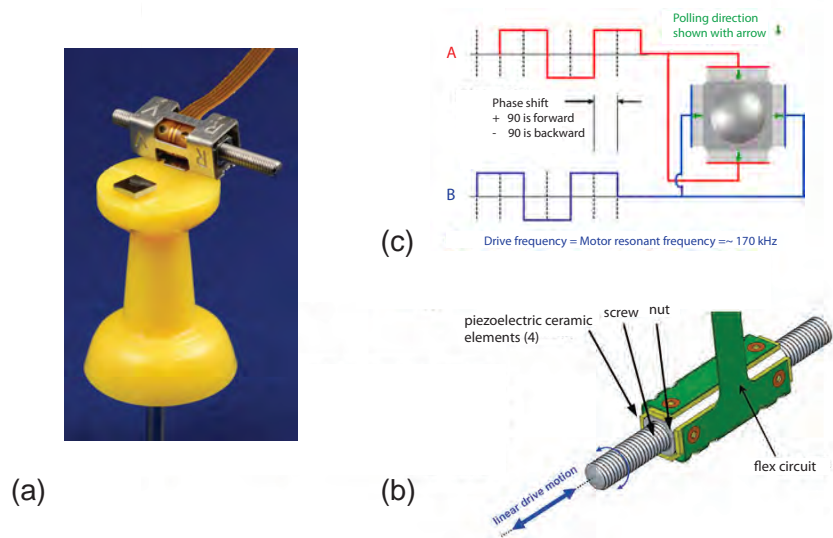
Figure 15: The squiggle motor from New Scale Technologies, Inc. is one of world's smallest linear motors. (a) Photograph of the motor giving the impression of its size. Next to the motor on top of the board pin is the motor drive ASIC. (b) CAD drawing illustrating the component of the motor. (c) Schematic illustration of electrical connections to the piezoelectric ceramic elements. Courtesy of New Scale Technologies, Inc.

screw. The actuators are pressed against the surface of the nut and excited with a 2-phase drive signal [see Fig. 15(c)] which imparts a wobbling "hula hoop" motion in the nut at the resonant frequency of about 170 kHz and thus causes the screw to rotate and translate. The translation of the screw is bidirectional depending on the phase difference between the excitatory phases. The design is very compact and has low manufacturing costs [194].

The other type of a bidirectional standing-wave motor is the bimodal motor. The first known motor of this type was invented in 1970s by Russian scientists [214]. They used 4 diagonally arranged electrodes to excite the longitudinal and bending mode oscillations in a plate-shaped actuator. The superposition of the oscillations led to an elliptical motion of surface points. The idea was commercialized by the company Nanomotion Ltd. (Yokneam, Israel). A selection of interesting designs of bimodal motors is offered by the company Physik Instrumente GmbH (Karlsruhe, Germany) in their *PILine* drive line. The operation of these motors is based upon resonant asymmetric excitation of a two-dimensional standing extension wave in a piezoceramic plate element. The basic design is shown in Fig. 16. The actuator consists of a piezoceramic plate having the dimensions LxWxH (x,y,z) and being polarized in the y-direction. The two largest faces of the plate are covered with electrodes – one common drain on the bottom face and two excitation electrodes on the top face each covering half
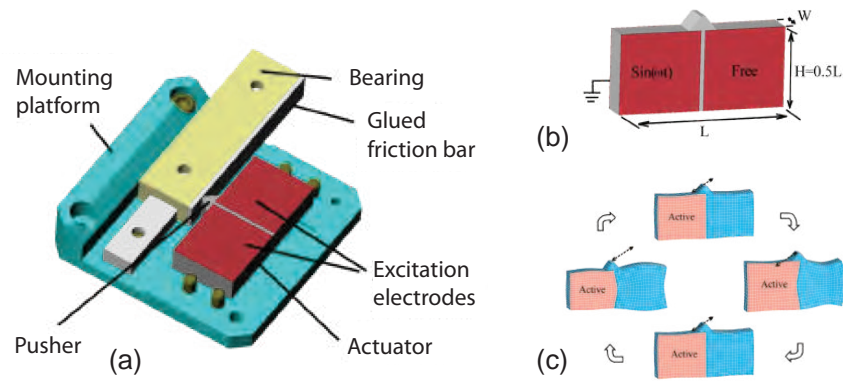
Figure 16: Bimodal standing-wave motor from Physik Instrumente (PI) GmbH. (a) CAD drawing of motor components in a linear stage. (b) Piezoceramic actuator with the indication of its dimensions and the placement of electrodes. (c) Harmonic analysis using a FEM-model showing the straight line motion of the pusher. Courtesy of PI.

of the surface. A wear-resistant pusher made of aluminum oxide is placed between these electrodes on one of the long perpendicular faces and pressed against a guided slider. The actuator is excited with a sinusoidal voltage applied to one of the excitation electrodes while the other floats. The excited oscillation can be described mathematically by two standing waves in x- and z-dimensions.[13] The pusher moves along a straight-line trajectory inclined at either $45°$ or $135°$ depending on the direction of motion [see Fig. 16(c)] and provides microscopical pushes which drive the slider at a resonant frequency of approximately $63\,$kHz. The direction of motion can be changed by applying the drive signal to the previously floating electrode and letting the other electrode float.

The other type of ultrasonic motors according to the classification from Fig. 14 is the traveling-wave type. It was invented by Sashida [174] in 1982 and commercialized one year later by Shinsei Corporation (Tokyo, Japan). The original invention was a rotary motor. Rotary motors of this type are nowadays ubiquitous in camera auto focus lenses and wrist watches. Linear traveling-wave motors, however, are much less popular [96] and more difficult to construct. They are mentioned here for the sake of completeness of the discussion. Traveling-waves can propagate on a closed ring-type stator easily in contrast to a finite medium, e.g. a bar, in which they get partially reflected upon hitting its boundaries which leads to the formation of standing waves. Thus, traveling-waves can be generated stably in a limited size medium only by superimposing two standing waves whose phases differ by $90°$ from each other both in time and space [207].

---

[13]Specifically, an extensional wave of the E(3,1) mode can be excited in the plate if its L/H ratio is approximately 2:1. For a detailed treatment of this topic, the interested reader is referred to the theory of wave propagation in elastic plates and to [213].

It follows that two vibration sources are required to generate one propagating wave decreasing the overall motor efficiency. Another difficulty in the successful application of traveling-wave motors is the construction of the support for the stator because no steady nodal points exist. Several designs of linear traveling-wave motors have been proposed [127, 98, 205]. In the design by Kurosawa et al. [127] two piezoelectric vibrators are installed at both ends of a steel rod. These vibrators excite and receive a traveling transverse wave. By adjusting a load resistance in one of the vibrators, a perfect traveling wave can be obtained. The wavelength is chosen as short as several mm in order to provide a stable surface contact to a slider which clamps the transmission rod with an appropriate force via a rubber coating. The design has a poor efficiency because the whole rod needs to be excited although only a small part of it is used for the output. No commercial application is known to the author.

2.3.3 Quasistatic motors

Quasistatic motors are the other large class of piezoelectric motors next to ultrasonic motors. Their name reflects the mode of operation in which, at least conceptually, several discrete stages can be distinguished and the operation can be stopped at any point while cycling through the stages in a *quasistatic* state. Thus, this type of operation is rather position than velocity controlled in contrast to ultrasonic motors in which there is no such control over the resonating structures. The term *quasistatic* should not be confused with the definition from thermodynamics in which infinitely slow processes are meant. Although operated well below its resonant frequency, a quasistatic motor driven at 1 or 10 kHz can hardly be called static. The main advantage of this kind of motors is their theoretically unlimited resolution (down to sub-nanometer range) as the amount of displacement imposed by the actuator(s) on the moving part can be controlled precisely even in open loop systems. As a matter of fact, most piezoelectric motors except of the traveling-wave type can, in principle, be driven quasistatically [96]. Still, due to their substantially higher drive frequency and amplified displacement ultrasonic motors are preferred in applications where high velocity and noiseless operation count. Quasistatic motors operate according to one of two principles – the inertial or the stepping principle.

As far as inertial principle motors are concerned, there are roughly two classes of motors belonging to this group – *stick-slip drives* drives incorporating a fixed actuator and *impact drives* which have a moving actuator. However, the former term is often used generically to describe both of these classes. In the actual stick-slip drives with a fixed actuator, two movement stages can be distinguished. First, the actuator expands slowly and the slider follows this movement due to
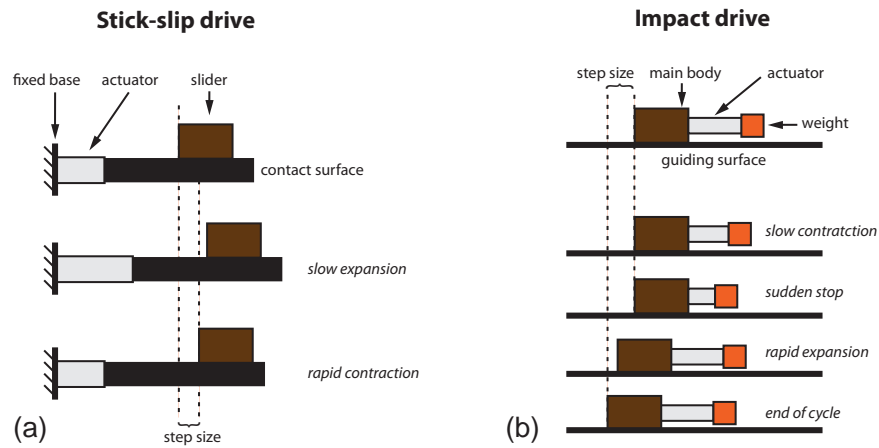
Figure 17: Schematic depiction of the actuation stages in (a) the stick-slip and (b) impact drive piezoelectric motors. The dotted lines indicate the magnitude of displacement per cycle (step size).

static friction (stiction). Next, the actuator contracts so rapidly that the slider is unable to follow this movement and lets the actuator slip back due to its own inertia and the not sufficiently high dynamic friction. This principle is depicted schematically in Fig. 17(a). In this way, a stepwise motion pattern of the slider is obtained. The direction of motion is determined by the mode of the slow movement (expansion or contraction). The above motion principle can be compared to the "tablecloth trick" in which dishes remain on the table after a quick pull of the cloth, while a slow pull makes the dishes follow the cloth. Commercial piezoelectric motors utilizing this principle are offered e.g. by New Focus (Santa Clara, USA) in their *Picomotor* products.

In impact drive motors, static friction and impulsive force caused by a rapid displacement of the actuator are utilized. An impact drive motor consists conceptually of three main parts: the movable main body, the actuator and the inertial weight. The main body is placed on a guiding surface to which it has frictional contact. The actuator is attached at one end to the main body and at the other end to the inertial weight. Neither the actuator nor the weight touch the surface. The drive cycle consists of four stages depicted schematically in Fig. 17(b). It starts with the actuator fully extended followed by its slow contraction so that the inertial force on the main body remains smaller than the static friction between the main body and the surface – the main body maintains its position. This contraction is stopped suddenly at the end of the process breaking the static friction and immediately a rapid extension of the actuator follows which causes impulsive inertial force to be exerted on the main body. The main body follows in the direction of the force (away from the inertial weight). This drive cycle results in a stepwise motion of the main body as in the stick-slip drive. In order to change the direction of motion the

Six step actuation processes of the piezoelectric inchworm motor
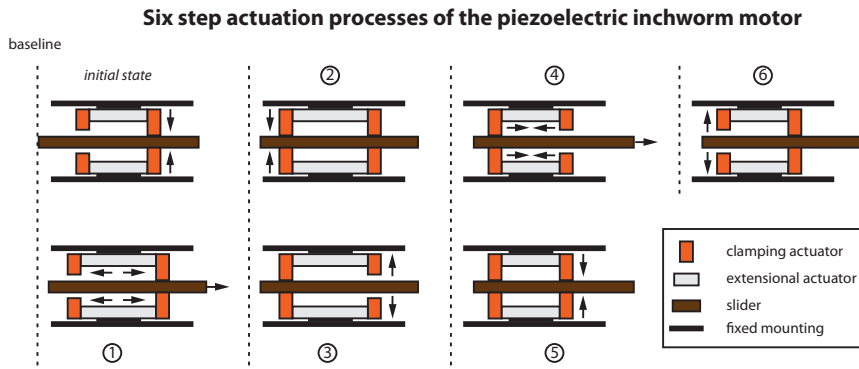
Figure 18: Schematic depiction of the actuation stages in an inchworm motor with two (pairs of) clamping and one (pair of) extensional actuator(s). Note the translation of the slider in step 1 and 4 indicated by a direction arrow. The dotted reference baseline indicates a common initial position in all pictograms.

extensional stage needs to become slow and the contraction stage fast. This kind of motors has been employed e.g. in a 3-DOF UHV (ultra high vacuum) positioning stage [227] and in a precision assembly device [228]. Impact drive motors are employed commercially in products of Owis GmbH (Staufen, Germany).

Quasistatic motors based on the stepping principle are sometimes called *clamping-type* motors in analogy to the working principle of the *inchworm motor* [143] which was the first motor of this type introduced to the commercial market by Burleigh Instruments, Inc. (NY, USA). Fig. 18 illustrates the actuation stages of a typical inchworm motor. The slider is initially clamped by one of the clamping actuators. In step ①, the extensional actuator expands increasing the distance between the clamping actuators. The clamped slider moves away from the open clamp. Subsequently the open clamp closes in step ② and the previously closed one opens – step ③. When the extensional actuator contracts in step ④, the distance between the clamps reduces and the clamped slider moves further in the desired direction. Finally, in steps ⑤ and ⑥, the clamping actuators change their roles again and the whole cycle starts anew. By reversing the clamping sequence the direction of motion becomes reversed. The maximal stroke of a single cycle depends on the length and maximum strain of the extensional actuator. The no-load motor velocity depends on the stroke and the drive frequency. The holding force of the motor is dependent on the blocking force of the clamping actuators as well as the friction coefficient between them and the slider. The well-ordered sequence of clamping and unclamping or contact establishment and disestablishment in the inchworm motor is typical for all stepping principle motors, also for the *walking type motors* which will be described in detail in the next section.

The discussion of the walking type stepping principle quasistatic motors has been purposely postponed and is covered now in a separate section. While the overview of other motor types from the previous section was supposed to provide a possibly wide range of illustrative examples, it was necessarily superficial. In this section a more detailed discussion of the walking drive principle (sect. 2.4.1), motor construction and the fabrication process of the drive units (i.e. legs) (sect. 2.4.2) is presented.

2.4.1 The walking principle

In the walking type motors several drive elements (legs) alternately engage and disengage in a frictional contact to a movable slider. This sequence is similar to the clamping/unclamping mechanism of the inchworm motor. However, in walking type motors both the clamping and advancing of the slider is realized by the same legs in contrast to the separate set of clamping and extensional actuators in the inchworm motor. Thus, the drive elements of the walking motor can be intuitively compared to legs which can move up and down as well as forward and backward and the whole movement cycle can be compared to a walking sequence of these legs on a movable treadmill – i.e. the slider. Several different designs of the drive elements are conceivable including stacking one longitudinal mode (clamp/unclamp movement) and one shear mode (forward/backward movement) actuator as in the PiezoWalk drives from Physik Instrumente GmbH or using one of the many possible designs of piezoelectric benders [209, 172] as long as the design allows elongation of the bender. An especially advantageous design of the drive elements in terms of displacement amplitudes is obtained when monolithic multilayer actuators can be made behave functionally like extensible benders. This kind of drive elements is employed in the piezoelectric motor modeled in this work. The technology is patented by the companies Physik Instrumente GmbH [142] and PiezoMotor Uppsala AB [114]. Further details on the fabrication process of the drive units are given in the next section, while the mathematical models describing motion of the legs are derived in sect. 3.2 and 3.3. A graphical illustration of the walking principle utilizing leg elements in the form of extensible piezoelectric benders is shown in Fig. 19. From the functional point of view, each leg can be conceptually seen as consisting of two elongated longitudinal mode actuators which can extend and contract independently because of their electrical separation. These actuators are mechanically coupled so that an elongation/contraction of just one of them causes the whole structure to bend. A pure elongation or contraction is only possible if an electrical field of the same magnitude is applied to both of them.
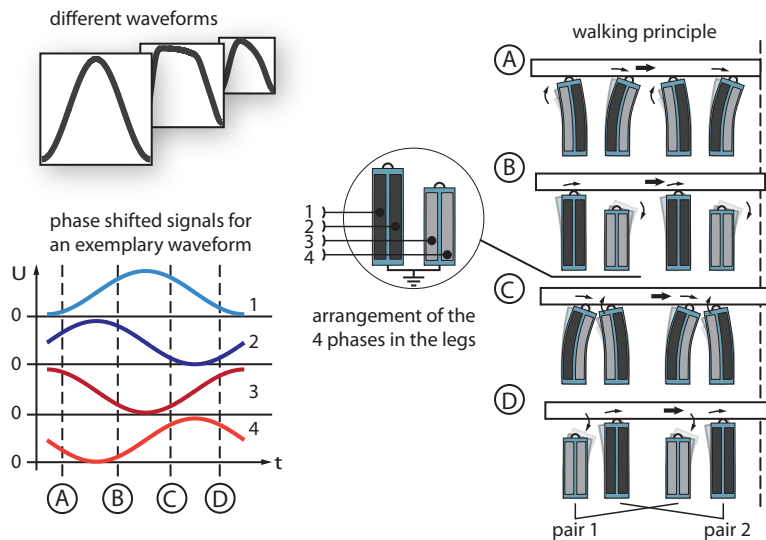
Figure 19: Drive principle of walking piezoelectric motors. One walking cycle is shown for an exemplary sine-shaped driving waveform. The drive signal consists of four phase-shifted electrical phases (numbered 1-4). The phases are connected to the legs as shown in the encircled region. The four legs are arranged in two pairs, each pair receiving the same driving signals (e.g. first and third leg from the left). The capital letters next to the walking stages correspond to the sampling time of the drive signal. Darker shading indicates higher drive voltage, arrows indicate the direction of motion of leg tips and of the slider.

In a walking cycle, the legs alternately establish contact to a movable slider which is pressed against them with some kind of preload (see next section). The contact to the slider is maintained by those legs which are most extended and while in contact, these legs advance the slider in the direction of their bending motion due to friction. This alternating contact sequence is a necessary condition for the walking principle to work (cf. sect. 3.4.1). It follows that at least two legs are required in a walking type motor. However, in order to ensure static stability of the slider, it has to be supported at least at two different points along its length at any given time. For this reason, four legs in two pairs are employed in practical designs; also in the PiezoLegs motor considered in this work. Each leg in a pair receives the same control signals – two signals per leg for each of the longitudinal mode actuators. Thus, a four phase signal is necessary to drive the motor consisting of two pairs of legs.[14] The higher the driving signal (i.e. voltage) the higher the electric field and consequently the elongation of a given actuator. In the walking sequence of Fig. 19, an exemplary sine-shaped four phase drive signal is used. There is a 90° phase shift between phase 1 and 2. Phase 3 and 4 are phase shifted 180° with

---

[14]A pair, or an m-tuple, can consist of m legs in a theoretical design of the walking motor. This fact is accounted for in the general motor modeling strategy of chapt. 3.

regard to phase 1 and 2, respectively. The effect is as follows. At the time point marked with an Ⓐ, phases 1 and 4 are relatively low while phases 2 and 4 relatively high. Thus all legs are bent – pair 1 to the left and pair 2 to the right. Pair 2 is at the moment slightly higher than pair 1 and thus maintains contact to the slider which has been forwarded by its bending motion to the right. In the next step, Ⓑ, pair 2 contracts while pair 1 has taken over the contact to the slider and advances it while bending to the right. At time point Ⓒ, pair 1 reaches its maximal bending to the right while pair 2 being now bent to the left expands to take over the contact to the slider. Finally, in Ⓓ, pair 1 has retracted and pair 2 being now in frictional contact with the slider moves it to the right. The next time step in this sequence would again be Ⓐ completing one walking cycle. During this cycle, the slider has been all the time advanced to the right. In order to change the direction of motion phase 1 would need to be swapped with phase 2 and phase 3 with phase 4 or the sequence Ⓐ-Ⓓ be reversed. In any case, in order for the motor to move in a given direction both pairs of legs need to move most of the time in the same direction while contacting the slider. The non-contact times are used to reposition the legs before contacting the slider again. This requirement together with the alternating leg contacts to the slider provides the basic rules of the walking principle.

Besides the sine-shaped driving signals (waveforms), other periodic waveforms as well as phase relations between them are conceivable [145, 146] and employed in order to optimize particular aspects of motor performance (e.g. speed, maximal stall force, etc.). By using different waveforms, important insights into the internal workings of the motor can be gained. In the following chapter (chapt. 3), the *force* waveform, which improves the stall force characteristics of the motor, will be used additionally to the *sine* waveform. This will prove useful in identifying a nonlinearity in leg deflection characteristics (sect. 3.3.3). It will be also shown that in reality there are overlapping contact times between both pairs of the legs and the slider and how these contact times are influenced by the choice of a particular waveform (sect. 3.4.1). Finally, in chapt. 5, a bio-inspired waveform generation strategy is proposed. In simulation, this strategy proves to be superior to any particular fixed periodic waveform. Its practical application would require an independent control over each of the four legs as opposite to the pairwise control. Before proceeding to the chapters concerned with motor modeling and waveform generation, the last section of this chapter provides details on motor construction and leg fabrication process.
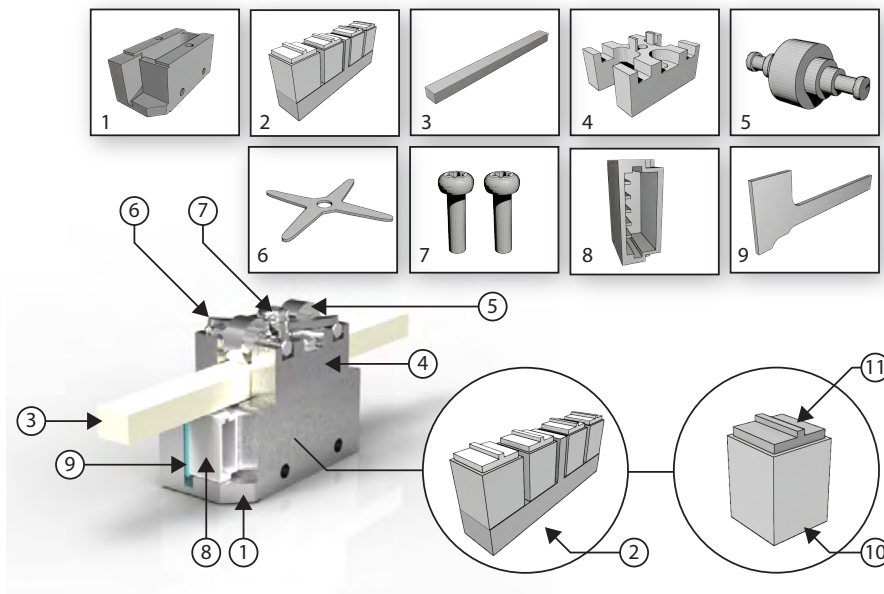
Figure 20: Computer rendering of the walking piezo motor (PiezoLegs). The motor consists of only a few parts which are numbered and displayed in separate boxes. Inside of the lower housing (1) the drive unit (2) with four piezoelectric leg elements (10) is placed. Each leg has a wear-resistant cap made of aluminum oxide on its top face (11). The description of all parts can be found in the running text.

2.4.2 Walking motor construction

The different drive strategies used in piezoelectric motors including the walking principle can be understood easily. The actual construction of a device utilizing these principle is a more demanding technological challenge. On overview of this process is sketched below.

The commercially available walking piezo motor PiezoLegs considered here is produced by the Swedish company PiezoMotor Uppsala AB. Similar motors are offered by the German company Physik Instrumente GmbH. The motor consists of only a few parts which are shown in Fig. 20. Inside of a steel lower housing marked with (1) there is a drive unit (2) consisting of four leg elements made of a soft-type PZT. Each leg is a piezoceramic multilayer bimorph (10) covered with a wear-resistant aluminum oxide cap (11). Backfaces of the legs are coated with electrodes and soldered to a flexible printed circuit board (flex circuit, PCB) (9) on which a 5-pin socket (8) (JST SH BM05B-SRSS_TB) is mounted. The socket is the interface to the driving circuitry (see chapt. 6) which provides the legs with a 4-phase signal and a common ground. A 50 mm long ceramic bar (3) (drive rod, slider) is placed on top of the legs and pressed against them by means of two roller bearings (5) whose outer ring can roll freely on the slider. The inner ring is elongated and supported by the upper steel housing (4). The

upper and lower parts of the motor housing are screwed together with M1.6 hexagon cap or torque screws ⑦. The preload force required to press the slider against the legs is generated by a stack of cross-shaped leaf springs ⑥. The central part of the springs has a whole in it and is screwed to the upper housing while the arms of the springs lay on the elongated parts of the bearings pressing them against the slider. The preload level can be adjusted with the central screw.

Especially interesting from the technological point of view is the fabrication process of the drive elements (legs). According to the classification from sect. 2.3.1, the drive elements are composite actuators because they are both multilayer and bending mode actuators. Multilayer structure is chosen in order to increase the displacement and decrease the driving voltage at cost of a higher current and lower structural rigidity. There are two basic techniques for the fabrication of a multilayer structure – *cut-and-bond* and *tape-casting* method [209, 208] which is also used for multilayer capacitors. In the first method, multiple polished ceramic discs are prepared and stacked together with metal foils in-between the layers serving as electric leads. The minimal layer thickness in this method is limited to about 1 mm and thus it is not suited for small-sized, low-voltage actuators.[15] In the second method, ceramic *green sheets* with printed electrodes are prepared, laminated and co-fired with internal electrodes.[16,17] Much thinner layers below 100 μm and lower driving voltages are possible with this method. A variation of the tape-casting method [185, 186] is used to produce the drive elements of the walking motor. Several steps which the method consists of are described in detail in appendix A.

This chapter provided the reader with the basic knowledge about the piezoelectric technology in general and the construction as well as the working principle of the walking piezoelectric motor in particular. The next chapter opens the main part of this work concerned with modeling of the walking motor.

---

[15]A multilayer actuator with 90 1 mm layers would have to be 9 cm long and would generate ten times smaller displacement in relation to its length for the same amount of applied voltage as compared to a 9 mm long actuator consisting of 90 100 μm thick layers.

[16]"Green" refers to the approximate color of the ceramic slurry, i.e. a mixture of ceramic powder and organic binders, formed in the shape of a flat sheet by a forming machine.

[17]Co-firing refers to the fact that electrodes can be applied already to the green material and sintered in one step. A prerequisite for this process is a ceramic material which can be sintered at relatively low temperatures below the melting point of the electrodes.

3 | PHYSICAL MODEL OF MOTOR DYNAMICS

ABSTRACT

In this chapter a novel dynamic model of a contemporary linear piezoelectric motor is presented. The model is based on physically meaningful parameters and macroscopically measured data in fully assembled state. The model describes the frictional interaction between multiple piezoelectric legs and a ceramic rod. It consists of two orthogonal dynamics which are coupled together by means of preload and frictional forces. Linearity of the model is maintained through most of the modeling stages with clear indication of nonlinear effects due to hysteresis, friction and impact dynamics of the legs. Unknown model parameters are estimated within a global optimization procedure and bounds on parameter values are indicated. The presented model explains the linear drive frequency/velocity as well as the nonlinear load force/velocity characteristics of the motor within its full operational range. The insights gained throughout the modeling process indicate the possibilities of design improvements. Moreover, the model is able to explain the resonance phenomena limiting the range of motor operation and is used to develop an alternative drive strategy in chapt. 5. The content of this chapter is based on publication I.

3.1 INTRODUCTION

The previous chapter has introduced the walking piezoelectric motor and provided details on its construction and fabrication process (sect. 2.4) as well as laid the mathematical foundation (sect. 2.2.3) for modeling of piezoelectric phenomena. These prerequisites will prove very useful in formulating the physical model of the motor in this chapter which marks the beginning of the main part of this thesis. The derivation of a physical motor model will provide a framework for understanding the interaction between the legs and the drive rod, the effect of different drive signals on motor performance and the performance limiting factors. In chapt. 5 this physical model will be used to validate a bioinspired drive strategy and show its superiority to classical approaches.

As far as models of quasi-static legged motors are concerned, there exist only a few of them in the literature. These models either rely on transfer function identification techniques [145] (see also chapt. 4) or they are based on the finite element method (FEM) [9]. While the first approach is well suited to provide a motor model based on

macroscopic measurements in a narrow region of operation, it provides little physical insights and falls short of reproducing the holistic behavior of the motor. On the other hand, FEM-based approaches require a good knowledge of motor construction and low-level material properties but can accurately reproduce its low-level behavior. The disadvantage lies in their high computational costs. Moreover, it is often not possible to obtain low-level experimental data for the model if the motor is fully assembled or expensive sensors are required in order to obtain the measurements. Merry [146] recently proposed a contact dynamics model which accurately describes the behavior of a nano-positioning stage employing the legged motor for frequencies below 50 Hz. However, the motor is suited for a much higher range of frequency up to 3 kHz [200]. Moreover, the proposed model does not consider the effect of tangential load on motor velocity and requires a dedicated numerical solver. The focus of the above models is put on precise positioning capabilities and low-velocity operation in load-free condition.

This chapter presents a physical model of the legged piezoelectric motor which can be used e.g. as force generator in small-sized robotic applications. The model is based on physically meaningful parameters and macroscopically measured data in fully assembled state. The presented model explains the behavior of the legged motor within its full range of operation even under load. In this chapter, the focus is also put on functional aspects of motor operation which shows possible design improvements and anticipates an alternative drive strategy for even higher motor velocities. This chapter is organized as follows. In sect. 3.2 a kinematic model of the legs is derived and a general notation for a motor driven by N legs is introduced.[1] Leg dynamics as well as the effect of hysteresis on leg deflection is presented in sect. 3.3 while the two-dimensional interaction dynamics between the legs and the drive rod is presented in sect. 3.4. In sect. 3.5 the optimization procedure used to find the unknown model parameters is introduced followed by a discussion on model shortcomings in sect. 3.6.

---

[1]Following notation with regard to mathematical expressions is used in this chapter. Constants like N or general terms like z-dimension are given with a regular sans-serif typeface. The only exception concerns the inertia I (capital "i") which has serifs in order to distinguish it easily from an l (lowercase "l"). Variables like z_s, U^+ or M^A are given with an italic serif typeface. The same convention holds for vector-valued expressions like **a** or **D** but bold-faced fonts are used. Additionally, calligraphic letters like in $\mathcal{D}$ or $\mathcal{L}_z$ are used to denote the functions which represent final expressions for model components and are used as their labels in the block diagrams.
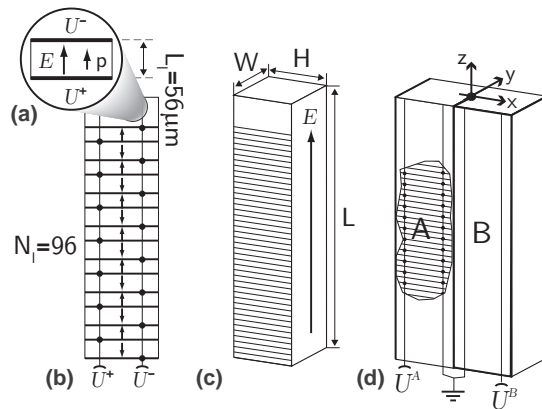
Figure 21: Simplified structure of a multilayer piezoelectric bimorph. (a) detailed view of a single piezoelectric layer between two electrodes. The direction of polarization p and of the electric field E are indicated. (b) piezoelectric stack consisting of N_l layers. Electrical connections between the electrodes and two voltage sources are indicated with dots, the resulting directions of electric field with arrows. (c) stack dimensions. (d) bimorph element consisting of two stacks (A and B) connected to independent voltage sources and a common ground.

3.2 LEG KINEMATICS

Legs are the basic constituent and functional elements of the piezoelectric motor introduced in the previous chapter. In the following section, a kinematic model of a multilayer piezoelectric bimorph, i.e. a single leg of the walking motor, is derived based on the inverse piezoelectric effect and the theory of elastic deflection of beams. Furthermore, a general notation for a motor consisting of N pairs of M legs each is introduced. In accordance with the walking principle (see sect. 2.4.1) all legs belonging to one pair perform the same movement. Sect. 3.2.2 describes the electrical signals (waveforms) needed to drive the legs of the walking motor.

3.2.1 Piezoelectric bending beam

Piezoelectric bimorphs come in different versions due to differences in manufacturing methods [191]. Those employed in the PiezoLegs motor are tape-casted multilayer bimorphs with interdigital electrode configuration [209]. Fig. 21 shows a simplified structure of such a bimorph element while the construction and fabrication details of similar structures can be found in sect. 2.4.2. To a good approximation, the bimorph consists of a series of N_l soft-type ceramic (EDO EC-76)

layers which alternate in the direction of polarization p (Fig. 21[a]) and together constitute a stack of height L. The ceramic layers are separated with screen-printed electrodes which are connected to two external voltage sources U^+ and U^- in such a way that the resulting electric fields coincide in polarity with the polarization p in the corresponding layers and cause their elongation.[2] As each layer experiences the effect of its own electric field, the overall effect is a large electric field experienced by the entire stack (Fig. 21[c]). Two stacks which are coupled together mechanically form a bimorph. Fig. 21(d) shows how the different stacks A and B are connected to two driving voltage sources U^A and U^B and a common ground. A positive voltage applied to any of the stacks causes its expansion in z-dimension. If one stack expands more than the other, the whole bimorph also bends in x-dimension because of their mechanical coupling. Thus a piezoelectric bimorph is a special form of a piezoelectric bender.

While extensive research has been done in modeling and design of piezoelectric benders [191, 190, 58, 89, 220, 129, 60] in general, the variety of actual designs requires an individual approach for each motor type. In the following, the static relation between the applied voltages and the expansion and bending of the bimorph is derived based on the Euler-Bernoulli theory of elastic deflection of beams [150, 69]. For this purpose, each multilayer stack is considered a single piezoelectric bar with an enhanced elongation due to its actual multilayer structure (see above) and reduced rigidity.[3] Fig. 22(a) shows the piezoelectric bimorph in form of a cantilever beam consisting of two parts A and B. The plane connecting the two parts forms the neutral axis (NA) of the beam. For the following analysis, the beam is assumed to be homogenous, with uniform rectangular cross-section and is subjected only to pure bending and small deflections. Only internal forces due to the inverse piezoelectric effect are considered. When the beam reaches a steady bending state, there is a static equilibrium of moments M and forces F acting on different parts of the beam. Additionally, the strains S at the interface plane between A and B must be equal

$$S^A - S^B = 0 \tag{19a}$$

$$F^A + F^B = 0 \tag{19b}$$

$$M^A + M^B = \left(\tfrac{H}{2}\right)F^A + \left(-\tfrac{H}{2}\right)F^B. \tag{19c}$$

---

[2] Note that the direction of polarization of each particular layer is imposed during the polling process and thus has to coincide with the direction of the respective electric field.

[3] The structural rigidity of a multilayer structure, in the simplest case, can be seen as series connection of multiple springs. For this reason, the overall structural rigidity of a multilayer structure has to be lower than the one of a bulk material.
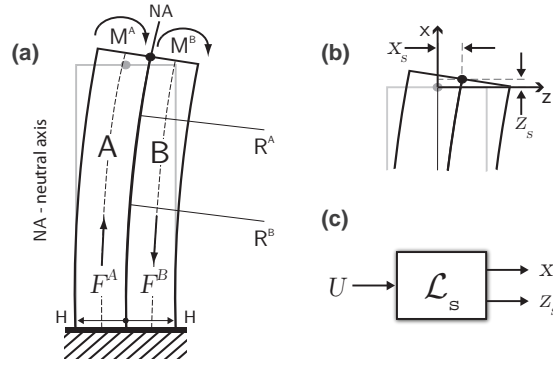
Figure 22: Bending beam model of the piezoelectric bimorph. (a) forces and torques acting on the beam. (b) static position of the piezoelectric leg when equilibrium of internal forces and moments is reached. (c) block abstraction of static leg position model.

The interface strains can be found by superimposing axial strains (a) and strains due to bending (b) and piezoelectricity (p)

$$S^A = S^A_a + S^A_b + S^A_p \tag{20a}$$

$$S^B = S^B_a + S^B_b + S^B_p. \tag{20b}$$

As the bimorph is a type 33 bender the general linear model of piezo-electricity [1] can be reduced to the following coupled equations:

$$D_3 = d_{33}T_3 + \epsilon^T_{33}E_3 \tag{21a}$$

$$S_3 = \underbrace{s^E_{33}T_3}_{S_a} + \underbrace{d_{33}E_3}_{S_p} \tag{21b}$$

with D and S being the electric charge and mechanical strain, respectively. d_{33} is a piezoelectric charge constant, ϵ^T_{33} dielectric displacement per unit electric field under constant stress T and s^E_{33} compliance under constant electric field E. The variables T and E stand for stress and electric field accordingly. In a static equilibrium condition $F^A = -F^B = F$. Assuming upward directed forces to be positive, the axial strains at the neutral axis are found as

$$S^A_a = \frac{1}{\varepsilon WH}F \tag{22a}$$

$$S^B_a = -\frac{1}{\varepsilon WH}F \tag{22b}$$

where ε is Young's modulus of the beam defined in (66). The strains due to the inverse piezoelectric effect are

$$S^A_p = d_{33}E^A = \eta\frac{d_{33}}{L_l}U^A \tag{23a}$$

$$S^B_p = d_{33}E^B = \eta\frac{d_{33}}{L_l}U^B \tag{23b}$$

53

where L_l thickness of a single ceramic layer and $\eta \in [0,1]$ a factor corresponding to the quality of electrode connections in the manufacturing process. The strains due to bending can be derived through geometrical consideration [150] to be

$$S_b^A = -\frac{H}{2R} \tag{24a}$$

$$S_b^B = \frac{H}{2R}, \tag{24b}$$

where H is the width as shown in Fig. 21. From differential calculus, the curvature is known to be

$$\frac{1}{R} = \frac{d^2x/dz^2}{[1+(dx/dz)^2]^{3/2}} \tag{25}$$

which for small deflections reduces to

$$\frac{1}{R} \approx \frac{d^2x}{dz^2}. \tag{26}$$

Since the curvatures at the interface are equal the same holds true for the radii of curvature

$$R^A = R^B = R. \tag{27}$$

This identity together with the Euler-Bernoulli bending moment equation

$$\frac{d^2x}{dz^2} = \frac{M}{\varepsilon I}, \tag{28}$$

where $I = WH^3/12$ is the axial moment of inertia about the axis z through the centroid of the rectangular cross-section of each of the two parts of the beam, leads to the equality of bending moments

$$M^A = M^B = M. \tag{29}$$

Combining (24) and (28), the equations for bending strains are obtained as

$$S_b^A = -\frac{H}{2R^A} = -\frac{H}{2\varepsilon I}M \tag{30a}$$

$$S_b^B = \frac{H}{2R^B} = \frac{H}{2\varepsilon I}M. \tag{30b}$$

Using (19c) and (19a) and resolving the particular strain terms according to (22), (23) and (30), the axial force is found to be

$$F = \eta \frac{4d_{33}\varepsilon WH}{5L_l}(U^B - U^A) \tag{31}$$

and the bending moment is

$$M = \eta \frac{2d_{33}\varepsilon WH^2}{5L_l}(U^A - U^B). \tag{32}$$

Using equation (28) together with the above expression for the bending moment (32) and performing double integration with cantilever boundary condition, the deflection in x in dependency on z is obtained.

For pure bending, the bimorph has to deform into circular configuration and by means of a geometrical consideration, the deflection at its tip is also given by Nash and Potter in [150] as

$$x_s = \frac{ML^2}{2\varepsilon I}. \tag{33}$$

With the above relations, it is possible to compute the steady-state deflection and elongation of the tip of the beam in the xz-plane in dependence on the applied voltage and relative to its potential-free origin. The elongation in z-dimension equals

$$z_s = \tfrac{1}{2}L(S^A + S^B). \tag{34}$$

The following function $f_z^s : \mathbb{R}^2 \to \mathbb{R}$

$$f_z^s(U) \overset{\text{def}}{=} z_s = \eta \underbrace{\frac{d_{33}L}{2L_I}}_{C_z'} N^+ U \tag{35}$$

yields this elongation for a given two-phase input $U = (U^A\ U^B)^T$ with N^+ being one of the following prefilters:

$$N^+ = (1 \quad 1) \tag{36}$$
$$N^- = (1 \quad -1). \tag{37}$$

The deflection at the tip in x-dimension equals x_s and corresponds to (33). Defining a function $f_x^s : \mathbb{R}^2 \to \mathbb{R}$ similar to (35) and using (32) leads to

$$f_x^s(U) \overset{\text{def}}{=} x_s = \eta \frac{3d_{33}L^2}{10L_I H} N^- U. \tag{38}$$

Taken together, the relations derived in (35) and (38) result in the following definition of static leg position as coordinate of the leg tip

$$\mathcal{L}_s(U) = \begin{pmatrix} x_s \\ z_s \end{pmatrix} = \begin{pmatrix} f_x^s(U) \\ f_z^s(U) \end{pmatrix}. \tag{39}$$

3.2.2 Driving waveforms

The previous section has established the relation between the applied voltage U (the driving voltage) and the static position of the tip of a single piezoelectric leg. In a multi-legged motor, multiple legs need to be provided with driving voltages. In general, a motor can consist of N legs, $N \in \mathbb{N}$, which can be arranged in various configurations [155, 117, 185, 35] and be driven independently by a driver signal D defined as

$$D = \begin{bmatrix} U_{(1)} & U_{(2)} & \ldots & U_{(N)} \end{bmatrix} = \\ \begin{pmatrix} U_{(1)}^A & U_{(2)}^A & \cdots & U_{(N)}^A \\ U_{(1)}^B & U_{(2)}^B & \cdots & U_{(N)}^B \end{pmatrix}. \tag{40}$$
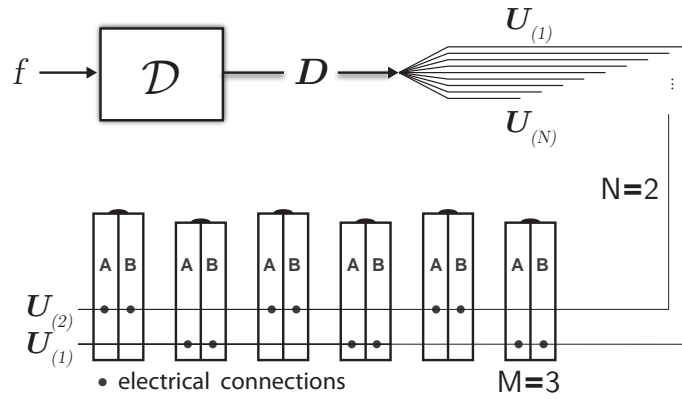
Figure 23: Schematic depiction of the electrical connections between the driver $\mathcal{D}$ providing driving voltages to a theoretical motor consisting of 2 triples of legs. All legs belonging to the same triple receive an identical driving voltage and thus move in unison. The driving voltages are output from the driver at the driving frequency f.

In the PiezoLegs motor, the legs are arranged in a row. At least two legs (a leg pair) have to move in unison in order to establish contact with the drive rod at two different points and ensure static stability in z-dimension. If more legs make contact with the drive rod simultaneously, an even stronger motor design could be achieved (see sect. 3.4.1). In the definitions to follow, it is assumed that the motor is driven by N driving voltages each connected to M different legs. Fig. 23 shows this schematically for a theoretical motor design.

In case of the PiezoLegs motor, $M = N = 2$. The motor can be driven with different waveforms depending on the particular aspect of its performance (e.g. speed, motion linearity, stall force) to be optimized. While a few basic waveforms can be found through reflection on the driving principle of the motor [186, 145], others are estimated through a computationally intensive optimiztion task [146].

Two different waveforms (*force* and *sine*) are used in this chapter for the sake of functional analysis of the motor. These can be seen in Fig. 24. The *force* waveform is of particular interest for this work as it is supposed to improve the load characteristic of the motor (i.e. stall force maximization). The reason for this will become clear in sect. 3.4.1. The *sine* waveform is used in addition in order to illustrate the nonlinearity in leg deflection (see sect. 3.3.3) and because of its simple mathematical description (see below).

To find a common mathematical description of the waveforms, the notion of a waveform-generating function $\hat{w} : \mathbb{R}^K \rightarrow [0, 1]$, $K \in$
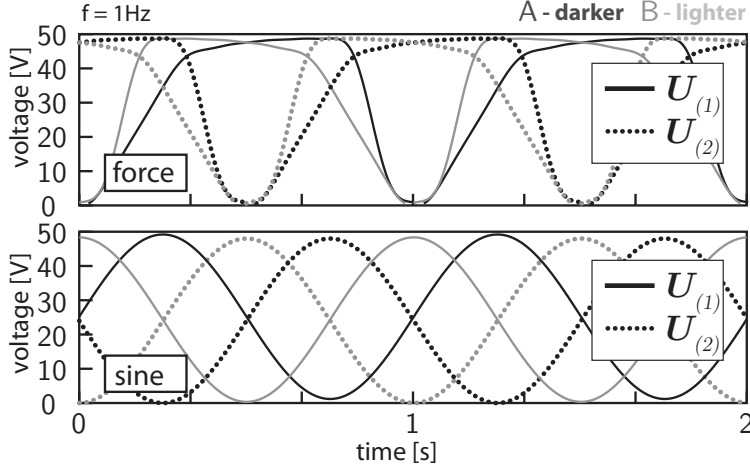
Figure 24: Diagrams showing 4 electrical phases of two different waveforms (*force* and *sine*) used to drive the walking motor. Phases connected to distinct leg pairs are coded by the line style (solid and dotted lines). Phases connected to different parts of the same leg are intensity-coded.

$\mathbb{Z}^+, \mathsf{K} \geq 3$ is introduced. The function is parametrised by $\mathsf{K} - 3$ parameters, drive frequency f, phase shift ϕ and time t. The waveform generating function $\widehat{w}^{\mathsf{f}}$ for the *force* waveform was estimated by finding a sixth order Fourier series fit to the waveform data obtained from the manufacturer. With $R^2 > 0.99$ as quality criterion on the fit, the following function was obtained:

$$\widehat{w}^{\mathsf{f}}(f, \phi, m) \stackrel{\text{def}}{=} \mathsf{a} + \sum_{i=1}^{6} \mathbf{a}_i \cos(i(ft + \phi)w) + \\ m \sum_{i=1}^{6} \mathbf{b}_i \sin(i(ft + \phi)w) \tag{41}$$

with $\mathsf{w} = 6.238$, $\mathsf{a} = 0.674$ and

$$\mathbf{a} = (\text{-0.452, -0.197, -0.052, -0.002, 0.013, 0.013}),$$
$$\mathbf{b} = (\text{0.124, 0.042, -0.035, -0.042, -0.009, 0.008}).$$

For the above generating function, the driving voltages for the two pairs of legs in the walking motor equal respectively:

$$\boldsymbol{U}^{\mathsf{f}}_{(1)}(f) = \mathsf{U}_{\mathsf{max}} \big(\widehat{w}^{\mathsf{f}}(f, 0, -1) \quad \widehat{w}^{\mathsf{f}}(f, 0, 1) \big)^T \tag{42a}$$
$$\boldsymbol{U}^{\mathsf{f}}_{(2)}(f) = \mathsf{U}_{\mathsf{max}} \big(\widehat{w}^{\mathsf{f}}(f, \pi, -1) \quad \widehat{w}^{\mathsf{f}}(f, \pi, 1) \big)^T \tag{42b}$$

where $\mathsf{U}_{\mathsf{max}}$ is a motor specific voltage limit of $48\,\mathrm{V}$. As time is an implicit parameter of equation (42), the only remaining parameter
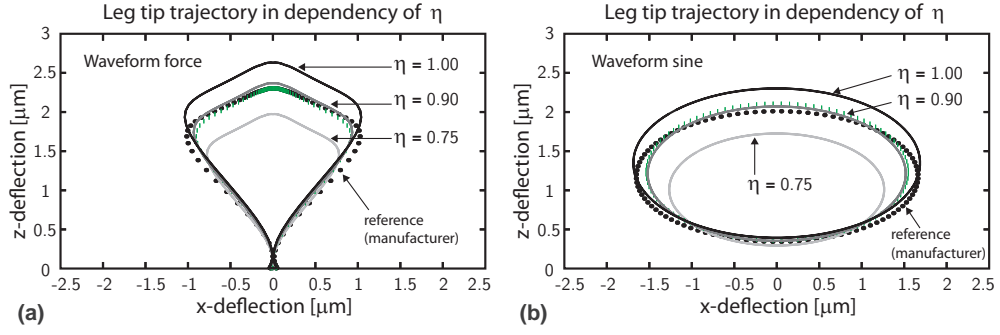
Figure 25: Trajectories of the leg tip described by the kinematic model for (a) *force* and (b) *sine* waveforms when different quality factors of the electrode connections are used. Reference trajectories based on manufacturer's data are shown with dotted lines.

which has to be given explicitly is the driving frequency f. At this point, it it possible to define the *force* driver as

$$\mathcal{D}^{\mathbf{f}}(f) = \begin{bmatrix} \boldsymbol{U}^{\mathbf{f}}_{(1)}(f) & \boldsymbol{U}^{\mathbf{f}}_{(2)}(f) \end{bmatrix}. \tag{43}$$

The driver for the *sine* waveform can be defined in an analogous way. With the waveform generating function

$$\widehat{w}^{\mathbf{s}}(f,\phi) \overset{\text{def}}{=} \tfrac{1}{2}\big[\sin(2\pi f t + \phi) + 1\big] \tag{44}$$

the driving voltages are

$$\boldsymbol{U}^{\mathbf{s}}_{(1)}(f) = \mathsf{U}_{\text{max}}\big(\widehat{w}^{\mathbf{s}}(f,0) \quad \widehat{w}^{\mathbf{s}}(f,\pi/2)\big)^{T} \tag{45a}$$

$$\boldsymbol{U}^{\mathbf{s}}_{(2)}(f) = \mathsf{U}_{\text{max}}\big(\widehat{w}^{\mathbf{s}}(f,\pi) \quad \widehat{w}^{\mathbf{s}}(f,3\pi/4)\big)^{T} \tag{45b}$$

and the *sine* driver becomes

$$\mathcal{D}^{\mathbf{s}}(f) = \begin{bmatrix} \boldsymbol{U}^{\mathbf{s}}_{(1)}(f) & \boldsymbol{U}^{\mathbf{s}}_{(2)}(f) \end{bmatrix}. \tag{46}$$

With the kinematic model of the leg from the previous section and the above definitions of the waveforms, the trajectory followed by a leg can be computed for a particular driving voltage. Data given by the manufacturer describes the static position of the tip of a leg in xz-plane by means of two constants $\mathsf{C}^{*}_{\mathsf{x}}$ and $\mathsf{C}^{*}_{\mathsf{z}}$ as:

$$x_s = \mathsf{C}^{*}_{\mathsf{x}}(U^{A} - U^{B}) \tag{47a}$$

$$z_s = \mathsf{C}^{*}_{\mathsf{z}}(U^{A} + U^{B}). \tag{47b}$$

The leg trajectories according to these relations are shown in Fig. 25 as dotted curves. The leg trajectories according to the kinematic model from sect. 3.2.1 are shown in the same figure for different values of

Table 3: Summary of model parameters – piezoelectric constants and leg kinematics.

Name	Value	SI unit	Description
d_{33}	$583 \cdot 10^{-12}$	C/N	charge constant
s_{33}^E	$415 \cdot 10^{-12}$	m^2/N	elastic compliance
L_l	$56 \cdot 10^{-6}$	m	layer thickness
N_l	96	-	number of layers
J	0.9	-	quality factor
C_x	$45.5 \cdot 10^{-9}$	m/V	deflection const.
C_z	$25.6 \cdot 10^{-9}$	m/V	elongation const.
H	0.0014	m	stack breadth (x)
L	0.004	m	stack length (z)
W	0.003	m	stack depth (y)

the quality factor η. In order to match the reference trajectories, a gradient search for η was performed. As an objective, the least squares error between the reference and model-generated trajectories was used. As a result η of 0.86 and 0.91 was obtained for the *force* and *sine*, respectively. These values have to be ascribed to the imperfections in the manufacturing process and agree with the values found in the literature [19].

For all following derivations of the motor model, a constant η of 0.9 is assumed. By referring to (35) and (38) and defining

$$C_x = \eta C_x' \tag{48a}$$
$$C_z = \eta C_z' \tag{48b}$$

the kinematic model (39) can be reformulated in matrix notation as

$$\mathcal{L}_s(U) = \begin{pmatrix} x_s \\ z_s \end{pmatrix} = \begin{pmatrix} C_x & 0 \\ 0 & C_z \end{pmatrix} \begin{bmatrix} \mathbf{N}^- \\ \mathbf{N}^+ \end{bmatrix} U. \tag{49}$$

3.3 LEG DYNAMICS

While the kinematic model derived in the previous section explains the tip trajectory data provided by the manufacturer, it has several shortcomings. First, a kinematic model does not describe the time behavior of the legs and thus of the walking motor which can be driven with driving frequencies up to 3 kHz. Second, function (49) maps only the driving voltage to the position of a leg. However, the driving principle of the real motor relies on the interaction between the legs and the drive rod including normal and frictional forces. Finally, all piezoelectric motors exhibit some form of hysteresis [209]
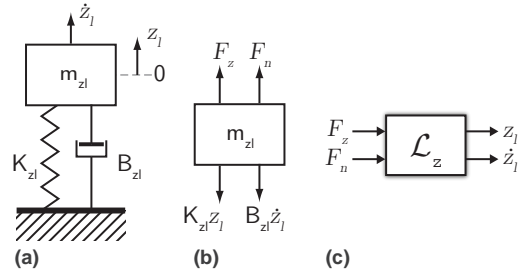
Figure 26: Linear oscillator model of the dynamics of the leg in z-dimension. (a) shows an MSD model of the leg. (b) is a free-body depiction and (c) a block abstraction of the model.

and other forms of nonlinear behavior like e.g. creep [119, 111]. This section addresses the above-mentioned shortcomings by providing a dynamic model of the leg, considering interaction with external forces and introducing a hysteretic nonlinearity into the model. In particular, the dynamic behavior of a leg is split into two independent dynamics in z- (sect. 3.3.1) and x-dimension (sect. 3.3.2) which will be coupled back together in sect. 3.4 where the interaction between the legs and the drive rod is considered. In sect. 3.3.3 a deflection nonlinearity due to hysteretic effects is introduced into the model based on a simple model assumption and macroscopic data measurements.

3.3.1 Single leg z dynamics

The periodic movement of a piezoelectric leg elicited by an external driving voltage can be compared to the movement of an oscillator driven by a periodic external force. Moreover, as long as linear modeling techniques are applied, the dynamics of this movement can be separated conveniently into the dynamics of two linear oscillators in z- and x-dimension. This section focuses on the former case.

Fig. 26(a) illustrates a damped linear oscillator model of the leg in z-dimension. This lumped parameter model (Mass-Spring-Damper or MSD model) consists of an effective mass m_{zl} connected to a fixed ground with a spring having stiffness K_{zl} and a damper having a damping factor of B_{zl}. These lumped parameters have to be deduced from real physical parameters of the piezoelectric leg. The stiffness of a single piezoceramic layer of the piezoelectric stack shown in Fig. 21(a) is known to be $K_l = 1/s_{33}^E$. Refraining from the consideration of other intermediate layers, the stiffness of the whole stack can be seen as a series connection of N_l springs with this stiffness. Following this

consideration, the structural stiffness of the whole leg can be seen as a parallel connection of two stacks resulting in the overall leg stiffness

$$K_{zl} = \tfrac{2}{N_l} K_l \tag{50}$$

in z-dimension. When an external force F_{ext} is applied to the leg tip in negative z-direction, the leg contracts by the amount

$$z_{ext} = F_{ext}/K_{zl} \tag{51}$$

measured from its tip at $z = 0$. The amount of leg contraction measured from an arbitrary position z in negative z-direction, i.e. $z = -L$ at the base, is defined by the function $f_z^d : \mathbb{R}^2 \rightarrow \mathbb{R}$:

$$f_z^d(z, F_{ext}) \overset{\text{def}}{=} \tfrac{1}{K_{zl}} \tfrac{L+z}{L} F_{ext} \tag{52}$$

which can be reformulated in terms of leg contraction from its tip as

$$f_z^d(z, \cdot) = \tfrac{L+z}{L} f_z^d(0, \cdot), \tag{53}$$

where the dot is a placeholder for the second function argument and underlines the fact that this argument does not affect the above definition. In order to find the effective mass of the leg at its tip which corresponds to m_{zl} in the linear oscillator model, an energy approach is followed. As the damping factor B_{zl} of the leg in z-dimension is not known and it can not be estimated easily without direct experiments on the leg, it is neglected in the following derivation of the effective mass. This simplifies the mathematical treatment of the problem as no energy dissipation needs to be taken into account. The modeling decision is justified by the fact that damping is supposed to affect the behavior of the leg only for much higher driving frequencies than the rated operation of the PiezoLegs motor (see sect. 3.4.1) and can not have a considerable effect on the value of the derived effective mass. Moreover, damping remains incorporated into the actual oscillator models and is analysed further in sect. 3.5.

With (52) the kinetic energy of an infinitesimally small cross-sectional leg element at position z can be formulated as

$$dE_z^k(z, F_{ext}) = \tfrac{m}{2} \left[\tfrac{df_z^d(z, F_{ext})}{dt} \right]^2 \tfrac{dz}{L} \tag{54}$$

with m being the mass of a single leg. Using relation (53) and integrating over the entire beam length yields the overall kinetic energy function as

$$E_z^k = \int_{-L}^{0} dE_z^k = \int_{-L}^{0} \tfrac{m}{2} \left[\tfrac{df_z^d(0, F_{ext})}{dt} \left[\tfrac{L+z}{L} \right] \right]^2 \tfrac{dz}{L}$$

$$= \tfrac{m}{6} \left[\tfrac{df_z^d(0, F_{ext})}{dt} \right]^2. \tag{55}$$

The potential energy function E_z^p corresponds to the work which is necessary to move the load-free end of the leg from its origin at $z = 0$ to the new position z_{ext}

$$E_z^p = E_z^p(z, F_{ext}) = \int_0^{z_{ext}} \mathsf{K}_{zl} z dz$$

$$= \tfrac{1}{2} \mathsf{K}_{zl} \left(f_z^d(0, F_{ext}) \right)^2. \tag{56}$$

The gravitational force due to the weight of the leg is neglected as it is 6 orders of magnitude smaller than the normal forces exerted on the leg in the motor (see sect. 3.4.1). Under the assumption that there is no energy dissipation in the system, the overall energy has to remain constant.[4] Computing

$$d(E_z^k + E_z^p)/dt = 0 \tag{57}$$

gives the equation of motion for the leg tip in z-dimension as

$$\tfrac{\mathsf{m}}{3} \frac{d^2 f_z^d(0, F_{ext})}{dt^2} + \mathsf{K}_{zl} f_z^d(0, F_{ext}) = 0, \tag{58}$$

thus the effective mass of the leg equivalent to m_{zl} in the linear oscillator model has to be

$$\mathsf{m}_{zl} = \tfrac{1}{3}\mathsf{m}. \tag{59}$$

The mass m of a single leg is estimated to be about $0.25\,\mathrm{g}$ from the knowledge of its volume and the density of the ceramics. In the above derivation of the effective mass, the notion of an external force F_{ext} was used. Two actual forces are assumed to affect the motion of the linear oscillator – the electromotive force F_z originating in the inverse piezoelectric effect and defined as

$$F_z(\boldsymbol{U}) \overset{\mathrm{def}}{=} \mathsf{K}_{zl} z_s = \mathsf{K}_{zl} \mathsf{C}_z \mathbf{N}^+ \boldsymbol{U} \tag{60}$$

and the normal force F_n from interaction with the drive rod (see sect. 3.4). Fig. 26(b) illustrates the oscillator model as a free body diagram with the indication of these forces. The state space representation of this model according to Fig. 26(a) and incorporating the external forces as inputs is

$$\begin{pmatrix} \dot{z}_l \\ \ddot{z}_l \end{pmatrix} = \begin{pmatrix} 0 & 1 \\ -\mathsf{K}_{zl}/\mathsf{m}_{zl} & -\mathsf{B}_{zl}/\mathsf{m}_{zl} \end{pmatrix} \begin{pmatrix} z_l \\ \dot{z}_l \end{pmatrix} +$$
$$\begin{pmatrix} 0 & 0 \\ 1/\mathsf{m}_{zl} & -1/\mathsf{m}_{zl} \end{pmatrix} \begin{pmatrix} F_z \\ F_n \end{pmatrix}. \tag{61}$$

---

[4]Note that this implies an energy conservative system (damping neglected) for which the constancy of the total energy can be assumed. A more general approach based on the principle of least action, would involve finding the solution to $\frac{d}{dt}\left(\frac{\partial L}{\partial \dot{z}}\right) = \frac{\partial L}{\partial z}$ with $L \equiv E_z^k - E_z^p$ being the *Lagrangian* [57].
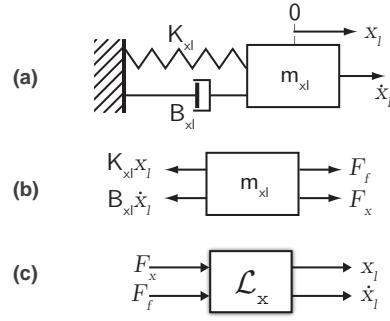
Figure 27: Linear oscillator model of the dynamics of the leg in x-dimension. (a) shows an MSD model of the leg. (b) is a free-body depiction and (c) a block abstraction of the model.

The abstract representation of the z-dynamics which can be seen in Fig. 26(c) and is used later in the motor model is defined as the state space output of the above representation and reads

$$\mathcal{L}_z(F_z, F_n) = \begin{pmatrix} z_l \\ \dot{z}_l \end{pmatrix}. \tag{62}$$

3.3.2 Single leg x dynamics

Similar energy argument as in the previous section can be brought forward to derive the dynamics of a linear oscillator in x-dimension (see Fig. 27[a]). If an external force F_{ext} acts on the leg in x-direction at the position z, it creates a bending moment M_{ext}. Knowing (28), a deflection function f_x^d can be defined similar to (52) as

$$\frac{d^2 f_x^d}{dz^2} \overset{\text{def}}{=} \frac{d^2 x}{dz^2} = \frac{1}{\varepsilon I} M_{ext} = \frac{L+z}{\varepsilon I} F_{ext}, \tag{63}$$

since the amount of deflection in x depends on the z-coordinate (cf. (28)). Double integration over the entire length of the beam with cantilever boundary conditions leads to

$$f_x^d(z, F_{ext}) = \frac{1}{6\varepsilon I}(z + L)^3 F_{ext}. \tag{64}$$

The deflection at the tip of the leg due to an external force equals

$$x_{ext} = f_x^d(0, F_{ext}) = \frac{1}{6\varepsilon I} L^3 F_{ext}. \tag{65}$$

Using equation (50) Young's modulus of the leg ε can be computed as

$$\varepsilon = \frac{L}{W(2H)} K_{zl} = \frac{L}{s_{33}^E N_l WH} \tag{66}$$

and thus the spring constant has to be

$$K_{xl} = \frac{6\varepsilon I}{L^3} = \frac{4H^2}{s_{33}^E N_l L^2}. \tag{67}$$

In order to derive the effective mass m_{xl} of the leg tip in x-dimension, the kinetic energy function is defined in analogy to (54) and (55) as

$$dE_x^k(z, F_{ext}) = \frac{m}{2} \left[\frac{df_x^d(0, F_{ext})}{dt} [(\frac{z}{L}) + 1]^3 \right]^2 \frac{dz}{L}. \tag{68}$$

Integrating this equation over the entire length of the leg yields

$$E_x^k(z, F_{ext}) = \int_{-L}^{0} dE_x^k dz = \frac{m}{14} (f_x^d(0, F_{ext}))^2. \tag{69}$$

The potential energy function corresponds to the work required to move the leg tip to the position x_{ext} and equals

$$E_x^p(z, F_{ext}) = \int_0^{x_{ext}} K_{xl} x dx = \frac{1}{2} K_{xl} (f_x^d(0, F_{ext}))^2. \tag{70}$$

Assuming no energy dissipation as in sect. 3.3.1, the equation of motion for the oscillator in x-dimension is found to be

$$\frac{1}{7} m \frac{d^2 f_x^d(0, F_{ext})}{dt^2} + K_{xl} f_x^d(0, F_{ext}) = 0 \tag{71}$$

and thus the effective mass is

$$m_{xl} = \frac{1}{7} m. \tag{72}$$

In case of the x-dimension oscillator, two external forces are considered as well. The piezoelectric electromotive force F_x defined as

$$F_x(\boldsymbol{U}) \stackrel{\text{def}}{=} K_{xl} x_s = K_{xl} C_x \mathbf{N}^- \boldsymbol{U} \tag{73}$$

and a frictional force F_f coming from the interaction with the drive rod and defined in sect. 3.4.2. These are depicted schematically in the free body diagram in Fig. 27(b). The state space representation of leg dynamics in x-dimension according to the model in Fig. 27(a) and including the external forces is easily found to be

$$\begin{pmatrix} \dot{x}_l \\ \ddot{x}_l \end{pmatrix} = \begin{pmatrix} 0 & 1 \\ -K_{xl}/m_{xl} & -B_{xl}/m_{xl} \end{pmatrix} \begin{pmatrix} x_l \\ \dot{x}_l \end{pmatrix} + \begin{pmatrix} 0 & 0 \\ 1/m_{xl} & -1/m_{xl} \end{pmatrix} \begin{pmatrix} F_x \\ F_f \end{pmatrix} \tag{74}$$

with the abstract representation of Fig. 27(c) defined as

$$\mathcal{L}_x(F_x, F_f) = \begin{pmatrix} x_l \\ \dot{x}_l \end{pmatrix}. \tag{75}$$

3.3.3   Hysteretic nonlinearity

At all modeling stages so far, only linear modeling techniques have been used. However, piezoelectric ceramics are ferroelectric materials and thus fundamentally nonlinear in their response to applied electric fields showing hysteresis as well as time-dependent creep. These can have a considerable effect on the actual performance of the motor and are difficult to model exactly even if low-level experimental data is provided [56, 231, 226, 118]. Newcomb and Flin showed in [153] that the nonlinear effect of hysteresis on the extension of a multilayer piezoelectric stack is especially strong if the stack is voltage-driven and proposed a charge drive to achieve a much higher degree of linearity. In [209], Uchino gives many examples of hysteretic behavior for different piezoelectric materials with the majority of them showing a strong strain response to low electric fields which saturates with increasing field level. For the bimorph leg considered in this work, this indicates that leg deflection might be strongest for a small increase in one of the phases U^A or U^B of the driving voltage while the other remains close to ground potential. In this case, one of the stacks A or B would experience a relatively high increase in length not compensated, in terms of bending, by a corresponding increase in length in the other stack. If the effect of hysteresis on leg deflection is strong, it should become visible in the macroscopic behavior of the motor, even though hysteresis can not be observed directly in the assembled state.

Fig. 28(a) shows that this is indeed the case. The PiezoLegs motor was driven with 5 different drive frequencies within its rated operation regime for which the corresponding average velocities were measured. These velocities were taken as normalized references (white bars having the value of 1) and compared to the average velocities of the legs (black bars) during contact periods with the drive rod according to the dynamic leg model of the previous sections. The average leg velocities were normalized with respect to the measured reference values. It was assumed that the legs were in perfect stiction condition with the drive rod when the contact was established as there was no external load force F_l exerted on the drive rod (cf. velocity decrease due to external load in sect. 3.5) and the motor was not driven up to its frequency limits (cf. resonance region in sect. 3.4.1). The latter constraint, i.e. moderate drive frequencies, also implies that the legs were not affected by damping to a considerable degree and could follow the trajectories predicted by the linear model of sect. 3.2.2. The contact periods were computed by comparing the elongations $z_{l(1)}$ of leg pair (1) with the elongations $z_{l(2)}$ of leg pair (2). Sect. 3.4.1 shows that in reality there have to be times of overlapping contact between both pairs of legs and the drive rod. Still, this does not affect the observations of Fig. 28 qualitatively. Similar results are obtained when full motor model – which considers the overlapping contact periods – of sect. 3.4 is employed and the velocity of drive rod measured.
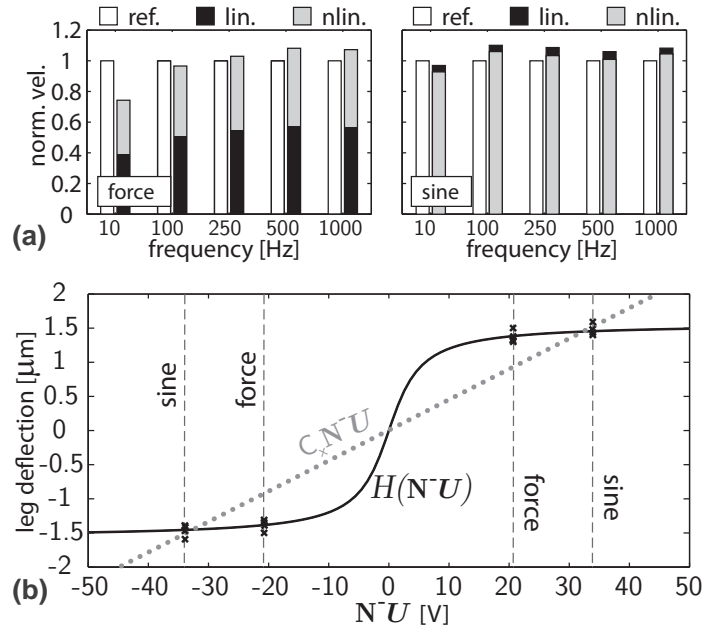
Figure 28: Leg deflection nonlinearity. (a) shows average leg velocity during rod contact for 5 different drive frequencies when linear (black bars) leg deflection is assumed. White bars show the actually measured rod velocity. All data is normalized with respect to the measured rod velocity. (b) shows leg deflection in dependence of the difference between the driving voltage phases. Dashed lines show the maximal/minimal voltage difference for the *force* and *sine* waveforms. Black crosses are data derived from (a) which indicate a change in leg deflection that leads to the equality between the average leg and the measured rod velocity. The black curve is a nonlinear least square fit on these data. Grey bars in (a) show the average leg velocity when the nonlinearity is employed in the model.

The above experiment was done for both the *force* and *sine* waveforms as shown in Fig. 28(a). For the *force* waveform, the average leg velocity according to the linear leg deflection model (49) and the corresponding linear electromotive force (73) is about 50 % slower that the actually measured drive rod velocity. For the *sine* waveform leg velocity becomes about 10 % higher than the reference. This observation agrees with the conjecture that leg deflection should increase faster for small differences between the two phases $U_{(i)}^A$ and $U_{(i)}^B$ of the driving voltage at small voltage levels. This is the case for the *force* waveform for which the difference $\mathbf{N}^- U_{(i)}$ remains relatively small compared to the *sine* waveform (see Fig.24).

An exact model of hysteresis including dependency on the drive frequency [105] would need to be included already in sect. 3.2.1 where the strains due to inverse piezoelectric effect were considered in order to explain the nonlinear deflection. However, aside from the lack of experimental data this approach would complicate the mathematical treatment of the problem and could not be solved analytically for common hysteresis models like Preisach [105], Jiles-Atherton [113] or the MRC model [118]. In this chapter, an alternative approach based on macroscopically measured data and assumptions made at the beginning of this section (especially the assumption of stiction) is followed. Instead of considering the electric field/strain relation on the level of piezoelectric stack modeling, a leg deflection nonlinearity is introduced on the level of dynamic leg model. When in stiction, the average rod velocity has to correspond to the average leg velocity in x-direction. If it is higher, then for the same drive-frequency-dependent contact time the deflection of the leg has to be larger and the other way round. Fig. 28(b) illustrates this relation graphically. The dotted line is the linear dependency of leg deflection in x-dimension on the difference between the phases of the driving voltage. Dashed lines illustrate the minimum and maximum levels of this difference for both of the considered waveforms.[5] Black markers on these lines are data derived from Fig. 28(a) and illustrate how the maximal/minimal deflection of the legs would need to change in order for the average leg velocity to match the measured velocity of the drive rod. As the derived data points have origin symmetry, a nonlinear curve passing through these points would have a sigmoid shape. The following function

$$H(u) = \chi_0 \arctan(\chi_1 u) \tag{76}$$

with two scaling parameters χ_0 and χ_1 was chosen in order to capture the nonlinear deflection characteristics of the legs. The function is shown as a black curve in Fig. 28(c) for the values χ_0 and χ_1 obtained in the optimization process (see Table 6). With the nonlinear deflection characteristics, the definition of the electromotive force (73) changes to

$$F_x(\boldsymbol{U}) = \mathsf{K}_{\mathsf{xl}} \mathsf{C}_{\mathsf{x}} H\big((\mathbf{N}^-\boldsymbol{U})^T\big) \tag{77}$$

Fig. 28(a) illustrates with help of gray-shaded bars the change in average leg velocity normalized with respect to the measured rod velocity when the nonlinearity is introduced into the dynamic model of the leg. The result is a much better agreement between the model-predicted and actually measured velocities.

---

[5]The maximal and minimal levels are symmetric with respect to the (vertical) leg-deflection axis since their absolute values are equal.

Table 4: Summary of model parameters – leg dynamics.

| Name	Value	SI unit	Description
K_{xl}	$1.14 \cdot 10^7$	N/m	leg eff. stiffness (x)
K_{zl}	$5.02 \cdot 10^7$	N/m	leg eff. stiffness (z)
m_{xl}	$1.76 \cdot 10^{-5}$	kg	leg eff. mass (x)
m_{zl}	$4.10 \cdot 10^{-5}$	kg	leg eff. mass (z)

3.4 MOTOR DYNAMICS

The dynamic leg model of the previous sections provides the base for the actual motor model where the interaction of multiple legs with the drive rod and external forces needs to be considered. Sect. 3.2.2 has introduced the general notation of a driver signal which supplies a multi-legged motor with driving voltages. The following sections builds up on this notation in order to arrive at a multi-legged motor model. Subscript (i) labels a particular leg pair. Multivalued vector signals in block diagrams have a drop shadow added. The addition of a scalar to a vector or matrix is element-wise.

Figure 29 illustrates the interaction forces between the legs and the drive rod in the two-dimensional dynamic model of the walking motor. The normal forces $F_{n(i)}$ in z-dimension depend on the magnitude of the preload force F_p (due to leaf springs, see Fig. 20) and the elongation of all legs having contact with the drive rod and counterbalancing the preload. The normal forces are also responsible for the coupling between the x- and z-dynamics as they allow frictional interaction between the legs and the drive rod in x-dimension. These forces are further considered in sect. 3.4.1. In x-dimension friction forces $F_{f(i)}$ develop between the drive rod and legs in contact with it. These forces depend on the normal forces, external load F_l, contact history, relative velocities and possibly many other factors according to the friction model in use and are further considered in sect. 3.4.2.

3.4.1 Motor z dynamics

The z-dynamics of the legged motor consists in the interaction between the drive rod and the legs as shown in Fig. 30(a). An MSD model of the drive rod with the mass m_r, effective spring constant K_{zr} and damping B_{zr} is shown on top of the linear oscillator model of the leg from sect. 3.3.1. z_r and $z_{l(i)}$ denote the position of the drive rod and a leg tip, respectively. K_n represents the effective stiffness at the interaction interface between the ceramic surfaces of the drive rod and the legs. In the following, K_n is assumed in the order of $10^{10}\,N/m$ according to stiffness characteristics of aluminium oxide ceramics. K_{zr} corresponds to the stack of leaf springs and is known to be $10^5\,N/m$.
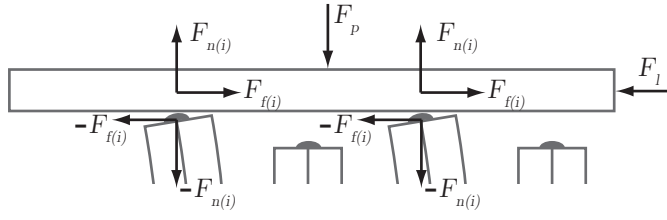
Figure 29: Two-dimensional dynamics in the motor model. $F_{n(i)}$ are normal forces between the legs and the rod in z-dimension. $F_{f(i)}$ are frictional forces in x-dimension. F_p and F_l are external forces – normal preload and tangential load, respectively.

Damping B_{zr} is negligible as the preload force from the prestretched leaf springs is transferred to the drive rod through solid metal roller bearings and is included in the model only for the sake of generality. The mass of the rod m_r is known to be 20 g. When the rod is pressed against the legs by means of a preload force F_p normal forces F_n build up at the contact spots according to

$$F_n = F_n(z_r, z_l) = K_n \langle z_l - z_r \rangle \tag{78}$$

with $z_l = [z_{l(1)}, \ldots, z_{l(N)}]^T$ and $\langle \cdot \rangle$ being a singularity function used to model the discountinous contacts due to the impact dynamics of the legs and defined for a vector input $u = [u_{(1)}, \ldots, u_{(N)}]^T$ as

$$\langle u \rangle = \left(\langle u_{(1)} \rangle, \ldots, \langle u_{(N)} \rangle \right)^T$$
$$\langle u_{(i)} \rangle = \begin{cases} u_{(i)} & , \text{ if } u_{(i)} \geq 0 \\ 0 & , \text{ otherwise.} \end{cases} \tag{79}$$

From the above definition it is clear that the computed normal forces are nonnegative, i.e. directed upwards to counteract the preload force. Fig. 30(b) illustrates the different forces acting on the drive rod. It should be noted that generally M legs in a pair/tuple move in unison establishing a contact with the rod and thus the computed normal forces need to be multiplied with this factor. The state space representation of the drive rod dynamics according to the model in Fig. 30(a) and incorporating the preload and normal forces is

$$\begin{pmatrix} \dot{z}_r \\ \ddot{z}_r \end{pmatrix} = \begin{pmatrix} 0 & 1 \\ -K_{zr}/m_r & -B_{zr}/m_r \end{pmatrix} \begin{pmatrix} z_r \\ \dot{z}_r \end{pmatrix} + \begin{bmatrix} 0 & \mathbf{0}_{1N} \\ 1/m_r & \{M/m_r\}_N \end{bmatrix} \begin{bmatrix} F_p \\ F_n \end{bmatrix} \tag{80}$$
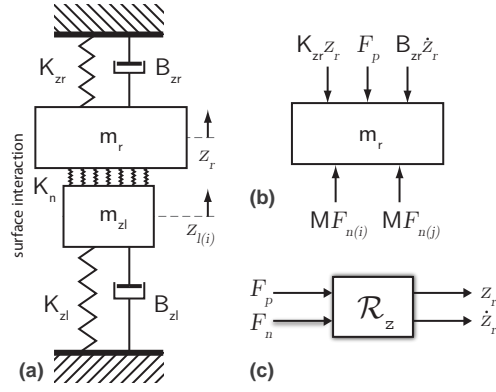
Figure 30: Motor dynamics in z-dimension shown exemplary as (a) an MSD model of one leg in contact with the drive rod. (b) shows a free-body digram of the drive rod with normal forces from two leg pairs (i) and (j). (c) block abstraction of the drive rod.

with the following state space output

$$
\mathcal{R}_z(F_p, \boldsymbol{F}_n) = \begin{pmatrix} z_r \\ \dot{z}_r \end{pmatrix}.
\tag{81}
$$

In (80), square brackets denote a block matrix, $\mathbf{0}_{1N}$ is a 1xN matrix (here a row vector) filled with 0 and the expression in curly braces

$$
\{u\}_N = \mathrm{diag}(\underbrace{u, \dots, u}_{N})
$$

is a diagonal matrix having the value between the curly braces on its diagonal.

The normal forces acting on the legs need to have the opposite sign to those acting on the rod. The general external force F_{ext} included in the dynamic leg model of sect. 3.3.1 can be substituted now as F_n and the state space representation of leg dynamics from (61) can be adjusted to represented multiple legs as

$$
\begin{bmatrix} \dot{z}_l \\ \ddot{z}_l \end{bmatrix} = \begin{bmatrix} \mathbf{0}_{NN} & \{1\}_N \\ \{-K_{zl}/m_{zl}\}_N & \{-B_{zl}/m_{zl}\}_N \end{bmatrix} \begin{bmatrix} z_l \\ \dot{z}_l \end{bmatrix}
$$
$$
+ \begin{bmatrix} \mathbf{0}_{NN} & \mathbf{0}_{NN} \\ \{1/m_{zl}\}_N & \{-1/m_{zl}\}_N \end{bmatrix} \begin{bmatrix} F_z \\ F_n \end{bmatrix}
\tag{82}
$$

with the corresponding state space output

$$
\mathcal{L}_z(\boldsymbol{F}_z, \boldsymbol{F}_n) = \begin{bmatrix} z_l \\ \dot{z}_l \end{bmatrix}.
\tag{83}
$$
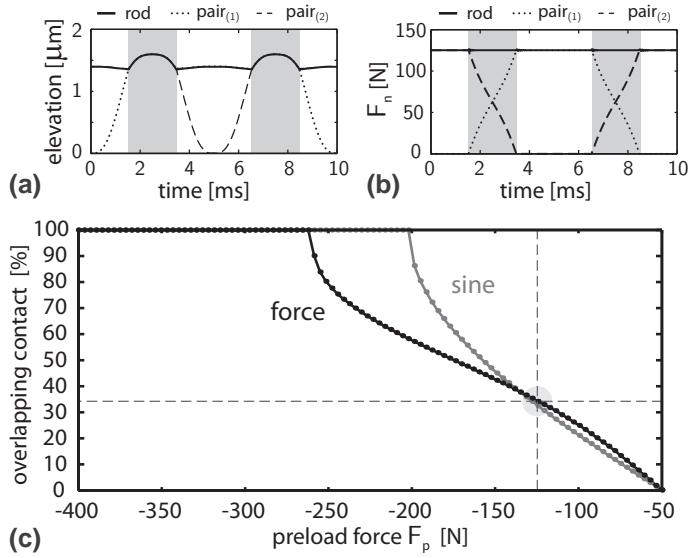
Figure 31: Change in drive rod elevation (a) and normal force magnitude (b) over one leg movement period when *sine* waveform is used. Grey-shaded regions mark overlapping leg-pair contacts. Simulation data is shown for an exemplary preload of $-125\,\mathrm{N}$ (intersection of dashed lines in [c]) and driving frequency of $100\,\mathrm{Hz}$. (c) shows the times when both of the two leg pairs in the walking motor have contact with the drive rod as percentage of leg movement period. When driven with the *force* waveform, the motor can withstand higher preload forces.

The definition of the electromotive force (60) remains unchanged for the multi-legged case. The function is only provided with a driver signal $\boldsymbol{D}$ instead of a single driving voltage $\boldsymbol{U}$:

$$\boldsymbol{F_z} = F_z(\boldsymbol{D}) = \mathsf{K_{zl}C_z}(\mathbf{N}^+\boldsymbol{D})^T. \tag{84}$$

The above definitions constitute a complete model of the z-dynamics of a multi-legged motor. Although it is not possible to observe the legs-rod interaction in the PiezoLegs motor in the assembled state, this model sheds light on some aspects of this interaction. First, there have to be times when multiple legs (from different leg pairs) have contact with the drive rod. Second, there have to be limits on the magnitude of the preload force since the legs can not lift infinitely large loads. Third, there are bandwidth limits on the motor.

Fig. 31 addresses the first two of the above statements. Fig. 31(a) and (b) show how the drive rod elevation and the magnitude of the normal force that acts on the drive rod (solid curves) change in time. The simulation was done for an exemplary preload force of

−125 N and drive frequency of 100 Hz. Also indicated are elongations and contributions to the normal force experienced by the drive rod coming from the two different pairs of legs of the walking motor (dashed and dotted curves). Grey-shaded regions in these figures show periods when both of the leg pairs have contact with the drive rod (overlapping contact). The diagram in Fig. 31(c) shows how the times of overlapping contact, as percentage of one movement period T, change for different levels of preload force. These times should approach 0 % (immediate transition in contact with the drive rod from one leg pair to another) for small preload and reach 100 % for some large preload force when the driving principle is violated since leg pair can develop enough force to lift the drive rod. The model can reproduce this behavior and indicates that the motor can be driven with higher preload when the *force* waveform is used as opposed to the *sine* waveform. Although the exact preload levels and the shape of the curves from Fig. 31(c) have not been validated experimentally, this observation agrees with the recommendation of the manufacturer to use the *force* waveform for high-preload operation. This can be explained by the fact that the maximal difference in elongation of two different pairs of legs is larger for *force* than for the *sine* waveform. In particular, the maximal level of preload for a given waveform can be determined by noting that

$$\max_{t \in (0,T]} \left| z_{l_{(1)}}(t) - z_{l_{(2)}}(t) \right| > \left| F_p \right| / (M K_{zl}), \tag{85}$$

or in other words, that during one movement period, the difference in the elevation of two different leg pairs has to be larger than the contraction of M legs (belonging to one pair) induced by the preload.[6] As the level of preload has direct influence on the magnitude of static friction (see next section), the above inequality provides insights into possible improvements to the motor design in terms of stall force limit. These range from waveform-based optimization of the left-hand side difference in (85) to the deployment of more legs in a pair or stiffer design of the legs. A more exact inequality would have to include the effect of hysteresis on leg elongation also in z-dimension and is beyond the scope of this work.

The last question to be addressed in this section concerns the bandwidth limits of the motor. The manufacturer allows rated operation up to 3 kHz. The reason for this can also be revealed in simulation. Fig. 31(a) has shown the exemplary change in drive rod elevation for the drive frequency of 100 Hz. Fig. 32 shows how the peak-to-peak magnitude of this elevation changes when the drive frequency increases. A resonance peak exists at 3 kHz, followed by further peaks

---

[6]Note that this is a necessary condition for the walking principle to work. However, this condition is not sufficient since the direction of leg movement in x-dimension is not considered.
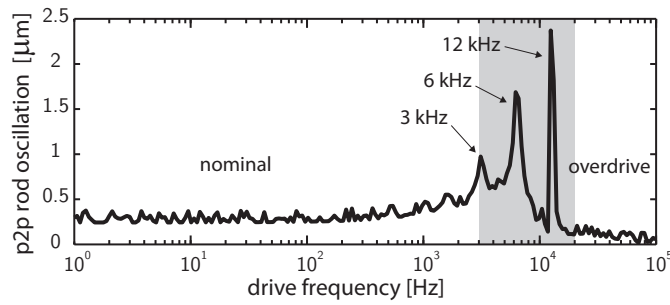
Figure 32: Amplitude of the peak-to-peak drive rod oscillations in z-dimensions for an increasing drive frequency. The simulation data confirms the existence of a 3 kHz resonance peak given by the manufacturer of the PiezoLegs motor. Additionally, the simulation data anticipates two further resonance peaks and a non-resonant operation region beyond 15 kHz.

at 6 and 12 kHz. Resonant behavior in z-dimension affects the operation of the motor in x-dimension as no proper contact between the drive rod and the legs is ensured. Indeed, the PiezoLegs motor stops moving when driven at 3 kHz and for higher frequencies within the grey-shaded region loud cracks and even sudden changes in movement direction occur. Besides the nominal and resonant range of operation, the simulation predicts a third region beyond 15 kHz – overdrive region – in which the oscillations virtually disappear. In order to test this condition the motor was driven at a drive frequency of 20 kHz for a short time due to the flow of high currents and the risk of a breakdown.[7] No audible noises typical for quasi-static motors in their nominal range of operation up to several kHz could be heard and the motor moved at the velocity of 150 mm/s which is an order of magnitude higher than the nominal range of operation allows. This finding indicates the possibility of design improvements in terms of maximal drive velocity ranging from the design of an intelligent current controller to the deployment of electrodes which could conduct higher currents. The magnitude of the oscillations in the resonant region could be decreased by introducing an additional damping.

3.4.2 Motor x dynamics

The previous section has stressed the importance of z-dynamics on the performance of the legged motor. This section focuses on the

---

[7]This problem could be alleviated by employing an integral current control or temperature monitoring strategy. A burst-wise operation in the overdrive region for short periods of time is also conceivable.
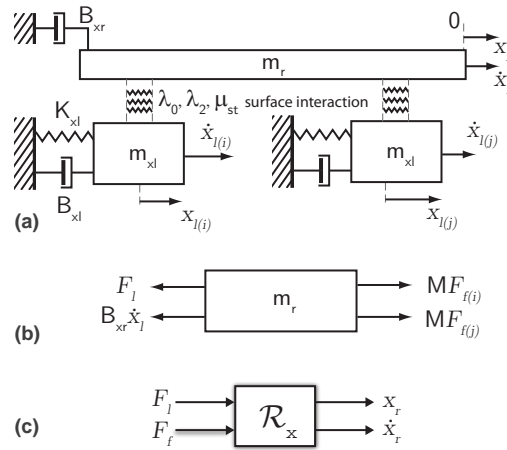
Figure 33: Motor dynamics in x-dimension. (a) shows an MSD model of the drive rod with two interacting leg pairs (i) and (j). (b) is a free-body diagram of the drive rod from (a) and (c) its block abstraction.

x-dynamics where frictional interaction between the legs and the drive rod takes place. Fig. 33(a) shows an MSD model of the x-dynamics using the example of a drive rod and two legs as introduced in sect. 3.3.2. The drive rod has a mass m_r, position x_r and velocity $\dot{x}_r$. Its movement in x is determined by frictional interaction with the legs in contact, a velocity-dependent damping term B_{xr} assigned to friction in the roller bearings and an external load force F_l in x-dimension. Fig. 33(b) shows this exemplary as a free-body diagram. The frictional forces due to the interaction with the legs need to be multiplied with a factor M according to the number of legs which move in unison.

As friction plays the most important role in the driving principle of the motor, it is essential to describe this phenomenon accurately. The frictional interaction between the legs and the drive rod relies on dry sliding friction. There exists a number of models which describe sliding friction [160]. The models show high diversity with regard to the modeling technique, number of parameters and computational effort. An overview is given e.g. in [10] and an extensive study of friction phenomena can be found in [16, 18] and more recently in [17]. Because of the nature of frictional interaction between the legs and the drive rod, in particular stick-slip effects and high dynamic range, the friction model to be used in this chapter had to unite static and dynamic friction phenomena, be continuous at zero velocity crossing, suitable for low velocities and include stiction. Two models fulfilling these prerequisites were taken under consideration – the

Bliman-Sorine [26] and the LuGre [40, 11] model. The LuGre model was chosen finally due to its better damping properties at zero velocity crossing [74] and a more intuitive treatment of friction parameters which suit the lumped parameter modeling strategy followed in this chapter. In this model, two surfaces make contact at a number of microscopic asperities which are modelled as elastic bristles. When a tangential force is applied, these bristles deflect like springs giving rise to friction force. The LuGre model can be described by a set of three equations

$$F_f = \lambda_0 u + \lambda_1 \dot{u} + \lambda_2 v \tag{86a}$$

$$\dot{u} = v - u|v|/g(v) \tag{86b}$$

$$\lambda_0 g(v) = F_c + (F_s - F_c)\exp(-(v/\nu)^2) \tag{86c}$$

where u is the average deflection of the bristles, v relative velocity between the two surfaces and λ_0, λ_1, λ_2 model parameters which describe stiffness, damping properties of the bristles and velocity-dependent damping between the surfaces in contact. The parametrization of function g in (86c) has been proposed to describe the Stribeck effect [40]. F_s and F_c denote the stiction and Coulomb friction level and ν is the Stribeck velocity.

The above set of equations (86) is not yet applicable as a friction model for the multi-legged motor. First, friction has to be computed for every leg (leg pair) in contact with the drive rod. Second, the contacts are discontinuous due to the impact dynamics of the legs. And third, not all parameters can be treated as constants. By defining a contact matrix C_N using the singularity function from (79) as

$$C_N = \text{con}(F_n) = \text{diag}\left(\frac{<F_{n(1)}>}{F_{n(1)}}, \ldots, \frac{<F_{n(N)}>}{F_{n(N)}}\right) \tag{87}$$

which has a 1 as its (i)-th diagonal element if the leg pair (i) has contact with the drive rod and 0 otherwise, (86a) can be reformulated in vector notation as

$$F_f(\dot{x}_l, \dot{x}_r, F_n) = C_N\left(\lambda_0 u + \lambda_1 \dot{u} + \lambda_2(\dot{x}_l - \dot{x}_r)\right) \tag{88}$$

where $\dot{x}_r$ is the drive rod (motor) velocity and $\dot{x}_l$ is a vector of leg velocities. Vector u can be found through numerical integration of

$$\dot{u} = (\dot{x}_l - \dot{x}_r) - u|\dot{x}_l - \dot{x}_r|/g(\dot{x}_l, \dot{x}_r, F_n). \tag{89}$$

as long as the contact between the drive rod and a corresponding leg pair is established. The initial condition upon contact reestablishment with leg pair (i) is obviously $u_{(i)} = 0$. The function g has been redefined from (86c) as

$$\begin{aligned} g &= g(\dot{x}_l, \dot{x}_r, F_n) \\ &= \frac{\mu_{st}F_n}{\lambda_0}\left[\widehat{\mu}_{dn} + (1 - \widehat{\mu}_{dn})\exp(-(\dot{x}_l - \dot{x}_r)^2/\nu^2)\right]. \end{aligned} \tag{90}$$

In the above definition, constant stiction has been made dependent on the variable normal force and a constant static friction coefficient μ_{st} according to the Amonton-Coulomb laws (cf. discussion in sect. 3.6). Coulomb friction is usually expressed in terms of a dynamic friction coefficient which does not exceed the static friction coefficient, therefore – assuming the common definition $F_c = \mu_{dn}F_n$ – the dynamic friction coefficient is replaced by a normed parameter $\widehat{\mu}_{dn} \in [0,1]$ for which $\mu_{dn} = \mu_{st}\widehat{\mu}_{dn}$. Assuming that there is no significant damping at the contact interface between the ceramic surfaces, i.e. $\lambda_1 = 0$, the friction model is characterised by 5 parameters. These will be estimated in the next section.

Having defined friction force according to the LuGre model, the extension of the dynamic leg model from sect. 3.3.2 to the multi-legged case proceeds analogously to the previous section. By defining F_f as the friction force and following the block matrix notation, the state space representation (74) becomes

$$
\begin{bmatrix} \dot{x}_l \\ \ddot{x}_l \end{bmatrix} = \begin{bmatrix} \mathbf{0}_{NN} & \{1\}_N \\ \{-K_{xl}/m_{xl}\}_N & \{-B_{xl}/m_{xl}\}_N \end{bmatrix} \begin{bmatrix} x_l \\ \dot{x}_l \end{bmatrix}
$$
$$
+ \begin{bmatrix} \mathbf{0}_{NN} & \mathbf{0}_{NN} \\ \{1/m_{xl}\}_N & \{-1/m_{xl}\}_N \end{bmatrix} \begin{bmatrix} F_x \\ F_f \end{bmatrix}
\tag{91}
$$

and the state space output is

$$
\mathcal{L}_x(F_x, F_f) = \begin{bmatrix} x_l \\ \dot{x}_l \end{bmatrix}.
\tag{92}
$$

The definition of the electromotive force remains basically unchanged from (77) except that it is evaluated for a driver signal D now and thus has a vector-valued output

$$
F_x = F_x(D) = K_{xl}C_x H(\mathbf{N}^- D)^T.
\tag{93}
$$

Based on Fig. 33, the drive rod state space equations are

$$
\begin{pmatrix} \dot{x}_r \\ \ddot{x}_r \end{pmatrix} = \begin{pmatrix} 0 & 1 \\ 0 & -B_{xr}/m_r \end{pmatrix} \begin{pmatrix} x_r \\ \dot{x}_r \end{pmatrix}
$$
$$
+ \begin{bmatrix} 0 & \mathbf{0}_{1N} \\ 1/m_r & \{M/m_r\}_{1N} \end{bmatrix} \begin{bmatrix} F_l \\ F_f \end{bmatrix}
\tag{94}
$$

with the corresponding output

$$
\mathcal{R}_x(F_l, F_f) = \begin{pmatrix} x_r \\ \dot{x}_r \end{pmatrix}.
\tag{95}
$$

F_l is an external tangential load force and will be further considered in the next section in context of the load characteristics of the motor.

The complete model of a multi-legged motor including the interaction between the drive rod and the legs both in x- and z-dimension

(a)   (b)
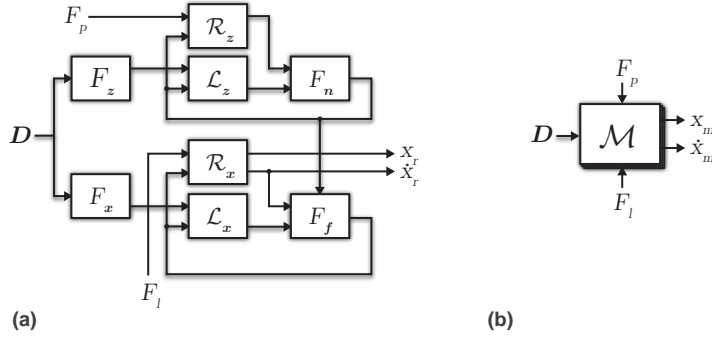
Figure 34: Schematic depiction of the overall motor model as (a) an interconnection of model components and (b) a block diagram abstraction.

Table 5: Summary of model parameters – motor dynamics.

Name	Value	SI unit	Description
K_n	10^{10}	N/m	interface stiffness (z)
K_{zr}	10^5	N/m	preload spring stiffness (z)
m_r	0.02	kg	drive rod mass

is depicted in Fig. 34(a). A block diagram depiction was chosen to visualise the flow of signals between different model components in a clear manner. Also for the sake of clarity, the signals were not explicitly labeled. The exact equations governing the behavior of particular blocks were defined in this section. Except of the friction block which couples the z- and x-dynamics through normal forces and has an additional input, all blocks have inputs on the left and outputs on the right-hand side with top-down numbering order. Vector-valued signals have a drop shadow. Fig. 34(b) shows a black box abstraction $\mathcal{M}$ of this model with a driver signal D, preload F_p and tangential load F_l as inputs and motor position x_m (=x_r) and velocity $\dot{x}_m$ (=$\dot{x}_r$) as outputs.
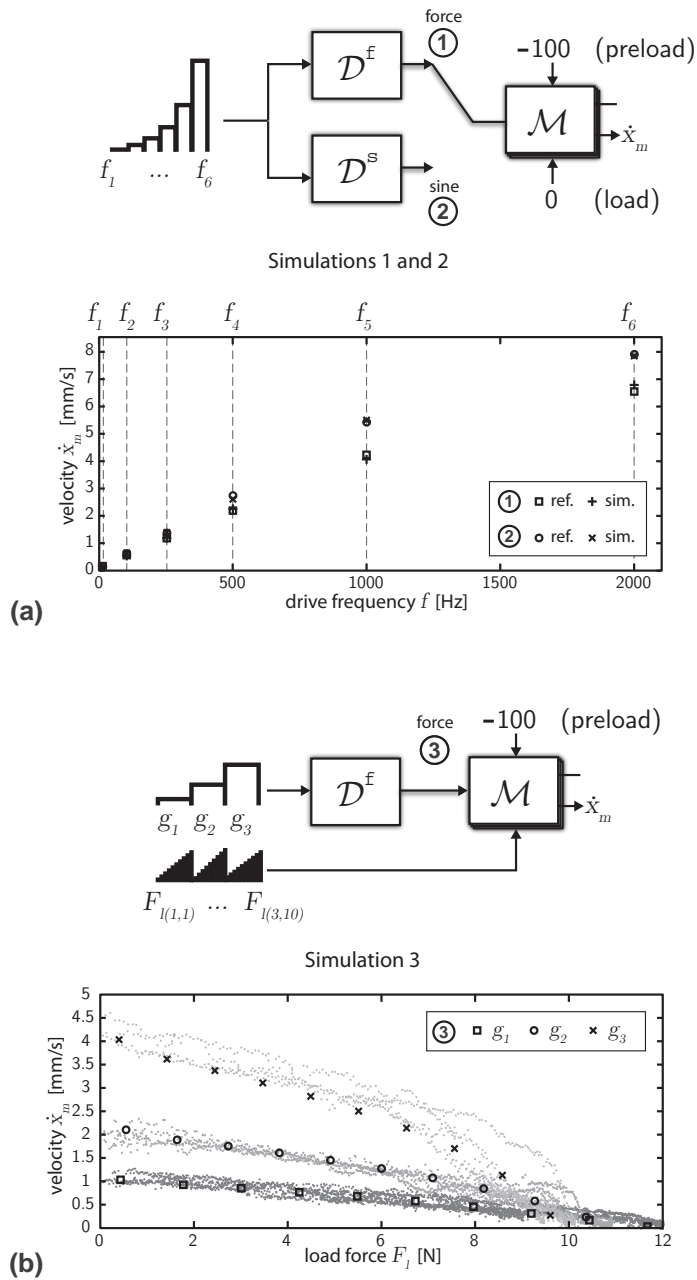
3.5 PARAMETER OPTIMIZATION

While the previous section has established a lumped parameter model of the coupled dynamics of a multi-legged motor, two more questions still need to be addressed. First, what are the values of the unknown parameters which could not be derived from the knowledge of material properties or model assumptions. And second, how accurate does the

model describe the behavior of the actual PiezoLegs motor in terms of macroscopically measurable data. This section addresses both of these questions with help of three experiments which were carried out with the PiezoLegs motor. As a result, reference data as well as an optimization procedure for model parameter identification have been found. It will be shown that the proposed model explains the measured data.

The purpose of the first two experiments was to find the damping coefficients B_{xl}, B_{zl} of the legs and B_{xr} of the drive rod as well as the nonlinear leg deflection parameters χ_0 and χ_1 from sect. 3.3.3. For this purpose, at least two different waveforms which produce distinct maximal leg deflections had to be used. Furthermore, the PiezoLegs motor had to be driven with several drive frequencies spanning its nominal range of operation in order to identify possible damping effects. The experiment had to be carried out in a load-free condition in order to prevent additional leg deflection and slipping (stiction condition). The PiezoLegs motor was driven with 6 increasing drive frequencies $f_1 = 10\,\text{Hz}, \ldots, f_6 = 2000\,\text{Hz}$ within its rated operational range either with the *force* (first) or the *sine* waveform (second experiment). The preload force F_p in z-direction (leaf spring, see Fig. 20) was set to $-100\,\text{N}$ and there was no tangential load force F_l applied in x-direction (load-free operation). For each drive frequency, the corresponding average motor velocity $\dot{x}_m$ was computed based on drive rod position measurements with a linear encoder having the resolution of 61 nm. These velocities were used as reference values for model evaluation. Two simulations mimicking the above experiments were designed in Matlab/Simulink (The MathWorks Inc., Natick, MA, USA) and used in an optimization procedure (see below) to find values of the unknown parameters which result in a best match between the measurement and simulation. Fig. 35(a) shows the simulation design.

The measured reference and the simulated velocity data is shown in the diagram on the right. The simulation data is shown for an already optimized set of parameters including the friction parameters from the previous section. A good agreement between the measured and simulated data can be seen within the full operation range of the motor. The experiments indicate linear relation between the drive frequency and motor velocity. The slight deviation from the linear trend at 2 kHz is to be attributed to the proximity of the first resonance peak of the z-dynamics at 3 kHz rather than to the damping effects as the motor can be driven at substantially higher velocities beyond the resonance region (see sect. 3.4.1).

Figure 35: Three simulations used in the parameter optimization procedure and their results. (a) load-free motor was driven with the *force* and *sine* waveforms and 6 increasing drive frequencies (f_1-f_6) within the nominal operation region. The measured (ref.) and simulated (sim.) data is shown for the optimized parameter set. (b) the motor was driven with 3 increasing drive frequencies (g_1-g_3) for each of which an increasing load was applied to the drive rod in 10 discrete steps. The magnitude of the load was based on the linear division of the measured data into 10 discrete values for each test frequency. The actually measured raw data for different frequencies is shown as intensity-coded dots. The simulation result for the optimized parameter set is shown by means of different markers.

As the driving principle of the motor relies on friction and the stiction condition assumed in the previous experiments is violated under tangential load, an additional experiment had to be designed in order to estimate the friction parameters which also explain dynamic friction effects under load. In particular, when tangential load is applied, a decrease in motor velocity is observed until the motor stops moving for a load approaching its stall force limit. To a first approximation, this velocity decrease is linear but becomes nonlinear for high drive frequencies and high loads due to permanent slipping of the legs. Especially for high drive frequencies a large variation in the measured velocities is observed not only between different motors but also for subsequent measurements performed with the same motor. A plausible explanation of this observation lies in the fact that friction is sensible to surface contamination and the friction coefficient may vary due to scraping effects (see next section). For this purpose, in the third experiment all measurements were carried out with 4 different motors. In particular, for each motor the position of its housing was fixed to ground and a force sensor was connected in series between one end of the movable drive rod and an extension spring connected to a fixed wall. When driven at a certain drive frequency and moving away from the wall, the drive rod caused spring elongation and thus continous increase of the tangential load F_l which was measured by the force sensor. At the same time, the velocity of the motor $\dot{x}_m$ was measured with help of a linear encoder as in the previous experiments. The experiment was repeated for each motor at 3 different test drive frequencies $g_1 = 250\,\text{kHz}$, $g_2 = 500\,\text{Hz}$ and $g_3 = 1\,\text{kHz}$ using the *force* waveform. The measured raw data from all experiments is shown in the diagram on the right-hand side of Fig. 35(b). The data points are intensity-coded according to their drive frequency. A simulation corresponding to the above experiment was implemented in Matlab/Simulink. For practical reasons the increasing tangential load was not applied continuously but in 10 discrete steps as seen schematically in the left-hand side of Fig. 35(b). The results of the simulation are depicted with help of different markers in the diagram on the right-hand side. Again, there is a good agreement between the simulation and the measurements. The proposed motor model captures the most important trends in the measured data, i.e. the nonlinear velocity decrease for high loads and higher stall force limits for lower drive frequencies. An even better agreement could be obtained if the model would be fitted to one particular motor and a dedicated weighting scheme would be used in the optimization procedure.

The optimization procedure which was employed in this chapter is differential evolution (DE) [166]. A global optimization algorithm was used due to the diversity of local minima for an optimization problem with 10 parameters representing either not directly measurable prop-

erties of the legs or highly nonlinear friction phenomena. Differential evolution was preferred as it converges faster and with more certainty than adaptive simulated annealing [197] and requires only a few control variables. 10 unknown model parameters including the damping coefficients, leg deflection nonlinearity scaling factors and LuGre friction model parameters from the previous section were optimized. These parameters formed a parameter vector or a population member. An initial population consisted of 70 members which were uniformly distributed over a physically plausible parameter space. The quality of each population member was evaluated by means of a simple objective function. The parameter values of the current member were assigned to the motor model and the three simulations described above were run one after another. The velocity data from each simulation was collected and compared to the reference data from the experiments. The computed least squares error was used as the quality measure. Although the default parametrization of the differential evolution algorithm was used, the optimization procedure converged to a solution after only 50 iterations – see Fig. 36. The choice of parameters used in the simulations of Fig. 35 and presented in Table 6 was obtained after 100 iterations. Although the objective functions are abundant in local minima for the given parameter space, clusters of optimal parameter values can be identified. Fig. 36(b) and (c) show this exemplary for the leg parameters which can not be measured directly. Objective function values of all parameter vectors evaluated during 223 iterations are shown by means of intensity-coded dots (higher/-darker intensity codes lower objective value). Fig. 36(b) shows that in the linear oscillator model of the leg there is a stronger damping in x- than in z-dimension and that the range of possible values for B_{xl} is much more narrow than the range for B_{zl} which does not have a strong influence on model performance. This observation has a direct correspondence to the actual design of the PiezoLegs motor in which the space between the legs is filled with a resin-like substance which influences damping in x- but not in z-dimension. In contrast, Fig. 36(c) shows that the choice of parameters for the nonlinear leg deflection function from sect. 3.3.3 is essential for the performance of the model. The parameters χ_0 and χ_1 need to have values within a clearly identifiable oval region. This can be explained by observing how the shape of the deflection function (76) changes when varying these parameters (see results in Fig. 28).
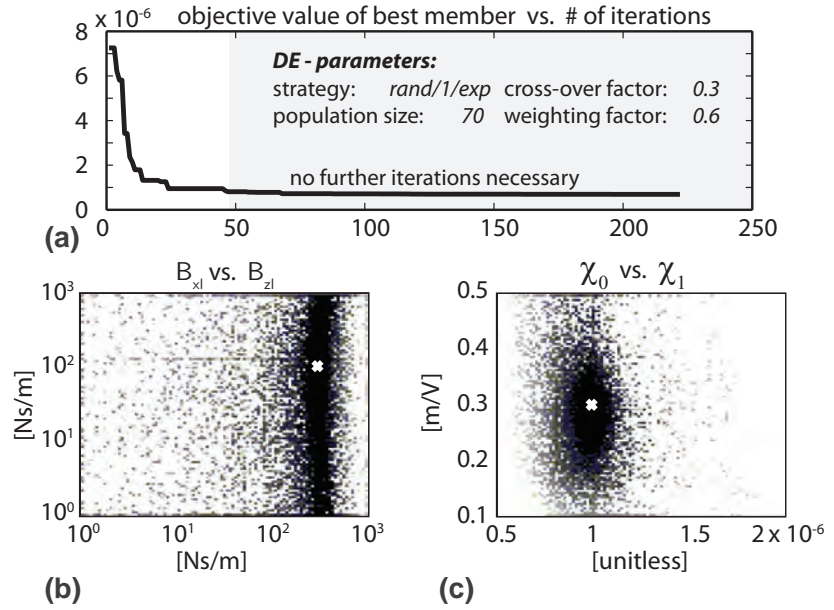
Figure 36: Objective function values. (a) shows the development of the objective value of the best population member over an increasing number of iterations. Default parametrization used in the differential evolution algorithm is indicated. (b) and (c) show the objective value of all population members as intensity-coded dots (higher/darker intensity codes lower objective value) for a choice of parameters. In (b) damping factors and in (c) nonlinear deflection parameters of the legs are considered. White markers show the choice of parameters obtained after 100 iterations and presented in Table 6. Note that the parameter values in (b) are logarithmically while in (c) linearly scaled.

Table 6: Summary of unknown model parameters obtained in the optimization process after 100 iterations.

Name	Value	SI unit	Description
B_{xr}	91.12	Ns/m	rod damping coeff.
B_{xl}	299.88	Ns/m	leg eff. damping (x)
B_{zl}	101.02	Ns/m	leg eff. damping (z)
χ_0	$9.95 \cdot 10^{-7}$	-	deflection coeff.0
χ_1	0.30	m/V	deflection coeff.1
λ_0	$9.41 \cdot 10^6$	N/m	bristle stiffness
λ_2	284.44	Ns/m	viscous friction
ν	$0.89 \cdot 10^{-2}$	m/s	Stribeck velocity
μ_{st}	0.14	-	static friction coeff.
$\widehat{\mu}_{dn}$	0.10	-	dyn. friction coeff.

3.6 DISCUSSION

The legged motor model presented in this chapter together with the set of model parameters found in the optimization process explains the behavior of the PiezoLegs motor in terms of its velocity and load characteristics. The modeling strategy followed in this chapter is based on the lumped parameters approach and the identification of unknown model parameters is based solely on macroscopically measurable data in fully assembled state. For these reasons, several simplifications have been made throughout the modeling process and are discussed in this section.

First, except of the coupled linear equations of piezoelectricity from sect. 3.2.1, leg dynamics has been considered under a pure mechanical point of view. This is justified by the fact that for the nominal range of operation the behavior of piezoelectric legs is dominated by their mechanical response. The quality of power supply has implicitly been assumed ideal. However, if the motor were driven with much higher drive frequencies, e.g. in the overdrive region of Fig. 32, the influence of leg capacitance or ceramic material permittivity would have a much stronger effect on the response speed of the legs.

Second, sect. 3.3.3 has introduced leg deflection nonlinearity in x (hysteresis). While this modeling decision has been motivated and justified by the experiment in Fig. 28 and the optimization results in Fig. 36(c), the model does not consider hysteretic effects in z. In contrast to x-dynamics, an explicit model of hysteresis in z is not possible with the modeling strategy based on macroscopic measurements. Furthermore, a hysteretic effect in z can not be identified easily as the elevation of the drive rod is not measured experimentally. Still, the linear model of leg elevation introduced in sect. 3.4.1 is able to predict the resonance and overdrive regions of Fig. 32 as well as the higher level of preload force possible with the *force* waveform as indicated in Fig. 31. As long as no extreme levels of preload force are used and the transitions in contact with the drive rod between different leg pairs are guaranteed, the linear model of leg elevation seems to be sufficient. As far as the hysteresis in x-dimension is concerned, it should be noted that the sigmoid function used to model leg-deflection nonlinearity [see equation (76)] is chosen arbitrarily. Specifically, the slope of the arctan function determined by the parameter χ_1 is not supported by experimental data since only two waveforms were used in the experiments. However, the choice of a sigmoid function in general is motivated in sect. 3.3.3. The specific form of this function could only be estimated by measuring the actual deflections of the legs.

Another modeling simplification concerns the computation of the structural stiffness of the legs. In sect. 3.3.1 it has been assumed that a leg consists of two independent piezoelectric stacks, each of them composed of a number of piezoelectric layers which can be treated as

a series connection of springs. In reality, the two stacks are formed by the same end-to-end ceramic layers and the functional discrimination between the stacks is conditioned only by the placement of electrodes in between these layers. An exact model of structural stiffness of such a composite structure is not trivial and has not been further pursued in this work. For a modeling approach, see e.g. [76]. The simplified spring model provides a resonably good approximation of the actual stiffness of the composite structure as the predicted resonance regions and the level of load forces which the legs can hold correspond to the actually measured values.

Also in case of interaction with the drive rod, several modeling simplifications have been made. In sect. 3.4.1, the preload force F_p acts on the point mass model of the drive rod and is assumed constant. In the actual PiezoLegs motor design, the drive rod is a relatively long ceramic bar which is pressed against the legs by means of a stack of leaf springs and two roller bearings on the opposite sides of the motor housing (Fig. 20). When the drive rod moves, the position of its center of mass changes which may lead to the development of torque and drive rod instability affecting leg contact. The simplified model view is justified by the fact that the preload force is chosen high enough to ensure permanent contact to the legs within the rated operation range and that there are always $M \geq 2$ legs in contact to ensure static stability. This is not the case in the resonance region and if the behavior of the motor in this particular region were of interest, the exact distribution of forces along the drive rod would need to be considered. Also the level of preload may be assumed constant as the change in drive rod elevation in the $2 \cdot 10^{-6}$ m range has a little effect on F_p given the effective stiffness K_{zr} of the leaf springs in the 10^5 N/m range. It would be interesting to analyse the effect of the K_{zr}/K_{zl} ratio on the magnitude of drive rod oscillations and the development of normal and frictional forces. Higher K_{zr} would lead to a higher resonance level but also to higher F_p variation. The interaction with legs in x-dimension is governed by friction. The LuGre model has been chosen in order to unite the static as well as dynamic friction phenomena within one modeling framework. Still, frictional effects can be observed which are not covered by the present model. One of them is the effect of surface contamination on the magnitude of the friction coefficient mentioned in the previous section. When the motor is driven at a high drive frequency under increasing tangential load, the legs hit the drive rod more often at the same spots due to velocity decrease (surface of the drive rod above the legs is not forwarded or forwarded slowly). At the same time, the drive rod is scraped clean of potential contaminations which may lead to the increase of friction coefficient and thus improved load characteristics. Friction may also change in dependence of the time of contact and the true area of contact between the legs and the drive rod. These factors have not

been considered in the present work. For a more in-depth treatment of this topic see [218].

In summary, the modeling decisions of this chapter have resulted in a motor model consisting of a collection of systems not exceeding second order which can be extended to cover additional aspects of motor operation, especially if low-level experimental data were provided. Based on the macroscopic velocity and load force measurements, an optimization procedure had to be employed in order to find the model parameters which were not known or could not be measured directly. A more complete analysis would be required in order to estimate the sensitivity of the model to parameter variation and indicate directions for further improvements. Nevertheless, the previous section has shown that the optimization process converges quickly to a high quality solution even with standard parametrization applied and that the bounds on parameter values can be identified. The derived physical model accurately describes the linear drive frequency/velocity as well as the nonlinear load force/velocity characteristics of a real walking motor within its full operational range. The model will be used in chapt. 5 to investigate the effects of a bioinspired drive strategy on the performance of the walking motor.

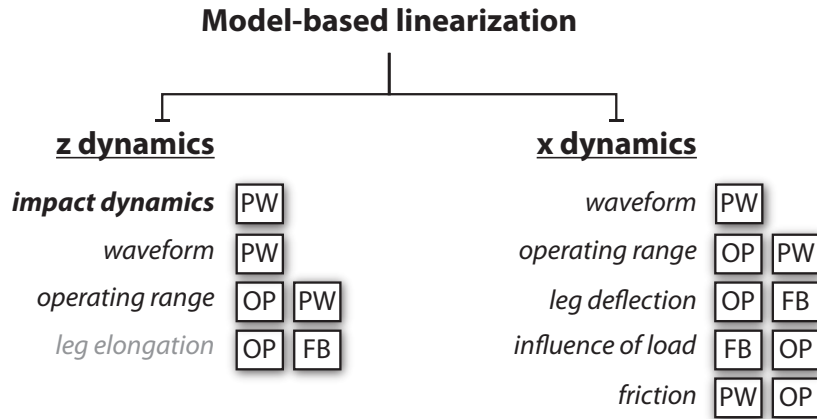# 4 | GRAY-BOX IDENTIFICATION OF SEMIPHYSICAL MOTOR DYNAMICS

ABSTRACT

This chapter presents an experimental approach for deriving a semiphysical model of the walking motor. The difficulties related to the linearization and control theoretical application of the physical model are discussed and a modeling approach based on statistical data evaluation proposed. The new approach results in three motor models of increasing complexity which are independent of the low-level piezoelectric properties of the driving elements and the impact dynamics of the legs. The basic model establishes a static relation between motor velocity and drive frequency for a free-moving motor. The second model is a nonlinear extension of the first model which introduces external load forces. The final model introduces time-dependent aspects by employing system identification techniques. The content of this chapter is partly based on publication II.

4.1 INTRODUCTION

The motor model derived in the previous chapter reproduces the behavior of the actual walking motor within its full range of rated operation and can be used to anticipate alternative drive strategies, possible design improvements, etc. These issues will be addressed in the next chapter in which a bioinspired drive strategy will be proposed. In this chapter an alternative modeling approach based on system identification techniques will be motivated and utilized. The main reason for a yet another motor model is the necessity to control the motor in practical applications. This goal cannot be achieved easily with the model from the previous chapter due to several reasons including its nonlinear nature which complicates the design of a suitable controller and the level of detail which is beyond the capacity of real-time controllers and online simulations. A linearization attempt resulting in a simplified model is required. The following sentence from a lecture by Richard Feynman [70] motivates this strategy:

> Finally, we make some remarks on why linear systems are so important. The answer is simple: because we can solve them!

Fig. 37 illustrates the selection of nonlinearities of the physical model together with possible means of their linearization. The physical model consists of two dynamics (x and z-dynamics, see chapt. 3) and

Model-based linearization

	z dynamics		x dynamics	

impact dynamics | PW

waveform | PW

operating range | OP | PW

leg elongation | OP | FB

waveform | PW

operating range | OP | PW

leg deflection | OP | FB

influence of load | FB | OP

friction | PW | OP

Figure 37: Overview of nonlinearities in the walking piezoelectric motor as identified in the physical motor model from the previous chapter and possible methods of their linearization (PW – piecewise linearization, OP – operating point linearization, FB – feedback linearization). Impact dynamics (in bold face) of the legs plays the determinant role in the switched-mode behavior of the motor. Leg elongation nonlinearity not included in the motor model is shown in gray-shade for the sake of completeness (cf. sect. 3.3.3).

can be considered a *hybrid switched-mode* [130, 7, 4] or *jump parameter* [199] system. This consideration lies in the fact that the system is subject to a sudden change in the values of its parameters depending on the contact condition between the legs and the drive rod. Any linearization attempt has to address this issue first. The most straightforward approach is to differentiate between 4 cases in which either one pair, the other, both leg pairs or no legs have contact with the drive rod; the latter being an artificial case. In this manner a piecewise system [161, 54] consisting of several subsystems for each case is obtained. However, this increases the number of state matrices which can become dramatically high if other nonlinearities are to be split into piecewise linear components. In order to reduce the number of subsystems, several realizations of state switching are conceivable and shown in Fig. 38. The states are depicted as numbered circles with the necessary conditions for being in the particular state shown next to them. State transition conditions are not shown on purpose as the actual implementation may range from a finite-state automaton to a Markov process.

Fig. 38(a) shows the obvious case with the cycling *one leg pair – both pairs – other leg pair …* transitions. Assuming both leg pairs behave identically and resetting their state periodically reduces the number of states by one [Fig. 38(b)]; neglecting the contact dynamics during the overlapping contact condition and using a periodic reset would yield a single state implementation [see Fig. 38(c)]. The no-contact condition (floating drive rod) is ignored in all cases. Although
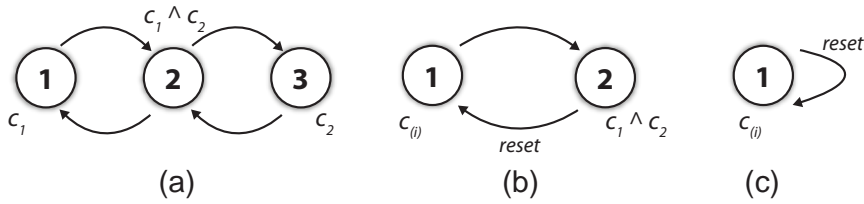
Figure 38: Possible realizations of state switching for the impact dynamics of the legs. (a) shows the basic realization with three states where either leg pair 1 (c_1) only, both leg pairs ($c_1 \wedge c_2$) or leg pair 2 (c_2) only have contact with the drive rod. (b) two-states simplification of (a) with a reset signal. (c) a further simplification neglecting contact transition dynamics.

theoretically possible, the piecewise linearization strategy proposed in Fig. 38 could not be attained in a practical control scenario due to the high switching frequency of the process (up to 3 kHz) and the non-observability of the states. The latter issue is especially prohibitive in a force control scenario when the motor is severely disturbed by external forces. However, for relatively slow nanopositioning tasks under negligible loads the above linearization strategy could prove useful in a robust control scenario.

The high switching frequency of the motor remains an obstacle for any further linearization attempt of the model from chapt. 3. However, before proceeding to the next section in which an alternative modeling strategy based on an experimental approach is proposed, other analytic possibilities will be sketched shortly for the sake of completeness. Please note, that the goal of the following discussion is not to arrive at a realistic control-theoretical motor model but rather to shed light on possible pitfalls related to the analytic linearization approach. Focusing again on Fig. 37, the behavior of the motor strongly depends on the choice of the driving waveform (see sect. 3.2.2 and chapt. 5) which affects the level of leg deflection, elevation, drive rod contact times, etc. and thus determines the linearization procedure of the other nonlinearities. The only sensible choice seems to be the linearization for a particular waveform choice.

The term operating range in Fig. 37 relates to the upper bandwidth limit of the drive frequency. It has been shown in Fig. 32 of sect. 3.4.1 that the motor can be driven with frequencies beyond its rated operation. In this case, several regions of operations between and beyond the resonance regions could be distinguished and the model split into several piecewise linear models. However, the ultrasonic mode of operation is likely to lead to further difficulties due to increased current consumption, temperature rise, etc. Last but not least, this would further increase the switching frequency of the motor. For these

reasons, choosing an operating point below 3 kHz seems to be the best solution.

The nonlinearity related to leg deflection was considered in sect. 3.3.3. For many waveforms a suitable operating point could be chosen or even a piecewise model proposed. An alternative approach could be based on feedback linearization [73] but this would require the knowledge of leg states which are not observable in the real motor. A variation of this technique is shown in chapt. 7 where it is used to compensate the effects of external load on motor velocity.

Last but not least, the operation of the motor is based on friction. The nonlinear LuGre model from the previous chapter proved to be suitable to explain the friction phenomena in the walking motor (see sect. 3.4.2). Operating point linearization of this model in the stiction or slippage regions are possible [74, 156]. However, these simplifications obviously neglect either the dynamic or quasi-static aspect of motor operation. Moreover, linearization for the stiction condition increases model complexity by introducing two additional model states, both of which are neither controllable or observable. A piecewise attempt, possibly with a different friction model, seems to be better suited but it poses the non-trivial problem of mediation between the cases.

Considering the multitude of difficulties in analytic motor model linearization, a different approach has been chosen in this chapter. In the following sections, the motor is seen as a gray-box [187] whose input, output and transfer characteristics can be experimentally measured but little knowledge of its internal workings is assumed. The model will be derived based on an measurement and subsequent (least square) statistical data evaluation. In sect. 4.2.1 the basic linear model of the unloaded case is presented. This model is extended by the nonlinear influence of mechanical load in sect. 4.2.2 and the dynamic transfer characteristics in sect. 4.2.3. The final model will be used in chapt. 7 to develop a load force compensation strategy which linearizes the model completely and to design an explicit force controller.

4.2 GRAY–BOX MODELING

It is customary to distinguish between three levels of prior knowledge when modeling dynamical systems. These are referred to as white, gray or black-box models [187] with black standing for no knowledge, white for full knowledge and gray being the in-between case. According to this definition, the physical motor model from the previous chapter is "gray" as some parameters were not known and needed to be estimated. Sjoberg [187] differentiates additionally between physical and semiphysical gray-box modeling depending on

the employment of first principles in the modeling process. Thus, while the model established in the previous chapter was physical, the model to be derived in this chapter is semiphysical in accordance with this widespread classification.

4.2.1 Static unloaded behavior

The development of the motor models in this chapter is based on experimental data obtained for $N = 4$ different PiezoLegs-motors driven with the *force* waveform since later the motors will be applied as force generators in a small-sized robot joint (see chapt. 7 and 8). The motors were equipped with magnetic linear encoders (NANOS-Instruments GmbH, Hamburg, Germany) which allow a relative position measurement with an accuracy of 61 nm. The position data was sampled at 200 kHz. In the unloaded case, the translatory movement velocity of the drive rod (motor velocity v_m) shows an approximately linear dependency with respect to the drive frequency f of the four-phase voltage system.

In its basic form, the motor model assumes a linear relation between the motor drive frequency f and the drive rod velocity v_m. In order to evaluate this assumption, each motor j was driven with 6 different drive frequencies ranging from 10 to 2500 Hz and its drive velocity was measured. The obtained measurement pairs $\{f_k, v_k\}$ with $k \in \{1, \ldots 6\}$ were used to compute the least squares estimates of the regression coefficients a_j for each of the N motors:

$$a_j = \frac{\sum_k f_k v_{k,j}}{f_k^2}, \quad j = 1, \ldots, N. \tag{96}$$

The regression was assumed to pass through the origin which is justified as for the trivial case of $f = 0$ Hz the motor does not move. The average slope $\bar{a}$ of the freq.-vel. line for the average motor model was computed as the mean value of the results from (96) for the N motors:

$$\bar{a} = \frac{1}{N} \sum_{j=1}^{N} a_j. \tag{97}$$

Fig. 39(a) illustrates the results. Their numerical values are summarized in Table 7. The average slope $\bar{a}$ is shown as a bold line in the diagram. Its quality was evaluated with the R^2 coefficient of determination on the measurements done for all motors. The value of $R^2 = 0.88$ shows that the linearity assumption is plausible. It explains most of the data in the operating range of the PiezoLegs-motor. Still, the correlation deteriorates for frequencies approaching f_{lim} = 3 kHz. In order for the motor to remain in its linear domain, a new limit f_{max} of 2000 Hz for the maximum drive frequency is defined. It prevents the motor from reaching the resonance limit f_{lim} and assures the linearity of the basic model. In the following, the drive frequency signal
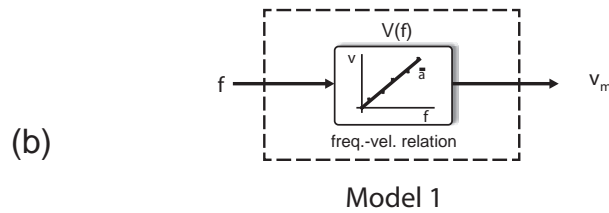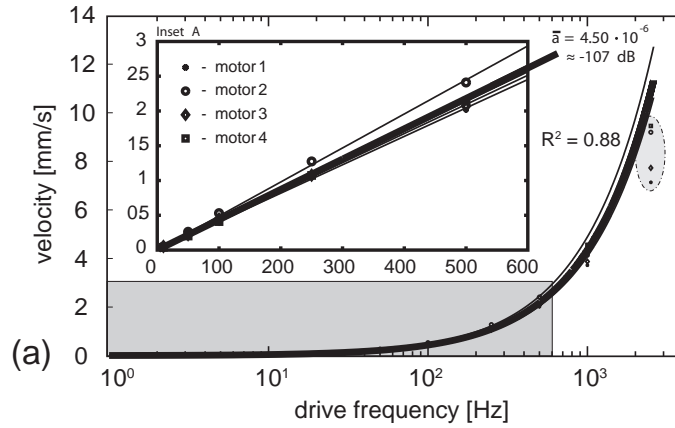
Figure 39: Linear dependency between motor drive frequency f and the velocity v_m of the drive rod. The main diagram in (a) illustrates least squares linear fits on the measured motor data for 4 different motors. The shaded region is magnified in the linearly scaled inset A. The slope a and the coefficient of determination R^2 are given for the average linear fit (bold line). The encircled set of points at 2500 Hz was not included in the regression analysis – it illustrates that the linear dependency deteriorates for frequencies approaching f_{lim}. (b) shows the basic motor model.

is assumed not to exceed f_{max} if not noted otherwise. The basic linear model, as shown in Fig. 39(b), is expressed by

$$v_m = V(f) = \bar{a}f \tag{98}$$

Table 7: Frequency scaling factors computed for all motors and their average value expressed in decibels.

Motor j	Freq. scaling factor a_j
1	$4.25 \cdot 10^{-6}$
2	$5.13 \cdot 10^{-6}$
3	$4.34 \cdot 10^{-6}$
4	$4.26 \cdot 10^{-6}$
average motor	$\bar{a} = \mathbf{4.50 \cdot 10^{-6}}$ $\approx -\mathbf{107}$ dB

The unit of all data is $[m/s \cdot 1/Hz]$.

where f is the motor drive frequency, $V(f)$ is the freq.-vel. relation as introduced above and v_m is the velocity of the drive rod.

4.2.2 Static behavior under load

The linear freq.-vel. dependency is valid only in the unloaded case. If an external force is applied to the drive rod of the motor, the velocity decreases nonlinearly with increasing force. To quantify this observation, the motor housing position was fixed and a force sensor (ME-Meßsysteme GmbH, Hennigsdorf, Germany) was attached to one end of the movable drive rod. This force sensor has two mechanical connectors, the second of which was attached to a fixed point via an extension spring. The sensor can measure forces up to 25 N with a resolution of 0.1 N. Fig. 40(a) shows the top view of this experimental setup. All N motors were driven with several fixed frequencies laying in their linear range of operation. For each frequency f_i, the pulling force F_k on the drive rod up to F_{max} (10 N) and the motor velocity $v_{k,i}$ were measured while the moving rod stretched the extension spring. Fig. 40(b) illustrates the results for three drive frequencies $f_1 = 250$, $f_2 = 500$ and $f_3 = 1000$ Hz.

The velocity decreases nonlinearly with increasing force levels. This tendency can be captured by a monotonically decreasing polynomial fit of the form:

$$V(f,F) = \sum_{j=0}^{M} b_j(f) F^j \tag{99}$$

where M is the order of the polynomial fit, F is the external force on the system (in the experiment generated by the extension spring) and $b_j(f)$ are the drive frequency dependent coefficients. For the fit at each frequency dependant force-velocity curve, a third order polynomial was chosen. The fits are represented by the bold curves in Fig.40(b). The dashed lines are the error estimates on the corresponding fits and represent bounds on the fits which contain at least 50 % of the data samples used in the fitting process if the samples are assumed to be independent and with a constant variance.

For the generation of a motor model for the loaded case, it is inefficient to use a set of polynomials for several drive frequencies as defined in (99). However, the relation between drive frequency, force and velocity shown in Fig. 40(b) can be separated conveniently by using the average frequency scaling factor ā introduced in (97).
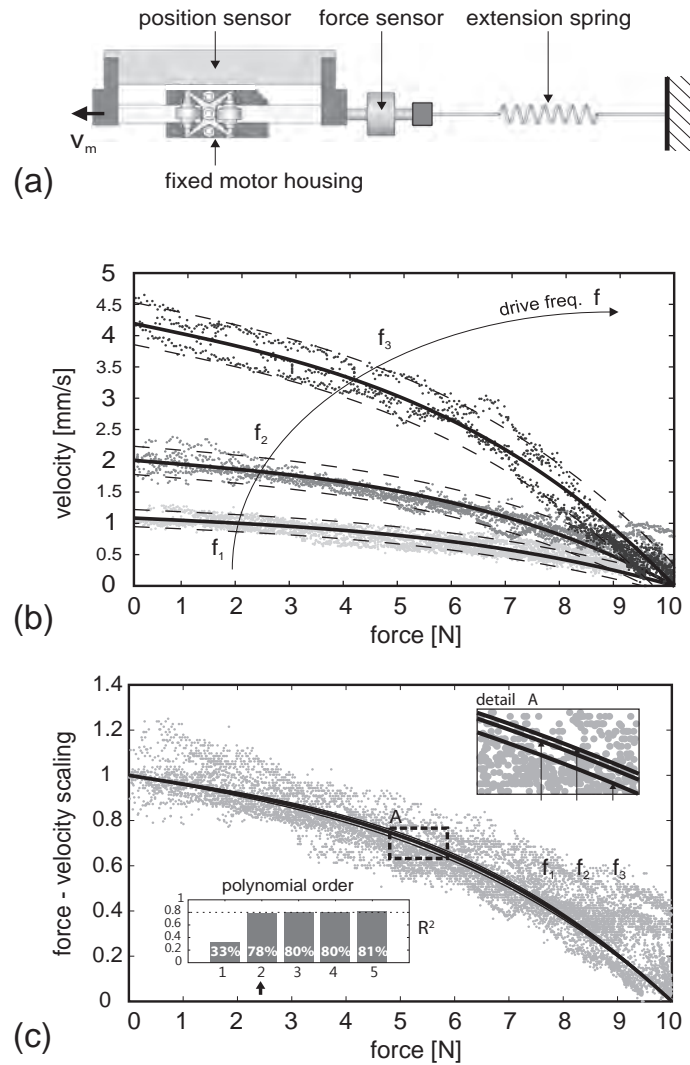
Figure 40: Effect of external force on the drive rod movement velocity v_m.
(a) shows the top view of the experimental setup used to obtain
velocity and force measurements for increasing motor drive fre-
quencies in (b). The bold lines illustrate third order polynomial
fits on data measured for 4 different motors. The dashed lines
are error bounds on the corresponding fits. (c) shows the effect
of scaling the data points from (b) with the corresponding fre-
quency and the linear frequency scaling factor $\bar{a}$ from sect. 4.2.1.
The bold line shows an average third order polynomial fit on all
freq.-normalized force-velocity data points. The quality of the fit
in dependency of its order is presented in the lower inset. Detail
A shows the normalization effect when applied to the polynomial
fits from (b). Note that the bold line is not shown in the detailed
view for the sake of clarity.

In the first step, the frequency dependency of the data points $\{v_{k,i}, F_k, f_i\}$ is eliminated according to:

$$v_k^* = \frac{v_{k,i}}{\bar{a} \cdot f_i} = \frac{v_{k,i}}{V(f_i)},$$ (100)

resulting in normalized data points $\{v_k^*, F_k\}$. The normalization effect is depicted in Fig. 40(c). Although measured for different drive frequencies, the data points from Fig. 40(b) fall close together for corresponding force levels when normalized. All of these normalized force-velocity data points were used in the second step to estimate least squares polynomial fits of increasing order according to:

$$\min_{\mathbf{b}} \left\| \mathbf{F}\mathbf{b} - \mathbf{v}^* \right\|_2^2$$ (101)

where

$$\mathbf{F} = \begin{pmatrix} 1 & F_1 & F_1^2 & \dots & F_1^M \\ 1 & F_2 & F_2^2 & \dots & F_2^M \\ \vdots & \vdots & \vdots & \ddots & \vdots \\ 1 & F_k & F_k^2 & \dots & F_k^M \\ \vdots & \vdots & \vdots & \ddots & \vdots \\ 1 & F_n & F_n^2 & \dots & F_n^M \end{pmatrix}$$ (102)

is the matrix of force measurements which are raised up to the power of M,

$$\mathbf{v}^* = \begin{pmatrix} v_1^* \\ v_2^* \\ \vdots \\ v_k^* \\ \vdots \\ v_n^* \end{pmatrix}$$ (103)

and $\mathbf{b}$ is a column vector of $M + 1$ coefficients. The estimation process was based on linear least-squares polynomial curve fitting with constraints [80]. The constraints can be motivated by the general behavior of the motor. In particular, the polynomial fit has to:

1. have the value of 1 for the load-free case (max. velocity);

2. have the value of 0 for the maximal external force F_{max} (velocity is zero, stall case);

3. be strictly monotonically decreasing for $F \in [0, \cdots, F_{max}]$ (as can be seen in the data).

Even with the above constraints, a polynomial fit of the order $M = 2$ already captures most of the variation in the normalized data resulting in R^2 values of 0.8 (compare Fig. 40[c]).[1] The bold curve is a polynomial of second order computed for freq.-normalized data obtained

---

[1]Higher orders polynomials with $M \to \infty$ were not considered due to their complexity and the lack of analytic solution methods.
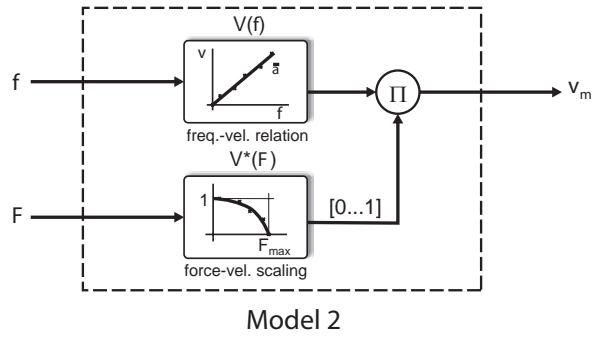
Model 2

Figure 41: Enhanced motor model including the nonlinear effect of an external force F acting on the drive rod ($V^*(F)$).

with 4 different motors. Furthermore, the polynomials from Fig. 40(b) overlap if normalized by dividing them with the corresponding value $V(f_i)$. This can be seen in the detailed view of Fig. 40(c) and confirms the assumption that it is possible to separate the effects of frequency and force on the motor velocity. Specifically, the frequency dependant polynomial from (99) can be approximatively expressed as a product of two independent functions:

$$V(f, F) \approx V(f) \cdot V^*(F). \tag{104}$$

where $V^*(F)$ is a constrained polynomial fit on the normalized force-vel. data as introduced above. The first of the three constraints on the polynomial fit ensures that the equation for the force-dependent velocity (104) reduces to the load-free case from (98). The second constraint reflects the fact that the motor stops moving when its stall force limit is reached. For this limit a constant value of F_{max} is assumed (waveform and frequency dependent variations are neglected; cf. Fig. 35 and Fig. 51). The third constraint reflects the tendency observed in the measured data and prevents the polynomial fit from having only statistical significance due to the scatter in the data (stick-slip effects between the legs and the rod and noise).

   With the above observations a motor model for the loaded case can be established, resulting in the following model equation:

$$v_m = V(f) \cdot V^*(F). \tag{105}$$

The model is depicted as a block diagram in Fig. 41 and the coefficients for the normalized polynomial fits $V^*(F)$ up to M = 3 are listed in Table 8.

4.2.3 Linear dynamics

The previous sections have shown how the drive frequency and external force are related to the motor velocity. Still, the relation from (105)

is just a static mapping which does not consider any time constants of the motor system. In the following, a discrete dynamic system model for the PiezoLegs-motor is derived using system identification. The identification techniques allow to estimate a whole dynamic model or just a set of parameters from experimental data *"when it is difficult to obtain reasonable models using only physical insight or if the modelled processes are too complex to remain at the physical modeling level only"* [192].

A linear time-invariant system can be expressed in form of difference equations as follows:

$$
\begin{aligned}
y(t) + c_1 y(t - T) + \ldots + c_{n_c} y(t - n_c T) = \\
d_0 u(t) + d_1 u(t - T) + \ldots + d_{n_d} u(t - n_d T) + \\
\varepsilon(t) + e_1 \varepsilon(t - T) + \ldots + e_{n_e} \varepsilon(t - n_e T)
\end{aligned}
\tag{106}
$$

with $u(t)$, $y(t)$ and $\varepsilon(t)$ being system input, output and disturbance at time t, respectively. T is the cycle time of the system. In a compact ARMAX notation [135] the above equation can be expressed as:

$$
C(z^{-1})y(t) = D(z^{-1})u(t) + E(z^{-1})\varepsilon(t)
\tag{107}
$$

where

$$
C(z^{-1}) = \qquad 1 + c_1 z^{-1} + \ldots + c_{n_c} z^{-n_c}
\tag{108a}
$$
$$
D(z^{-1}) = \qquad d_0 + d_1 z^{-1} + \ldots + d_{n_d} z^{-n_d}
\tag{108b}
$$
$$
E(z^{-1}) = \qquad 1 + e_1 z^{-1} + \ldots + e_{n_e} z^{-n_e}
\tag{108c}
$$

and z^{-1} is the backward shift operator. The transfer function for an ARMAX model is given by

$$
\frac{D(z^{-1})}{C(z^{-1})}.
\tag{109}
$$

For the identification of the PiezoLegs-motor, a sum of sines input signal was used. The signal can be considered a frequency-modulated (ν: modulation frequency) drive frequency input (f) of the following form

$$
u(t) = \sum_{j=1}^{n} A_j \sin(2\pi \nu_j t + \phi_j).
\tag{110}
$$

The input was sampled at the rate $T = 5$ ms and consisted of $n = 20$ different frequency components spanning the range from 0 to 100 Hz

Table 8: Coefficients of the polynomial fits on normalized force-vel. data up to the third order.

| M	b_3	b_2	b_1	b_0
1	-	-	−0.1000	1.0000
2	-	−0.0094	−0.0060	1.0000
3	−0.0006	0.0000	−0.0384	1.0000

(the Nyquist frequency of the sampling system). The amplitudes A_j were randomized and the phase offsets ϕ_j computed according to the formula by Schroeder

$$\phi_j = \frac{\pi k^2}{n} \, , \qquad k = 1, 2, \cdots, n \qquad (111)$$

which improves/minimizes the crest factor of a multisine signal [65].[2] Each motor was driven with 5 independent inputs generated according to (110). The motor was load free in order to prevent the nonlinear force effects described in the previous section from corrupting the linear identification. The measured data for each motor was merged into a single experiment in order to increase the number of input-output samples and evaluated using the Matlab System Identification Toolbox (Matlab, The MathWorks Inc., Natick, MA, USA). Four different models were estimated using the prediction error method (PEM) which gives the least squares estimates of the coefficients from (108). In this work, no external disturbances were assumed. The results of the experiment can be seen in Fig. 42.

---

[2]The crest factor is the ratio of peak values to the average value of a signal. The minimal crest factor of 1 indicates no peaks. Signals with a low crest factor are useful for system identification since they inject more power into the system at the frequencies of interest. Using a low crest factor input signal can improve the signal to noise ratio of the resulting plant output. [162]
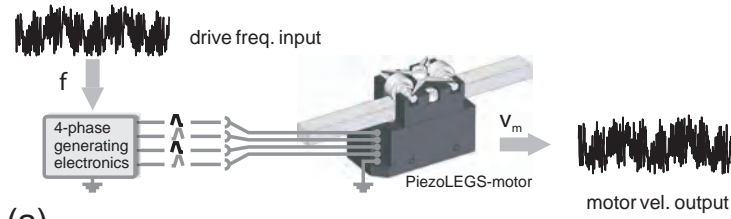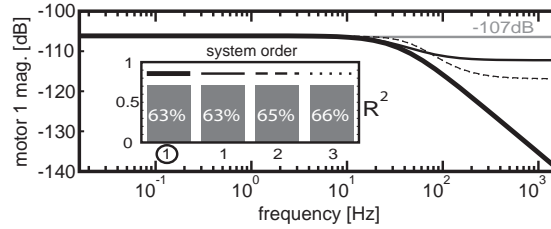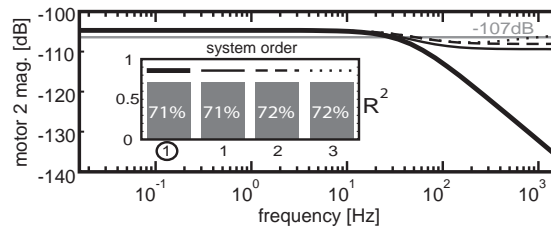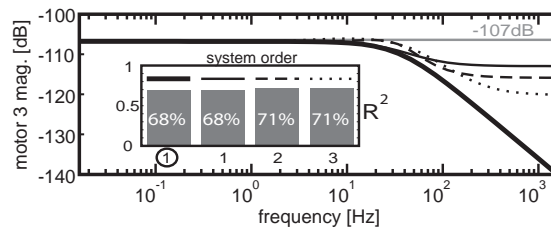
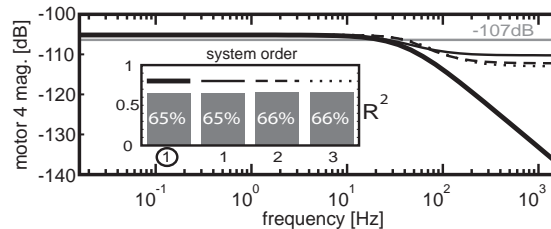**Figure 42:** System identification experiment and its results. (a) is a schematic depiction of the experiment in which frequency modulated drive frequency signal (input) was used to drive the PiezoLegs-motor while the motor velocity response (output) was measured. The diagrams (b)-(e) are bode magnitude plots of the transfer functions obtained in the experiment for each of the 4 motors. In each diagram, the -107 dB magnitude from Fig. 39 is indicated (gray line). The estimated transfer functions were linear state space models (no assumptions on model structure) of increasing system order as well as a lowpass approximation (encircled first-order system). The quality of their fit with respect to the real output signal was evaluated using the R^2 coefficient of determination measure.

Four general discrete linear models up to the order of 3 and a lowpass model have been estimated using PEM. Except of the lowpass model, no assumption on model structure was made. As can be seen in Fig. 42(b-e) all models manage to explain over 2/3 of the variation in the system output and the estimated gains for all systems up to about 20 Hz lay close to the -107 dB average slope ā from (97). The lowpass model was chosen as it explains 70% of the data while being the simplest one and bearing a physical significance. The difference equation for a discrete lowpass with the time constant τ and gain K is given by:

$$y(t) = (1 - \frac{T}{\tau + T})y(t - T) + \frac{KT}{\tau + T}u(t) \tag{112}$$

or in the notation from (108) by:

$$C(z^{-1}) = 1 - (1 - \frac{T}{\tau + T})z^{-1} \tag{113}$$

$$D(z^{-1}) = \frac{KT}{\tau + T} \tag{114}$$

with the transfer function [see (109)]

$$G(z) = K\frac{T}{(\tau + T) - \tau z^{-1}} \tag{115}$$

The numerical estimates of these parameters for all motors and for the average motor model are summarized in Table 9.

It should be noted that in the strict sense, the identification experiment delivered a linear model of the motor together with the 4-phase generating electronics (see chapt. 6.2) which converts the drive frequency signal into the amplified analog 4-phase signal. Still, the electronics can be considered with a pure time delay of 50 μs (the signal propagation time through the amplification stage) and thus neglected in the model because this delay is of two orders of magnitude smaller than the data sampling rate and the loop rate of the force controller designed for the motor in sect. 7.3. The estimated lowpass model can be easily combined with the static model (105) from the previous section. There are two reasons for this.

First, because in (105) the nonlinear force effect has been separated from the freq.-vel. relation and can be considered a (force dependent) constant. Accordingly

$$G(z) = G(\mathcal{Z}\{V(f, F)\}) = G(\mathcal{Z}\{V(f)V^*(F)\}) \tag{116}$$
$$= V^*(F)G(\mathcal{Z}\{V(f)\}) \tag{117}$$

where $\mathcal{Z}\{.\}$ is the Z-transform operator.

Second, because there is a correspondence between the slope of the freq.-vel. relation from (97) and the estimated gain K of the lowpass. By assuming
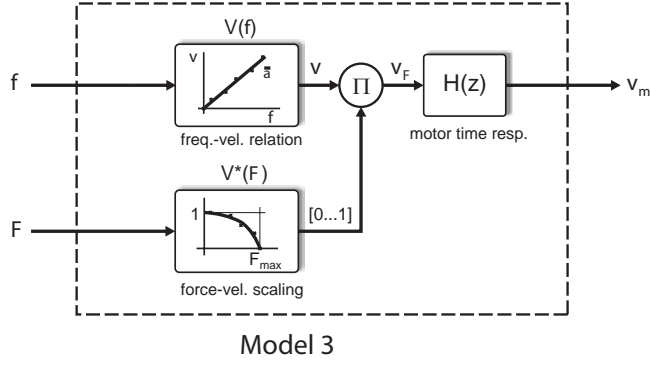
$$a \approx K \tag{118}$$

Model 3

Figure 43: Enhanced motor model including a first-order dynamics $H(z)$.

and

$$H(z) = \frac{1}{K}G(z), \tag{119}$$

the final motor model becomes:

$$v_m = \mathcal{Z}^{-1}\{H(z)\mathcal{Z}\{V(f)\}\} \cdot V^*(F). \tag{120}$$

This model is depicted in Fig. 43 with v_F and v_m corresponding to u and y from (112).

The final model has linear dynamics but is still nonlinear due to the force-vel. scaling. In sect. 7.2 a load compensation strategy based on feedback is proposed which restores the linearity of the model. This will allow the employment of linear control theory to design a force controller in sect. 7.3 and lay the foundation for a practical application of the walking motor in a bioinspired control scenario of chapt. 8.

4.3 DISCUSSION

This chapter has introduced three motor models based on an experimental approach which are suitable for the application in real time control scenarios. The first and simplest model establishes a static relationship between velocity and drive frequency in the load-free case. It was shown that the movement behaviors of four different motors are similar enough to be replaced by one average frequency scaling factor ā. The second model extends the first by introducing the influence of an external force which pulls at the drive rod of the motor. The nonlinear force-velocity relationships which arise for each drive frequency were normalized by using the average frequency scaling factor ā from the first model. The normalized force-velocity data can be fit with a polynomial. Here, a second order polynomial was chosen which results in a squared correlation value of 80 %. A further increase of the polynomial order does not improve the quality of the

fit since the underlying data points are scattered. Several reasons are conceivable to explain that.

First, there exists a noteworthy variance of the basic velocity data because of the nonlinear drive rod movement caused by the stepping pattern of the four piezoelectric legs. Second, slipping-effects between drive rod and piezoelectric legs might occur which change the rod position abruptly. Third, noise in the force measurement arises from the analog nature of the measurement. However, the compensation of the first two effects would call for additional submodels based on material interactions and frictional effects. This would obscure the straight-forward modeling strategy followed in this chapter. The third motor model extends the second model with the time aspect. No causal system can generate an action immediately. With the system identification techniques described in section 4.2.3, linear time-invariant models of increasing order have been estimated for load-free piezo motor movements. It has been shown, that already a first-order system is sufficient to describe the time dependency of the motor. Higher-order systems did not result in higher quality fits. However, note that strong differences can be observed in the decline of the gains for systems of different orders in the magnitude plots of Fig. 42. If motor operation above $100\,\mathrm{Hz}$ – i.e. the maximum frequency included in the multisine signal used in sect. 4.2.3 – were of primary interest, the identification experiment would have to focus on frequencies above this value in order to return a more reliable estimation of the gain at high drive frequencies.

As far as system identification techniques are concerned, only one research group is known to the author to have tried to model the walking piezoelectric motor using the experimental approach. Merry [145] performed several identification experiments at fixed frequencies with noise artificially added to the drive signals. Their experiments resulted in a third order LTI model of the motor together with a high precision linear stage (compound system model). Despite its superb performance in low frequency precision positioning application, the estimated model has one serious shortcoming in terms of this work.

Table 9: Gains and time constants of the lowpass dynamic model estimated for all motors and their average values assumed in the motor model.

| Motor j	Gain K_j	Time const. τ_j
1	$4.92 \cdot 10^{-6}$	$4.5 \cdot 10^{-3}$
2	$5.80 \cdot 10^{-6}$	$3.8 \cdot 10^{-3}$
3	$4.56 \cdot 10^{-6}$	$4.6 \cdot 10^{-3}$
4	$5.51 \cdot 10^{-6}$	$4.0 \cdot 10^{-3}$
average motor	$\overline{K} = \mathbf{5.19 \cdot 10^{-6}}$ $\approx \mathbf{-106\ dB}$	$\overline{\tau} = \mathbf{4.22 \cdot 10^{-3}}$

The unit of all time constants is [s].

The model does not consider any kind of external load on the system which has been shown (see sect. 4.2.2) to affect the walking motor in a nonlinear manner and is particularly important for a force control scenario. Also, the model is set up with an implicit linearity assumption which proves true for low drive frequencies but has been shown (see sect. 4.2.1) to deteriorate for higher frequencies. The model by Merry [145] as well as the motor model of this chapter could be improved by using nonlinear identification techniques [187] and/or by extending them with a suitable disturbance model part.

As a final comment, it should be stressed that the experimental approach based on system identification has several inherent limitations. First of all, it has limited validity since the identification experiment needs to be carried out for a certain working point, input type, etc. Second, it gives little physical insight since it is meant primarily as means of description of system's overall behavior [192]. Other limitations relate to noisy measurements, lack of certain measurements or the actual time variance of model parameters. However, the experimental strategy is easy to employ and results in models which can be directly employed for control-theoretical purposes. When motor-design improvements, alternative drive strategies or the coverage of a broad range of drive conditions are important, then a physical model as the one from previous chapter should be used. This contrast between the two types of models will further bear significance in the later chapters of this work. The physical model will be used in the next chapter (chapt. 5) in order to theoretically investigate a bioinspired drive strategy in which all legs are driven independently (and not in pairs). The control theoretical model from this chapter will find its practical application in chapt. 7 and 8 where, respectively, a load force compensation strategy and a bioinspired application in an antagonistic robot joint will be shown.

CONTROL PART
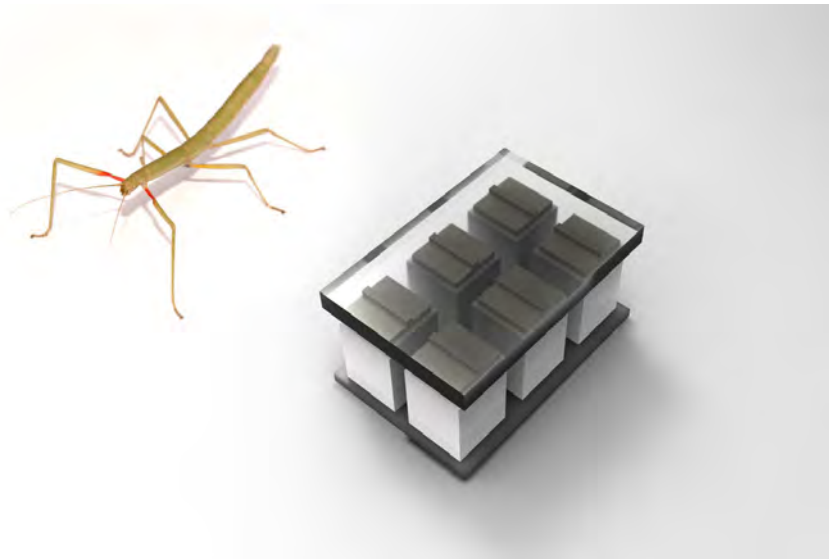
5 | BIOINSPIRED GENERATION OF OPTIMAL DRIVING WAVEFORMS

ABSTRACT

Walking is the most common way of locomotion in land living animals and poses a problem whose solution has been fine-tuned by nature during millions of years of evolution. Multi-legged animals like insects gracefully coordinate their legs on different substrates and maintain stability even under strong disturbances. Their superb walking performance is a natural inspiration for a novel drive strategy in the walking motor. This chapter discusses different possibilities of an architectural mapping between a bioinspired model of hexapod walking and the piezomotor. Specifically, a novel drive strategy is proposed in which all piezoelectric legs are allowed to be driven independently and not in pairs as in the classical drive strategy. Based on the physical model of motor dynamics, it is shown that the bioinspired strategy significantly improves the performance of the motor in terms of its force generating capabilities as well as maximal drive velocity. Furthermore, the novel approach is described by a moderate number of intuitive parameters and produces a variety of velocity-dependent gaits as known from the research on animals.

5.1 INTRODUCTION

The previous two chapters were concerned with the derivation of motor models which can faithfully describe motor behavior in response to given drive signals and an external load when a standard drive approach as intended by the manufacturer of the walking motor is employed. This chapter marks a new part of this thesis which is concerned with both theoretical and practical issues with regard to the drive strategy and control of the motor. The discussion in the following chapters is organized as follows. The current chapter investigates theoretically an alternative drive strategy based on biological findings on insect walking and the dynamical model from chapt. 3. In particular, it shows that the performance of the motor can be significantly improved if every leg is allowed to be driven independently as opposed to the pairwise strategy (cf. sect. 2.4.1). In the next chapter (chapt. 6), the practical issue of the actual generation of drive signals at different frequencies is addressed. The last chapter of the control part (chapt. 7) focuses on the design of a load compensation strategy and a force controller based on the gray-box model from chapt. 4.

The choice of driving waveforms has a significant influence on the performance of the walking motor (cf. sect. 3.2.2). Simu et al. [186] proposed two rudimentary drive strategies similar to the stick-slip and impact drive mechanism (called inertial stepping in their work) from sect. 2.3.3 which result in a relatively high motor speed on the cost of high velocity fluctuations and a presumably poor load capacity. As an alternative, in the same work, they proposed a trapezoidal and the well-known sinusoidal waveforms which are practically used in the commercial product. Building on their results, Merry et al. [145] parametrized the sinusoidal waveform and derived an asymmetrical waveform which improves motor velocity constancy on the cost of lower drive velocity. In a later work, Merry et al. followed this strategy and proposed an optimization strategy based on 4th order Fourier series description of the waveforms [146]. Each of the 4 waveforms was described by 8 different parameters, resulting in altogether 32 parameters. As a result, motor velocity constancy could be improved on the cost of further motor velocity decrease. However, their strategy is based on an extensive optimization process with a dedicated solver. The high-dimensional solution is highly susceptible to manufacturing differences in individual motors, thus questioning the actual performance improvement in practical applications. So far, the waveform optimization efforts in the literature were concentrated on improving motor performance in load-free nanopositioning tasks and assumed the legs to move pairwise to ensure static stability. This contrasts with the high-load capacity, high-speed objectives of this thesis. But even more importantly, it seems that the engineering efforts fostered with computationally-intensive, high-dimensional optimization processes are not able to deliver significant improvements in motor performance. An analogous observation comes from robotics, where the immense differences in comparing the walk of an animal and a robot are clearly visible. Following this analogy and considering the fact that the drive principle of the motor is based on "walking", it is useful to look for a biologically inspired solution [149].

The abundance of biological literature on walking is not surprising if one considers that one of the defining characteristics of animals is their movement [24]. The scientific analysis of walking began in 1870s (promptly before the discovery of piezoelectricity) as the result of a dispute, lingering from ancient times, about whether or not all four feet of a galloping horse are ever off the ground at the same time [158]. The answer, given in 1872 by the photographer Eadweard Muybridge, triggered a broad interest in walking and, particularly, in how animals are able to generate the rhythmic walking movement. The scientific efforts led to the conclusion that the mechanism by which the nervous system generates the rhythmic movements of the leg during walking is basically the same in animals as diverse as the cat and the cockroach [158]. Experiments have been performed with cat [85],

crayfish [42], locust [171], ants [233], flies [225], cockroach [159, 55] and stick insects [47, 49]. Generally speaking, walking can be seen as a coordinated action of (at least two) legs which has to account for the stability of the whole body while at the same time maximizing propulsion and minimizing strain across the body [61]. While walking, animals have to control the number of degrees of freedom which is usually larger than that necessary to perform the task and be able to adapt to unpredictably changing environment or even a loss of a leg [123]. Considering the difficulty of the task from the engineering point of view, it is stunning with what ease even simple animals like insects can "solve" the problem of walking. In this context, insects are an especially interesting group of interest not only for the biologists due to the simplicity of their nervous system but also for this work because of their multitude of legs which they need to coordinate during walking.

The research on insects carried out at Bielefeld University since 1981 by Holk Cruse and his coworkers has brought about a repertoire of findings and a kinematic model of the walking behavior of a stick insect *Carausius morosus*.[1] A part of this model is used in this chapter (see next section) to realize a novel coordination mechanism between the legs of the walking motor. However, before proceeding to the description of the model, it is worthwhile to focus on the differences and similarities between the leg of an insect and a piezoelectric leg. Fig. 44 illustrates the legs schematically during one walking cycle. Perhaps the most noticeable difference in this depiction is the reversed concept of a "ground". Neglecting the climbing or upside down walking situations, an insect stands on a ground which is under its body and toward which it is pulled by the gravitational force. Furthermore, normally it is the insect that moves on a static (immobile) ground. In case of the motor and neglecting its specific mountings, the drive rod plays the role of a movable ground which is placed on top of the fixed drive unit with legs and which is pushed against them by means of a preload (leaf springs in Fig. 20). The thick black arrows in Fig. 44 indicate the direction of forward motion either of the insect's body or the drive rod of the motor. While the insect moves preferably forward and takes a turn in order to change the direction of motion, the forward and backward motion are fully symmetrical cases in the motor. In the following discussion only forward motion is considered (for a comment on backward motion refer to the discussion in sect. 5.5).

Further differences are exhibited in the legs themselves. An insect leg is functionally a 3 DOF serial manipulator consisting of multiple segments connecting rotary joints. A piezoelectric leg is a 2 DOF

---

[1]This research has its root in much earlier works and dates back to 1921 and the publication on the stick insect *Dyxippus* by Buddenbrock [36] and later works of Wendler [222], Bässler [15] and Cruse [45, 46].
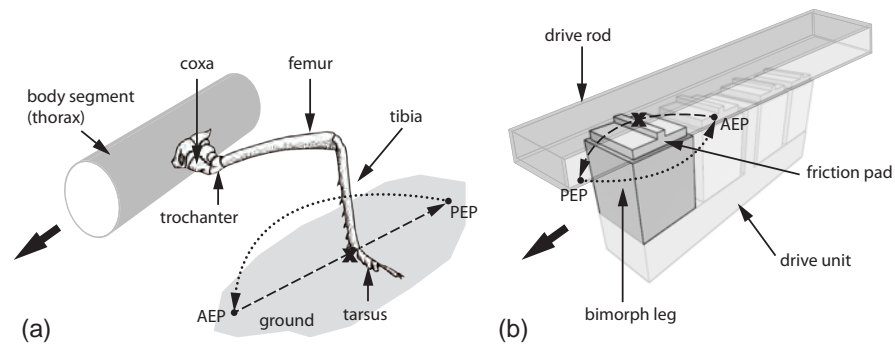
Figure 44: Schematic depiction of an insect leg and a piezoelectric leg performing one walking cycle. (a) the insect leg consists of several segments connected with joints resulting in three functional DOF. (b) the piezoelectric leg is a multilayer bimorph bender which can perform an in-plane movement. Each walking cycle consists of two main stages, the stance stage (dashed line) in which the leg contacts the ground (or the drive rod) and the swing stage (dotted line) in which the leg is freely repositioned. The trajectories in (b) are highly exaggerated. The contact spots tarsus/ground and friciton pad/drive rod are marked with an x-symbol. The resulting directions of motion are indicated with a thick arrow for both insect's body and the drive rod of the motor.

piezoelectric bender. For an in-plane motion, the former is redundant while the latter is not. The walking cycle of an insect leg consists functionally of two stages – the power stroke (also called the stance or support phase) and the return stroke (also swing or recovery phase). During the power stroke, the leg contacts the ground where it can support and propel the body. During the return stroke, the leg is lifted off the ground and swung freely to the starting position for the next power stroke [47]. This starting position is called the *anterior extreme position* (AEP) (also touch-down position).[2] While performing the power stroke, which is a retraction/backward movement in forward motion, the leg moves toward and ends at the *posterior extreme position* (PEP) (also lift-up position) from which the next return stroke is started. Adapting the biological terms, the power stroke can be defined as the in-contact motion from AEP to PEP and the return stroke as the contactless motion from PEP to AEP. These are indicated in Fig. 44 with dashed and dotted lines, respectively. Note that due to the difference in the static vs. movable "ground" concept, the directions of power and return strokes are swapped for the insect and piezoelectric legs given the indicated direction of motion. The current leg position in the walking cycle is marked with an x-marker by which the position of a leg tip (tarsus base or friction pad center) is meant. Thus both legs in the schematic depiction are in the middle of their power strokes.

---

[2]*Anterior* (Latin *ante*; before) is an anatomical term of location and refers to the front (head) end of an animal if it has a distinct head. The opposite (rear) end is called the *posterior* (Latin *post*; after) end.

Also note the difference in the shape of the power stroke trajectory. While it resembles a straight line compared to the arched return stroke in case of the insect, it has an arched shape in case of both the power and return strokes in the motor. These shapes are due to the differences in the relative compliance of the legs and the "grounds" which they touch. An insect leg is relatively compliant compared to the stiff ground it walks on while a piezoelectric leg is relatively stiff compared to the stiffness of the preload (cf. sect. 3.4.1). The last difference to be mentioned here concerns the movement velocity of the legs. The velocity of a piezoelectric leg can vary from a theoretically infinitely small (cf. next chapter on drive electronics) to as large as several thousands of cycles (steps) per second. This is in a strong contrast to the relatively narrow velocity bandwidth of insect leg movement [81, 123, 86].[3] Fortunately, none of the above differences seems to be a fundamental issue in terms of an adaptation of the bioinspired strategy in the motor.

Having the one-leg considerations in mind, the following discussion turns to the problem of coordination of multiple legs. The subsequent sections are organized as follows. The next section introduces the kinematic model of leg coordination in hexapod walking and argues how this bioinspired model can be transformed to suit the architecture of the walking motor. Next, sect. 5.3 describes the implementation of the bioinspired trajectory generator together with leg coordination rules which can be optimized to improve specific aspects of motor performance. In sect. 5.4, an actual optimization in terms of maximal stall force and maximal motor velocity is performed with the physical motor model from chapt. 3. The results show a significant improvement in motor performance as compared to the classical drive strategy utilizing the *force* or *sine* waveforms. Finally, a critical discussion of the proposed drive strategy is presented in sect. 5.5.

5.2 LEG COORDINATION RULES

The difficulty of walking can easily be underestimated upon superficial consideration. It seems to be a fairly automatic behavior which does not require much effort to be solved. This is obviously not true considering the huge gap in walking performance between animals and machines after 50 years of robotic research efforts. For a descriptive overview, the interested reader is referred to [149]. In insects, three pairs of legs consisting of up to 18 joints need to be controlled simultaneously. Moreover, the number of legs which are mechanically coupled via body and ground varies from one moment to the next

---

[3] A stick insect at its maximal movement velocity reaches about 2.5 steps a second. However, for other insects, e.g. cockroaches, this maximal velocity can be much higher.
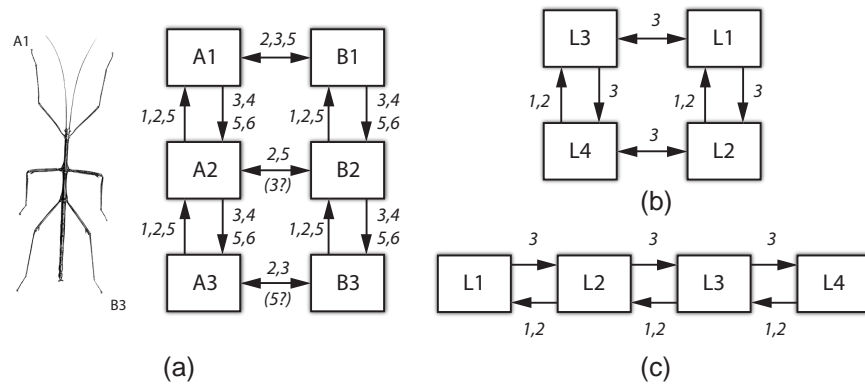
Figure 45: Block diagrams showing leg coordination rules which couple the step cycles during walking. The labeled boxes correspond to particular legs and the arrows indicate the directions of leg-state information flow between the legs. Numbers next to the arrows denote the coordination rules (summarized in Table 10). (a) known coordination rules for the six legs of a stick insect as in [61]. Labels A1 to A3 stand for left front, middle and hind leg, respectively, and B1 to B3 for corresponding right legs. By considering only four legs with a reduced set of coordination rules (1-3), simplified block diagrams are obtained. (b) and (c) show two alternatives for the walking motor. The labels L1 to L4 stand for the ordered sequence of the first up to the fourth leg of the drive unit. In the actual motor, L1 with L3 and L2 with L4 are hardwired to move in unison.

and the external conditions such as friction, compliance and slope of the substrate are unpredictable [61]. This section attempts to briefly sketch some biological findings on insect walking and introduces a kinematic model of hexapod walking developed as a result of these findings.

Behavioral experiments on stick insects have shown that the mechanisms which produce a proper coordination of the walking legs (even when walking is disturbed) can be described by a set of rules [47, 48]. Each of the rules is active only during certain fractions of the step cycle [47, 61] and relies on a specific state information only from the one leg it applies to and its direct neighbor legs. In other words, no explicit central knowledge of the state of all legs is required to account for the observed phenomena in insect walking.[4] The identified leg coordination mechanisms (rules) are summarized in Fig. 45(a) and Table 10. In Fig. 45, particular legs are depicted as rectangular blocks. The arrows between these boxes indicate the direction of state information flow between the legs. The numbers next to the arrows correspond to the particular rules, as described below and summa-

---

[4]This is an example of a distributed (or decentralized) vs. central control approach. For an extensive discussion on this topic, the interested reader is referred to the classic work by Rodney Brooks [34]

rized in Table 10, which mediate between the legs. Numbers with a subsequent question mark have not yet been proven experimentally in a sufficient way. As of the time of writing of this thesis, there are six coordination rules described in literature [61]. These rules describe the influence that an action of one leg imposes on its direct neighbour legs (see Table 10).

Rule 1 exerts an inhibitory influence on anterior legs (i.e. it is *rostrally* directed) during the return stroke. As soon as a leg is lifted off the ground, it suppresses the lift-off of the next anterior leg. In other words, this rule can prolong the power stroke of anterior legs. The net effect is that *Rule 1* supports the maintenance of static stability as it inhibits the neighboring legs to swing and loose ground contact at the same time.

Rule 2 also works on anterior legs but in an excitatory manner and only for some time after the swing-stance transition of the given leg. Upon touch-down of a leg, this rule facilitates the lift-off of the next anterior leg. Thus, this influence can shorten the duration of the power stroke of anterior legs. Because of its effect at the beginning of a power stroke, this rule favors temporal coherence between step cycles.

Rule 3 is directed toward posterior legs (i.e. it is *caudally* directed). This excitatory rule is active during the power stroke and varies in the magnitude of its influence. The closer a leg gets to its normal lift-off position, the stronger it encourages the posterior leg being in stance to lift-off and "catch-up" to maintain the walking rhythm. Thus, also this rule supports temporal coherence between step cycles.

The above rules ascertain the emergence and maintenance of a rhythmic coordinated walking behavior. The other three known rules are more situation specific and less important for walking [47], especially in the context of the walking motor.

Rule 4 is a targeting mechanism as it tries to place the legs in similar location as the anterior legs were already standing. In stick insects, the AEP of the swinging leg depends on the current position of the next anterior leg [61]. This influence occurs also between the front legs and the corresponding antennae [47]. The main function of this

Table 10: Summary of the coordination rules which couple step cycles in a stick insect together with their assumed functions according to [61].

Rule	Action	Goal
1	suppress lift-off	avoid static instability
2	facilitate early protraction	support temporal coherence
3	enforce late protraction	support temporal coherence
4	aim touch-down location	exploit prior foothold
5	distribute propulsive force	share load efficiently
6	enforce correction step	avoid stumbling

mechanism is presumably to help a leg find ground contact – an essential function when climbing on branches [47].

Rule 5 is motivated by the observation that an increase of load in one leg of a stick insect causes other legs to prolong their power strokes. Hence, the additional load becomes more effectively distributed among the legs [179].

Rule 6 is a correction rule which prevents legs from stepping on each other. If a leg steps on the tarsus of its neighbor leg, a correction movement is elicited [180].

Evidently, all the rules rely on some kind of state information (i.e. in-swing, in-stance, distance-to-PEP, etc.). Cruse [47] distinguishes between three parameters influencing the transitions between the states. These are position, load and phase in the step cycle of the other leg, i.e. the leg which is sending this information to the leg under consideration. The first two depend on proprioceptive information describing the state of the leg itself and the third has to be mediated via neuronal pathways from neighbor legs. Fig. 45(a) shows that these local influences between the legs are either *ipsilateral* (between legs on the same side of the body) or *contralateral* (i.e. between legs on the opposite sides of the body). Turning back to the technical application in the walking motor, several issues have to be addressed. The first one is the different arrangement of legs of which there are four instead of six and which are all arranged ipsilaterally. Fig. 45(b) and (c) show two proposals of architectural mappings between the original hexapod model and the bioinspired motor driver. Clearly, both alternatives have to consist of four legs but they differ in the way the legs are interconnected. First of all, only the first three rules are considered here. Rules 4-6 (perhaps with the exception of *Rule 5*; see discussion in sect. 5.5) have little meaning for the walking motor since the trajectories of the legs cannot overlap and no "gaps" in the flat surface of the drive rod or climbing situations are possible. The first three rules are somehow redundant in the sense that they all aim at the (re-)establishment of coordination between the legs. However, as so far there are no sufficient findings known to the author on their absolute importance for walking and since they may have an effect on the time needed for a coordinated walk to emerge, the first three rules have been selected as the minimal functional set for the bioinspired motor driver. In both Fig. 45(b) and (c), the ipsilateral rules 1-3 are retained as in the original model. In (b), the contralateral influence of *Rule 3* is proposed additionally between L1 and L3 and between L2 and L4. This could lead to a better coordination between those legs as in the classical pairwise drive strategy. However, this solution lacks the coordination between L2 and L3. The introduction of this coordination would result in L2 communicating with all other legs which does not suit the original distributed control concept. In the end, the arrangement (c) was chosen due to its simplicity and better correspondence

to the physical arrangement of legs in the walking motor. In this case, only ipsilateral influences are considered and extended with a forth leg. Another difference between the motor and the stick insect lingers in the lack of any sensory feedback about the true states of the legs in the motor. Still, this does not affect the validity of the bioinspired approach. First, in the dynamic simulation all states are perfectly known and second, an optimized solution can be applied to a real motor since it works under well-defined conditions which are covered by the simulation. Finally, a real-world setup with sensory feedback about the legs is conceivable as well.

5.3 TRAJECTORY GENERATION

Despite the differences between the hexapod model from biology and the actualities of walking motor construction, it seems that the bioinspired drive strategy can be applied to the motor. Two practical issues have to be addressed on this way. First, the legs have to follow adjustable trajectories during the swing and stance phase of their walking cycle. Second, there has to be a technical coordination mechanism between the legs based on the selection of coordination rules from the previous section. Each of these general issues will be addressed in this section.

In the original biological work, the kinematic model of hexapod walking is implemented by means of a distributed artificial neural network controller called *Walknet* [49, 123, 61] . Corresponding to its local nature, the controller for each individual leg is subdivided into three independent modules [123]. Two modules, a swing and a stance network, control the movement of the leg during the return and power strokes, respectively. The transition between them is controlled by a third module – a selector network. Altogether, there are six almost identical single leg controllers, which communicate their current states to their immediate neighbors, generate leg movements and receive global commands from a higher control level. *Walknet* is able to reproduce a multitude of behaviors observed in stick insect (different gait patterns, avoidance behavior, etc.), has a simple structure, can generalize over a considerable range of untrained situations and is remarkably tolerant with respect to external disturbances [49]. Despite these advantages, the original implementation bears only little practical significance to this work. In case of the walking motor, the walking scenario is much simpler, the legs have a different morphology, no generalization capability is aimed at and an explicit implementation of the coordination rules from previous section is pursued. For the original implementation in terms of artificial neural networks, discussion on the capabilities of the original model and its possible extensions the reader is referred to [123, 61] and more recently to [181, 176].
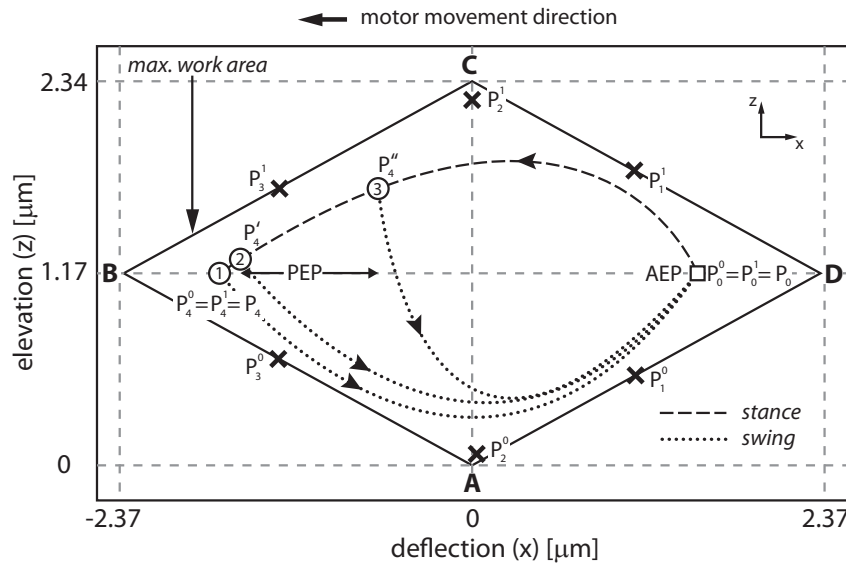
Figure 46: Leg movement trajectories within the rhomboidal work area of the piezoelectric leg. Extreme positions marked with A, C, B and D stand for the (electric-field-free) origin, maximal elongation in z and maximal deflection in x to the left and right, respectively. The stance trajectory is shown with a dashed line, while three alternative swing trajectories, depending on the PEP shift with a dotted line. The terminal points of the trajectory determining Bezier curves are indicated with a square or a circle marker. The x-symbols represent exemplary locations of the control points of a quartic Bezier curve.

Turning to the practical implementation in the motor and as far as the generation of leg trajectories is concerned, it is useful to recall sect. 3.2.2. The legs of the walking motor can follow two-dimensional trajectories defined by the time course of two driving voltages. The region reachable by the tip of a leg (its maximal work area) is defined mainly by the piezoelectric properties of the leg and the maximal driving voltage U_{max}. Assuming U_{max} of 48 V and recalling equation (47), the maximal work area has a rhomboidal shape as shown in Fig. 46. A valid leg trajectory either during the power or the return stroke has to remain within this work area since any point outside the convex hull of A, B, C and D means at least one of the driving voltages above U_{max}. Further requirements on leg trajectory include its smoothness and an easy as well as an intuitive way of shape modification. Additionally, the swing and stance trajectories need to be joined at the transition points between the power and return strokes. It is also desirable that the area determined by the joined curves covers as much of the work area as possible. The last requirement is motivated by the fact that a wide curve in x-dimension means a long step and the possibility of higher motor velocities whereas a large distance between the swing and stance curves in z-dimension allows

116

higher preloads (cf. sect. 3.4.1). Several choices of polynomial curves were considered including splines, B-splines, Bézier-splines, Bézier and NURBS [141, 173]. In the end, the Bézier curve was chosen since it fulfills the above requirements while being the least computationally intensive one. Fig. 46 shows an exemplary stance trajectory (dashed curve) together with several possible swing trajectories (dotted curves) using quartic Bézier curves. The curves are determined by the location of the control parameters P_i with $i \in \{0, \ldots, 4\}$. A superscript of 0 or 1 is used to differentiate between the control points for swing (no contact) or stance (contact) trajectories, respectively. Since a Bézier curve is contained within the convex hull of its control polygon (the polygon formed by connecting the control points with lines in an ordered manner beginning at P_0) the curve remains within the work area of a leg as long as the control points remain in it. Further, by setting $P_0^0 = P_0^1 = P_0$ for AEP and $P_4^0 = P_4^1 = P_4$ for the maximal PEP, the stance and swing trajectories remain always joined (endpoint interpolation). The control points are placed close to the edges of the work area rhombus whose longest diagonal is used as the transition line between power and return strokes. This is motivated by the desire to maximize the step length (faster motor) and the distance between the swing and stance curves (higher preload possible, cf. sect. 3.4.1). Mathematically, a Bézier curve $B(t)$ is expressed by

$$B(t) = (B_x(t) \quad B_z(t))^T = \sum_{i=0}^{n} \binom{n}{i} (1-t)^{n-i} t^i P_i \qquad (121)$$

with $n = 4$ for a quartic curve and t being the Bézier parameter defined over the interval $[0, 1]$. The control points P_i have two-dimensional (x, z)-coordinates which are either fixed or variable depending on the role of a specific control point (see below and the next section on parameter optimization). The (longest) stance trajectory is defined by the control points

$$P_0, P_1^1, P_2^1, P_3^1 \quad \text{and} \quad P_4 \qquad (122)$$

while the swing trajectory by

$$P_4^-, P_3^0, P_2^0, P_1^0 \quad \text{and} \quad P_0. \qquad (123)$$

Note the dash in P_4^- which indicates the variability of P_4 as the actual lift-off point at the beginning of a return stroke – the actual stance trajectory ends at P_4^-. This accounts for the variability in the length of the power stroke as described in the previous section on leg coordination rules. Technically, this variability is realized by a shift in the location of PEP which can lead to a premature stance-swing transition (see below). In Fig. 46, three different swing trajectories are sketched depending on the actual lift-off point (latest for P_4 and premature for P_4' or P_4'').

For the further discussion, it is useful to introduce the indexing operator $\Im$ [198] which returns its particular coordinate if applied to a point. Hence, for $P = (x, z)$

$$\begin{align} \Im_x P &= x \tag{124a}\\ \Im_z P &= z. \tag{124b} \end{align}$$

This means that e.g. $\Im_x A = \Im_x C = 0\,\mu m$ and $\Im_z B = \Im_z D = 1.17\,\mu m$ when referring to Fig. 46. The control parameters for leg trajectories are summarized in Table 11 using the above notation. The table contains either fixed parameters or parameters meant for optimization (see next section). The z coordinate of AEP and PEP is fixed on the longest diagonal of the work area. Also fixed is the x coordinate of the middle control point P_2^1 of the stance trajectory. The last four parameters influence the PEP shift and are described in more detail at the end of this section. Other parameters need to be computed in dependency of the parameters in the table or the actual lift-off point P_4^-. The following equations are used for the computation of remaining control parameters for the stance

$$\begin{align} \Im_x P_1^1 &= k_1 \Im_x P_0 \tag{125a}\\ \Im_z P_1^1 &= -m \Im_x P_1^1 + \Im_z C \tag{125b}\\ \Im_x P_3^1 &= k_3 \Im_x P_4 \tag{125c}\\ \Im_z P_3^1 &= m \Im_x P_3^1 + \Im_z C \tag{125d} \end{align}$$

Table 11: Control parameters for leg trajectories. Shading indicates parameters meant for optimization within the allowed range of values. For other control parameters, see equations (125)-(126). s.f. abbreviates "scaling factor".

Name	Description	Min	Max
$\Im_x P_0$	x coordinate of AEP	1.50e-6	2.34e-6
$\Im_z P_0$	z coordinate of AEP	1.17e-6	1.17e-6
$\Im_x P_4$	x coordinate of maximal PEP	-2.34e-6	0
$\Im_z P_4$	z coordinate of maximal PEP	1.17e-6	1.17e-6
$\Im_x P_2^1$	x coordinate of P_2 in stance	0	0
$\Im_z P_2^1$	z coordinate of P_2 in stance	1.17e-6	2.34e-6
k_1	s.f. for computation of $\Im_x P_1$	0	1
k_3	s.f. for computation of $\Im_x P_3$	0	1
r_1	PEP shift according to rule 1	0	-0.3
r_2	PEP shift according to rule 2	0	0.3
r_2^*	Action time of rule 2	0	0.4
r_3	PEP shift according to rule 3	0	0.3

and for the swing trajectory

$$\Im_x P_1^0 = \Im_x P_1^1 \tag{126a}$$
$$\Im_z P_1^0 = m\Im_x P_1^0 \tag{126b}$$
$$\Im_x P_2^0 = 0.5(\Im_x P_0 + \Im_x P_4^-) \tag{126c}$$
$$\Im_z P_2^0 = m|\Im_x P_2^0| \tag{126d}$$
$$\Im_x P_3^0 = k_3 \Im_x P_4^- \tag{126e}$$
$$\Im_z P_3^0 = m|\Im_x P_3^0|. \tag{126f}$$

The above equations ascertain the location of the control points on the circumference of the work area rhombus of Fig. 46 and define several simple relations for the computation of the intermediate control points. The scaling factor $m = 0.5$ is the absolute value of the slope of a straight line collinear with any side of the work area rhombus from Fig. 46.

Two parts are still missing in the above considerations for the generation of actual trajectories. First, the computation of the Bézier parameter t in (121) and second, the realization of swing-stance transitions. Fig. 47 addresses these issues with help of two circuits for the stance and swing Bézier parameter generating units. Since the trajectories need to be generated for each leg individually, all leg-specific variables are provided with a subscript (i) according to the notation from chapt. 3. Both units compute the Bézier parameters by summing up discrete increments Δt. These increments are computed as time differences $\Delta\tau$ scaled with a velocity factor v_x which corresponds to the horizontal curve traverse velocity in Hz. The velocity may vary from 0 to 3 kHz.[5] Maximal velocity $v_x^{\max}$ is assumed to be constant for the return stroke since fast leg repositioning is desirable. Furthermore, this decision is motivated by biological findings [87]. The output of both stance and swing units is affected by logical control variables $S_{(i)}^0$, $S_{(i)}^1$ and $R_{(i)}$ which are defined further below in this section.[6] The output of the swing unit $t_{(i)}^0$ varies from 1 at a lift-off down to 0 at a touch-down event. As soon as AEP is reached, the logical input $R_{(i)}$ is asserted and used to reset the output $t_{(i)}^1$ of the stance unit to 0. During the stance movement $t_{(i)}^1$ increases up to 1 for the maximal PEP as long as a premature swing transition is not elicited. Two additional scaling terms are used either to account for the prolonged stance movement according to the optimization result of *Rule 1* (influence of posterior legs, see below) or for the accelerated return stroke after a shortened

---

[5] The additional scaling factor of 2 reflects the fact that the walking motor may be driven up to 3 kHz (rated operation) but v_x corresponds to the traverse velocity of just a half of one walking cycle. In other words, v_x has to be doubled in order to correspond to the drive frequency in the classical (pairwise) mode of operation. The scaling factor hides this from the end-user.

[6] The default configuration of the switches, in all figures, corresponds to the condition of a logically true input.

(a)

(b)
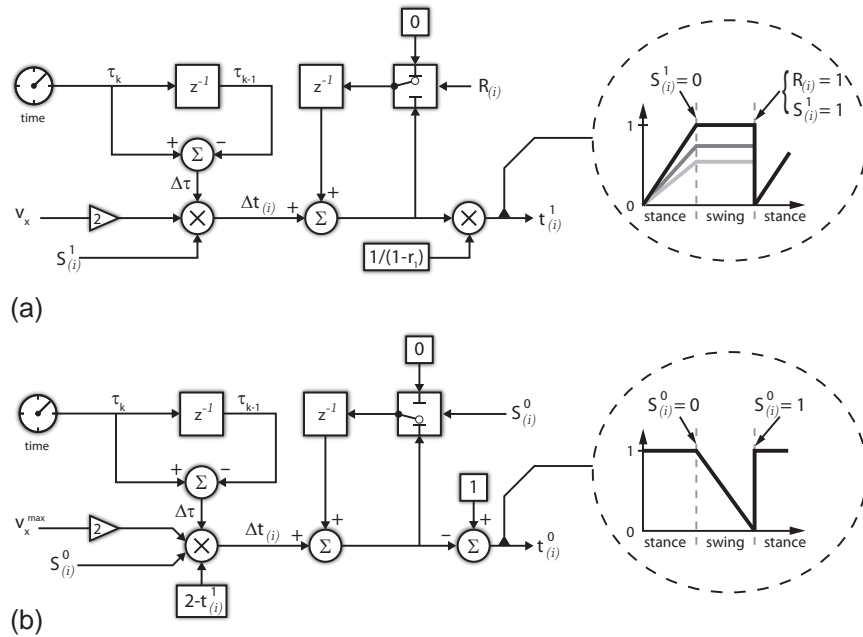
Figure 47: Block diagrams illustrating the computation of Bézier parameters for the (a) stance and (b) swing parameter generating units. Both units consist of a time derivative and position integrating circuits. The actual temporal output depends on the velocity input v_x and three logical signals $S^0_{(i)}$, $S^1_{(i)}$ and $R_{(i)}$. Exemplary outputs are shown in the encircled diagrams. In (a) the output is additionally scaled in dependence of the r_1 parameter value (prolonged stance phase) while in (b) the swing movement of a leg is accelerated after a shortened stance stage. Note that the output of the stance unit is less than 1 for a premature lift-off, while the output of the swing unit always changes from 1 down to 0.
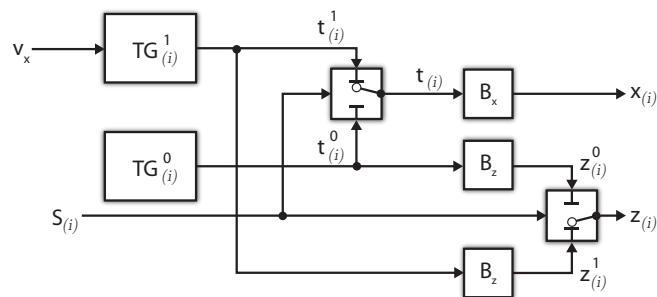
Figure 48: Trajectory generator module consisting of two Bézier parameter generating circuits as in Fig. 47 (TG1$_{(i)}$ – stance, TG0$_{(i)}$ – swing) and Bézier coordinate computing blocks B$_x$ and B$_z$. The signal flow is determined by two switches and a logical signal $S_{(i)}$.

stance phase.[7] Taken together, the swing and stance circuits constitute a trajectory generator (TG) for each leg – see Fig. 48. The trajectory

---

[7]This facilitates the detachment of a leg from the drive rod when in swing.

generator acts as a simple switch between the outputs of the swing and stance circuits which are subsequently fed into Bézier coordinate computing blocks according to (121).

So far in this section, the generation of leg trajectories has been considered in a bottom-up manner for a single-legged case. It has been mentioned that the actual trajectory depends on the state of the leg mediated by logical control flow variables and leg coordination rules. Now it is time to cover these additional aspects of multi-legged trajectory generation. Each leg can be in one of two major states: (0) in-swing or (1) in-stance. Additionally, a leg can be at a transition point between these states corresponding to its location either at AEP or PEP. Technically, the determination of the state for a leg (i) occurs according to

$$
\begin{aligned}
(1) \quad & t_{(i)}^1(k) > t_{(i)}^1(k-1) \\
(0) \quad & t_{(i)}^0(k) < t_{(i)}^0(k-1),
\end{aligned}
\tag{127}
$$

where k represents the discrete time parameter ($t_{(i)}(k)$ is the output of one of the Bézier parameter generating circuits at discrete time step k). In other words, a leg is in stance as long as $t_{(i)}^1$ is increasing or it is in swing as long as $t_{(i)}^0$ is decreasing (cf. Fig. 47). Two auxiliary variables are used additionally in order to cover the transition cases. These are

$$
A_{(i)} := \left[t_{(i)} \leq 0 \right]
\tag{128a}
$$

$$
P_{(i)} := \left[\underbrace{(1 + r_1 - \Delta P - t_{(i)})}_{D_{(i)}^{\text{PEP}}} \leq 0 \right]
\tag{128b}
$$

corresponding to AEP-reached and PEP-reached conditions, respectively. The right-hand side of the latter definition corresponds to the remaining distance to PEP $-D_{(i)}^{\text{PEP}}-$ during stance phase and will become clear only after completing this section with the technical implementation of leg coordination rules. This leads to the definition of the control flow variable $S_{(i)}^0$ as

$$
S_{(i)}^0 := (t_{(i)}^0(k) < t_{(i)}^0(k-1)) \wedge \overline{A_{(i)}}
\tag{129}
$$

and $S_{(i)}^1$ as

$$
S_{(i)}^1 := (t_{(i)}^1(k) > t_{(i)}^1(k-1)) \wedge \overline{P_{(i)}}
\tag{130}
$$

The reset signal $R_{(i)}$ for the stance circuit upon reaching AEP is equivalent to $A_{(i)}$

$$
R_{(i)} := A_{(i)}.
\tag{131}
$$

The above computations (129)-(131) need to be performed for each leg and can be seen as a leg-state unit or module (LS).

The coordination rules between the legs are realized technically by means of a PEP shift ΔP which can prolong or shorten the stance phase according to the textual description from the previous section. This is summarized in Table 12. *Rule 1* and *2* are both rostrally directed

assuming the leg numbered with a 1 to be at the front of the motor. *Rule 1* is an inhibitory rule (r_1 parameter values in Table 11 are less or equal 0) and is active as long as the return stroke takes place.[8] *Rule 2* has an excitatory effect on PEP shift and it is active only for some time after the swing-stance transition. This is realized with help of an additional parameter r_2^*. The last implemented rule – *Rule 3* – is also excitatory but caudally directed and active during the power stroke. Additionally, in contrast to the other rules, it does not cause a fixed PEP shift but it depends on the actual distance to PEP, thus its influence varies with time.

In the bioinspired waveform generator, each leg implements (a subset) of the above rules in a Walknet rules module (WR). Taking a top-level view, the complete waveform generator consists of three modules for each leg. These are the trajectory generating (TG), leg state (LS) and Walknet rules (WR) modules. Fig. 49 illustrates the bioinspired architecture with help of a block diagram. Note the distributed nature of the bioinspired approach since the information exchange takes place only between directly neighboring legs (horizontal signal flow in the shaded region of Fig. 49). Trajectories for each leg are generated as a set of (x, z)-coordinates in response to a velocity input v_x in Hz. Before being forwarded to the motor (see chapt. 3) they need to be transformed into driving voltages by the driver D according to

$$U_{(i)}^A = \frac{1}{2} \left[\frac{x_{(i)}}{C_x} + \frac{z_{(i)}}{C_z} \right] \tag{132a}$$

$$U_{(i)}^B = \frac{1}{2} \left[\frac{z_{(i)}}{C_z} - \frac{x_{(i)}}{C_x} \right] \tag{132b}$$

which is the reformulation of (47) in terms of x and z as independent variables.

---

[8] In [47] the rule is actually defined as being active during the return stroke and some time afterward but this has been neglected here.

Table 12: Subset of leg coordination rules as implemented in the simulation of the walking motor.

Rule	Direction [from → to]	PEP shift (ΔP)	Condition
1	$\text{leg}_{i+1} \to \text{leg}_i$	r_1	if $t_{(i)}^0(k) < t_{(i)}^0(k-1)$
		0	otherwise
2	$\text{leg}_{i+1} \to \text{leg}_i$	r_2	if $t_{(i+1)}^1 \le r_2^*$
		0	otherwise
3	$\text{leg}_i \to \text{leg}_{i+1}$	$r_3(1 - D_{(i)}^{\text{PEP}})$	-
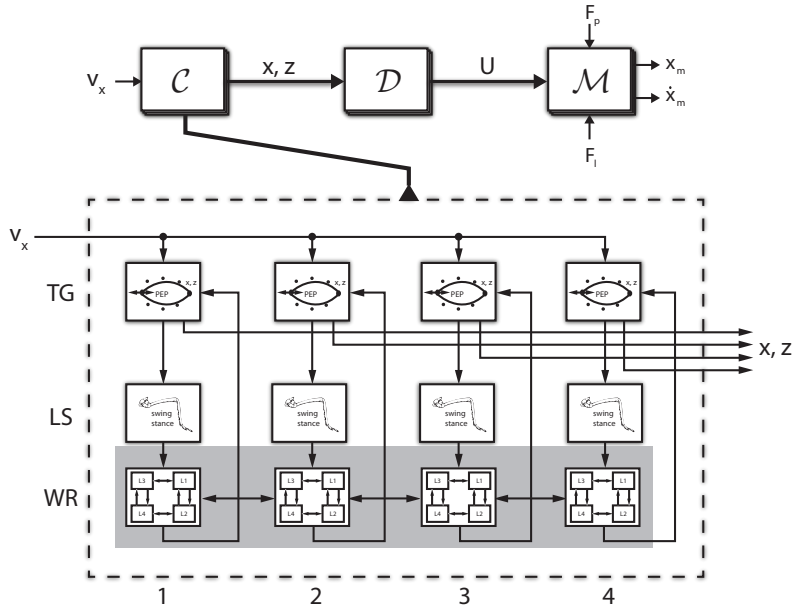
Figure 49: Top-level block diagram of the bioinspired waveform generator. The controller C generates a set of (x, z)-coordinates (trajectories) depending on the drive velocity v_x and leg coordination rules. The trajectories are mapped to a set of drive voltages U by the driver D and fed into the motor M. For the choice of architecture from Fig. 45(c) the controller consists of four trajectory generators (TG), leg state (LS) and Walknet rules (WR) modules. Note that the coordination rules affect only the directly neighboring legs.

5.4 PARAMETER OPTIMIZATION

Having established the bioinspired waveform generator in the previous section, the next logical step is to test its performance. In an ideal case, the bioinspired strategy should be able to generate a continuous variety of rhythmic gaits as known from biology [82] and excel the classical motor driving approaches (see chapt. 3 and sect. 5.1) in terms of a given performance criterion like maximum motor velocity or stall force. For this purpose, the unknown parameters (shaded in Table 11) need to undergo an optimization process.

Independently of the particular performance criterion, an optimization process has to account for stability during motor operation, i.e. during walking. In walking animals, a statically stable walk is characterized by their center of gravity being inside the polygonal base defined by the legs having ground contact and supporting the body. Dynamically stable gaits like running or trotting [24] are not considered here. In the walking motor, the issue of static stability reduces basically to the provision of drive rod contact by at least two legs.[9] A number of leg contacts less than two is used as a criterion for exclusion by heavily

---

[9]A free movement of the drive rod is constrained to one dimension (x) through motor construction. Assuming a sufficiently long drive rod, approximately uniform

penalizing the objective function during optimization (see below). Furthermore, since the focus of this work is put on the application of the walking motor as a force generator (see especially chapt. 7-8), the natural objective of the optimization is to maximize its force-generating capabilities. According to Table 11, there are altogether 9 unknown parameters to be optimized. Despite this moderate dimensionality, the optimization landscape is abundant in terms of local minima and thus an evolutionary algorithm [166] was chosen as in chapt. 3. Also the optimization procedure was set up in a similar way to the one in sect. 3.5 (see Fig. 35(b)). For this purpose, the already optimized motor model from sect. 3.5 was used. This time the bioinspired waveform generator according to the implementation from the previous section was utilized and each leg was driven independently.[10] As a drive frequency, a constant value of v_x^{max} was chosen since the maximal drive velocity is most critical in terms of stability when the swing velocity is set to maximum as well.[11] In order to provide means of force-generation maximization, the motor was loaded increasingly in a stepwise manner. 12 linearly spaced loads $F_{l,i}$ between 0 and 20 N were applied to the drive rod and the corresponding motor velocities $\dot{x}_{m,i}$ for $i \in \{1, \ldots, 12\}$ logged. The optimization problem was formulated in terms of the average motor velocity as follows

$$\arg \min_{\delta} O(\delta) = \arg \min_{\delta} \quad \mathsf{w}_1 \underbrace{\left\lfloor \mathrm{tr}(\boldsymbol{C_N}) < 2 \right\rfloor}_{\text{logical: 0 or 1}} + \frac{1}{\frac{1}{12}\left(\sum_i \dot{x}_{m,i}\right)}, \qquad (133)$$

where δ is the vector of unknown to-be-optimized parameters, $\mathrm{tr}(\boldsymbol{C_N})$ is the trace of the contact matrix defined in (87) and w_1 is a weight term of 10000 for penalizing the contact condition of less than two legs. The initial state of all legs was at AEP (P_0) in order to avoid random penalties for a possibly good parameter choice due to a disadvantageous initial condition[12]. After a fixed number of 100 iterations, the optimization task was stopped. The optimized set of parameters was then used to evaluate the performance of the bioinspired drive strategy. First, the issue of stability was addressed. Fig. 50(a) shows drive rod contacts with particular legs (in stance) over several walking periods for three different drive frequencies. Even for the maximal drive frequency of 3 kHz, at least two legs support the drive rod. In this case, the contact patterns resemble the pairwise drive strategy with alternating contacts between legs 1 & 3 and 2 & 4. For lower drive frequencies, the amount of legs being in stance at the

---

preload distribution and non-resonant operation, the movement of the drive rod in x is stable as long as it is supported at two or more distinct points.

   [10] This can easily be done in the simulation but is not possible in the real motor due to the hardwired pairwise driving strategy; cf. sect. 5.5.

   [11] This follows from the fact that more legs are in stance for low drive velocities resulting in an increased overall stability.

   [12] For a random initial condition, an (otherwise) optimal solution could be rejected if less than two legs contacted the drive rod at the initial stage due to the high penalty.
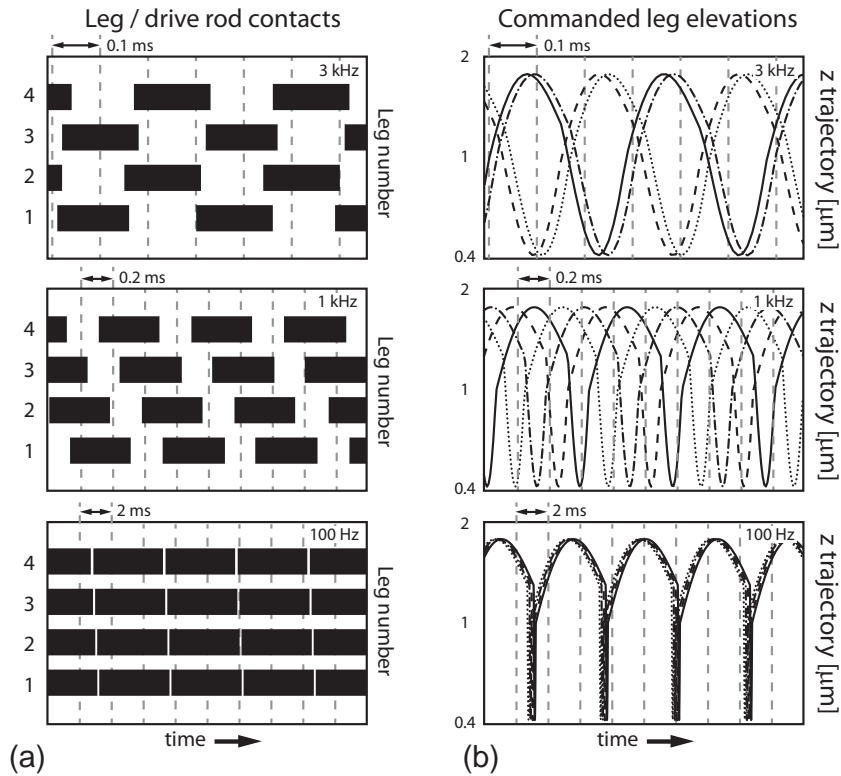
Figure 50: Velocity-dependent generation of gaits. The black bars in (a) indicate contact periods between the legs and the drive rod. Typical insect gait patterns known from the biology [61] albeit with a much higher frequency bandwith can be observed. For low drive velocities, all legs tend to contact the drive rod with only short swing periods repositioning one leg at a time. For higher velocities, the stance and swing phase durations converge until they become approximately equal. At this point, alternating contacts between the drive rod and two leg pairs known from classical control approaches can be recognized. In (b) the corresponding commanded leg elevation trajectories are shown (leg 1 – solid, 2 – dashed, 3 – dash-dotted and 4 – dotted line).

same time increases. At 100 Hz a metachronal or wave gait [82, 149] can be observed in which all legs are in stance most of the time and a series of return strokes propagates occasionally among them. These velocity-dependent patterns are two extremes of a continuum of gaits with a varying duty cycle β [82] as known from the biology. Since drive rod contact depends on leg elevation, z trajectories are shown additionally to the different gait patterns in Fig. 50(b). For the wave gait, the trajectories for different legs fall close together. Also note the different curve traversal velocities during the swing and stance phases.

The results of optimization are promising. Not only in terms of stability but also in terms of force generation. Fig. 51 illustrates these results with help of a load force vs. motor velocity diagram recorded
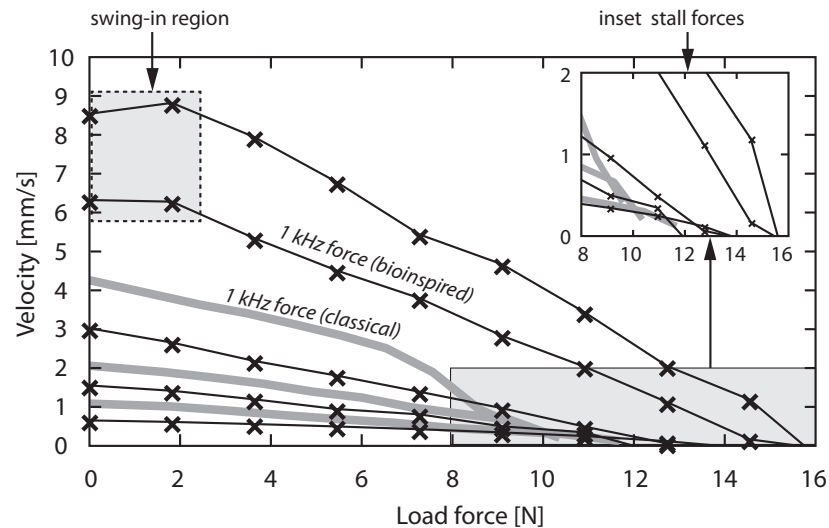
Figure 51: Load force vs. motor velocity characteristics with the bioinspired waveform generation optimized for force compared to the classical drive strategy with the *force* waveform. The x-symbols show simulated velocities at increasing load force levels as long as the commanded direction of motor motion could be maintained. The results are shown for 5 exemplary drive frequencies (100, 250, 500, 1000 and 1500 Hz). Thick gray curves correspond to motor load characteristics measured at 250, 500 and 1000 Hz for the classical force waveform (see also Fig. 35). The bioinspired strategy is superior to the classical one in terms of both the velocity and stall force limits. The dashed region to the left shows high frequency transient phenomena (see Fig. 52). The inset to the right shows the stall force limits with an increased vertical resolution.

with the optimized set of parameters. Gray curves are the real motor characteristics known from Fig. 35(b). x-markers represent the simulation data for velocities above 0 mm/s and are grouped together with interpolating lines according to one of the 5 drive frequencies they were measured at. For the sake of clear depiction, only two load curves at 1 kHz are labeled – the real curve for the classical *force* waveform and the simulated curve for the bioinspired approach. The latter curve is clearly superior to the former one. Both the drive velocity and stall force limit are about 50 % higher in the bioinspired approach as compared to the classical drive strategy. The stall force limits for the bioinspired drive approach are illustrated additionally in Fig. 52(b) for a larger number of drive frequencies. While higher stall force limits could be expected from the increased amount of legs in contact with the drive rod and the optimization objective, the superior velocity performance is an additional and most welcome gain. This gain can only partly be attributed to a longer step size in the bioinspired solution (cf. Fig. 25(a) and 52(a)). For a more detailed discussion on the reliability of simulation results, the reader is referred to the next section. Another interesting phenomenon in the optimization results

126
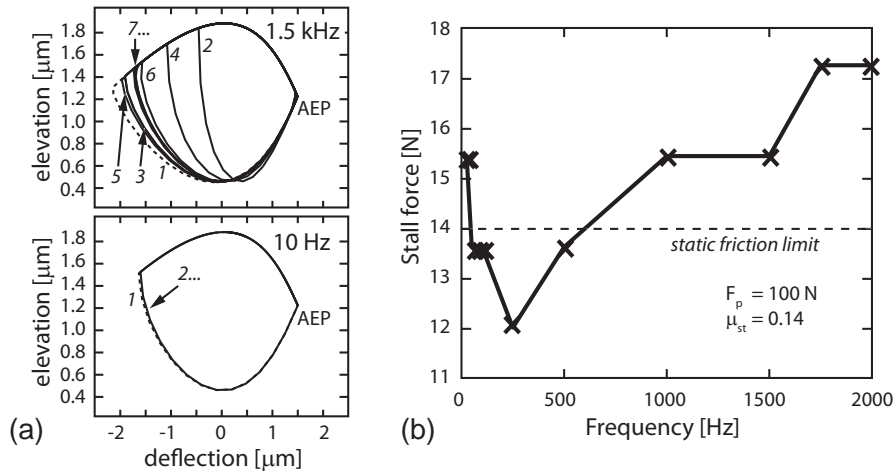
Figure 52: Transient (swing-in) phenomena and stall force limits in the force optimized bioinspired waveform generation. (a) shows the initial leg trajectory (1, dashed line) starting from AEP and the subsequent trajectories (2, 3, 4 etc.) up to the point when a stable movement pattern could be observed (number followed by an ellipsis). For high drive velocities, several movement cycles preceded the stable pattern aka swing-in period. (b) stall force limits shown for 11 exemplary drive frequencies between 10 and 2000 Hz. The static friction borderline, corresponding to the friction coefficient from sect. 3.4.2, is shown with a dashed line.

is highlighted in the dashed region to the left of Fig. 51. For high drive frequencies (in the figure 10 and 1.5 kHz), the no-load velocity is smaller than the velocity at the first load level of approx. 2 N. This phenomenon is termed *swing-in*.[13] It is explained graphically in Fig. 52(a). For low drive frequencies, the paths followed by the legs do not differ significantly between the initial and the ongoing trajectories. However, as the drive frequency increases the emergence of a steady coordination between the legs is delayed. For 1.5 kHz it takes about 7 walking cycles until a steady trajectory can be observed. Thus, in a strict sense, the transient (swing-in) region of Fig. 51 is not a part of the load characteristics of the motor but only a transient phenomenon. However, no further effort was put into correcting the load characteristics due to the illustrative purpose of the swing-in region and because its suppression was not an objective during the optimization. In sect. 5.2 it has been already mentioned that the emergence of a stable walk depends on the per se redundant leg coordination rules but that their relative importance has not been sufficiently quantified yet.

---

[13]In analogy to the German *Einschwing*-Verhalten.

5.5 DISCUSSION

The main purpose of this chapter was to investigate theoretically an alternative drive strategy in which all legs of the walking motor are allowed to be driven independently. It was natural to look for a biologically inspired solution since the task of multi-leg coordination had been efficiently solved by nature a long time ago [24]. The advantage of the bioinspired approach over the classical drive strategy in force generation was conceptually clear (see below) but has only become obvious after an evaluation on a physical motor model.

First of all, the proposed approach is intrinsically adaptive. While the pairwise drive principle enforces symmetric relations between the legs which leads to fixed phase relations in the driving waveforms, the bioinspired solution benefits from the self-defending stability. The coordination rules result in the emergence of a continuum of gaits which are velocity-dependent and allow at times all the legs to support the drive rod leading to a stronger motor. As far as the pairwise strategy is concerned, other authors [146] proposed an optimization approach which may lead to an improved drive performance in terms of velocity constancy or reduced wear but at the same time shows the limits of the classical drive approach. Despite the great flexibility in waveform design, their approach necessarily ends up in a rigid solution with fixed waveforms. Moreover, the obtained set of 32 parameters (cf. 9 parameters in the bioinspired drive strategy) bears little meaning as compared to the clear definition of AEP, PEP and the control points from sect. 5.3. Still, a practical advantage of the solution from [146] lies in the fact that it can be directly applied to the real motor. The bioinspired strategy requires separate signal paths to the piezoelectric stacks of each leg – altogether 8 instead of the 4 hardwired electrical phases. However, this constraint is only superficial and can be easily bypassed in the manufacturing process. The overhead due to additional wiring is well motivated by the possible improvement in motor performance shown in the last section.

It should be stressed that the transfer of coordination rules to the walking motor (see sect. 5.2) and the design of the optimization process (see previous section) were the result of an intuitive choice rather than a series of trials and errors. On one hand, this speaks for the intuitiveness and robustness of the proposed drive strategy. On the other hand, it leaves a lot of space for further research and iterative improvements. The particular choice of coordination rules and architectural mapping from the original hexapod model to the walking motor was in spirit of the N-legged general modeling strategy from chapt. 3. Both the physical model and the bioinspired drive approach based on Walknet are applicable in their present form to motors with an extended number of legs ordered in one row. However, *Walknet* with its many extensions [181, 176] unfolds its true power only when

applied purposefully as a model of walking in insects. Although it is not necessary to deal with leg amputation, ground irregularities or avoid high obstacles [123] in the walking motor, it is conceivable to design a more insect-like motor (e.g. with six legs arranged in two rows). In this case, bioinspiration would go one step further – not only in the means of control but also in the architectural design. Still, even for the motor in its present form it is credible to consider different inter-leg coordination mechanisms (cf. Fig. 45(b). Moreover, if the motor were provided with additional sensing capabilities, other coordination rules were likely to augment its performance. For example, a load sensing capability in the legs (based on direct piezoelectric effect and voltage monitoring) together with the application of *Rule 5* could lead to a higher mechanical load capacity. Last but not least, the bioinspired strategy together with a sensory feedback would likely be tolerant against imperfections and wear in the mechanical components of the motor.

As far as the optimization results are concerned, several issues need to be addressed. First of all, the optimization aimed at improving the force-generating capabilities of the motor. This was done indirectly by trying to keep the instantaneous motor velocity as high as possible for the increasing levels of loading up to 20 N. Other objectives like maximizing average (no-load) motor velocity (see below), reducing wear, etc. are conceivable. The ability to satisfy different optimization objectives is a soft measure of the flexibility of the proposed approach. Besides force optimization, another optimization task was started with the objective to maximize motor velocity. The optimization problem was formulated as

$$\arg \min_{\delta} \quad w_1 \underbrace{\left\lfloor \mathrm{tr}(\boldsymbol{C_N}) < 2 \right\rfloor}_{\text{logical: 0 or 1}} + w_2 \frac{1}{\bar{\dot{x}}_m} + w_3 \mathrm{std}(\dot{x}_m), \qquad (134)$$

where $\bar{\dot{x}}_m$ is the average motor velocity over a certain distance and $\mathrm{std}(\dot{x}_m)$ is the standard deviation of the instantaneous motor velocity – this term is supposed to minimize large deviations from the average value for a smoother operation of the motor. The velocity-related weights w_2 and w_3 were chosen as 10 and 3, respectively, so the objective function preferred solutions of high average velocity and possibly low velocity variation as long as they were statically stable. Fig. 53 shows the results in a diagram and Table 13 summarizes the optimal parameter values for both the max. force and max. velocity optimizations. The diagram refers to Fig. 35(a) and 39(a) and shows the real velocity data for a selection of drive frequencies up to 2 kHz when the classical *sine* and *force* waveforms are employed. The simulation data utilizing the bioinspired approach is shown with black and gray x-markers for the force (see previous section) and velocity maximizing optimizations, respectively. The latter result improves the no-load velocity of the motor as compared to the force maximizing strategy
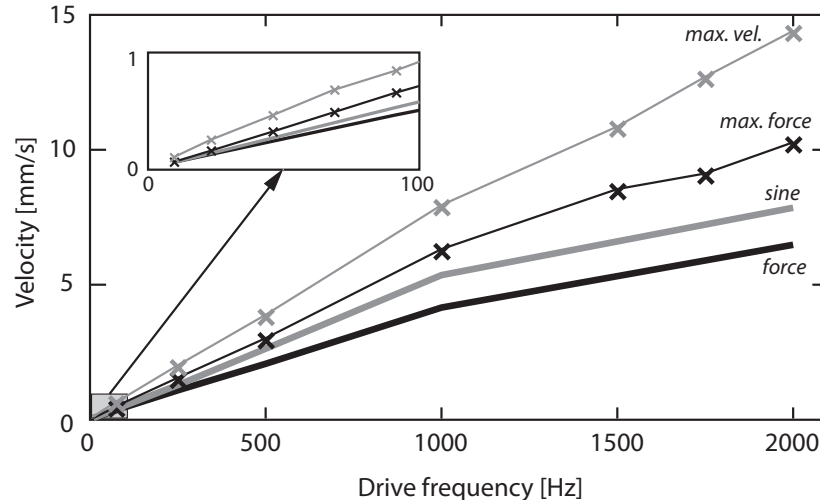
Figure 53: Classical vs. bioinspired waveform generation in terms of average motor velocity when no external loading was applied. The thick lines correspond to unloaded motor velocities measured for two classical waveforms – sine and force (see sect. 35). The x-symbols show simulated motor velocities for the bioinspired waveform generation when optimized for max. velocity and max. (stall) force output. In all cases the bioinspired strategy is superior to the classical one.

almost by 50 % and overpowers the classical strategy by 100 % even if compared to the faster *sine* waveform. Actually, this result is very close to the theoretical limit of 15 mm/s at 2 kHz for the pairwise drive strategy.[14]

The superb force and velocity maximizing results raise a question of the reliability of the theoretical results from the simulation. The question can only be answered upon evaluating the reliability of the

---

[14]The theoretical limit corresponds to the case when the legs contact the drive rod interchangeably over the longest diagonal of the work area and the instantaneous leg velocity is transmitted to the drive rod under the condition of perfect stiction.

Table 13: Optimized parameter values for max. force and max. velocity optimizations.

Parameter	Max. force optimization	Max. velocity optimization
r_1	-0.1987	-0.0337
r_2	0.3000	0.3000
r_2^*	0.2410	0.4000
r_3	0.3710	0.3000
k_1	0.5000	0.5000
k_3	1.0000	1.0000
$\Im_x P_0$	1.5000e-6	1.5000e-6
$\Im_x P_4$	-2.3467e-6	-2.3467e-6
$\Im_z P_2^1$	2.3500e-6	2.3500e-6

physical motor model from chapt. 3 – please refer to the discussion in sect. 3.6. At this point two additional comments are to be made. In the context of motor force maximization, Fig. 52(b) shows stall force limits for the bioinspired strategy over a range of drive frequencies. In sect. 3.5, it has been shown that the physical motor model with the LuGre friction model is able to account for the frequency-dependent stall force limits observed in the motor. In Fig. 52(b) frequency dependency can be seen as well. Here, the stall forces are higher than under the application of the classical *force* waveform which is most welcome but they also show a tendency to increase with drive frequency which contrasts with the result from chapt. 3. Furthermore, these forces are partly higher than the static friction limit for the estimated friction coefficient μ_{st} of 0.14. Although, in dynamic operation, it is possible to achieve stall forces higher than the static limit, this result does not seem to be reliable. Supposedly, it is the effect of model limitations in emulating the dynamic friction with linear terms [see equation (86a)]. The contribution of dynamic friction in the interaction between the legs and the drive rod is not bounded in the linear approximation. Still, this modeling decision did not prevent the physical model from explaining the experimental data and is not supposed to fundamentally challenge the superiority of the bioinspired force generation. In the context of velocity maximization, much higher velocities than with the classical drive approach, close to the theoretical limit for the pairwise strategy, can be observed. However, this would require the legs to travel the entire distance along the horizontal diagonal of the work area rhombus and contrasts with the leg deflection nonlinearity introduced in sect. 3.3.3. Since the physical motor model does contain the nonlinearity, another explanation is needed. Furthermore, in the bioinspired approach no velocity decrease close to the resonance region of 3 kHz (cf. Fig. 39(a)) is observed. This is presumably another advantage of the bioinspired approach since the actual leg trajectories differ among legs and are devoid of pure frequency components to a larger degree than in the classical approach.

As a last comment in this section, the issue of direction change is discussed. So far in the discussion, the motor was assumed to move in one direction – forward – according to the direction of the stance trajectory. As far as *Walknet* is concerned, the issue of backward walking has been addressed recently and a solution proposed [176, 177]. In the walking motor, the direction change is realized classically by issuing the driving waveforms backwards. This method cannot be used in the bioinspired approach since AEP and PEP need to be swapped as well and the coordination rules adjusted (mirrored in the simplest case). However, the direction change in the motor can be realized also by swapping the driving voltages $U_{(i)}^A$ and $U_{(i)}^B$ for each leg (i) without the need of a change in the direction of waveform traversal. The latter solution is actually implemented in the drive

electronics of the motor and described in more detail in the next chapter.

6 FREQUENCY MATCHING IN WAVEFORM GENERATION

ABSTRACT

This chapter is concerned with the issue of generating the driving waveforms at a particular frequency. On this account, the motor-drive electronics developed for this work is introduced with the focus on the waveform generating unit and the dependency between its internal register settings and the frequency output. An algorithm based on the solution to the Bézout's identity is proposed to match the desired frequency. The algorithm is evaluated and the problems related to the limitations of the target hardware indicated. In a next step, an efficient approach based on a look-up table is proposed and shown to reduce the frequency errors to less than 1%. Additionally, this chapter compares the developed electronics with commercial products and introduces a motor direction change strategy based on phase swapping.

6.1 INTRODUCTION

So far, in the discussion of the walking motor, either the standard, i.e. *sine* and *force*, or the bioinspired Bézier-based waveforms (see previous chapter) were considered. In all these considerations, it has been implicitly assumed that the waveforms can be generated at arbitrary feasible frequencies and, to a smaller degree, that the direction of motor motion can be changed at any given time. These implicit assumptions are motivated by the fact that they are related to an external motor driver rather than to the motor itself. Both the generation of waveforms at a given frequency and the change of direction of motor motion are most relevant in any practical application. Any control strategy depends on a reliable motor-drive interface which is responsible for the generation of driving waveforms. From this point of view, it is necessary to explicitly address these issues. This is additionally motivated by the fact that the commercially available motor-drive electronics have many shortcomings including their relatively large size (in comparison to the motor), low maximal drive frequency and the dependency of an external pulse generating control system.

As an example, a commercial drive system for the walking motor may consist of a driver module TMCM-090 [80x50 mm (WxH)] and a base board BB-035 [90x60 mm (WxH, arranged perpendicularly to the driver module)] from the German company Trinamic Motion Control (Trinamic Motion Control GmbH & Co. KG, Hamburg, Germany). Beside its large volume, this system depends on the external pro-

vision of a pulse wave and does not include any control or signal processing logic. The external pulses are limited to the frequency of 384 kHz which means that for a waveform stored with a moderate amount of 256 points the maximal motor-drive frequency equals 1500 Hz – well below the rated limit for the motor. If more complicated waveforms or better time resolution are required, the drive frequency limit will shrink further (e.g. 187.5 Hz for a waveform with 2048 data points). This chapter introduces the motor-drive electronics which was designed and manufactured with the goal to overcome the above limitations. The design objectives were small size, modularity, high waveform resolution and drive frequency as well as the inclusion of the control logic and a rich interface to an external sensory equipment on one board. The latter objective is related to the application of the walking motor as a muscle-like force generator in chapt. 8 in which case motor position, velocity and external load need to be measured.

This chapter is organized as follows. The motor electronics is introduced shortly in the next section. In sect. 6.3, the problem of frequency matching in waveform generation is explained and a solution proposed. The same section also discusses the issues related to motor direction switching. Finally, sect. 6.4 discusses the achieved functionality and gives several proposals of further improvements.

6.2 WAVEFORM GENERATING ELECTRONICS

The motor-drive electronics is shown in the photographs of Fig. 54. It consists of two boards, a *control* and a *power unit*, which are stacked together. The separation into two individual boards facilitates modularization since the *control unit* is independent of the *power unit*. The *power unit* is responsible for converting the digital representation of waveforms into analog signals ranging from 0 up to 50 V. The conversion is done with a D/A-converter (AD7305, Analog Devices Inc.) and the subsequent amplification with analog amplifiers (OPA548F, Texas Instruments Inc.). Other amplification modules like the D-class amplifier are conceivable.[1] The *control unit* is governed by a micro-controller (ATxmega 128A1U, Atmel Corp.) which is responsible for bus communication with other devices if required, runs the control algorithms (see the next two chapters) and is a digital signal processor (DSP). In this context, on the *control unit* board there are additionally two quadrature counters (LS7366RTS, LSI Computer Systems Inc.) providing an interface for linear encoders, two instrumental amplifiers

---

[1]A D-class amplification module has also been designed withing the scope of this work, however it is not further considered here. Its advantage lies in a higher efficiency and a more compact size – 8 instead of 4 amplifiers can be placed on one board. However, because of the necessity of a high frequency PWM modulation of the analog waveforms, the maximal drive frequency drops. The module is also more susceptible to transient voltage peaks during the switching events.
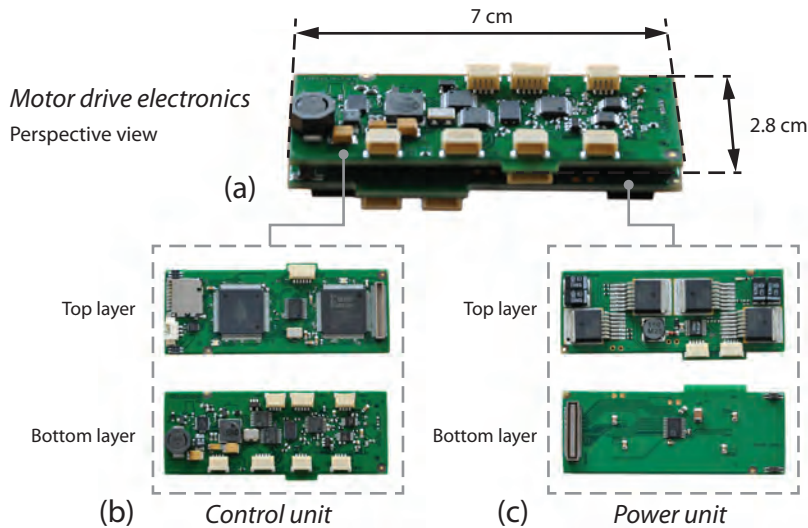
Figure 54: Motor-drive electronics (a) developed within the scope of this work and consisting of two stacked boards – the control unit board (b) and the power unit board (c).

with additional analog low pass filters for the amplification of analog signals and two SPI interfaces for other sensors (cf. chapt. 8). The board is also equipped with an μSD slot as an extensible non-volatile storage. Next to the microcontroller, the other main part of the board is an FPGA (Spartan-3E XC3S500E, Xilinx Inc.) configured as a waveform generator. The online configuration is done from the microcontroller via an SPI interface. The transmitted commands, which can contain several kilobytes of data describing a specific waveform, are protected with a Hamming code. Despite this rich functionality, the overall size of motor electronics when both the *control* and *power units* are stacked equals 70x28x15 mm (WxHxD). The circuit diagrams together with the PCB layout views of all four layers of the *control unit*, *analog power unit* and the *D-class power unit* are attached in appendix C (Fig. 79-90). Further details can be found in [14, 219]. In Fig. 55 the whole architecture is shown schematically with a conceptual sketch of the internal structure of the *waveform generator*. The top-level boxes represent the motor electronics as described above and the sensorized drive (the walking motor together with a sensory equipment) which will be described in more detail in chapt. 8. The intermediate box shows the top-level hierarchy of the *waveform generator* which receives commands from the microcontroller via an SPI interface and manages its current state with a finite state machine. Depending on the state and the values of several internal registers, different actions are performed in the actual generator module which provides a digital representation of the waveforms for further transmission to a DAC via a D/A interface. The generator part contains a clock divider which divides the main system clock of 100 MHz into two clock signals – *counter* and *address*
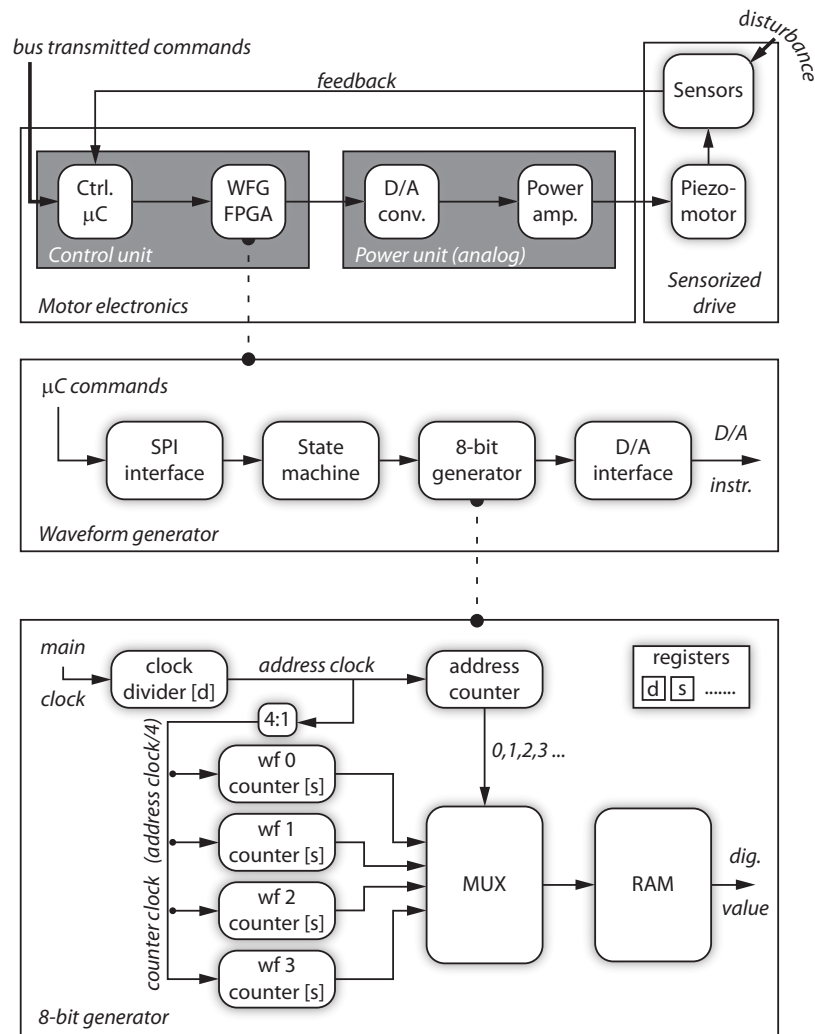
Figure 55: Schematic depiction of the components in the drive electronics of the walking motor. On the top-level the electronics consists of a *control* and a *power unit*. The *power unit* is basically an amplification stage. The *control unit* contains the control logic and an FPGA-based *waveform generator*. The generator issues in an ordered manner the current digital values (8-bit resolution) of all four phases of a given waveform stored in a RAM block. This functionality is realized with help of synchronous counters. The drive frequency is affected by a clock division factor *d* and a counter increment *s*. Up to 4 different waveforms can be stored in the internal RAM with 2048 (11 bits) values each. For details see appendix C.

clock – of different frequencies depending on the value of a division factor $d \in [0, \dots, 2^{16} - 1]$. The *counter clock* is exactly 4 times slower than the *address clock*. With each rising edge of the *counter clock*, the

values of 4 counters are incremented by the step size s defined by the value of a corresponding 6-bit register and ranging from 1 to 64. Every counter value is an index pointing to a RAM block storing the digital representation of a waveform. The phase shifts between the waveforms are realized by setting different initial values of the 4 counters. The other clock signal – the *address clock* – has to be 4 times faster than the *counter clock* since it increments an address counter (mod 4 arithmetic) responsible for the ordered selection of each of the 4 counters before their next increment. Four different waveforms with the vertical resolution of 8 bits and the time resolution of 11 bits can be stored in the internal RAM of the FPGA employed. An RTL (register transfer language) schematic of the waveform generator can be seen in appendix C (Fig. 91).

Clearly, the two factors d and s have a direct influence on the drive frequency since they influence the rate and order, respectively, in which the data points belonging to a particular waveform are issued. More specifically, the drive frequency can be seen as a function of the two variables d and s according to

$$f(s,d) = \frac{f_{\text{clock}}}{4(d+1)} \frac{(s+1)}{2048}, \tag{135}$$

where f_{clock} is the main system clock of 100 MHz and 2048 corresponds to the time resolution of a waveform. For $s = 0$, the maximal waveform resolution is achieved and the maximal drive frequency (for $d = 0$) still lies at about 12 kHz.[2] However, when computing the value of d for a desired frequency f and $s = 0$ according to

$$d(f) = \left(\frac{f_{\text{clock}}}{4f} \frac{(\overbrace{s}^{=0}+1)}{2048} \right) - 1 \tag{136}$$

and substituting d back to (135), it becomes apparent that the desired frequency f rarely can be met. Fig. 56 illustrates the problem. While the error in desired drive frequency is relatively small for low drive frequencies, it becomes seriously large for frequencies above 500 Hz, exceeding 10 % of the desired value for multiple frequencies above 2500 Hz. The problem can be alleviated by setting s to a larger value ($>$ 0) which corrupts waveform resolution but shifts the frontier for large errors to higher drive frequencies. This is quantified in Fig. 57 where the maximal error over the desired frequencies between 1 and 3000 Hz is plotted against the step register value $s \in [0,\ldots,63]$. A low error in the desired drive frequency could be realized by setting s constantly to a high value. However, in order to keep the error below 1 %, a value of 35 or more is required which leads to the effective waveform resolution below 60 points. This may be sufficient in many applications

---

[2]Practically, the actual maximal drive frequency is two times smaller due to the limitations in the ADC circuitry.
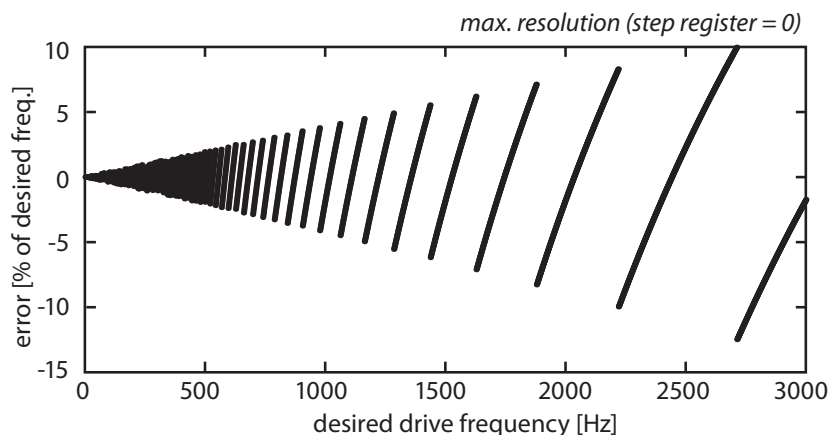
max. resolution (step register = 0)

Figure 56: Error in actual drive frequency computed according to (136) as percentage of desired drive frequency when maximal waveform resolution (register *s* set to 0) is used.
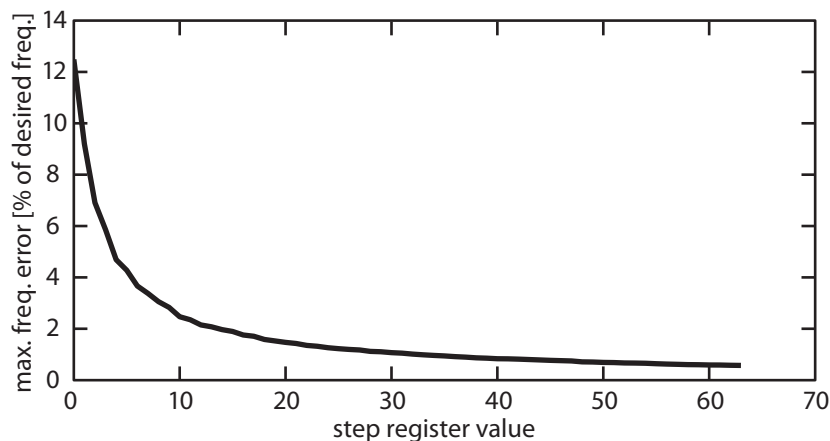

Figure 57: Maximal frequency error for a desired integer frequencies between 1 and 3000 Hz as a function of the step register value *s*.

but leads to another problem connected with the realization of motor direction switching. In the simplest case, direction switching can be achieved by running the waveform counters backwards. While simple and perfectly well suited for nanopositioning applications, this approach is not directly compatible with the bioinspired control strategy described in the previous chapter. It would require a direction-dependent swapping of AEP and PEP and possibly a special handling of leg trajectories during the switching events.[3] The direction change can be also realized by swapping the A and B phases belonging to the same legs. This approach does not affect the bioinspired strategy since one drive direction can be assumed and the actual direction change takes place in the low level circuitry of the waveform generator. Nevertheless, even this approach is haunted by practical issues. In

---

[3]In this case, spline or Bézier spline curves would be better suited as means of trajectory description since pure Bézier curves interpolate end points only.
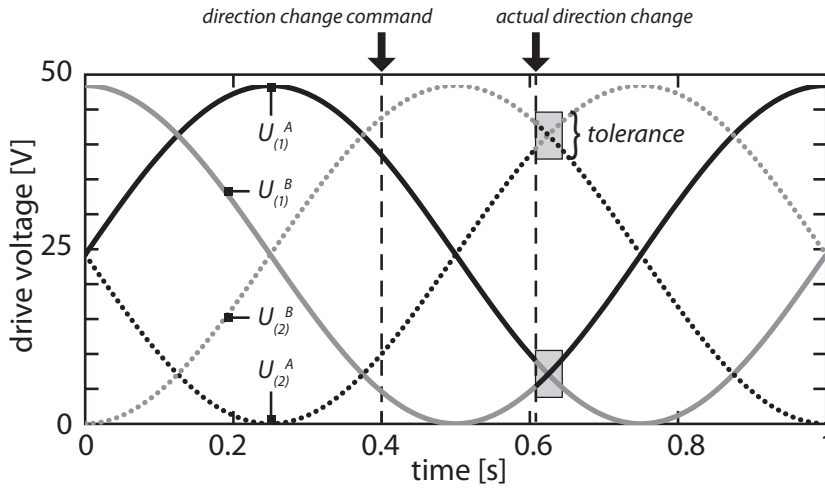
Figure 58: Illustration of a motor direction change event (commanded at 0.4 s) based on the swapping of electrical phases connected to the same pair of legs. The actual direction change occurs as soon as the respective phases fall into a tolerance window indicated with grayed boxes. Note that all phases swap at the same time for the example given with the *sine* waveform. This is not the case in general. The phases are shown in the convention of Fig. 24.

order to avoid sudden voltage changes in the electric phases, the switching should occur when they have the same or a very similar value (i.e. $U^A_{(i)} \approx U^B_{(i)}$ or, in other words, when the legs are not bent). Since the digital values are discrete, a tolerance window needs to be defined. As soon as the values of both waveforms fall into this window according to

$$|U^A_{(i)} - U^B_{(i)}| \leq \text{tolerance} \qquad (137)$$

a direction change may take place. Fig. 58 illustrates a phase-switching event for the *sine* waveform. If the tolerance window is small enough, no large voltage changes due to phase-swapping are possible. But if a small tolerance is set, the set of allowed values for the step size s shrinks. Large s values lead to larger differences between consecutive waveform points. In an extreme case, the difference may be larger than the tolerance window and possibly cripple the phase-swapping strategy. Fig. 59 shows the maximal difference between consecutive waveform points for the *force* and *sine* waveforms in dependency of the s value. Obviously, both maximal difference curves are monotonically increasing but they are susceptible to the increase in s to different degrees. The choice of s is much more critical for the *force* waveform. As a safety margin, the value of s should be chosen smaller than the argument for which the maximal difference curve reaches the tolerance value. For the given waveforms and the tolerance of 10, s should not exceed the value of 9. But such choice of s leads to frequency error issues as described earlier in this section.
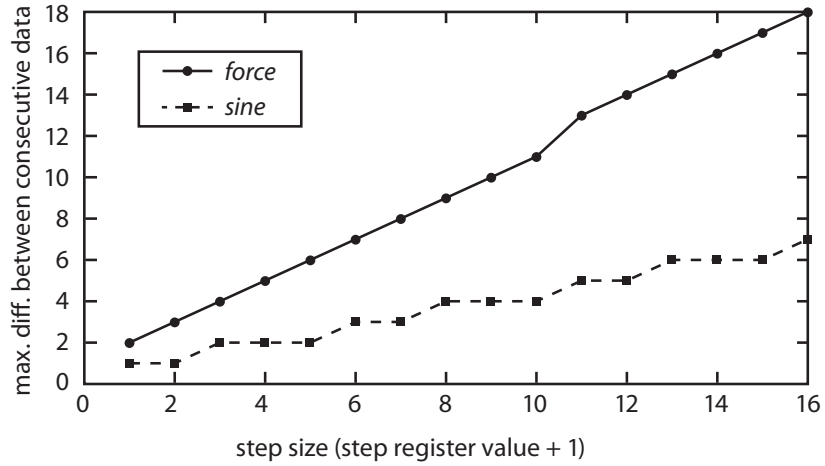
Figure 59: Maximal difference between consecutive waveform data points plotted for the *force* and *sine* waveforms against the waveform counter increment value (step size s).

Fortunately, this is not a dead-end situation. If one was able to choose variable s and d values in (135) in a way to arrive at a closest frequency match to the desired frequency within given bounds for both independent parameters, the frequency errors would decrease without violating the tolerance safety margin.

6.3 CONTINUED FRACTIONS APPROACH IN FREQUENCY MATCHING

In eq. (135), s and d are independent variables which can have a variety of non-negative integer values. In the actual implementation of the waveform generator, s is a 6-bit and d a 16-bit register which gives over 4 millions possible combinations of their values. Surely, it would be beneficial to know an algorithm which can find a solution s and d in nonnegative integer numbers giving the best possible match to the desired frequency f in a moderate number of steps. Setting $C = \frac{f_{clock}}{4 \cdot 2048}$, letting f be the desired drive frequency and reformulating (135), it can be seen that

$$-Cs + fd = C - f. \tag{138}$$

Equation (138) is an example of Bézout's identity [116] which has infinitely many integer solutions s and d as long as C and f are integer numbers and $C - f$ is the greatest common divider of C and f. A proof of this can be found in appendix B. Dividing both sides of (138) by $C - f$ (if $C - f \neq 0$) we arrive at

$$-\underbrace{\frac{C}{C-f}}_{a} s + \underbrace{\frac{f}{C-f}}_{b} d = 1. \tag{139}$$

The number 1 is a divider of both a and b. However, a and b are not necessarily integer numbers. Also, it is not known if they have another common divider greater than 1. Still, we are not looking for an exact solution to (139) but are rather interested in keeping the frequency error in (135) as low as possible. Thus, we could either round the coefficients a and b to the nearest integer values, check if these values are coprime, and then look for a nonnegative integer solution to s and d or develop an algorithm which can cope with real coefficients as well. The latter approach is pursued in appendix B, in which it is shown that the problem of finding two integer numbers ξ and η satisfying

$$a\xi + b\eta = 1$$

is closely related to finding the continued fraction expansion of a/b. If a/b is real (irrational), this expansion is infinite and approximates a/b better and better with every further expansion term.

At this point, two questions still need to be answered. First, how good is the solution computed by the algorithm from appendix B in terms of frequency error, especially if upper bounds on s and d are given due to a fixed width of the registers in the waveform generator. Second, how to cope with the fact that s and d in (135) have to be nonnegative integers, if ξ and η can be negative in general.

In order to answer the latter question, note that for frequencies f below 12 kHz, a in (139) is negative and b is positive. From this, one can conclude that the sign of s and d has to be the same. Since we are interested in approximative solutions, we may take the absolute value of s and d as our solution. This is motivated by the fact that s and d grow with every iteration. For positive s and d we have

$$(-C)|s| + f|d| = C - f \quad \Rightarrow \quad f(s,d) = C\frac{|s| + 1}{|d| + 1}$$

and for negative s and d (139) becomes

$$C|s| + (-f)|d| = C - f \quad \Rightarrow \quad f(s,d) = C\frac{|s| - 1}{|d| - 1}.$$

Already after a few iterations the difference between $\frac{|s|+1}{|d|+1}$ and $\frac{|s|-1}{|d|-1}$ will become relatively small.

As far as the quality of the solution is concerned, there are fixed bounds on the maximal values of s and d (available register widths) and the iterative approach has to be terminated before these bounds are reached. Fig. 60 illustrates frequency errors for a varying step register width between 5 and 12 bits and two different numbers of maximal iterations. Recall, that the waveform generator is implemented with 6 and 16 bits for the s and d registers, respectively. For this reason, only the bounds on s were varied as s saturates much faster than d. In Fig. 60(a) and (b), box-and-whisker plots are used to illustrate the distribution of frequency errors in dependency of step register width.
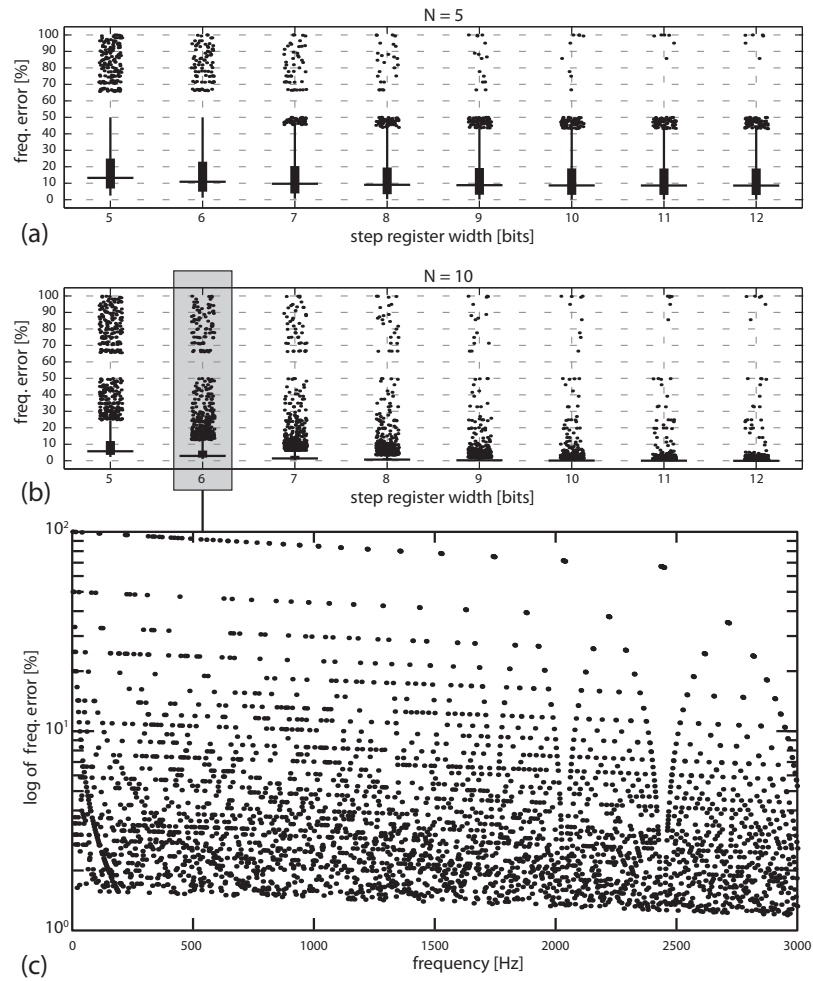
Figure 60: Frequency error distribution for integer frequencies between 1 and 3000 Hz when the iterative Bézout's identity solving algorithm is used (see sect. B.3). The distributions are illustrated with help of box-and-whisker plots in (a) and (b) for an increasing step register width and for different numbers of iterations (N=5 and N=10). Median values are indicated with horizontal lines; thick vertical bars correspond to the interquartile range (IQR); the whiskers span the range ±1.5IQR and the outliers are shown with help of dots having a random horizontal distribution for the sake of clearer illustration. In (c) the frequency errors are shown directly for the step register width of 6 and N=10.

More specifically, for each step register width value w and the integer frequencies $f \in [0, \ldots, 3000]$ the iterative algorithm from sect. B.3 was run and terminated before the computed s exceeded $2^w - 1$ or the computed d exceeded $2^{16} - 1$ or the maximal number of iterations N was reached. The so computed frequencies were subtracted from the corresponding desired values and the differences expressed as absolute percentage errors. Clearly, 5 iterations are not sufficient since the median of frequency error is close to 10 % and do not improve considerably with increasing w. For 10 iterations and w of 6, it drops

below 3.2 % and for w=8 already below 1 %. However, even for large register widths, there are still outliers close to 100 %. Even for 20 bits long registers, the calculations for several frequencies still produce large errors. The situation improves only when no bounds on s and d are set but the obtained solutions are orders of magnitude too large for a practical implementation. Note that if s_0 and d_0 are a solution to

$$as + bd = 1$$

then $s_0 + kb$ and $d_0 - ka$ with $k \in \mathbb{Z}$ are solutions as well [184]. Accordingly, by defining

$$w_1|s_0 + kb| + w_2|d_0 - ka| = s(k) + h(k) = f(k) \qquad (140)$$

with some weighting factors w_1 and w_2 we could try to minimize $f(k)$ and find an optimal but possibly smaller/minimized solution. However, the involved computations quickly overpower the capacities of the integrated circuits employed in the motor electronics. Another problem concerns the fact that even with a moderate register width, as with the 6 bits used for the storage of s, we should be reluctant to accept high s values even within the given bounds, because they degrade waveform resolution and because of the tolerance issues mentioned before.

In practical terms, when s and d are constrained according to the register widths in the actual implementation of the waveform generator, the frequency errors take the form of Fig. 60(c). This solution is not satisfactory since even for a low-median error, there are too many high-error outliers to treat them as special cases with dedicated solutions. The most practical way out seems to be the pre-computation of optimal solutions and their storage in a look-up table for a later access. This was done for the actual register widths in the waveform generator but the maximal value of s was additionally constrained to 8 because of the tolerance window considerations at the end of the previous section. The results are illustrated in Fig. 61. Even with the narrow interval of the allowed s values, the computed frequencies differ from the desired ones by at most 1.2 %. The minimal amount of storage required for the look-up table equals $3000(4 + 16) \approx 7.32$ kB for integer frequencies between 1 and 3000 Hz. For frequencies below 100 Hz a finer sampling is advisable but for these frequencies a constant s of 0 and the computation of d according to (136) is sufficient in terms of the error magnitude below 1 %.
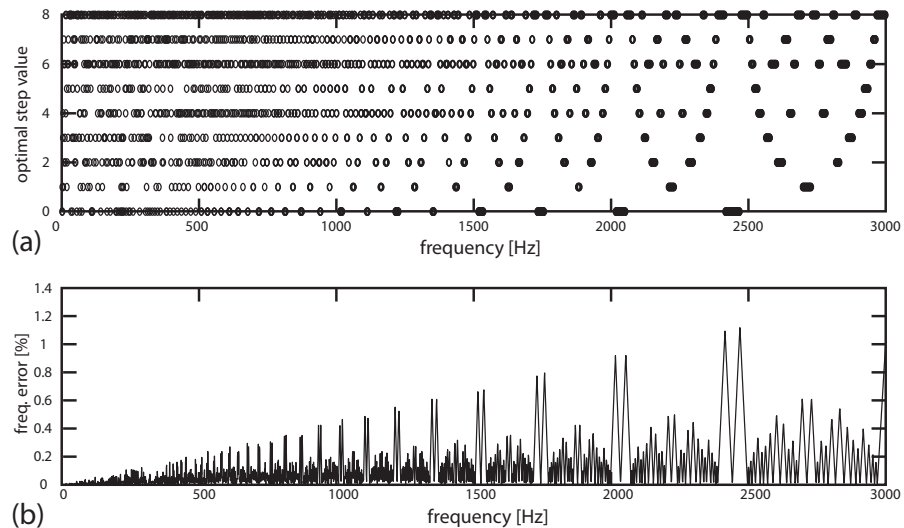
Figure 61: Optimal step register values (a) resulting in minimal frequency errors (b) precomputed and stored in a look-up table. The step register values have an upper bound of 8. Note the large spread of these values within the allowed range. Also note that the frequency error remains below 0.2% for most frequencies and never exceeds 1.2%.

6.4 DISCUSSION

This chapter presented the motor-drive electronics developed in order to overcome the weaknesses of the commercial electronics in terms of its size and drive frequency generating capabilities. The new electronics is several times smaller than the commercial products, despite the fact that it contains a self-sufficient control unit and a rich repertoire on communication and sensor interfaces. A further improvement in terms of size and efficiency is possible with a digital amplification power unit which can generate 8 electrical phases while retaining the dimensions of the analog power unit. Both amplification units can be used with the same control unit due to the modular design and the separation of control and amplification into distinct physical boards. The circuit diagrams and board layouts are included in appendix C. The new electronics is able to generate analog waveforms with a time resolution of 2048 points (11 bits) per period and the amplitude resolved with 8 bits corresponding to 256 voltage increments of 0.1875 V between 0 and 48 V. At the maximal time resolution, the maximal motor-drive frequency equals 6 kHz and is 32 times larger than in the commercial drive electronics. Higher maximal drive frequencies, even above 50 kHz, can be achieved if the time resolution is reduced. In this case, the new electronics can be used to test the overdrive region of operation mentioned at the end of sect. 3.4.

The generation of waveforms at a given frequency is affected by two parameters – the clock divider d and the waveform increment/step

size s, which form a linear equation for the drive frequency. An algorithm based on the solution to the Bézout's identity has been proposed in appendix B. The performance of the algorithm is affected by the physical limitations in the waveform generator which sets bounds on the maximal values of s and d. This results in severe errors in the computation of multiple frequencies. A solution based on the definition of an objective function was proposed but not further considered due to the limited computational capacities of the motor-drive electronics. A different algorithm based on the theory of integer optimization [152] with constraints [63, 62, 28] could be designed for the actual hardware architecture. Furthermore, the algorithm proposed in this thesis is not meant as an efficient way of computing s and d in (135) but rather as a mathematical proof of concept illustrating the different challenges related to its practical implementation. A more efficient approach would be based on a variant of the *Extended Euclidean Algorithm* [124, 33]. Efficient binary [32, 196] and accelerated [221, 193] implementations have been proposed also for parallel and VLSI architectures [41, 201]. The optimal choice of s and d within given constraints on possible register values has been in the end solved by pre-computing these values offline (by exhaustive search) and storing them in a look-up table. The proposed strategy is not only extremely efficient in terms of its online performance and low storage requirements but most of all it reduces the median of frequency errors to 0.2 % with several outliers below 1.2 %. Moreover, the low errors are achieved with the maximal bound on s set to 8 which is well below the 6-bit register limit and is compatible with the tolerance limit of 10 required by the phase-swapping direction change strategy of sect. 6.2. The capability of a faithful generation of driving signals at a desired frequency will prove useful already in the next chapter, where a load compensation mechanism based on drive frequency adjustments is developed.

As a closing remark, it should be stressed that the proposed solutions for the generation of waveforms at a given frequency are to a large degree specific for the particular implementation of the waveform generator. For this reason, the mathematical theory and the algorithm of appendix B are kept on a general level (i.e. without architecture specific bounds or assumptions about the particular form of the frequency equation). Another frequency generation approach could be based on the implementation of one of various frequency synthesis methods like phase-locked loop (PLL) or direct digital synthesis (DDS) [44]. This approach would have the advantage that a change is waveform resolution, because of the crude clock divider resolution for high drive frequencies, would not be necessary in order to match the desired drive frequency exactly.

7 DYNAMIC LOAD COMPENSATION AND FORCE CONTROL

ABSTRACT

This chapter extends the control theoretical model of chapt. 4 with a load compensation strategy based on force feedback and drive frequency adjustments. The net effect is the restoration of model linearity and a significant improvement in velocity characteristics of the walking motor even under load. Based on the linearized model, standard control design techniques are applicable to design a force controller. Theoretical limits on the performance of the controller are derived. The actual performance of the controller is evaluated both in simulations and experiments by pulling on tendons of different elasticities. It is shown that the walking motor can be successfully employed in a force generation scenario if the force transmission occurs through tendons of a moderate or high stiffness. The content of this chapter is mainly based on publication II.

7.1 INTRODUCTION

In chapt. 4 of this thesis, a control theoretical motor model based on system identification has been derived with the objective of a linear description of the dynamics of the walking motor and the application of the motor as a force generator in a small-sized robot joint. The accomplishment of both objectives is hampered by the fact that the performance of the motor deteriorates nonlinearly under load. This poses a problem for the design of a force controller since the characteristics of the motor vary strongly in a force-control scenario. The main objective of this chapter is to develop a mechanism which compensates the non-linear force dependency of motor movement and restores the linearity of the final model from chapt. 4. Based on such compensated model, a linear controller can be designed to regulate the force generation of the motor.

This chapter is organized as follows. In the next section, a load compensation mechanism based on force feedback and drive frequency adjustments is proposed and shown to fully linearize the control-theoretical motor model and to significantly improve the linearity of actual motor operation. In sect. 7.3, a linear explicit force controller is designed and the theoretical limits on the performance of the controller are presented. Finally, the performance of the controller is evaluated in an experiment and simulation.

The control theoretical motor model derived in sect. 4.2.3 of chapt. 4 is linear only for a constant force input F (including the load-free condition of $F = 0$) and as such cannot be used in a linear force-control approach. However, by modifying the control signal in dependency of the magnitude of the external force, the nonlinear force effects can be compensated. In particular, if the drive frequency signal f is multiplied with the inverse of the normalized force-vel. polynomial $V^*(F)$

$$f_c = f \cdot \frac{1}{V^*(F)} \qquad (141)$$

the motor model becomes linear for the new control signal f_c. The above linearization is an example of feedback linearization [73]. Note, that it applies only if there are no limits on the magnitude of the control signal because as

$$F \to F_{max}, \quad V^*(F) \to 0 \ \text{ and } \ 1/V^*(F) \to \infty$$

which implies that the motor would need to be driven with frequencies above its operational limits in order to compensate big external forces. Due to this physical limitation, the compensation formulated in (141) has to be modified to include control-frequency saturating terms. The following set of equations introduces a saturation constraint on (141)

$$f_c = G_{comp}(f, F) = \begin{cases} f \cdot \dfrac{1}{V^*(F)} & , \quad F \leq F_{sat} \\ f \cdot \dfrac{1}{V^*(F_{sat})} & , \quad F > F_{sat}. \end{cases} \qquad (142)$$

F_{sat} is the saturation force level which needs to be computed in dependency of the actual external force and drive frequency values according to

$$f_{max} \cdot V^*(F_{sat}) - f = 0 \quad \text{and} \quad 0 \leq F_{sat} < F_{max}. \qquad (143)$$

The existence of an unique real solution F_{sat} for $f \in [0, f_{max}]$ is guaranteed because the polynomial $V^*(F)$ satisfies the constraints from section 4.2.2. Fig. 62(a) and (b) visualize the effect of compensation on the drive frequency signal with a growing external force. The F_{sat} border indicates force levels for which the compensated frequency f_c reaches the f_{max} limit of 2000 Hz. The gray-shaded area in the diagram is the saturation region in which f_c remains at the f_{max} level.

The compensated motor model is depicted in Fig. 62(c). The drive frequency which is fed into the motor after the compensation equals f_c. For $F \leq F_{sat}$ (i.e. assuming $f_c \leq f_{max}$), the linearity of the final motor model from sect. 4.2.3 is restored since

$$V(G_{comp}(f, F)) \cdot V^*(F) = \bar{a} f \frac{1}{V^*(F)} \cdot V^*(F) = \bar{a} f, \qquad (144)$$
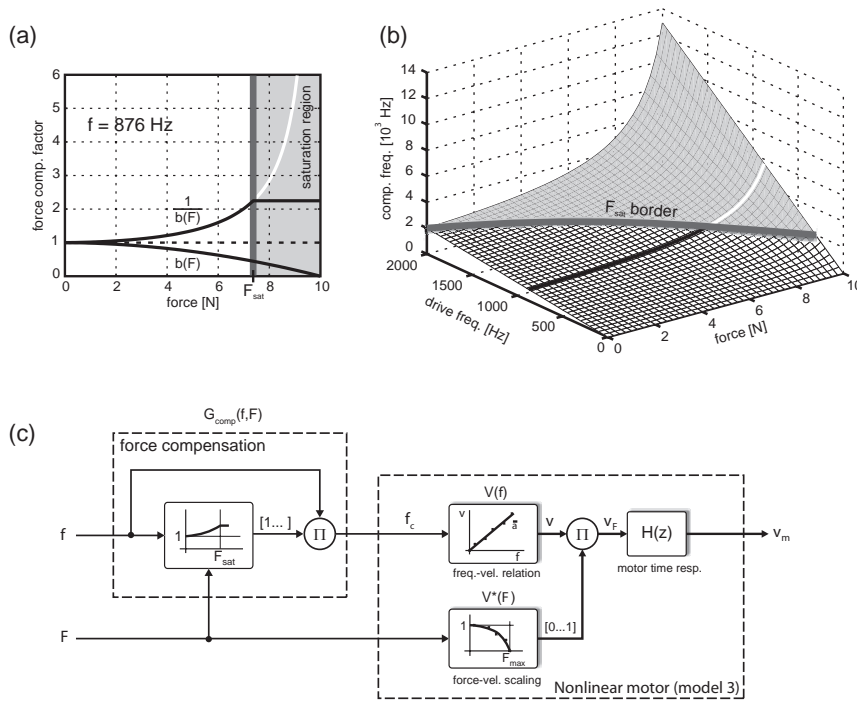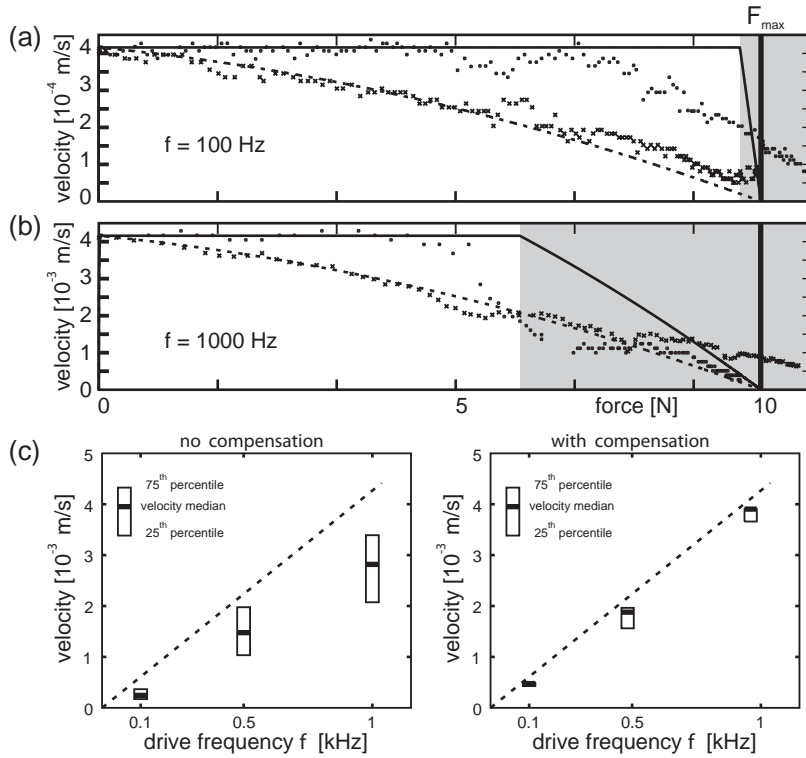
Figure 62: Effect of force compensation on motor drive frequency. (a) shows the normalized force-vel. polynomial $V^*(F)$ together with its inverse $1/V^*(F)$ representing a force compensation factor. The F_{sat} limit is given for a drive freq. of 876 Hz and indicates the border of the saturation region in which f_c remains at the f_{max} level of 2000 Hz. (b) illustrates the actual compensated freq. levels f_c in dependency of the motor drive freq. f and the external force F. Gray-shaded area is the saturation region. The black curve indicates the drive freq. of 876 Hz from (a). (c) shows the final nonlinear motor model from sect. 4.2.3 with force compensation which restores the linearity in motor operation.

according to (98) and (142).

The effect of compensation was evaluated experimentally by driving the PiezoLegs-motor with a moderate (100 Hz) and a high (1000 Hz) drive frequency in an experimental setup as the one in Fig. 40(a). The simulation and experimental results are shown in Fig. 63(a) for a drive frequency of 100 Hz and in Fig. 63(b) for 1000 Hz. The x-markers represent uncompensated, dots the compensated operation. The dashed and solid lines show uncompensated and compensated operation as predicted by the model. In simulation, the force compensation is perfect and maintains a constant motor velocity for increasing forces up to the saturation level F_{sat} where the solid lines start declining in Fig. 63(a) and (b). Experimental data shows the same behavior qualitatively. However, saturation sets in already at a lower force level. Additionally, the simulation assumes a fixed F_{max} level of 10 N

while the actual motor limit is device-dependent and may be larger (cf. chapt. 3 and 5). For a more formal evaluation of the compensation strategy for 100, 500 and 1000 Hz, Fig. 63(c) can be consulted. Here the entirety of motor velocity measurements for a given drive frequency is presented through its quartiles. For a linear operation, the median values of velocity distributions should coincide with the straight line representing the dependency of motor velocity on the drive frequency. This is the case for the right-side plot with active load compensation. The interquartile distance is larger for the higher drive frequencies. This corresponds to more frequent slip events between the legs of the motor and the drive rod. The macroscopic effect is a higher spread in the measured velocities.

Figure 63: Effect of force compensation on motor velocity. Simulation results are shown with (solid) and without (dashed lines) force compensation. The corresponding experimental data is shown in form of dots (with) and x-markers (without compensation), and was measured at two different drive frequencies, (a) 100 and (b) 1000 Hz. The gray-shaded area illustrates force levels for which the compensation is in saturation. In (c) velocity distributions are shown for three drive frequencies of 100, 500 and 1000 Hz when the load compensation was either active or not. For a perfect compensation, the median values should be close to the dashed line which illustrates the linear dependency between the drive frequency and motor velocity for an unloaded motor. With a compensation applied, the deviation from this line is minimal. The interquartile range grows with growing drive frequency. However, note that this effect is much stronger without the compensation. Also note that, since the data sampling rate was constant, there are fewer measurements for the higher drive frequency.
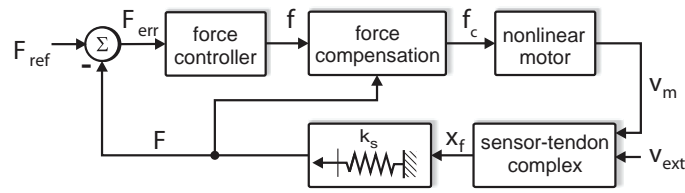
(a)
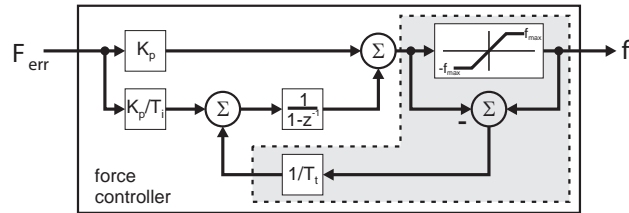
(b)

Figure 64: Force control architecture. The *force compensation* and *linear motor* blocks in (a) represent the compensated motor model from Fig. 62(c). The detailed view of the PI *force controller* with an antiwindup scheme (gray-shaded region) is shown in (b).

7.3 FORCE CONTROL

With the compensated motor model from the previous section, a linear force controller can be designed using standard approaches. In this context, only the linear part of the model from Fig. 62(c) needs to be considered if the external forces are smaller than F_{sat}. In this work, a discrete PI controller was designed and optimized using the Matlab Control System Toolbox. The design criteria were nominal stability of the closed-loop system, zero steady state error, high system bandwidth and limited control input. The force control architecture is depicted schematically in Fig. 64(a)-(b). It consists of a force controller, a force compensation unit and the linear model of motor dynamics. The frequency output f of the force controller is compensated for the nonlinear effects of the load force before being fed into the motor. The motor velocity v_m is integrated to obtain the motor position x which in turn is converted into a force signal via a tendon transmission system. The latter consists of several elasticities in series and is in the following called the sensor-tendon complex. This is depicted in Fig. 65(a). In order to compute the magnitude of the forces correctly, the different series elasticities between the drive rod of the motor and the joint have to be distinguished and taken into account. A schematic depiction of the sensor-tendon complex can be seen in Fig. 65(b). The force sensor is modelled as a mass with two elastic connectors having spring constants k_s and an additional elastic element with the spring constant k_t in series. The latter value approximates the effective stiffness of the
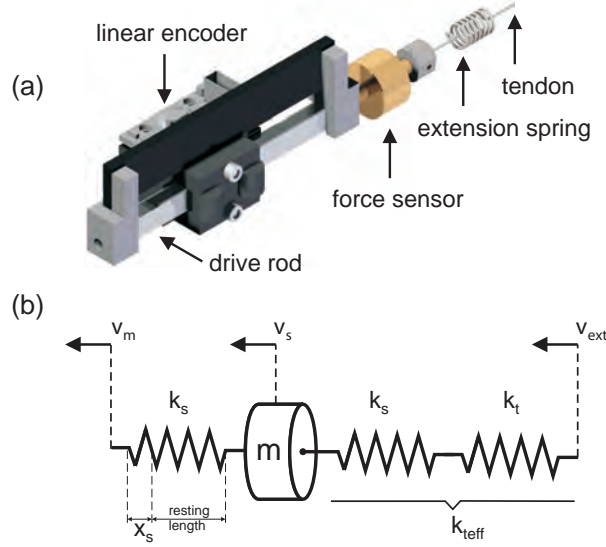
Figure 65: The walking motor as a force generator. In (a) a computer rendering of the motor equipped with a linear encoder and a force sensor connected to a series elasticity in form of an extension spring and a tendon is shown. In (b) the different series elasticities are depicted as a spring-mass model of the sensor-tendon complex. The force sensors consists of a mass m with two liner springs having the stiffness k_s.

Dyneema (Royal DSM, The Netherlands) tendon used in this setup. k_{teff} is the effective spring constant of the elastic elements connecting the force sensor to an external object like a wall or the pulley of a joint (see next chapter). v_m corresponds to the movement velocity of the motor drive rod while v_{ext} is an external velocity input. For a fixed wall, v_{ext} is obviously 0. p_s is an auxiliary state variable (momentum of the force sensor). The state-space equations of this model have been derived using the *bond graphs methodology*. The derivation process is described in appendix D. The final equations take the following form

$$
\begin{pmatrix} \dot{x}_s \\ \dot{x}_{teff} \\ \dot{p}_m \end{pmatrix} = \begin{pmatrix} 0 & 0 & \frac{-1}{m} \\ 0 & 0 & \frac{1}{m} \\ k_s & -k_{teff} & 0 \end{pmatrix} \begin{pmatrix} x_s \\ x_{teff} \\ p_m \end{pmatrix} + \begin{pmatrix} 1 & 0 \\ 0 & -1 \\ 0 & 0 \end{pmatrix} \begin{pmatrix} v_m \\ v_{ext} \end{pmatrix}
$$

(145)

and

$$
x_f = \begin{pmatrix} 1 & \frac{1}{1+\frac{k_s}{k_t}} & 0 \end{pmatrix} \begin{pmatrix} x_s \\ x_{teff} \\ p_m \end{pmatrix}
$$

(146)

where x-variables correspond to the amount of elongation of the elastic elements with corresponding subscripts. Additionally, x_f is the overall elongation of the force sensor (both elastic connectors having the spring constant k_s). When multiplied with $0.5k_s$ (series connection of the connectors), this product delivers the magnitude of the measured force. The force controller used in the architecture of Fig. 64 is a PI type

with an additional back-calculation antiwindup control scheme [215]. In the design process, the following set of parameters was obtained for the controller:

$$
\begin{aligned}
K_p &= 1975, \\
T_i &= 0.05, \\
T_t &= 15
\end{aligned}
$$

with the above constants being the proportional gain, the integral and the tracking time constants, respectively.

There are theoretical limits on the performance of the controller. As force generation depends on the displacement of the drive rod x in combination with the effective stiffness K of the tendon the motor pulls on, the controller can only track forces which do not require it to move faster than the maximal velocity v_{max} of the motor. In the following, these theoretical limits are derived and the actual performance of the force controller is evaluated. For this purpose, the consecutive reference force signal is used in the experimental setup shown in Fig. 40(a) with the controller from Fig. 64(b):

$$
F_{ref}(t) = \frac{A}{2} \sin(2\pi \nu t) + \frac{A}{2} \tag{147}
$$

The signal spans a range A of forces between its minimal and maximal value and contains a bias term because only pulling (positive) forces can be generated in the arrangement of Fig. 40(a) or a tendon-driven robot joint. The rate of the signal is varied by the frequency ν and its period is $T = 1/\nu$. The distance which the drive rod needs to travel in order to generate the reference force is given by

$$
x(t) = \frac{F_{ref}(t)}{K} \tag{148}
$$

for a given effective spring constant K. Note, that the effective spring constant is a simplification of the sensor-tendon complex as introduced above in order to simplify the mathematical derivation of the limit on the performance of the force controller as presented below. This theoretical limit is defined by the following equation

$$
v_{max} \geq \max_{t \in [0,T]} (|\dot{x}(t)|) = \max_{t \in [0,T]} \left(\frac{|\dot{F}_{ref}(t)|}{K} \right) \tag{149}
$$

which states that the rate of change in the reference signal cannot exceed the maximal velocity of the motor at any point and resolves into

$$
v_{max} \geq \frac{\pi \nu A}{K}. \tag{150}
$$

The theoretical limit from (149) can be replaced with a softer condition

$$
v_{max} \geq \frac{1}{T} \int_0^T |\dot{x}(t)| dt = \frac{1}{KT} \int_0^T |\dot{F}_{ref}(t)| dt \tag{151}
$$
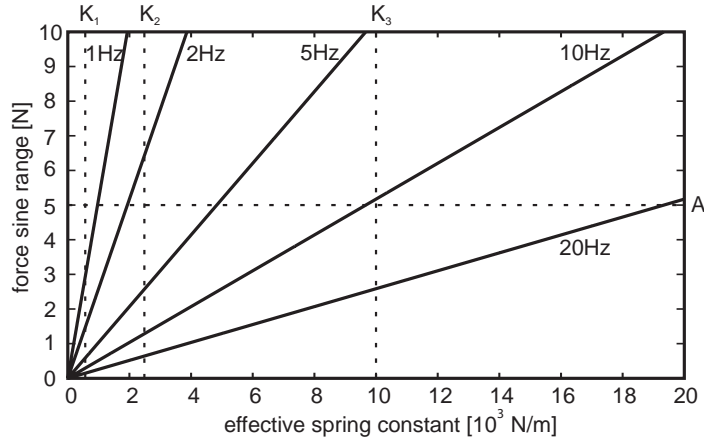
Figure 66: The theoretical limits of the range of a sine-shaped reference force signal in dependency of tendon stiffness and signal frequency according to (153). Dashed lines indicate the three effective spring constants (K_1, K_2 and K_3) and the force sine range A used to evaluate the performance of the controller experimentally – see Fig. 67.

which only requires that the average rate of change in the reference signal does not exceed v_{max}. Because of the periodicity and symmetry of the cosine, it follows that

$$\frac{1}{KT} \int_0^T |\dot{F}_{ref}(t)| dt \overset{\dot{x}=\cos}{\longleftrightarrow} \frac{4}{KT} \int_0^{T/4} \dot{F}_{ref}(t) dt \qquad (152)$$

and the inequality (151) leads to

$$v_{max} \geq \frac{4}{KT} \left[F_{ref}(t) \right]_0^{\frac{T}{4}} = \frac{2\nu A}{K}. \qquad (153)$$

Fig. 66 is the illustration of the theoretical force controller limits as defined in (153) for the PiezoLegs-motor due to its maximal velocity. It shows the maximal range of the reference sine-shaped force signal that a perfect controller could track on average for a given spring constant K and signal frequency ν.

The performance of the controller was evaluated both in computer simulations and in real experiments. For the purpose of the experiments, the motor was employed in the setup from Fig. 40(a). Three linear springs of increasing spring constants were used resulting in three effective stiffnesses $K_1 = 500$, $K_2 = 2400$ and $K_3 = 10000\,\text{N/m}$. As a reference sine-shaped force signals of the form shown in (147) were used. The reference signal was biased and spanned the range of $5\,\text{N}$ (A = 5) in order to be positive and remain in the well-compensated range of the motor. Seven different frequencies ν from 0.1 to 20 Hz were used in the real experiments. The measured force was then compared with the reference signal. The results of the simulations and
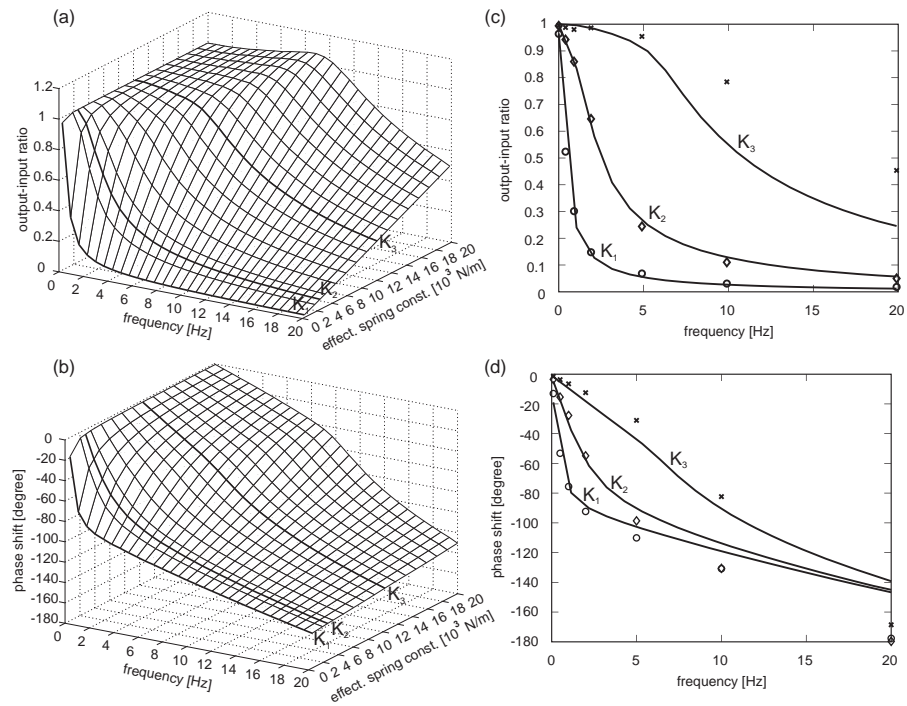
Figure 67: Three-dimensional Bode plots of force controller performance in dependency of tendon stiffness [(a) and (b)] computed from simulation data. (c) and (d) show the experimental data obtained for three stiffness levels (circles: $K_1 <$ diamonds: $K_2 <$ x-markers: K_3) and seven different frequencies. Thick curves are simulation results copied from (a) and (b).

experiments are summarized in Fig. 67 with the help of Bode-like diagrams.[1] The simulations were able to predict most of the experimental results. In the magnitude plots (a and c) the measured data deviates from the simulated only for the highest stiffness K_3. Surprisingly, in this case the real system performs better than expected from the simulations. One explanation for this are possibly nonlinear characteristics of the Dyneema tendon used in the experiments. When a soft spring is employed in series with the relatively stiff tendon, the first has a stronger influence on the elongation of the spring-tendon complex than the latter. When the spring is stiff, the nonlinear effects in the tendon gain on importance. In the phase plots (b and d) experimental data deviates from the simulated mostly for high-frequency inputs. Also in this case, the reason could be attributed to nonlinear stretch effects in the Dyneema tendon. In the simulations, the tendon is modelled as a linear spring with a constant stiffness.

---

[1]For a true bode diagram, the gain in the magnitude plot should be depicted in dB.

7.4 DISCUSSION

This chapter introduced a force-compensation strategy which restores the linearity of the control-theoretical motor model from sect. 4.2.3. The compensation is based on feedback linearization through the inversion of the nonlinearity [73]. In case of the walking motor, this corresponds to the inverse of the normalized force-velocity relation as introduced in chapt. 4. If this mechanism is used with the motor model or with the real motor, both can be considered linear systems. While in case of the simplified model the linearization is perfect, the true nonlinear system obeys the means of linearization only to a certain degree. There are several reasons for this with the most obvious one being the unmodeled dynamics. This ranges from the load-free lowpass approximation of sect. 4.2.3 which explains about 70 % of the experimental data, through nonlinear stick-slip effects under load, to nonlinear stretch effects in the force transmitting tendons. In practical terms, the proposed linearization strategy is affected by the physical limits on the control signal, i.e. the drive frequency. Despite these limitations, the proposed linearization strategy significantly improves the performance of the real motor under load. For moderate loads up to 5 N, the drive velocity can be retained at a nearly constant level. For higher loads, the modified drive frequency quickly approaches the saturation level. Moreover, high load forces lead to a more frequent slip between the piezoelectric legs and the drive rod and reinforce the nonlinear (frictional) influences.

For the purpose of the design of a force controller, the maintenance of linearity is important since it allows the application of a rich repertoire of mathematical methods [8]. In particular, model-based approaches are easily applicable [170]. However, in this work an explicit PI controller was designed. This decision was motivated by the fact that model-based control relies on the exact knowledge of the dynamics of the system to be controlled. Model inaccuracies deteriorate the performance of the controller. PI(D) controllers have the advantage of their high robustness against model inaccuracies and of a well established strategy for online tuning [188]. The designed controller was tested in the simulation and in real experiments by pulling on tendons of different elasticities. The obtained results were very similar which speaks for the reliability of the control-theoretical motor model as well as of the applied load-compensation and force-control strategy. A more advanced nonlinear control scheme [189, 107] could possibly improve the results further. However, this chapter has also shown that there are theoretical limits on the performance of a (perfect) force controller. For a sinusoidal force reference signal at 10 Hz and a tendon having the stiffness K_3, the peak-to-peak amplitude of the reference cannot exceed 5 N if the controller is supposed to track the reference perfectly according to the soft performance condition in equation (151).

The actual performance has to be worse due to time delays in signal propagation and motor inertia. In the simulation, the performance of the explicit force controller is at the level of 55 % which corresponds to the peak-to-peak amplitude of 2.75 N. In practical terms, the designed controller can be successfully applied in a force control scenario as long as the series elasticity remains at the effective level of 10 N/mm or above and the rate of change in the reference force does not exceed 10 Hz. In the next chapter, two walking motors together with the force controllers designed in this chapter will be employed in an antagonistic robot joint to act as muscle-like force generators.

APPLICATION PART
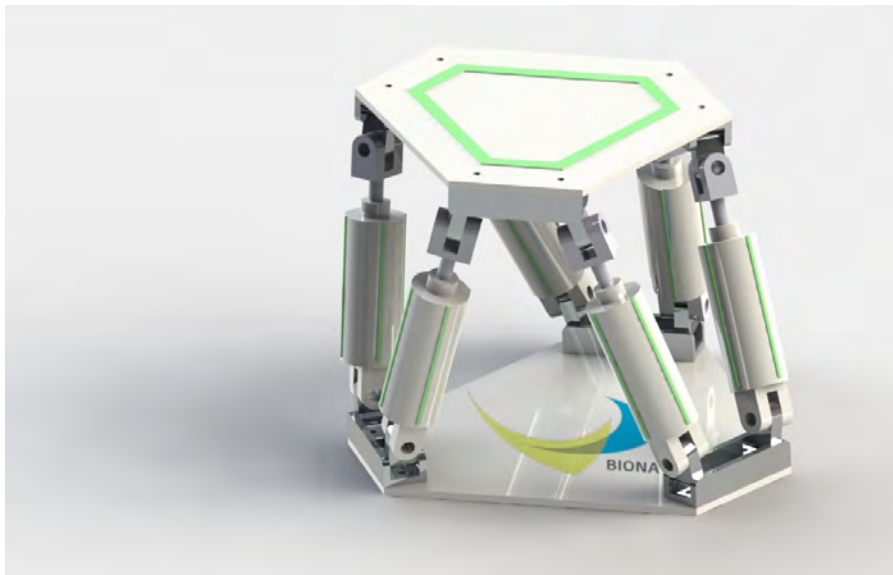
8 | MUSCLE-LIKE ACTUATION OF AN ANTAGONISTIC JOINT

ABSTRACT

This chapter presents a technical implementation of a 1-DOF robot joint driven by two virtual muscles. The macroscopic muscle functionality is described with a variant of Hill's model and mimicked by two force generators consisting of piezoelectric motors together with their explicit force controllers. The force generators are arranged in an antagonistic configuration. The generated forces are transmitted to the joint via elastic tendons. To prevent tendon slack, the force controllers are augmented with the concept of a virtual tendon. The complete system is tested in a simple positioning task. The content of this chapter is based on publications III and IV.

8.1 INTRODUCTION

Biological musculoskeletal systems are actuated by muscles, as their name implies, and use the antagonistic actuation principle – the movement of each joint is realized by a group of at least two muscles which pull on bones via elastic tendons [224]. It is not unreasonable to assume that the qualitative properties found in the majority of animal muscles have been selected for by evolution for their adaptive advantage with respect to the generation of movement [37]. In the field of robotics, recent years have brought a steady growth in the appreciation of the role of elasticity for walking [165] and human robot-interaction [71], thus opposing the classical rigid design paradigm. Buehrmann et al. [37] argue that not only elasticity but also various non-linearities in the common muscle model by Hill [102, 88] lead to various desirable properties with regard to the controllability of robotic systems like increased stability and robustness to noise. From the biological point of view, there are also important reasons to use the antagonistic actuation principle [84]. Beside the obvious reason that muscles can only pull, the antagonistic principle can be shown to be energy-optimal for various tasks like posture stabilization [183] and provides the joints with an intrinsic flexibility which is a key factor for any physical interaction with the environment [84]. Furthermore, biological and technical antagonistic systems are able to actively modulate their stiffness by means of co-contraction and thus adapt to changes in task requirements or in environmental con-

ditions [103, 183, 147].[1] Beside the above motivation for bioinspired technical solutions in robotics, i.e. improving the performance of robots in various natural situations like walking, grasping or throwing, another important reason for the research on muscle-like antagonistic actuation is the fact that we ourselves are biological systems. A successful integration of technical actuators and bioinspired control strategies could lead to a significant improvement in the quality of artificial limbs and a deeper understanding of the principles of the biological control of movement [67, 68, 27].

From a technical point of view, a successful transfer of biological principles on technical systems is difficult for at least two reasons. First, biological systems are often incomparably more complex than technical systems. They already are the "end product" of millions of years of evolution and cannot be reverse-engineered easily. Second, biological systems consists of different building blocks than the technical systems. A successful technical implementation not only depends on the understanding of its biological counterpart but also on bridging the gap between the different properties of the building blocks. This difficulty is the main research activity in the field of biocompatibility [31] and is well illustrated by the still unsuccessful technical realization of an artificial muscle [138]. Also the antagonistic actuation principle poses serious technical difficulties. The main disadvantage lies in the increased number of actuators which leads to an increased weight, larger space requirements and a more complicated mechanical design. The problem of increased weight and larger space requirements can be alleviated to some degree by using tendon-transmission systems to transmit forces which leads to a reduced inertia at the end effector and a higher flexibility in the placement of actuators [115, 206].

In the context of this work, the walking motors are interesting candidates for a bioinspired actuation with a redundant number of actuators due to their small size and high force-generation capability (see chapt. 1). Also the fact that the motors directly produce translational motion, enhances the muscle analogy as shown in Fig. 68. Two motors can be arranged in an antagonistic setup and rotate the joint by transmitting pulling forces via tendons connected to the joint.[2] The backward (to the left in Fig. 68) movement of a motor corresponds to the shortening of a muscle and generation of pulling forces on the joint. This 1-DOF arrangement with a pulley of constant radius is probably the simplest possible realization of an antagonistic actuation principle. The literature is abundant in similar antagonistic arrangements. Bicchi et al. [22] use pneumatic McKibben artificial muscles

---

[1]Co-contraction per se does not change the net torque acting on a joint and is a waste of metabolic energy from this point of view. However, co-contraction together with non-linear stiffness characteristics of the antagonistic muscles modulates the stiffness of the joint.

[2]In the actual implementation (see Fig. 72) the pulley joint consists of two "reels" with tendons wound around them and tendon ends fixed to the pulley.
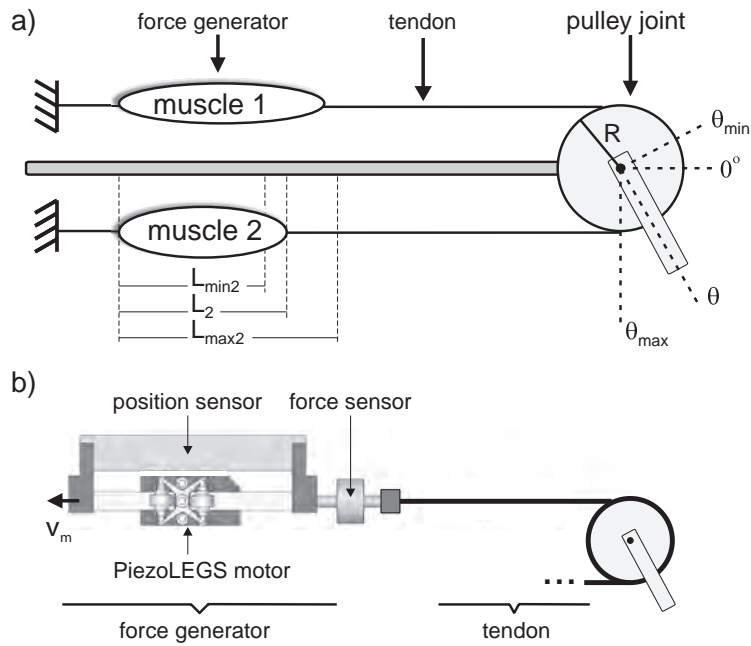
Figure 68: Basic antagonistic actuation concept. (a) Schematic depiction of a 1-DOF rotary joint driven by two antagonistic muscles connected to a pulley via tendons. θ is the actual angular position of the joint and $[\theta_{\min}, \theta_{max}]$ its operating range. (b) Technical realization of (a). A piezoelectric motor equipped with position and force sensors plays the role of a force generator. The motor is connected to a joint via a tendon. The second, antagonistic motor is left out in this depiction.

as actuators, Migliore [147] designs a mechanical non-linear spring element which can be compared to the passive stiffness characteristics of a muscle [230] and Grebenstein et al. [84] combine mechanical elements with active impedance control strategies. In the last two approaches, electromagnetic rotary motors are used. The common denominator of these approaches is the introduction of non-linear stiffness characteristics either to the series elasticities or the actuators in order to modulate the overall stiffness of the joint [183, 147]. This objective, however, is not further considered in this work. Specifically, although an antagonistic arrangement of actuators according to the depiction in Fig. 68 with non-linear muscle characteristics is employed, co-contraction as the prerequisite for stiffness modulation is not considered in this work. The originality of this chapter consists in the fact that no other work known to the author mentions piezoelectric motors in an antagonistic arrangement as described above and no other work uses piezoelectric actuators to mimic muscle characteristics by means of control. This chapter is meant as an experimental proof-of-concept

that a small-sized piezoelectric motor can be successfully applied as a force generator in a biologically inspired robot joint.

Specifically, in this chapter an antagonistic joint according to the idea from Fig. 68 is actuated with two piezoelectric force generators as introduced in chapt. 7. The reference force signal for the force controllers is computed according to the muscle model by Hill, whose particular implementation is described in sect. 8.2. The overall joint architecture together with the concept of a virtual tendon used to prevent tendon slack are presented in sect. 8.3. Finally, sect. 8.4 shows that the antagonistic setup with piezoelectric "virtual muscles" can be successfully employed in a simple position-control scenario. The discussion follows in sect. 8.5.

8.2 VIRTUAL MUSCLES

Classical studies of isolated muscles have described well the quasistatic force-length and force-velocity relations of the areflexive muscle [101].[3] Already in 1938, Hill proposed a muscle model [102] which is still the dominant model today. The model assumes that the muscle force depends on the length, velocity of shortening and level of activation of the muscle. The total force according to [2] can be calculated as

$$F = [aF_L(L)F_V(V) + P(L)]F_{\max} \tag{154}$$

with a being the muscle activation level, F_L the force from the force-length relation, F_V the force from the force-velocity relation and P the passive force of a muscle extended beyond its resting length. As these are normalized values, they have to be additionally scaled with $F_{\max}$ – the maximal force that can be generated by a given muscle. A system view of Hill's muscle model can be seen in Fig. 69. The particular implementation of the above relations followed in this work is adapted from [79]. Specifically, only the $F_L(L)$ relation is used to show the general feasibility of the presented approach. F_V and passive characteristics of the muscle are not considered. The role of particular terms in (154), muscle parameters and joint geometry in the production of movement and stiffness modulation can be found elsewhere [23, 38, 37, 230, 6]. The $F_L(L)$ relation is defined according to

$$F_L(L) = \exp\left[C \cdot \left|\frac{L - L_0}{\omega L_0}\right|^3\right] \tag{155}$$

which describes a bell-shaped curve. In the above equation, L_0 and L are the muscle resting length and the actual muscle length, respectively. The parameters C and ω have the values $\log 0.05$ and 0.4 according

[3] An areflexive muscle is devoid of its reflexes, like for example the stretch reflex [120], through deafferentation – the interruption of afferent connections of nerve cells.
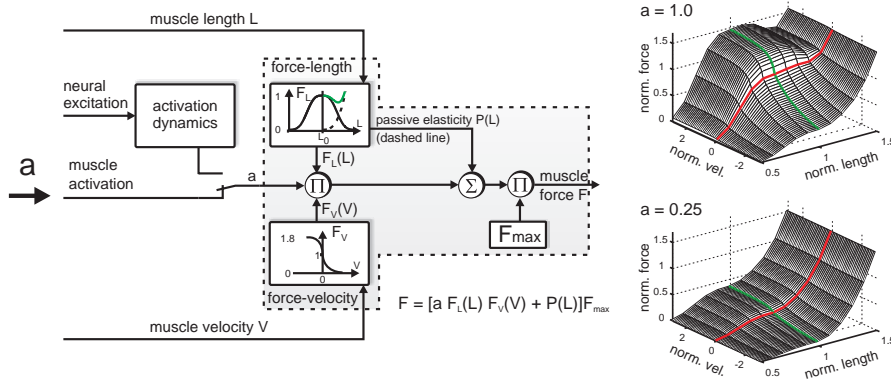
Figure 69: Hill's muscle model consisting of the force-length $F_L(L)$, force-velocity $F_V(V)$ and passive $P(L)$ characteristics of a muscle (dashed line in the force-length box). The normalized muscle force ($F_{max} = 1$) in dependency of its normalized length and velocity of shortening is depicted on the right side for two different levels of activation. Only the F_L relation is considered in this chapter.

to [79]. For $L < L_0$, the characteristics of the muscle on the ascending slope of the bell-shaped curve can be approximated with a linear spring [103]. Note, however, that the slope of this spring varies with the activation signal a in (154). Thus, by modifying the activation levels of the muscles in time, effectively a non-linear stiffness characteristics can be obtained. The activation signal in (154) can be issued either directly as a numerical value or originate from motoneuron activity measurement of a real muscle which can be converted to a numerical value in the *activation dynamics* box as shown in Fig. 69.[4] The $F_L(L)$ relation is characterized by L_0. Additionally, a muscle has a minimum length L_{min} to which it can contract and a maximum length L_{max} to which it can extend. In the following, these values are given as unit-less fractions of the resting length L_0 of a muscle. For a particular choice of these values and the joint geometry from Fig. 68, a mapping between the work space of the joint and the length of the antagonistic muscles has to be defined. Setting the radius of the pulley joint to a constant R of 1 cm, using θ to indicate its actual angular position and θ_{min} together with θ_{max} to define the operating range of the joint, the lengths of the muscles can be computed via a geometric transformation from the actual joint position. For the pulley joint, assuming stiff

---

[4]In order to describe the activation dynamics, a second order system can be used as in [230].

tendons connecting the motors to the joint, the transformation has the following form

$$L_{0(1)} = \frac{\theta_{\max} - \theta_{\min}}{L_{\max(1)} - L_{\min(1)}} R$$

$$L_{0(2)} = \frac{\theta_{\max} - \theta_{\min}}{L_{\max(2)} - L_{\min(2)}} R$$

(156)

where the numbers in parentheses correspond to the upper (1) or lower (2) muscle in Fig. 68.[5] The actual lengths of the muscles for a given position θ of the joint equal

$$L_{(1)} = L_{0(1)} L_{\min(1)} - (\theta_{\min} - \theta) R$$

$$L_{(2)} = L_{0(2)} L_{\min(2)} + (\theta_{\max} - \theta) R.$$

(157)

$L_{(1)}$, $L_{(2)}$ are the actual and $L_{0(1)}$, $L_{0(2)}$ the resting lengths of the muscles. $L_{\min}$ and $L_{\max}$ are unit-less numbers expressing the minimal and maximal muscle lengths as fractions of $L_{0(1)}$ and $L_{0(2)}$. The numbers in parentheses referring to particular muscles in (157) are omitted from $L_{\min}$ and $L_{\max}$ since theses values are in the following assumed equal for both antagonistic muscles (i.e. $L_{\min(1)} = L_{\min(2)}$ and $L_{\max(1)} = L_{\max(2)}$). For a force-length relation as defined in (155), the actual muscle lengths have to be normalized by dividing them by their corresponding resting lengths. The normalized muscles lengths L^* are computed as

$$L^*_{(1)} = L_{(1)} / L_{0(1)},$$

$$L^*_{(2)} = L_{(2)} / L_{0(2)}.$$

(158)

Given the particular geometry of the pulley joint and the measurement of its actual position θ, equations (156)-(158) together with the muscle characteristics from (154) and (155) can be already used to compute reference forces for the muscle-like force generation. Fig. 70 illustrates how such virtual muscles can be used in a position control scenario. A position controller suitable for an antagonistic drive [109] is used to generate activation signals a_1 and a_2 (no co-activation, see below) according to the sign and magnitude of the position error $\theta_{\text{ref}} - \theta$. Depending on the level of these activations and the actual (normalized) muscle lengths $L^*_{(1)}$ and $L^*_{(2)}$, the $F_L(L)$ relations are computed and forwarded to the corresponding force generators (see Fig. 71). The muscle models together with the technical force generators and the sensory length feedback act as virtual muscles in this setup. The

---

[5]Note that the elasticity of the tendon is neglected in this transformation which simplifies the mathematical treatment. As far as biological systems are concerned, tendons are usually used as energy storage elements to generate force economically and play an important role for example in the hooping of a kangaroo. Muscles used for a pure production of mechanical power, like in the wings of a dove, are virtually devoid of tendons [23].
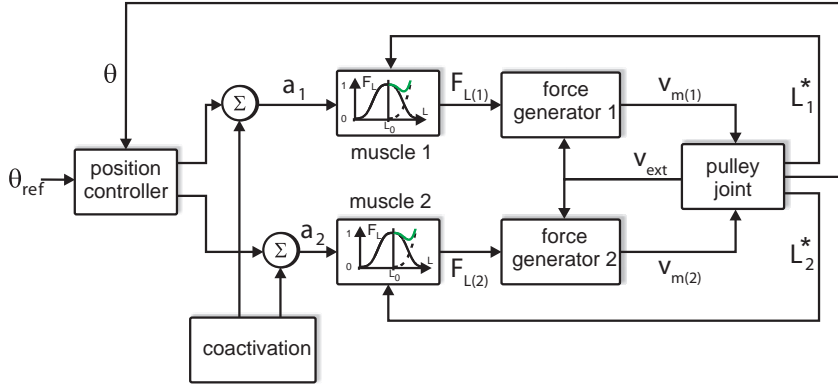
Figure 70: Schematic depiction of the position control loop employing two antagonistic force generators which mimic muscle characteristics and act as virtual muscles. The muscle co-activation block can be used to modulate the stiffness of the joint and is shown here for the sake of completeness but is not considered in this work.

activation signals a_1 and a_2 may also contain additional co-activation components which can be used in order to modulate the stiffness of the joint but this is not further considered in this work. For a detailed treatment of this topic, the reader is referred to [5].

In a tendon-driven joint, as the one in Fig. 68, the tendons have to maintain a certain minimal level of tension, since slack tendons cannot transmit forces. This requirement could be realized by adding a positive offset (bias) to muscle activations. However, this strategy is not followed here, since it obscures the actual role of co-activation in stiffness modulation and since the effect of such an offset varies in dependency of the actual activation level and muscle length. Moreover, tendon slack is a general problem in tendon-driven systems and as such should be solved independently of a bioinspired control strategy. These arguments speak for a solution on the level of the force controller. Fig. 71 shows how the force controller of chapt. 7 is extended in order to prevent tendon slack in the pulley joint of Fig. 68. In contrast to the force control scenario of chapt. 7, the sensor-tendon complex is not connected to a fixed wall but to the pulley joint and thus v_{ext} corresponds now to the tangential velocity of the points on the circumference of the moving pulley, i.e. the velocity of the tendon end at the pulley. Starting from an initial situation in which a tendon is under tension and integrating the velocity of the motor and the tangential velocity of the pulley, the displacements of the tendon ends at the motor x_m and at the pulley x_j can be computed. A slack condition is encountered if

$$x_{m(1)} + x_j < 0 \quad \text{or} \quad x_{m(2)} - x_j < 0, \tag{159}$$

for a positive motor displacement defined in the direction of v_m in Fig. 68(b) and a positive clockwise rotation of the joint. For some
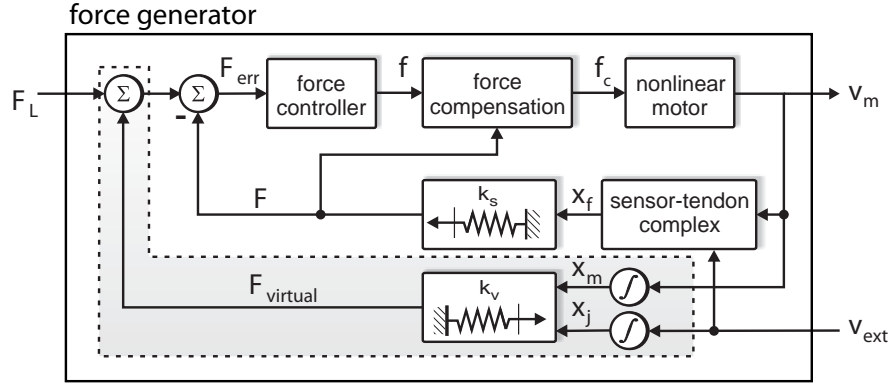
Figure 71: Force control architecture together with the concept of a virtual tendon (shaded area) preventing tendons from going slack. The above architecture is used as a force generator in Fig. 70. The actual force controller can be seen in Fig. 64.

initial angular joint position θ_0 in which tendons were under a minimal tension, x_j can be computed according to

$$x_j = R\frac{\pi}{180}(\theta - \theta_0) \tag{160}$$

in order to compensate for numerical integration errors. The positions of the motors can be also obtained directly, if position sensors are used. If a slack tendon is detected, the reference force for the force controller is modified by an additional term

$$F_{\text{virtual}(i)} = (x_{m(i)} - x_j)k_v. \tag{161}$$

The additional force term has a negative value by definition and causes the corresponding motor (i) to follow the movement of the joint as if pushing forces could be transmitted through tendons from the joint to the motor. Since no such tendons exist, this mechanism is called in the following a *virtual tendon*. The spring constant k_v of the virtual tendon determines how strong slack prevention is.

8.3 ANTAGONISTIC JOINT ARCHITECTURE

The position control architecture employing virtual muscles presented in the previous section has been so far considered from the conceptual point of view. This section addresses its practical realization and describes the actual technical implementation of an antagonistic tendon-driven joint with virtual muscles. The photograph of the complete setup is shown in Fig. 72. The setup consists of a pulley joint driven by two walking motors. Each motor is equipped with a non-contact linear position sensor/encoder (NANOS-Instruments GmbH, Hamburg, Germany). The sensor consists of a magnetic bar
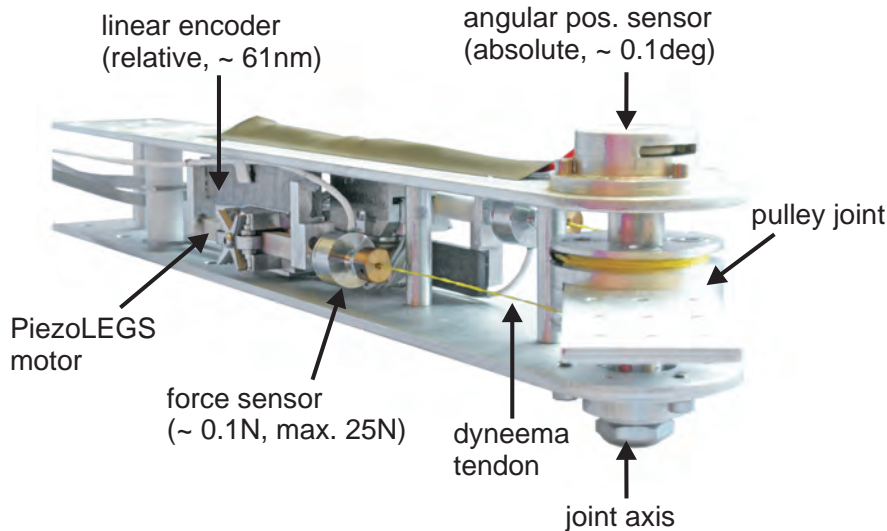
Figure 72: Photograph of the 1-DOF rotary joint consisting of a pulley actuated by two walking motors in an antagonistic arrangement. The sensory equipment providing signals necessary for slack prevention and muscle-like control is indicated. The second motor on the back side is not visible.

fixed to the drive rod and the sensor electronics mounted next to the bar on the motor housing. The encoder allows measurements of the drive rod position with an accuracy of 61 nm. Velocity measurements are obtained by numerical derivation. The amount of force acting on the drive rod is measured with a force sensor (ME-Meßsysteme GmbH, Hennigsdorf, Germany) with an accuracy of 0.1 N. The force sensor can measure pulling forces up to 25 N and has two mechanical connectors, one on each side. Additional elastic elements can be integrated into the actuators by connecting them in series to the force sensor. The direct tendon connection to the joint is realized with a high-performance polyethylene cord (DSM Dyneema B.V., EL Urmond, The Netherlands). The angular position of the joint is measured with a magnetic absolute position sensor (iC-Haus Germany, Bodenheim, Germany) with the resolution below 0.1 deg. The same architecture is also shown schematically in Fig 73. The hardware components consist of the pulley joint, two walking motors and the sensory equipment as well as the motor drive electronics (see chapt. 6 and appendix C). Formally, also the implementation of the waveform generator (see sect. 6.2) on the FPGA chip belongs to the hardware. The high level commands for setting joint position or muscle force are realized in an external application and transferred to the μC via a bus controller. The platform software on the μC is mainly responsible for bus communication, sensor reading, digital signal processing and force control. Note that if an analog power unit is used two motor drive electronics for each motor have to be used. With the digital

power unit which can generate 8 motor phases (cf. chapt. 6), one drive electronics is sufficient for the whole antagonistic setup.
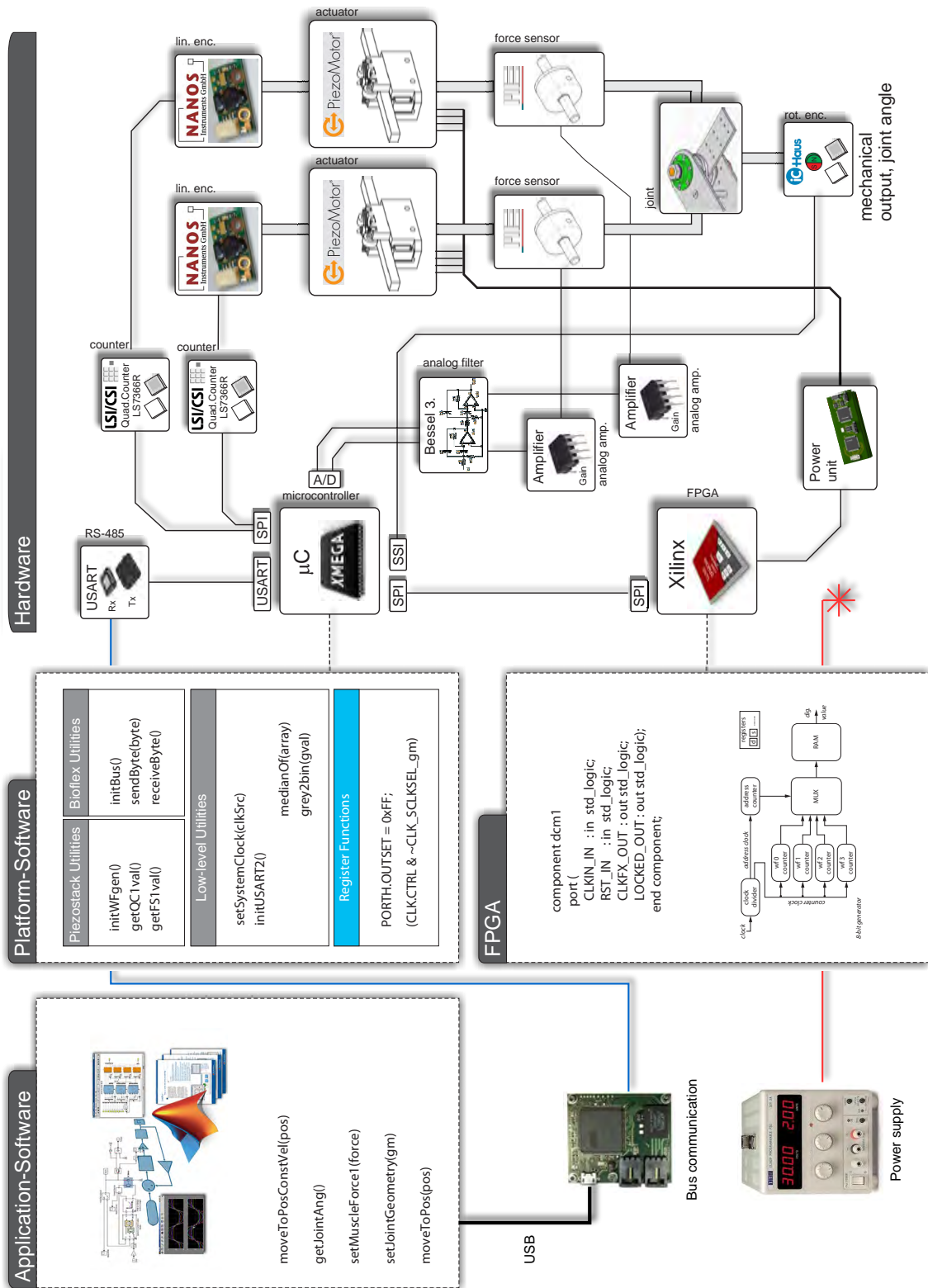
Figure 73: Iconic depiction of the different layers of the sensorized joint drive architecture. The hardware layer consists of the rotary joint actuated by two walking motors equipped with position and force sensors as well as the motor drive electronics indicated with some of its main components and the communication interfaces. The software consists of the low-level platform software in the μC and external application software transmitting commands to the μC through a bus.

8.4 POSITION CONTROL SCENARIO

The proof-of-concept that a small-sized piezoelectric motor can be successfully applied as a force generator in a biologically inspired robot joint consists in a simple positioning scenario. Specifically, the antagonistic joint is commanded to move to several reference positions in a stepwise manner. The position controller on top of the virtual muscles is implemented as a proportional controller with a constant gain G of 1. However, some adjustments to the simple proportional control scheme are necessary.

First, the output of the controller consists of two activations a_1 and a_2 in the domain $[0, 1]$ with 1 corresponding to full activation and 0 to no activation. Accordingly, the activations need to be limited to the valid range.

Second, the analog force sensors used in the joint are of the same type, but they are still two distinct entities suffering from manufacturing tolerances and measurement noise. This results in different sensory outputs even after a careful calibration. Accordingly, small position errors should not be weighted by the controller as much as large errors.[6]

And third, for a pure position control with no co-activation of the antagonistic muscles, the muscles should not work "against each other". Accordingly, only one muscle should be activated in dependency of the sign of the error.

Obviously, the position error is computed as

$$\epsilon_1 = \theta_{\text{ref}} - \theta. \tag{162}$$

This value is then transformed according to

$$\epsilon_2(\epsilon_1) = \epsilon_1 \big(1 - e^{-(\epsilon_1)^2}\big). \tag{163}$$

The net effect of the above transformation is the identity mapping for large errors and a flat smooth increase in error for small ϵ_1 values. In a next step, the transformed error is saturated

$$\epsilon_3(\epsilon_2) = \begin{cases} 1, & \text{if } \epsilon_2 > 1, \\ -1, & \text{if } \epsilon_2 < -1, \\ \epsilon_2 & \text{otherwise,} \end{cases} \tag{164}$$

and muscle activations computed as

$$a_1(\epsilon_3) = \begin{cases} 0, & \text{for } \epsilon_3 \geq 0, \\ -G\epsilon_3 & \text{otherwise,} \end{cases} \tag{165}$$

$$a_2(\epsilon_3) = \begin{cases} 0, & \text{for } \epsilon_3 \leq 0, \\ G\epsilon_3 & \text{otherwise.} \end{cases} \tag{166}$$

---

[6]Proportional weighting results in oscillations around the reference position due to noise and differences in sensor readings. To some degree, this is a natural phenomenon which can be observed for example when trying to keep one's own finger pointing precisely at a given point.
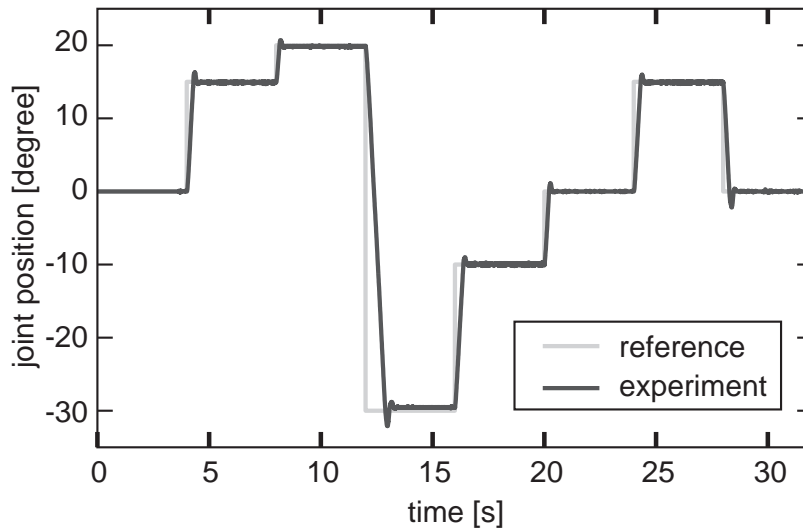
Figure 74: Step responses of the position controller acting on muscle-like force generators in a positioning task. The reference positions are indicated by a light-shaded while the experimental results by a dark-shaded curve.

Effectively, the simple proportional controller becomes adaptive in terms of error magnitude.

The computed levels of activation a_1 and a_2 are forwarded to the virtual muscles which generate pulling forces according to the $F_L(L)$ characteristics. Conceptually, it is clear that the joint will move in the direction of the larger of the two pulling forces. Since the proportional controller activates only one of the virtual muscles according to the sign of the position error, the joint has to approach the commanded positions.[7] Fig. 74 illustrates the results of the positioning tasks according to the control architecture from Fig. 70, if only the basic force-length relationship of the muscle model from sect. 8.2 is considered. F_{max} in (154) was set to 10 N which is the approximate stall force limit of the walking motor driven with the *force* waveform. As operating ranges for the muscles, L_{min} of 0.5 and L_{max} of 1.5 were chosen.[8]

The overall tracking performance is surprisingly good considering the fact that a proportional control was used and that the controller cannot influence the position of the joint directly but only through force generation with non-linear muscle characteristics. Relatively

---

[7]The not-activated virtual muscle still follows the movement of the joint keeping its tendon under minimal tension to prevent tendon slack, according to the concept of a virtual tendon in sect. 8.2.

[8]The operating ranges of *in vivo* muscles vary strongly depending on their function and the considered animal species. Burkholder [38] gives an exhaustive overview for vertebrate animals during movement. The values chosen for the experiment in this work are realistic but do not have any special meaning.

small overshoots can be observed in the measured data since there are no derivative nor damping terms in the controller. Also note that for the largest angular step from $20\,deg$ to $-30\,deg$ it takes about $1\,s$ for the joint to reach the new reference position. This observation is to be attributed to the finite speed of the motors. Nevertheless, a better positioning performance could be achieved with a pure position control scheme, not obscured by the intermediate muscle-like force generation, and possibly a more sophisticated position controller. However, neither a superb tracking performance, nor the role of muscle characteristics in the particular positioning task was the purpose of the experiment. In fact, the above experiment may be a starting point for further investigations concerning bioinspired control approaches utilizing small-sized piezoelectric motors.

8.5 DISCUSSION

This chapter presented an antagonistic 1-DOF robot joint driven by two virtual muscles. The joint consists of a pulley geometry with constant radius. The forces generated by the virtual muscles are transmitted to the joint via tendons. Each virtual muscle consists of a piezoelectric walking motor together with a force controller and a muscle model according to Hill [101]. The force controller, as introduced in chapt. 7, is augmented with the concept of a virtual tendon which prevents the tendons from going slack. It has been shown that a simple positioning task can be successfully realized with this setup even with a simple proportional position control acting on the virtual muscles.

The approach presented in this chapter was aimed at achieving a minimalistic robot joint actuated by two virtual muscles. This aim has motivated the choice of joint geometry which differs from natural geometries but offers a convenient mathematical treatment and does not obscure the influence of non-linear muscle properties on torque generation by variation in the length of lever arms [230]. Also the operating ranges of the muscles in the positioning experiment were not chosen referring to biological data for any particular species. These ranges were chosen to be symmetric about the muscle resting length and same for both muscles. It should be stressed that with the given technical system a positioning task could have been achieved in a better way by employing a direct position control without muscle mimetic. However, the presented approach was not meant as an evaluation of bioinspired control strategies but as a proof-of-concept that the walking piezoelectric motor can be used as a force generator in a feasible bioinspired control scenario – in contrast to the predominant application of piezoelectric motors in high precision positioning stages [117, 133, 145]. The feasibility of the presented approach is motivated by the small-size and high-force characteristics

of the walking motor which are especially important if a redundant number of actuators is used in an antagonistic setup. As far as the aspect of muscle-like bioinspired actuation is concerned, the author believes that the presented strategy offers substantial advantages over classical approaches when seen in the light of neurobionic control strategies [79, 182] or direct application of EMG-signals in prosthetic applications.

The concepts presented in this chapter are a foundation for further research. A natural extension of the simple control scheme would be to activate the muscles simultaneously. By these means, the overall stiffness of the joint could be modulated in addition to its position [103, 147]. In a future work, also the role of different muscle properties (like the force-velocity relationship) on positioning accuracy and stability could be examined.

9 | DISCUSSION

ABSTRACT

In this thesis, two novel motor models have been derived based on the analytic and experimental approach. Both models incorporate the effects of external loading on the performance of a walking piezoelectric motor. The analytic model was used in order to investigate an alternative drive strategy based on a bioinspired approach which significantly improves motor characteristics in terms of its force generation capabilities or maximal drive velocity. The experimental model was used to develop a load compensation strategy based on force feedback which restores the linearity in motor operation even under load. Based on the linearized model, an explicit force controller was designed whose theoretical and practical performance have been evaluated. In a next step, the walking motor together with the developed force control architecture was applied as a "virtual muscle" in a small-sized 1-DOF robot joint and tested in a simple positioning task. The feasibility of this kind of application has been confirmed. This chapter summarizes the main contributions of this thesis with regard to the objectives from chapt. 1. Additionally, this chapter contains recommendations for future research and possible applications of the walking piezoelectric motor, especially in the field of medical robotics.

9.1 CONTRIBUTIONS OF THE THESIS

The focus of this thesis was put on the development of dynamic models and bioinspired control strategies for the walking piezoelectric motor. In a broad sense three different use scenarios can be distinguished for dynamic models of a system [121], which have all been considered to a certain degree in this work. These are

- *analysis*,

- *identification*

- and *synthesis*.

As far as *analysis* is concerned, an analytic model has been developed as means to predict the future output of the walking motor, given its current state and the future inputs.

With regard to *identification*, an experimental model has been developed as means to identify the dynamics of the motor based on the measurements of its past inputs and outputs.

Finally, *synthesis* is concerned with the search for a new model which

can produce a desired output given a certain input. In this context, the creation of an antagonistic joint, a virtual muscle, a force controller or a bioinspired waveform generator can be seen as means to engineer new systems which are able to produce a desired output in terms of their tracking performance, force generation or stall-force maximization.

As far as the specific contributions of this work are concerned, these are recapitulated in this section together with the main objectives of this thesis according to their order defined in sect. 1.2.

Development of a motor model
The main objective of this work was to develop a model of the walking piezoelectric motor which can faithfully reproduce its dynamic behavior, especially under the influence of an external load. This objective was motivated by the desire to employ the motor in a force control scenario and the lack of any publicly available motor models of this kind. Macroscopically, the motor exhibits several non-linear phenomena including changing motor characteristics due to the choice of driving signals, frequency-dependent stall-force limits and decreasing drive velocity under load. Since the working principle of the motor relies on discontinuous frictional interaction between piezoelectric bimorph elements (legs) and a ceramic bar (drive rod), the practical derivation of a motor model is hampered by the difficulty to obtain experimental data of this interaction from a fully-assembled motor during its operation. In fact, the only measurements available to the author were the tangential position of the drive rod and the magnitude of the tangential load. Based on these measurements, two motor models have been developed within the scope of this thesis.

The first model (see chapt. 3) is based on the analytic approach and describes the low-level frictional interactions between the legs and the drive rod by means of several physically meaningful assumptions with ten unknown model parameters (see sect. 3.5). The feasibility of the modeling assumptions is confirmed in a global optimization process in which the unknown model parameters are identified and result in a motor model which can fully explain the experimentally measured data. Furthermore, clusters of physically meaningful parameter values are found as a side effect of the optimization process which is a strong indicator for a meaningful choice of model parameters.
The derived model is capable of reproducing the observed non-linear phenomena in the operation of the walking motor within the full bandwidth of its rated operation. In particular, the velocity of the motor does not change proportionally to the level of deflection of the legs when different driving signals are used. This phenomenon is explained by the introduction of a hysteretic nonlinearity, which is motivated by the existence of ferroelectric hysteresis in the piezo-electric material (see sect. 3.3.3). Also the frequency-dependent stall force limits and non-linear velocity decrease under load is faithfully

reproduced by the motor model. The nature of these phenomena is more complex since it involves frictional interactions in both the static and dynamic domains. For this reason, the choice of a suitable friction model is of paramount importance for the analytic motor model. Several extensions of the Coulomb friction model have been considered but could not reproduce the experimental data. These models incorporate a discontinuity at zero velocity crossing resulting in a strong variation of the frictional forces due to the transition between the static and dynamic part of the friction model. However, this behavior is an artifact of the oversimplified models. The transition between the static and dynamic regimes has been shown to be rather displacement- than velocity-dependent [168]. Furthermore, the increased level of static friction as compared to dynamic friction depends on the contact time between the surfaces [160]. These findings speak for the inapplicability of the discontinues models to describe the frictional phenomena in the walking motor, especially under high-frequency operation. The final choice of the LuGre friction model seems to be appropriate since the LuGre model reproduces the stick-slip transitions in a continuous manner. In this work, the LuGre model was extended in order to include the impact dynamics of the legs and the changing friction levels during the contact with the drive rod. The extended model accurately reproduces the non-linear velocity decrease under load which is to be attributed to the prevailing motor operation in the slipping regime. The nature of the frequency-dependent stall-force limits, although well reproduced by the model, is more difficult to explain. Hess and Soom [99], in their studies on the dynamic behavior of friction, show that the friction force is lower for decreasing than for increasing velocities. This leads to a hysteresis loop in friction force with varying velocity. The loop becomes wider at higher rates of velocity change. This effect corresponds to energy loss which is more severe for high driving frequencies and is reproduced well by the LuGre model. The macroscopic effect of decreasing stall-force limits in the walking motor could be attributed to this phenomenon. Beside reproducing the non-linear phenomena in motor operation, the analytic model also sheds light on other aspects affecting the performance of the motor. These include the resonant effects above 3 kHz drive frequency and the relationship between the shape of the driving signals and the maximal level of motor preload. The new insights can be utilized in order to develop an alternative motor-drive strategy beyond the region of rated operation (see next section) and improve the force generation characteristics of the motor. Furthermore, the analytic modeling strategy resulted in a collection of linear subsystems not exceeding second order with a clear indication of non-linear influences. The modular structure of the overall model allows an easy extension of the model to cover additional aspects of motor operation (cf. sect. 3.6), especially if low-level experimental data were provided.

Finally, the reproduction of low-level interactions between the legs and the drive rod in the physical model allows for its application in the optimization of driving signals [146] and the investigation of the feasibility of a biologically inspired drive approach (see below).

The second motor model derived in this work (see chapt. 4) is based on the experimental approach. Although the analytic model accurately describes the dynamics of the walking motor and the non-linear phenomena in motor operation, its disadvantage lies in its complexity and non-linear nature. This renders its online application in the prediction of motor response and in the design of a suitable force control strategy difficult. The experimental model is meant to address these issues. For this reason, several simplifying assumptions were made. First, only the holistic motor behavior in x dimension is considered. Second, the experimental model is valid only for one particular driving waveform (*force*). Third, the model is constrained to drive frequencies up to 2 kHz. These simplifications result in a linear model as long as a constant load is applied to the motor. However, since the main purpose of this model is the design of a linear force controller for the application in a force control scenario, the load cannot be assumed constant. The experimental model addresses this issue by including the non-linear load-velocity dependency with help of a frequency-normalized polynomial fit on the experimental data. The final model is non-linear but its linearity is eventually restored in chapt. 7 with help of a feedback linearization technique in the context of force controller design. Although the generality of the analytic model is lost, the experimental approach is well suited to describe the dynamics of the motor in most practical scenarios. The final model accurately describes motor behavior for drive frequencies below 2 kHz and load levels below 10 N. Finally, the simple structure of the experimental model allows for its application in the design of a linear force controller in chapt. 7.

Feasibility of a bioinspired drive approach
The second objective of this thesis was to investigate the feasibility of a bioinspired drive approach based on leg coordination mechanisms found in insects. This objective is motivated by the fact, that the motor in its current form can only be driven according to the walking principle (see sect. 2.4.1) in which the legs move in pairs receiving the same driving signals. This drive strategy is hard-wired in the motor and is supposed to ascertain a stable operation of the motor by always providing the drive rod with two supporting contacts to the legs. However, two reasons speak against this strategy. First, if more legs were allowed to contact the drive rod, the force generation capacity of the motor could be improved. This goal harmonizes with the application of the walking motor as a force generator followed in this work. Second, the waveform optimization strategy proposed

by Merry et al. [146] indirectly shows that even with a considerable flexibility in the design of the shape of the driving waveforms, only small improvements in the performance of the motor are possible. Thus Merry's approach can be seen as an evidence of the inherent limitations of the pairwise drive strategy. If a coordination mechanism existed which would ascertain a stable operation of the motor (i.e. at least two leg contacts at any given time) but would not rely on fixed pairwise relations among the legs, more legs could contact the drive rod resulting in a possibly stronger motor. This thesis has shown that such a mechanism exists and that the performance of the motor can be significantly improved not only in terms of force generation (up to 50 % higher stall force limits) but also in terms of maximal motor velocity (up to 100 % higher velocity, see chapt. 5). The proposed bioinspired solution relies on leg coordination mechanisms found in stick insects by Cruse et al. [47, 49]. Beside the idea of a non-standard application of the biological findings, the contribution of this work lies in a successful architectural mapping between the different morphologies of the original six-legged model and the walking motor. Moreover, a new strategy for waveform generation has been proposed which is intuitive and respects the admissible work area of the legs.

The evaluation of the bioinspired approach would not be possible without the physical model of motor dynamics developed in chapt. 3 of this thesis. In fact, the superiority of the bioinspired approach could only be shown in computer simulation since the real motor is hard-wired for the pairwise drive strategy. The necessary adjustments in the motor allowing the independent operation of all legs are minimal. The only component which has to be modified is the flex circuit connecting the external electrical phases to the legs of the motor. Unfortunately, this simple adjustment has to be done during the manufacturing process and was not possible for the author. Nevertheless, the theoretical results obtained in this work are reliable. This is motivated as follows. First, the biologically inspired coordination mechanism guarantees the stable operation of the motor. This can be easily seen by considering the number of legs contacting the drive rod at any time which is always greater than or equal two. Second, for low and moderate drive frequencies there are at least three or four legs contacting the drive rod most of the time which has to improve the load characteristics of the motor. Third, the shape of the waveforms can be varied flexibly which in the combination with independent control of the legs results in the largest possible waveform design flexibility. This fact should again be compared to the work by Merry et al. [146] since the motor model proposed by Merry, and used to evaluate the waveforms designed for the pairwise drive strategy, is less general than the physical motor model developed in this work. However, even with the less general model, Merry could show the accordance between the simulation and real experiment for the newly

designed waveforms. The new degree of freedom gained through the independent control of all legs can hardly result in a worse performance of the motor. In fact, the optimization process has shown that the performance of the motor improves rapidly even for a simple choice of the objective function. Considering the fact, that only two optimization criteria were pursued in this work – both resulting in a significant improvement in the performance of the motor – and that only one particular architectural mapping between the motor and the biological model with one particular selection of coordination rules were investigated, the proposed approach has the potential to further improve other aspects of motor performance.

Development of a force control strategy

The third objective of this work was the development of a force control strategy suitable for the application in a biologically inspired robot joint. In this context, two goals were followed. First, the experimental motor model from chapt. 4 was to be linearized in order to take advantage of the rich repertoire of mathematical tools for the design of a linear controller. Second, the controller to be developed was to consider the influence of series elasticity on force transmission.

The first goal was addressed by developing a load-compensation strategy based on force feedback in chapt. 7. The proposed strategy restores the linearity of motor operation even under load if moderate drive velocities up to 1 kHz and load levels up to 5 N are not exceeded. The experiments with active load compensation have shown that even though the effect of external force cannot be compensated completely for the whole operating range, the compensation keeps the motor velocity at a constant level for moderate drive frequencies and force levels. The above limits apply since the drive frequency of the motor cannot grow infinitely in order to maintain the desired drive velocity. Furthermore, for high levels of load the non-linear effects in motor operation due to friction gain in importance and cannot be compensated easily. For the moderate levels of load force, the compensated motor model can be considered linear.

The fulfillment of the second goal – design of a force controller – was based on the linearized motor model with load compensation. Although model based approaches were applicable, the actually designed controller is of PI type due to its better robustness against model uncertainties. The influence of series elasticities on force transmission was considered through the development of a sensor-tendon model incorporating the dynamics of the force sensor in series with an elastic tendon modeled as linear spring of a given stiffness. The designed controller was tested in the simulation and in real-world experiments by pulling on tendons of different elasticities and showing a good agreement between the model and the reality. It has been shown that the designed controller can be successfully applied in a force con-

trol scenario as long as the series elasticity remains at the effective level of 10 N/mm or above and the rate of change in the reference force does not exceed 10 Hz. It should be noted, that depending on the point of view, the designed force controller is either a linear PI type acting on a linearized motor or a non-linear adaptive controller incorporating the load compensation strategy acting on a non-linear motor. As an additional contribution of this work, the limits on the performance of a perfect force controller have been investigated theoretically in dependency of the effective stiffness of the force transmitting tendons. The performance of the designed controller lies at the level of 55 % of the theoretical limit.

Feasibility of a muscle-like force generation
The fourth objective of this work was to test the feasibility of a bioinspired application of the walking motor as a force generator in a small-sized robot joint. Two motors were supposed to actuate an antagonistic joint by transmitting pulling forces through tendons according to the concept in Fig. 3. The approach is bioinspired due to the antagonistic arrangement of the actuators and due to the idea that the motor together with a force controller and a suitable sensory feedback can mimic the force generation characteristics of a muscle. The long-term objective of such an approach is the possibility to control the technical actuators by means of myoelectric activity in prosthetic devices. Accordingly, a simple 1-DOF joint was built allowing for an antagonistic arrangement of the motors and the integration of position and force sensors as the pre-requirement for muscle mimicry based on the model by Hill (see chapt. 8). Additionally, in order to prevent tendons from going slack the force control architecture from chapt. 7 was extended with the concept of a virtual tendon. The force controllers were supposed to track reference forces according to the force-length relationship of a muscle for the given geometry of the joint, position of the "virtual muscles" and the levels of their activation. The final mechanical setup together with motor-drive electronics and control algorithms was tested in a simple position control scenario. Beside the audible operation of the motors, which could possibly be alleviated through damming in a practical application, the feasibility of the proposed strategy was confirmed. The joint could track the commanded positions with the largest overshoot below 5 % of the reference step signal which is a good result considering the complexity of the approach chosen. In fact, with the given technical system a positioning task could have been achieved in a better way by employing a direct position control without muscle mimetic. However, the strength of the proposed approach lies in the possibilities of its extension with regard to future applications and neurobionic control strategies. The contribution of this work lies in the novelty of the presented approach since piezoelectric motors have not been

employed as technical muscles or even force generators in any other work known to the author. This work confirms the feasibility of such application. The feasibility of muscle mimetic by means of control of technical actuators in general is a much broader question beyond the scope of this thesis. Presumably, a pure control-based approach without the integration of real elastic elements is not sufficient since no controller is fast enough to counteract a shock. Moreover, the exact role of joint geometry, co-activation of antagonistic muscles, non-linear muscle characteristics and reflexes in the generation of movement is still not sufficiently understood. Some of these open questions have been addressed recently in [5, 6]. The simplistic architecture with "virtual muscles" as presented in this work is a framework for further investigation of these topics.

Beside the above contributions, a small-sized motor-drive electronics as introduced in chapt. 6 has been developed within the scope of this work and the diploma thesis of Daniel Basa [14] as well as the Bachelor thesis of Tim Walther [219]. The newly developed electronics supersedes the commercially-available products due to its compactness and the possibility of waveform generation at much higher drive frequencies, above 50 kHz, as compared to commercial products. The latter feature is the foundation for the development of an alternative motor-drive strategy in overdrive mode (see next section). The circuit diagrams and the PCB layout images of the new electronics are included in appendix C.
Other minor contributions of this work are the development of an algorithmic and a practical approach for waveform generation at a desired drive frequency and of a motor direction switching strategy which is compatible with the bioinspired waveform generation approach (see chapt. 6).

9.2 FUTURE WORK

Beside the development of motor-drive electronics, the antagonistic joint and the practical control algorithms, the focus of this work was put on theoretical investigations with regard to motor model derivation and its bioinspired control. Accordingly, the focus of the future work is supposed to shift to practical work. Building on the investigations in this thesis the future work focuses on **motor design and control improvements** and **practical applications of the motor**.

Motor design and control improvements
The force generation capabilities of the walking motor are exceptional for a motor of its size and weight. However, at the same time the motor produces disturbing noises in the audible range and is relatively slow as compared to other motors of similar size. This impedes its
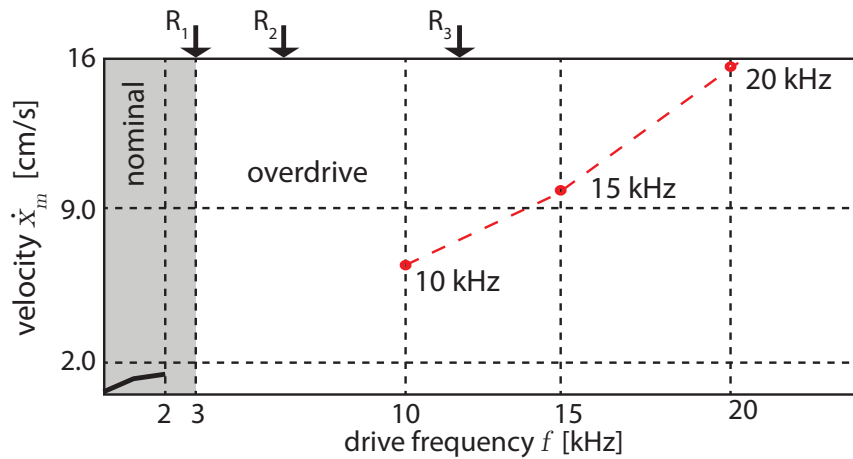
Figure 75: Motor velocity increase in the overdrive region of operation above 3 kHz for a sine-shaped driving waveform. Three sample measurements (red points) were done for a short-time operation at 10, 15 and 20 kHz resulting in up to ten times higher drive velocity as compared to the measurements in the nominal region of operation – black curve in the gray-shaded region. The locations of three resonant regions R_1-R_3 at 3, 6 and 12 kHz are indicated with arrows.

broader application. Based on the findings from the physical model of motor dynamics (see sect. 3.4.1) both of these deficiencies could be alleviated if the motor was operated at higher drive frequencies beyond the resonance region – i.e. in the overdrive region. Fig. 75 illustrates the idea which is supported by experimental data. If the motor is driven with drive frequencies above 10 kHz and the resonant regions, as predicted by the physical motor model and observed in the operation of the real motor, are avoided, the measured motor velocity is even ten times higher than the maximal rated velocity. Additionally, at such high drive frequencies no audible noises are generated. The difficulty in this kind of operation lies in the increased current consumption which leads to an increased temperature of the piezoelectric ceramics and may cause a permanent damage to the driving elements.[1] However, an intelligent control strategy is likely to allow the operation in the overdrive region. The high drive frequencies could be applied to the motor burst-wise for short periods of time. In addition, an integral current control or temperature monitoring strategy could be employed.

The performance of the motor can also be improved by allowing all legs to be driven independently according to the findings from

---

[1] In the ideal electrical approximation a piezoelectric element is a capacitor. The AC current flowing through a capacitor is proportional to its capacitance and to the rate of voltage change – i.e. the drive frequency in case of the walking motor. An increase in current flow results in temperature increase of the piezoelectric ceramics which leads to further current increase and further temperature increase. This positive coupling may lead to the loss of piezoelectric properties.

chapt. 5 and the discussion from the previous section. The theoretical framework is already given in this work and its practical realization depends only on a simple modification of the flex circuit within the production process of the motor. In this context, also alternative motor designs are possible which bear a stronger resemblance to the morphology of a stick insect. A six-legged motor with two rows of legs would not only be stronger but would additionally allow for a direct mapping between the leg coordination rules found in the stick insect and the legs in the motor. Further, as already mentioned in the discussion of chapt. 5, the direct piezoelectric effect could be used in order to actually sense the contact condition between the legs and the drive rod. In such case, the true feedback information would allow for the application of *Rule 5* and a better load sharing among the legs.

Practical applications of the motor
The construction of the 1-DOF rotary joint in this work was motivated by the possibility of a future bioinspired application in prosthetics, especially for small-sized prostheses of the hand. The size and weight of the motor allows for the integration of multiple motors in the forearm of an artificial hand and the force generation capabilities of the motor are sufficient to actuate artificial fingers. If motor-drive electronics could be miniaturized further (cf. digital amplification unit in chapt. 6), the characteristics of the motor improved (cf. stall-force maximization, overdrive region) and – most importantly – suitable biological control approaches developed, this kind of practical application becomes realistic.

Although the application of a piezoelectric motor in a force generation scenario is non-standard, it does not conflict with a more classical application which takes advantage of the precise positioning capabilities of piezoelectric motors. This feature is especially important in the field of medical robotics where the surgeon equipped with a high-magnification camera needs to precisely control the displacement of surgical tools. Fig. 76 illustrates several state-of-art robotic systems for minimally invasive (MI) surgery and the concept of an alternative system equipped with passively compliant arms and multiple-DOF tool holders. Each of these systems consists of several robotic arms which either hold surgical tools or a camera and enter the body of a subject through small openings called incision points. The entry point needs to be kept constant independently of the orientation of the tool in order not to further damage the organic tissue. The disadvantage of the systems (a) to (c) of Fig. 76 lies in the fact that a change in the orientation or immersion depth of the tool requires a new inverse kinematic solution and reconfiguration of a whole arm. This bears the risk of inter-arm collisions and makes a close placement of the different incision points difficult. Moreover, in order to keep the incision points constant, often a technically demanding, non-intuitive
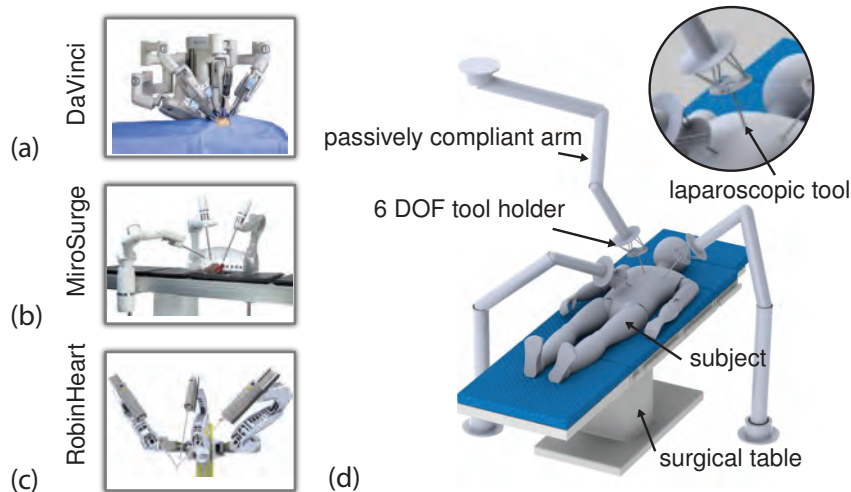
Figure 76: Robotic minimally invasive surgical systems including (a) the commercially available DaVinci [137] telerobotic system and a selection of research projects: (b) the MiroSurge [92] of DLR (Germany) and (c) the RobinHeart mc² [151] of the Foundation for Cardiac Surgery Development (Poland). (d) shows the conception of a surgical robot consisting of passively positionable arms and 6-DOF platforms for holding and adjusting the positions of laparoscopic tools.

calibration procedure has to be carried out. Some of these problems can be mediated e.g. by pre-operational planning and/or use of redundant arms. But this solutions depend on an increased complexity either on the hardware or the software side and do not support a more intuitive approach to the surgery. An alternative approach is shown in Fig. 76(d) where the MI-surgery robot consists as before of a few robotic arms, each of which holds now a 6-DOF platform to which a surgical tool is attached. In this setup the arms function mainly as passive holders for the actual tool holders. In other words, not the arms but the tool holders are responsible for orientation or immersion depth change of the tools. The main advantage of this setup lies in the absence of any large or unintuitive movements of the arms. In fact, a completely passive system with only a few degrees of freedom whose position could be fixed at a suitable location close to the incision point is sufficient for this kind of application. Any DOFs required for the tools are covered by the tool holders directly at the points of interest. The surgeon can shape the passive or actively compliant [3] arm into a suitable ergonomic configuration without the need of any special configuration procedure. From this point on, any additional movement of a relatively small magnitude is performed by the tool holder directly at the patient's body. The link between the idea of a surgical scenario as described above and the walking motor lies in the fact that the tool holder needs to be actuated. For this purpose small-sized and
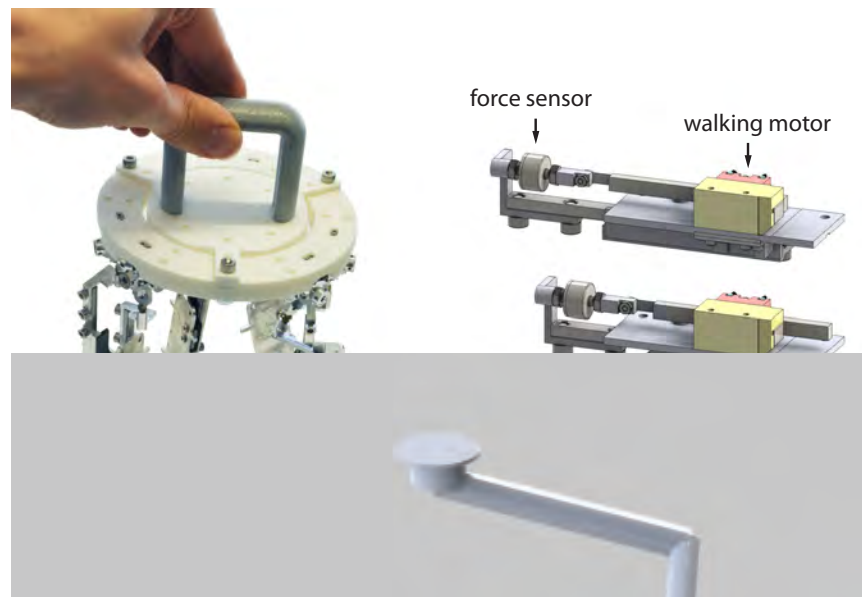
Figure 77: Concept and mechanical realization of a 6-DOF platform driven by the walking motors. (a) shows the passive mechanical construction of the platform supported by six "legs". (b) illustrates the principle of operation of an extensible platform leg when actuated by the walking motor. Each leg is equipped with position and force measuring sensors.

lightweight actuators are necessary in order not to increase the inertia of the robotic arm. Moreover, the actuators have to be able to generate large enough forces in order to hold the surgical tools together with their actuation units and allow for precise displacements. The velocity of the actuators is of second-rank importance. The walking motor is likely to fulfill this kind of practical requirements and offers the additional advantage of EMR-compatibility which is important in medical applications. In fact, a small-sized 6-DOF platform has been already built by the author and is depicted in Fig.77. The platform can change its orientation and position in all dimensions of the six-dimensional space by changing the length of the platform legs according to the inverse kinematic solution of a 6-UPS Stewart platform [52]. The passive mechanical construction shown in Fig.77(a) can be actuated by the walking motors according to the idea shown in Fig.77(b). Each platform leg is equipped with a force sensor. This makes this setup capable of a six-dimensional force measurement which can be used for example to prevent an extensive stress on the tissue at the incision point or to implement an impedance controller. The implementation of suitable control strategies for the 6-DOF platform is the actual work in progress.

A | APPENDIX A

ABSTRACT

This appendix contains a detailed description of the manufacturing processes involved in the production of the piezoelectric legs which are used as driving elements in the walking piezoelectric motor. The description is based on an extensive literature research. The actual production process may differ marginally.

The production process of the driving elements of the walking piezoelectric motor consists of several steps depicted schematically in Fig. 78. The following textual description is based on an extensive literature research carried out by the author [209, 203, 208, 185, 186, 132].

In a first step of the production process, an appropriate PZT ceramic powder composition (see sect. 2.2.2) has to be obtained. For this purpose relevant amounts of PbO, ZrO_2 and TiO_2 oxides together with other additives (doping) are weighed, mixed in water with a ball mill, dried and calcined at a high temperature of 800-1000° C.[1] Then a ball mill is used again to grind the mixed material into fine powder. Particle shape, size, distribution and compositional uniformity are the key factors to be controlled in the raw powder in order to realize reproducibility of piezoelectric characteristics [208]. The difficulty in the oxide-mixing and subsequent milling technique lies in the fact that particle sizes below $1\,\mu$m cannot be obtained, contamination by milling media occurs and compositional uniformity is inferior to e.g. wet chemical methods [208]. However, this method has proved to be a good compromise between low costs, reproducibility and good piezoelectric properties [203, 208]. For the walking piezo motor, soft-type PZT powder (EDO EC-76) with the grain size of $1.5\,\mu$m is used.

In a next step, the ceramic powder is mixed with a solvent (toluene) and dispersant/plasticizer (Ferro 704SMO1201 PT) to prevent settling, and is then ball-milled for 16 hours. Subsequently, a polymer binder (Ferro resin solution B74001) is added and the solution ball-milled again for 1 hour. In this way a ceramic slurry is obtained in which the powder body accounts for $50 - 60\,\%$ of the overall volume in the polymerized matrix [209]. The slurry is passed through a fine-mesh fabric and cast on a glass plate coated with an adhesive plastic film

---

[1]Calcination refers in this context to a thermal treatment process in the presence of oxygen with the goal to purify the ceramic powder from chemical impurities.

Raw oxide powders

weighing,
mixing,
milling,
calcination

PZT powder

binder, dispersant
solvent mixing

Ceramic slurry

tape casting
drying

Green sheet

internal electrode
screen printing,
drying and patterning

cutting

Green chip(s)

isostatic pressing
laminating

Green multilayer element(s)

sintering
binder evaporation

Multilayer element(s)

specific finishing
poling
ext. electrode application

Multilayer actuator(s)

Figure 78: Flowchart of the fabrication process of a multilayer actuator according to a variation of the tape-casting method. Boldface text indicates the fabrication stages and italic text the processes involved in the transition from one stage to another.

(Nitto tape SWT20). Either a tape caster or a special straight blade (*doctor blade*) is used to distribute the slurry evenly over the surface of the carrier. The normal distance to the carrier determines film thickness of the deposited layer. In case of the walking piezo motor the thickness is 56 μm. The casted layer is then dried at an elevated temperature and the solver evaporates. The layer becomes rubber-like (i.e. it has the elastic flexibility of a rubber or synthetic leather) and is called a *green sheet*. An electrode pattern is screen-printed on the green sheet using Au/Pd paste (Ferro E-1192) through a mask (screen). The paste consists of a fine metallic powder, polymeric binder and solver. The mask is a woven polyester screen (Saatilene Hitech 120.34) which can be penetrated only at certain spots. The paste is printed by a squeegee which presses it through the mask. Then the paste is dried and forms an additional 5 μm layer on the green sheet. This layer is milled with a fine milling tool to a desired shape (patterning) and forms an internal electrode.

The process is repeated and new green sheet and electrode layers are deposited on top of each other. However, the electrode patterns alternate with every layer between the ground and phase electrodes, whereas the phase electrodes are partitioned into two bimorph halves. Different electrode patterning techniques exist [209]. In case of the walking piezoelectric motor, conventional interdigital electrodes are used. After several (up to 100) PZT and electrode layers have been deposited the green sheet is cut into an appropriate shape – the *green chips*. Multiple green chips are laminated and pressed together using a hot press. The pressure of 47 MPa is applied for 2 minutes at room temperature followed by another 2 minutes at 60° C and 21 MPa. The obtained green elements are then heated to about 500° C to let the

binder evaporate in a N-rich atmosphere. After debinding the green elements are sintered at $1200 - 1300°\,$C for 1-2 hours in a furnace in Pb-saturated air.[2] During this process, the atoms in the powder particles diffuse across the boundaries of the particles, fusing the particles together and promoting crystal bonding without significant distortion of the molded shape. The process eliminates pores and increases ceramic density leading to a greater structural stiffness and fracture toughness [208]. The properties of the ceramic strongly depend on the number of pores and the grain size, as the grains grow and change shapes during sintering, besides the actual powder composition. Grain size of about $4\,\mu$m is considered optimal [203]. After sintering, the multilayer elements are not called *green* anymore. An Ag-paste (Cerdec) with a polymeric binder is deposited on the sidewalls connecting to the internal electrodes and sintered at a lower temperature $(650°\,$C) forming the external electrodes. The other faces are coated with a water-proof spray to prevent flash over. Four of the multilayer elements are glued to an aluminum holder with an adhesive (Epo-Tek 353ND) and diamond-polished to an equal height. A flexible circuit board is soldered with a Pb/Sn solder (Multicore Sn62RA10BAS86) to the external electrodes. Then the multilayer elements are poled by applying a 50 V voltage to all phases for 10 minutes at room temperature. Due to the remanent strain after poling, the by now multilayer actuators (legs) are diamond-polished again and aluminum oxide plates (caps) are glued on top of them to serve as wear resistant contact surfaces (friction pads) against the slider.

At this point the drive unit with four legs is ready and can be placed inside the motor housing. Before assembling the motor completely as described at the beginning of this section, an additional step is taken. The space between the legs in the basin of the lower housing, is filled with a resin-like substance to protect the drive elements from dust and humidity as well as to provide an additional support for the glued legs. Besides its protective function this resin-like substance has a strong effect on the damping characteristics of the moving legs as shown in sect. 3.5 of chapt. 3.

---

[2]After debinding the *green* bodies are sometimes called *brown*.

B | APPENDIX B

ABSTRACT

This appendix shows the derivation of the algorithm for the computation of a solution to the Bézout's identity. The algorithm can be used to compute an exact solution in finite time if all coefficients in the identity are integer numbers. It delivers an approximative integer solution for real coefficients.

B.1 BÉZOUT'S IDENTITY

Bézout's identity is named after the French mathematician Étienne Bézout and is a special case of a linear Diophantine equation. It states that for two integer numbers a and b with a or $b \neq 0$ and (a, b) being the greatest common divider of a and b, there exist two integer numbers ξ and η such that the following identity holds

$$(a, b) = a\xi + b\eta. \tag{167}$$

Proof [1]
Let D be a set of all natural numbers [2] having the form $ax + by$. The set is not empty since assuming e.g. $a \neq 0$, it has to contain at least one positive number out of

$$a = a \cdot 1 + b \cdot 0, \quad -a = a \cdot (-1) + b \cdot 0. \tag{168}$$

Let d be the smallest number in D, then for some ξ and η

$$d = a\xi + b\eta \tag{169}$$

and it holds that $n \geq d$ for any other number n in D. To show that $ax + by$ is divisible by d without a remainder for all integer x and y, let the opposite be assumed. This means that for some x_0 and y_0 the following equality has to be true

$$k = qd + r = ax_0 + by_0, \tag{170}$$

where $r \in \{1, 2, \ldots, d - 1\}$ is the remainder and q the quotient. From (169) and (170) it follows that r is a natural number smaller than d and

$$r = k - qd = ax_0 + by_0 - q(a\xi + b\eta) = ax + by \tag{171}$$

---

[1] The proof is compiled from [184].
[2] Adapting the traditional definition of natural numbers as positive integers.

for $x = x_0 - q\xi$ and $y = y_0 - q\eta$. But this means that r belongs to D and is smaller than d which contradicts the definition of D. Thus the expression $ax + by$ is divisible by d for all integer x and y. Further, both

$$a = a \cdot 1 + b \cdot 0 \quad and \quad b = a \cdot 0 + b \cdot 1$$

are divisible by d so d is their common divider. To proof that d is in fact their greatest common divider, let δ be a common divider of a and b. In this case there exist integer numbers t and u such that $a = t\delta$ and $b = u\delta$. It follows that

$$d = a\xi + b\eta = (t\xi + u\eta)\delta \tag{172}$$

and thus $\delta|d$, i.e. δ is a divider of d. So d is divisible by any other common divider of a and b. And because $d > 0$ a and b cannot have any common divider greater than d, i.e. $d = (a, b)$.

The above considerations show that for integer numbers a, b and m

$$ax + by = m \tag{173}$$

m has to be a multiple of $d = (a, b)$ if (173) is to be solvable in integer numbers. To show that this condition is not only necessary but also sufficient, let

$$a = a'd, \quad b = b'd \quad and \quad m = m'd.$$

a' and b' are obviously coprime integers and we have

$$a'\xi + b'\eta = 1. \tag{174}$$

If we can find ξ and η which solve (174) (see next section) and set

$$x_0 = m'\xi, \quad y_0 = m'\eta \tag{175}$$

it follows that

$$ax_0 + by_0 = a'dm'\xi + b'dm'\eta = (a'\xi + b'\eta)m = m \tag{176}$$

which shows $(a, b)|m$.
QED

B.2 EUCLIDEAN ALGORITHM AND CONTINUED FRACTIONS

From the previous section we know that to solve the Bézout identity it is sufficient to find integer numbers ξ and η which satisfy (174). Note that if one integer solution can be found, infinitely many other integer solutions follow from equating (173) and (176).

The question remains how to find ξ and η. This can be done by

employing the Euclidean algorithm or equivalently finding the continued fraction representation of a/b and performing some additional computations. This method is sketched shortly below. Later in this section, the continued fraction representation is used as a formal way of deriving the solution formulae. Finally, a simple algorithm for solving (174) is given in sect. B.3 as a Matlab [3] program.

The Euclidean algorithm is a method for finding the greatest common divider (a, b) of two integer numbers a and b and is named after the Greek mathematician Euclid who first described it in books 7 and 10 of his *Elements* [93]. Although well known, the algorithm is sketched here shortly in order to set up the notation and show its relation to finding the continued fraction expansion of a number. Let $a, b \in \mathbb{Z}$, q the quotient and r the remainder of the a by b division

$$a = qb + r. \tag{177}$$

From (177) it follows that every common divider of a and b has to be a divider of r as well. Thus $(a, b) = (b, r)$. By setting

$$a = n_0, \quad b = n_1, \quad r = n_2,$$

we have the following equalities for successive divisions

$$\begin{aligned} (n_0, n_1) &= (n_1, n_2), \\ (n_1, n_2) &= (n_2, n_3), \\ &\cdots\cdots\cdots \\ (n_{k-1}, n_k) &= (n_k, n_{k+1}), \end{aligned} \tag{178}$$

where n_3 is the remainder from the division of n_1 by n_2 and so on. Because $n_1 > n_2 > \ldots \geq 0$, this series of integers has to be finite. The last number $n_k \neq 0$ in the series (i.e. the following $n_{k+1} = 0$) is the greatest common divider of n_0 and n_1 (or a and b).

By memorizing the successive quotients $q_1, q_2, \ldots, q_k$ in the divisions of (178) according to

$$\begin{aligned} n_0 &= q_1 n_1 + n_2, \\ n_1 &= q_2 n_2 + n_3, \\ &\cdots\cdots\cdots \\ n_{k-1} &= q_k n_k \end{aligned} \tag{179}$$

or equivalently

$$\begin{aligned} \frac{n_0}{n_1} &= q_1 + \frac{1}{\frac{n_1}{n_2}}, \\ \frac{n_1}{n_2} &= q_2 + \frac{1}{\frac{n_2}{n_3}}, \\ &\cdots\cdots\cdots \\ \frac{n_{k-1}}{n_k} &= q_k. \end{aligned} \tag{180}$$

---

[3] The MathWorks Inc., Natick, MA, USA.

we also find the continued fraction expansion of $n_0/n_1 = a/b$ as

$$\frac{n_0}{n_1} = q_1 + \cfrac{1}{q_2 + \cfrac{1}{q_3 + \cfrac{1}{\ddots + \cfrac{1}{q_{k-1} + \cfrac{1}{q_k}}}}}. \tag{181}$$

Clearly, we can express every rational number n_0/n_1 in the above form with a finite number of terms [184]. In a more compact notation we can also write

$$q_1 + \frac{1|}{|q_2} + \frac{1|}{|q_3} + \ldots + \frac{1|}{|q_k} \tag{182}$$

or

$$[q_1; q_2, q_3, \ldots, q_k]. \tag{183}$$

Note that the fractional terms show up after a semicolon in the latter representation. Turning back to (174), setting $n_0 = a'$ and $n_1 = b'$, and computing either the series of quotients or the continued fraction expansion of n_0/n_1 we find at step k that $n_k = 1$. We can write

$$n_k = n_{k-2} - q_{k-1}n_{k-1} = 1 \tag{184}$$

and by successive reduction of terms as in

$$n_{k-1} = n_{k-3} - q_{k-2}n_{k-2}$$

we realize that

$$n_k = -q_{k-1}n_{k-3} + (1 + q_{k-1}q_{k-2})n_{k-2}$$

which after a series of further substitutions leads in the end to

$$n_k = 1 = n_0\xi + n_1\eta$$

for some ξ and η consisting of a combination of quotients $q_i \in \{1, \ldots, k-1\}$. This solves the Bézout's identity with integer coefficients.

Let us express the above findings in a more general framework related to continued fractions. Continuants or continuant polynomials are the key to the study of continued fractions [83]. The continuant polynomial $K_n(x_1, x_2, \ldots, x_n)$ having n parameters is defined by the following recurrence

$$K_0() = 1;$$
$$K_1(x_1) = x_1;$$
$$K_n(x_1, x_2, \ldots, x_n) = x_n K_{n-1}(x_1, \ldots, x_{n-1}) + K_{n-2}(x_1, \ldots, x_{n-2}). \tag{185}$$

It can be easily shown by induction [184] that the continued fraction

$$[a_0; a_1, a_2, \ldots, a_n] \tag{186}$$

can be equivalently expressed as

$$K_{n+1}(a_0, a_1, \ldots, a_n) / K_n(a_1, a_2, \ldots, a_n) = \frac{P_n}{Q_n} = R_n \tag{187}$$

where R_n is called the n-th convergent to the continued fraction (186) and $n \in \mathbb{N} \cup 0$. We also have [184]

$$(-1)^k = P_{k-1}Q_k - Q_{k-1}P_k \quad \text{for} \ \ k \in \{1, 2, \ldots, n\}. \tag{188}$$

We will use relations (185)-(188) in showing how continued fraction expansion can be used to (approximatively) solve the Bézout's identity with arbitrary real coefficients. But first, let us introduce an alternative way of finding the continued fraction expansion of a rational number q to the one shown in (179)-(180). Assume that we know the expansion to be

$$q = [a_0; a_1, a2, \ldots, a_n]. \tag{189}$$

By defining

$$x_k = [a_k; a_{k+1}, \ldots, a_n] \tag{190}$$

for $k \in \mathbb{N} \cup \{0\}$ (i.e. $x_0 = w$ and $x_n = a_n$) and knowing that $a_1, \ldots, a_n$ are natural numbers we see that $a_k < x_k$ and $x_k > 1$. We also see from the above definition that (190) can be expressed as

$$x_k = a_k + \frac{1}{x_{k+1}}. \tag{191}$$

Thus, from $a_k < x_k < a_k + 1$ and $x_{k+1} > 1$ we conclude that $a_k = \lfloor x_k \rfloor$ [4] and

$$x_{k+1} = \frac{1}{x_k - \lfloor x_k \rfloor}. \tag{192}$$

Using (192) and the equality $a_k = \lfloor x_k \rfloor$ we can compute all terms in (189). For a rational number the number of terms in (189), or in other words the series $\{a_n\}$, is finite (see above). Sierpiński [184] also shows that the expansion (192) has an unique normal form, i.e. there is only one possible finite expansion of q with $a_n > 1$. Now, if a real number p is irrational, the series $\{x_n\}$ and $\{a_n\}$ have to be infinite since we always have

$$x_{k+1} > 1$$

due to (192) and $0 < x_k - \lfloor x_k \rfloor < 1$. Let us show that $R_n = [a_0; a_1, a_2, \ldots, a_n]$ converges to p for $n \to \infty$. From (191) we can show that

$$x_0 = [a_0; a_1, a_2, \ldots, a_{n-1}, x_n]. \tag{193}$$

---

[4]With $\lfloor x_k \rfloor$ being the greatest integer not larger than x_k; also called the *entier* or *floor* function.

Recalling (185) and (187) we have

$$R_n = \frac{P_{n-1}a_n + P_{n-2}}{Q_{n-1}a_n + Q_{n-2}}$$

which after substituting a_n by x_n transforms to

$$x_0 = \frac{P_{n-1}x_n + P_{n-2}}{Q_{n-1}x_n + Q_{n-2}} \tag{194}$$

in accordance with (193). Because (194) is valid for all natural n we also have

$$x_0 = \frac{P_n x_{n+1} + P_{n-1}}{Q_n x_{n+1} + Q_{n-1}}$$

and thus

$$x_0 - R_n = \frac{P_n x_{n+1} + P_{n-1}}{Q_n x_{n+1} + Q_{n-1}} - \frac{P_n}{Q_n}.$$

Together with (188) we arrive at

$$x_0 - R_n = \frac{(-1)^n}{(Q_n x_{n+1} + Q_{n-1})Q_n}. \tag{195}$$

Because $x_{n+1} > a_{n+1}$ we may conclude

$$|x_0 - R_n| < \frac{1}{(Q_n a_{n+1} + Q_{n-1})Q_n} = \frac{1}{Q_{n+1}Q_n}. \tag{196}$$

To show the convergence of R_n to $p = x_0$ (or of the left-side term in (196) to 0), let us show that $Q_k \geq k$. For $k = 1$ it is trivial because $Q_1 = a_1$ is a natural number. The same holds true for $k = 2$ according to (185) and (187). Now, let us assume $Q_k \geq k$ for $k = n$ and $n \in \mathbb{N}$. Because Q_{n-1} and a_{n+1} are natural numbers we have

$$Q_{n+1} = Q_n a_{n+1} + Q_{n-1} \geq Q_n + 1 \geq n + 1,$$

which proves $Q_k \geq k$ for $k = n + 1$. Thus, by induction $Q_k \geq k$ is true for all natural k and we finally conclude that

$$|x_0 - R_n| < \frac{1}{n(n+1)} \tag{197}$$

which shows that R_n converges to p for $n \to \infty$.

In order to find a solution to (174) and thus to the Bézout's identity, let us write

$$\frac{P_n}{Q_n} = \frac{a'}{b'}.$$

Since a' and b' are coprime, it has to be

$$P_n = \pm a', \quad Q_n = \pm b', \tag{198}$$

where the upper sign is taken for a positive b and the lower sign otherwise. This follows from the fact that the expansion (189) has a negative coefficient a_0 for $w < 0$, i.e. $\text{sign}(a'/b') = -1$ and in this case P_n is negative. On the other hand, Q_n is always positive since it does not contain the term a_0.

Knowing the sign of a' and b' beforehand we may sketch the following sign table

a'	+	+	-	-
b'	+	-	+	-
P_n	+	$\ominus$	-	$\oplus$
Q_n	+	$\oplus$	+	$\oplus$

where the encircled signs do not correspond to their counterparts in the first two rows. A multiplication of P_n and Q_n with sign b restores the missing correspondence. From (188) we find out now that

$$\pm(-1)^n P_{n-1}b' \mp (-1)^n Q_{n-1}a' = 1, \tag{199}$$

which shows that

$$\xi = \mp(-1)^n Q_{n-1} \text{ and } \eta = \pm(-1)^n P_{n-1} \tag{200}$$

and solves (174). However, note that so far we have no explicit knowledge about the quality of this solution for irrational numbers. For issues connected with irrational numbers, the interested reader is referred to the theory of Diophantine approximations [128] and Padé approximants [12].

B.3 ALGORITHMIC SOLUTION TO BÉZOUT'S IDENTITY

The computation of an approximative solution to (174) is given below in form of a simple Matlab program. The algorithms used below are kept in a simple (not optimized) form in order to retain a clear correspondence to the mathematical theory from the previous sections. Let us redefine (174) as

$$ax + by = 1 \tag{201}$$

in order to contain ASCII characters only (i.e. $x = \xi$ and $y = \eta$). The program consists of two function: *cfe()* which computes the first n coefficients in the continued fraction expansion of a/b and *bezout()* which uses the values returned by *cfe()* in order to solve (201) in integer numbers.

```matlab
1  function as = cfe(a,b,n)
2  %%% cfe - finds n first coefficients of the
3  %          the continued fractions expansion
4  %          of a/b
5  %
6  %    as = cfe(a,b,n) returns the nmax coefficients
7  %            in a row vector as. For a rational a/b
8  %            length(as) may be < n.
9  %
10 %    Examples
11 %        cfe(1071,462,10)  returns [2,3,7]
12 %        cfe(0,5,10)       returns 0
13 %        cfe(23.4,pi,5)    returns [7,2,4,1,2]
14 %
15 %    See also floor.

16
17 assert(b~=0,'Division by 0.');

18
19 % initializes the first terms
20 xp = a/b;
21 ap = floor(xp);
22 as = [ap];

23
24 % sets threshold for finite precision computation
25 eps = 1e-6;

26
27 idx = 1;
28 while (idx<n)
29     tmp = xp-floor(xp);

30
31     % finite solution found
32     if tmp<eps, break; end

33
34     xn = 1/tmp;
35     an = floor(xn);
36     xp = xn;
37     idx = idx+1;
38     as(idx) = an;
39 end

40
41 % gets the normal expansion
42 if (idx>1) && (as(idx)==1),
43     as(idx-1)=as(idx-1)+1; as(idx)=[];
44 end
```

```matlab
function [x,y,e] = bezout(a,b,n)
%% bezout - finds an approximative solution
%           to ax+by=1 in maximally n steps
%
%   [x,y,e] = bezout(a,b,n) returns the integers
%             x, y and an error e for which
%             ax+by-1 = e.
%
%   Examples
%       [x,y,e] = bezout(421,111,10)
%               returns [-29,110,0]
%       [x,y,e] = bezout(771,-23,5)
%               returns [2,67,0]
%
%   See also cfe.

% get the first n or less coefficients from cfe
as = cfe(a,b,n);
n = numel(as);

% sign(b) determines the solution case
sb = sign(b);

% allocate memory for P and Q
ps = zeros(1,n);
qs = zeros(1,n);

% note the 1-based indexing in Matlab
ps(1) = as(1);
qs(1) = 1;

x = sb*qs(1);
y = (-sb)*ps(1);

if n>1
    ps(2) = as(1)*as(2)+1;
    qs(2) = as(2);
    x = -(sb)*qs(1);
    y = sb*ps(1);
end

if n>2
for ix=3:n,
    ps(ix) = ps(ix-1)*as(ix) + ps(ix-2);
    qs(ix) = qs(ix-1)*as(ix) + qs(ix-2);
end
```

```
47  x = (-sb)*(-1)^(n-1)*qs(n-1);
48  y = (sb)*(-1)^(n-1)*ps(n-1);
49  end
50
51  e = a*x+b*y-1;
```

For practical applications upper bounds on the solution (x, y) have to be set in order to terminate the computation for an irrational a/b since then Q_n and P_n grow infinitely for $n \to \infty$. Furthermore, a solution to (174) can be obtained more efficiently using a fast implementation of the *Extended Euclidean Algorithm* [124] which solves the Bézout's identity using the relation (184).

C | APPENDIX C

ABSTRACT

This appendix contains the circuit diagrams and PCB layout images of the motor drive electronics which has been developed within the scope of this thesis and the final theses of Daniel Basa and Tim Walther [14, 219].
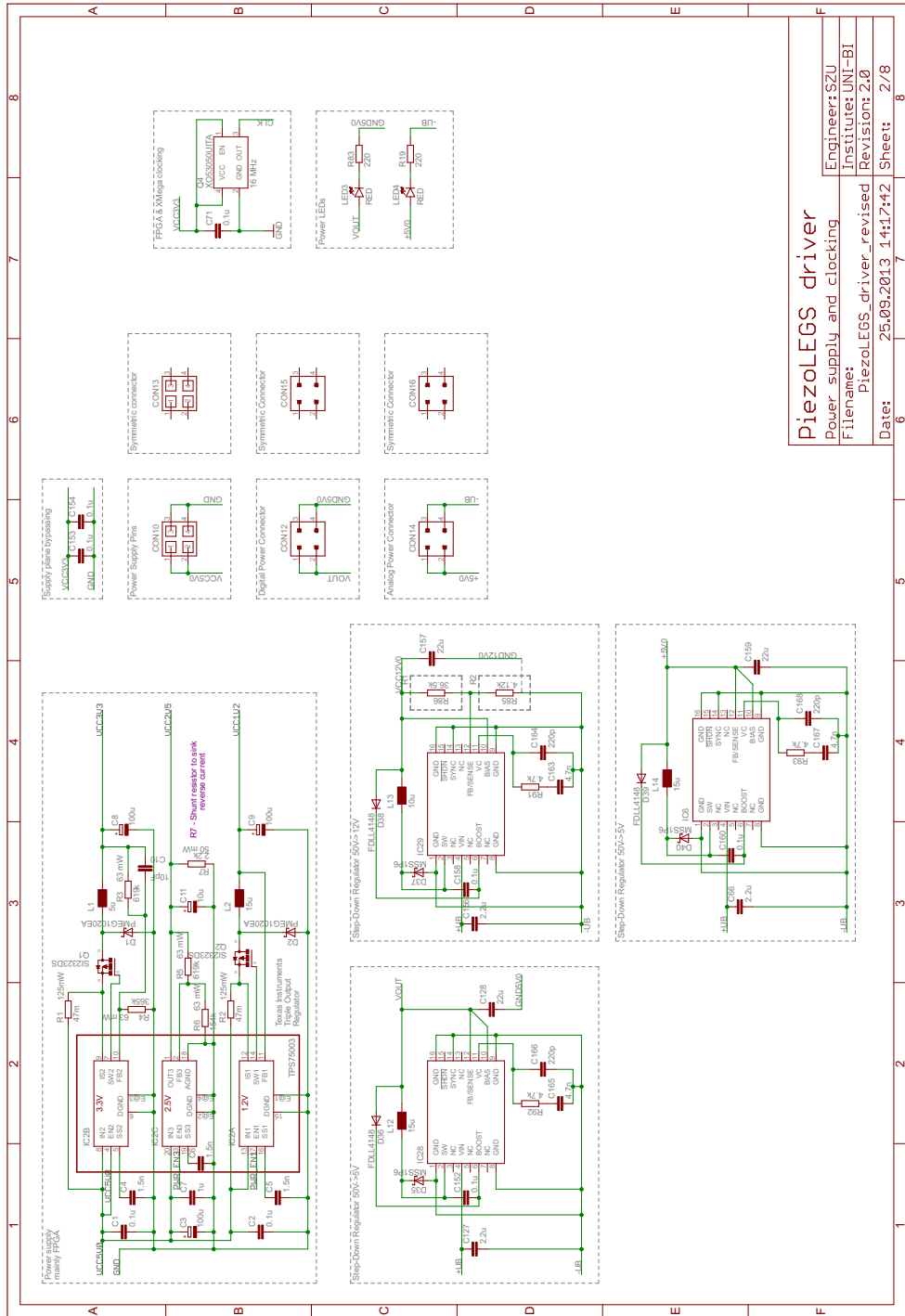
Figure 79: Circuit diagram: FPGA I/O configuration after [14].

Figure 80: Circuit diagram: power supplies and clock generation after [14].

Figure 81: Circuit diagram: Microcontroller I/O and SD interface after [14].

Figure 82: Circuit diagram: inter-board connectors and communication interface after [14].
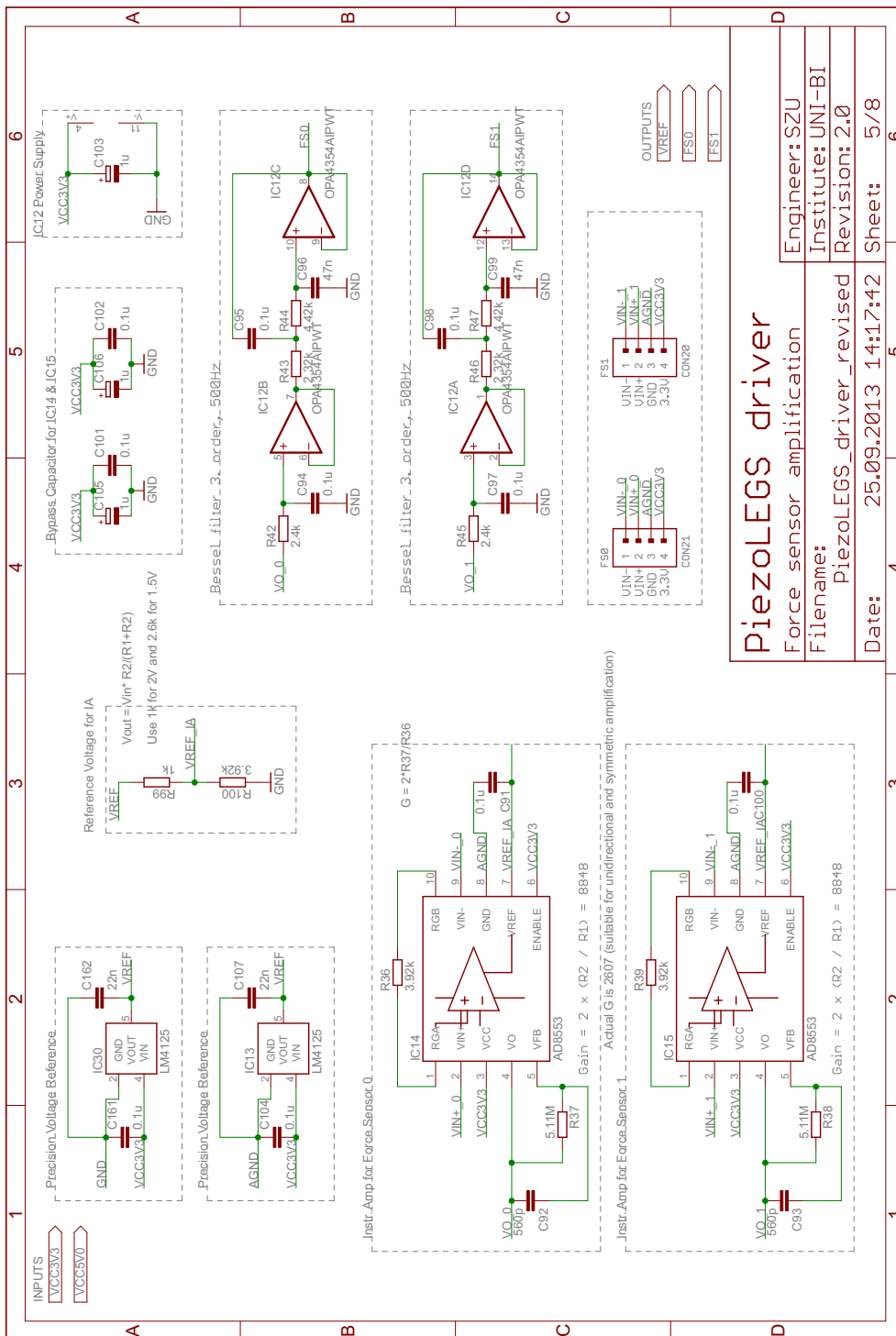
Figure 83: Circuit diagram: instrumentation amplifier and low pass filtering after [14].
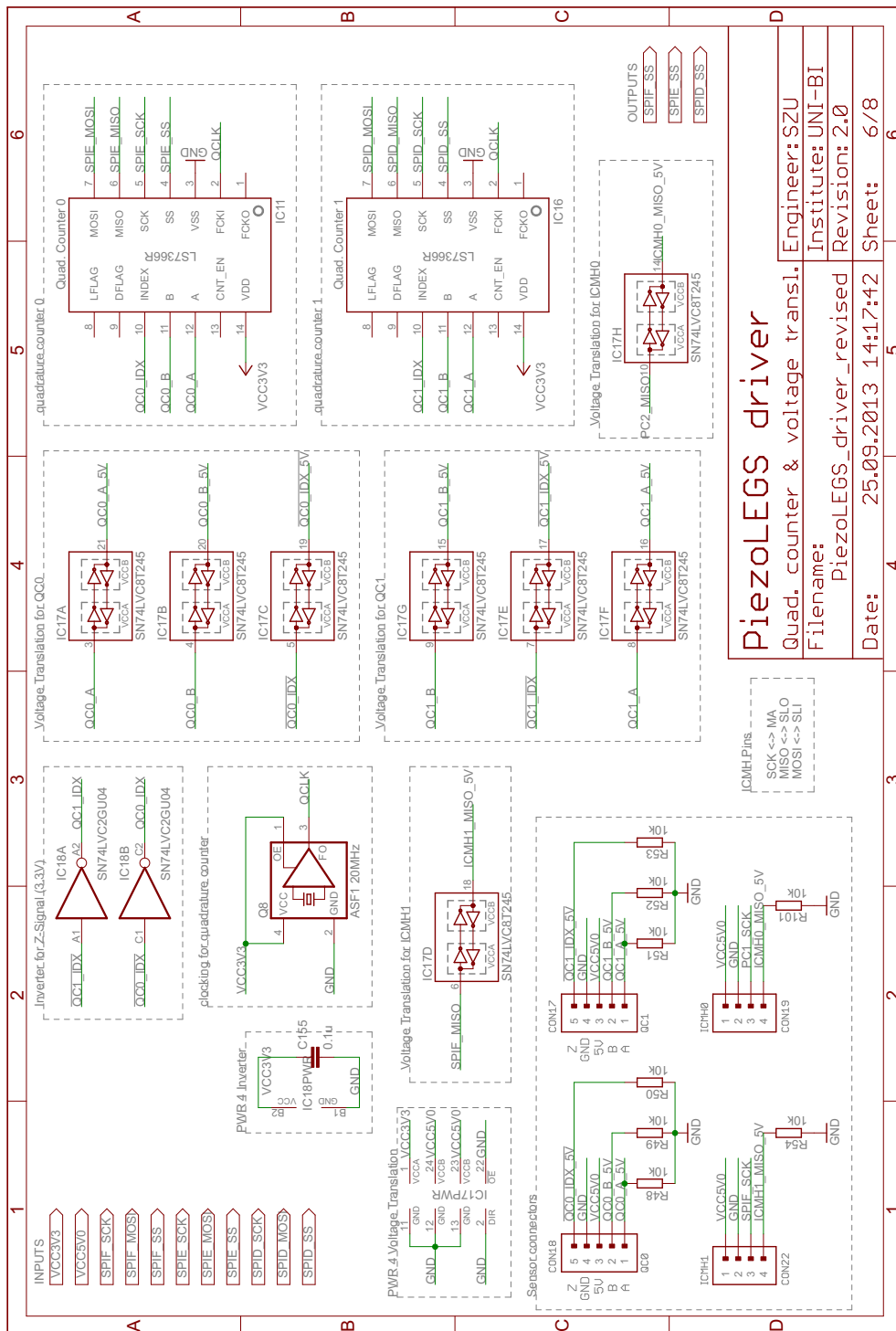
Figure 84: Circuit diagram: quadrature counters and voltage translators after [14].
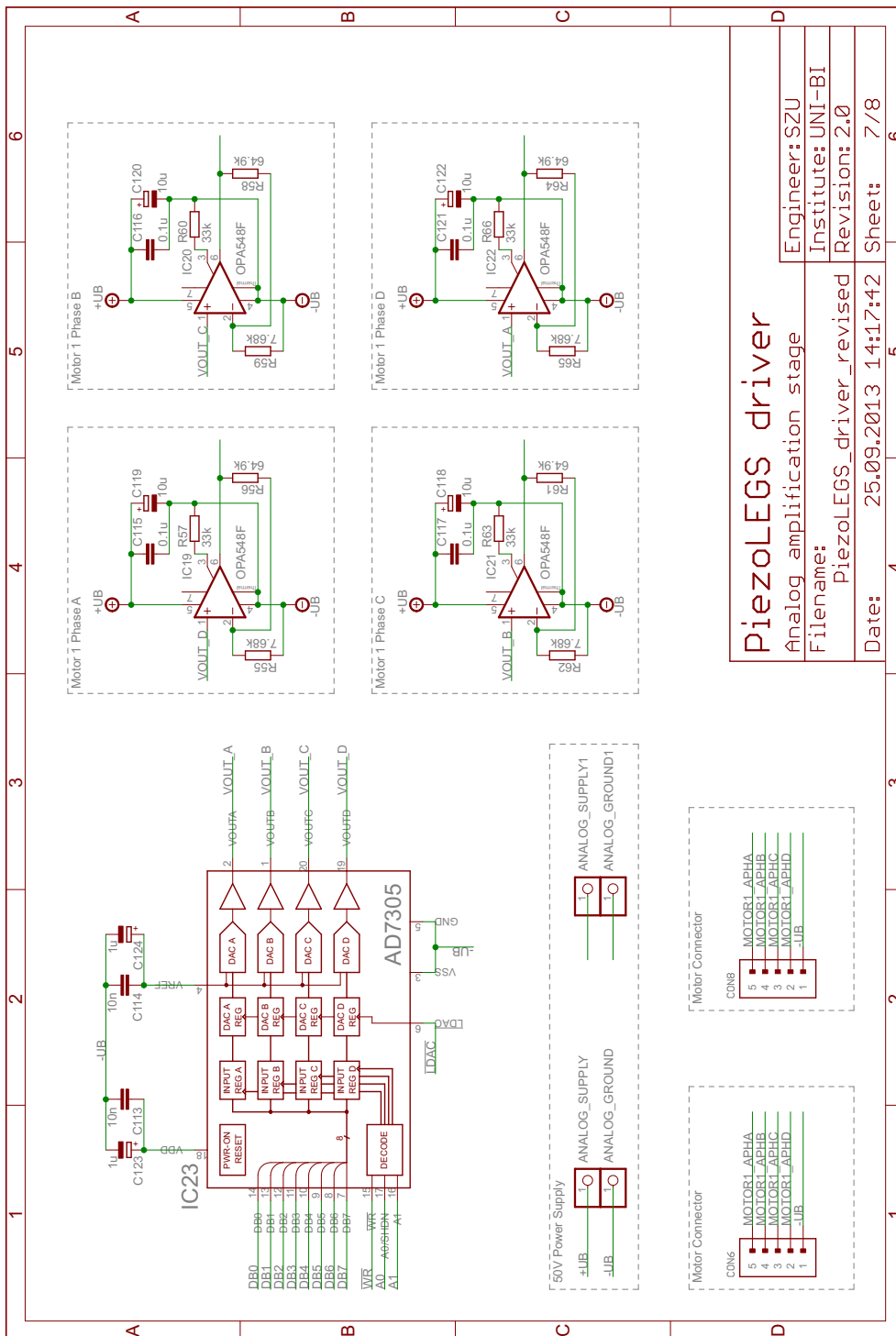
Figure 85: Circuit diagram: analog amplification unit (4 phases) after [14].
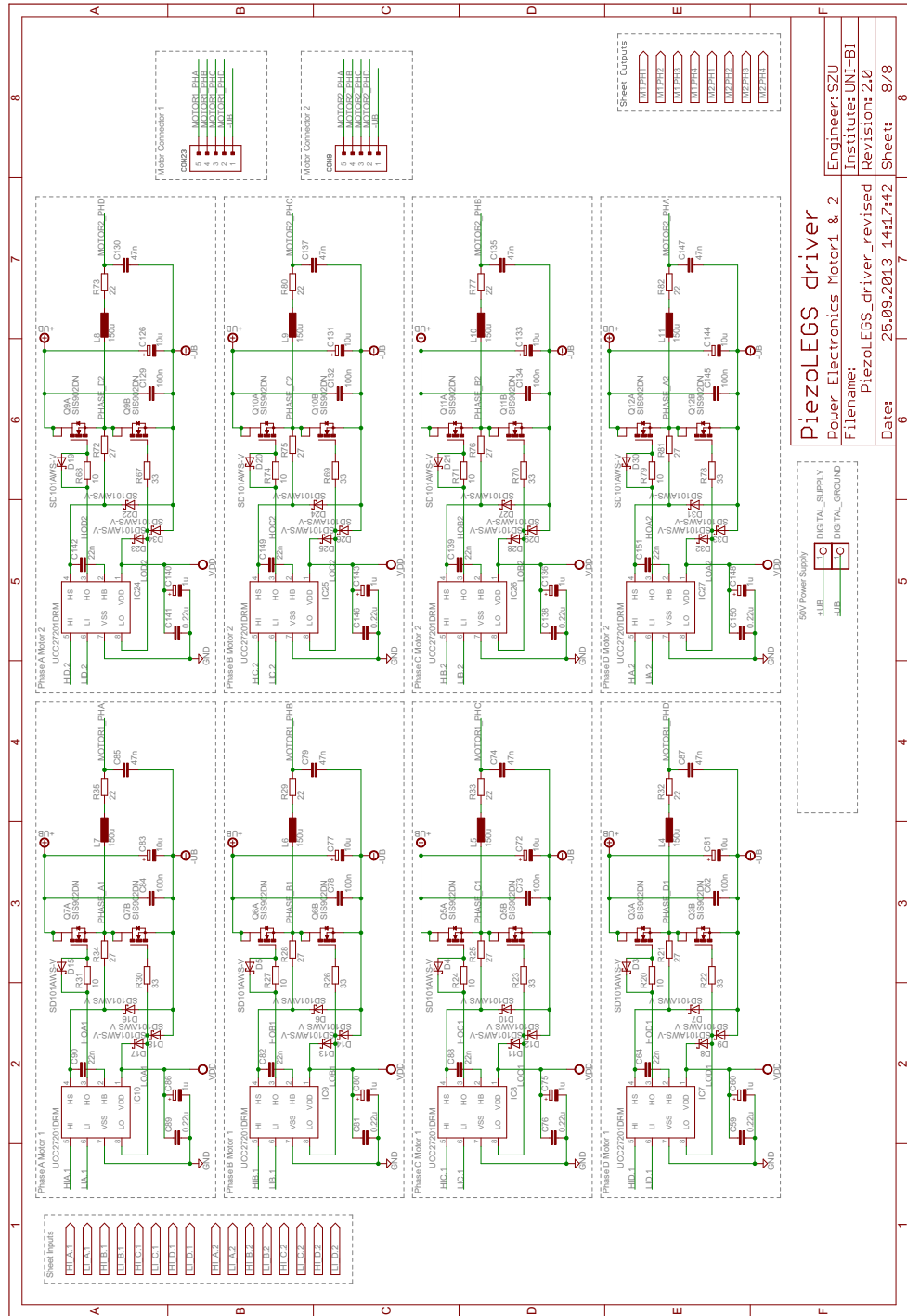
Figure 86: Circuit diagram: digital amplification unit (8 phases) after [14].
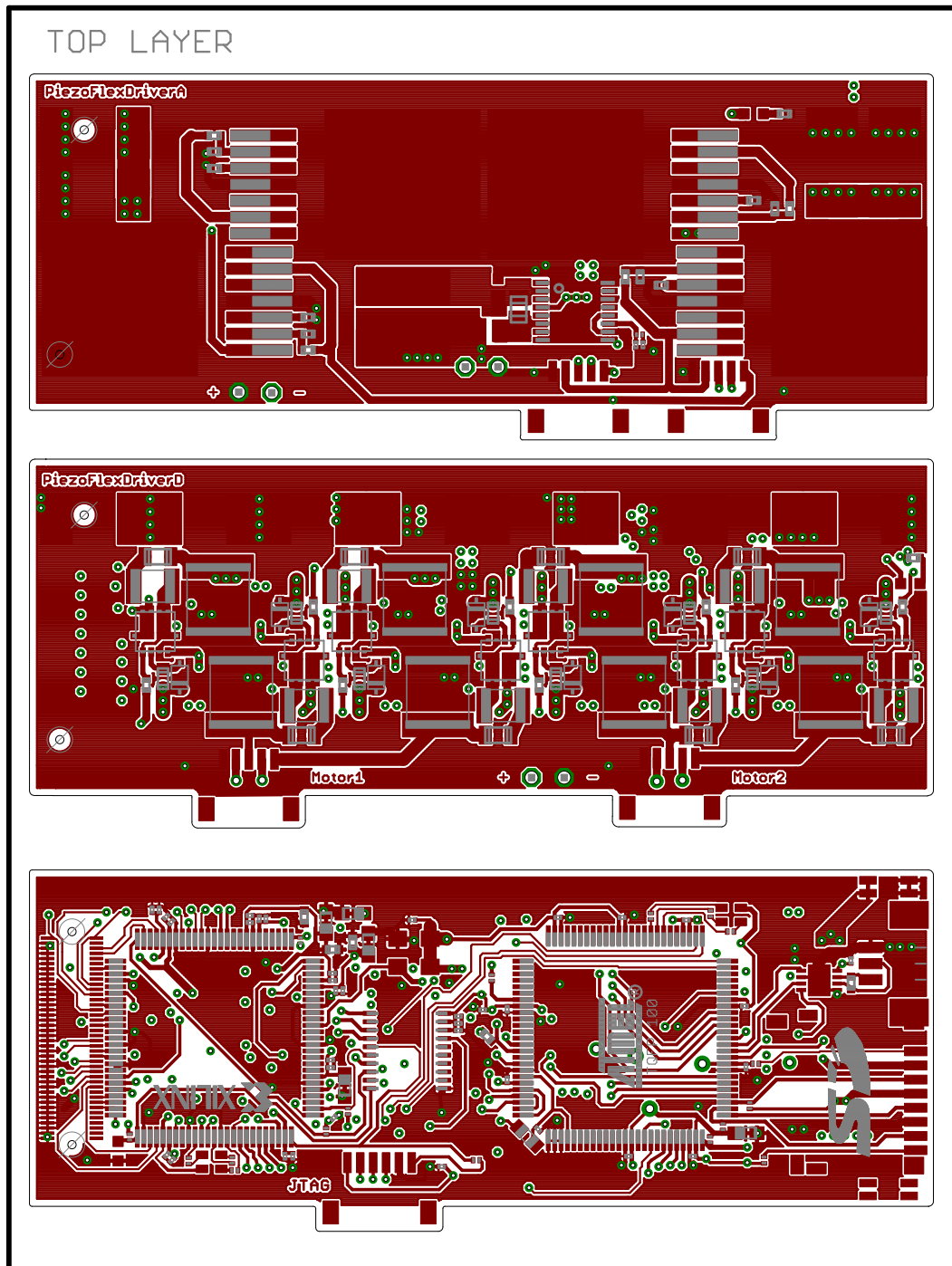
Figure 87: Layout of the top layer (layer 1) of the motor drive electronics. From the top: analog power unit, digital power unit and control unit. Scale 1.875 to 1.
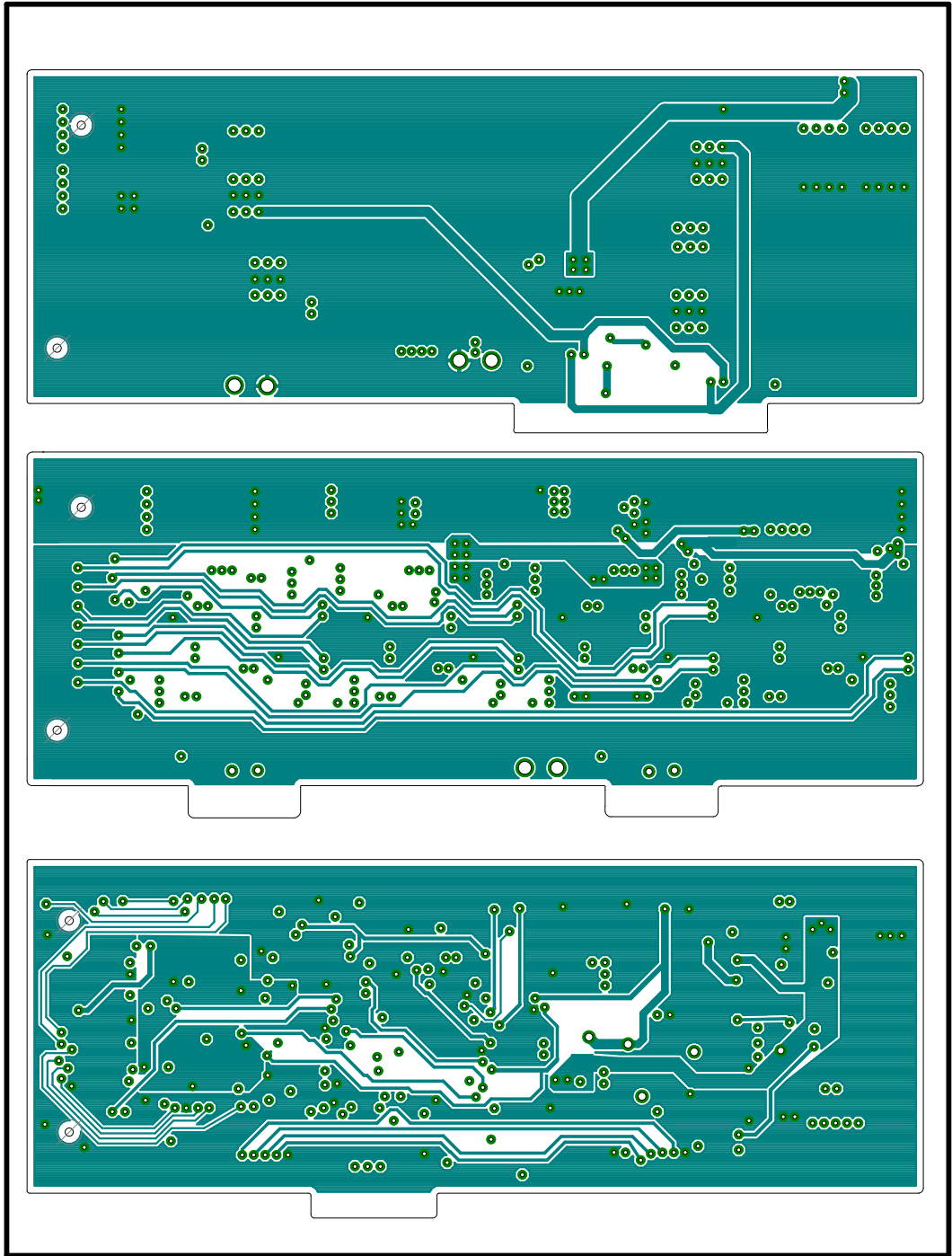
Figure 88: Layout of the intermediate layer (layer 2) of the motor drive electronics. From the top: analog power unit, digital power unit and control unit. Scale 1.875 to 1.
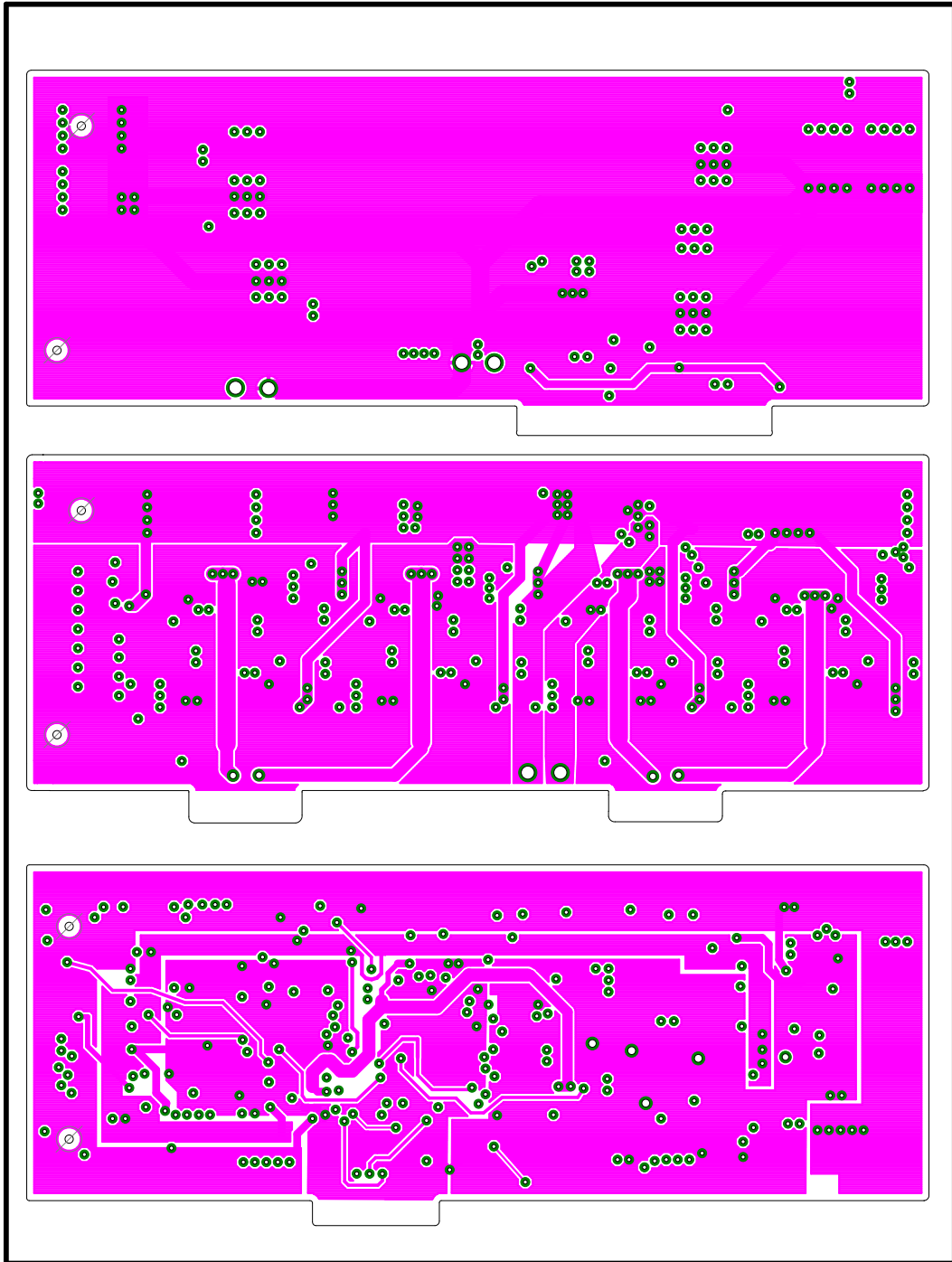
Figure 89: Layout of the intermediate layer (layer 3) of the motor drive electronics. From the top: analog power unit, digital power unit and control unit. Scale 1.875 to 1.

214
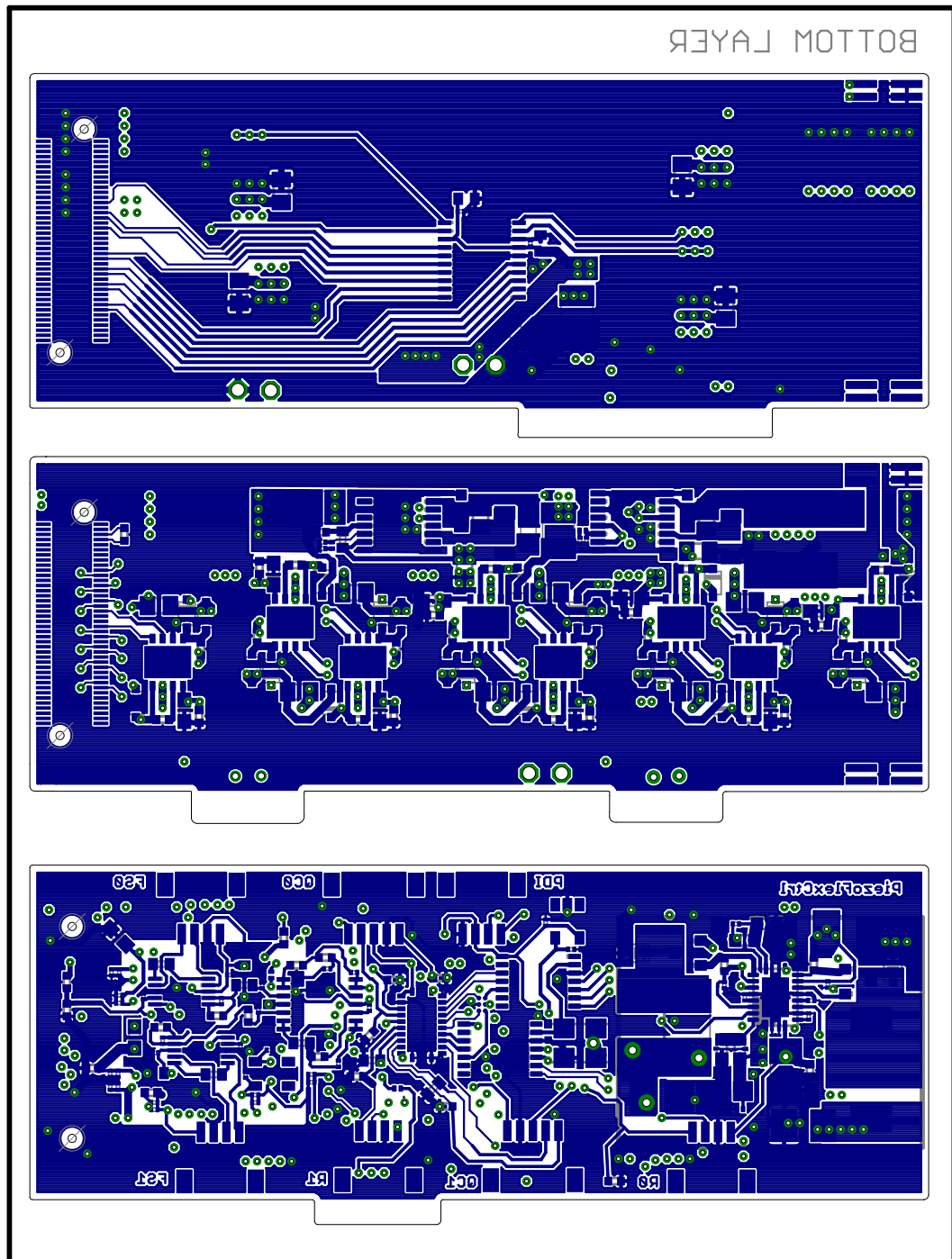
Figure 90: Layout of the bottom layer (layer 4) of the motor drive electronics. From the top: analog power unit, digital power unit and control unit. Scale 1.875 to 1.

215
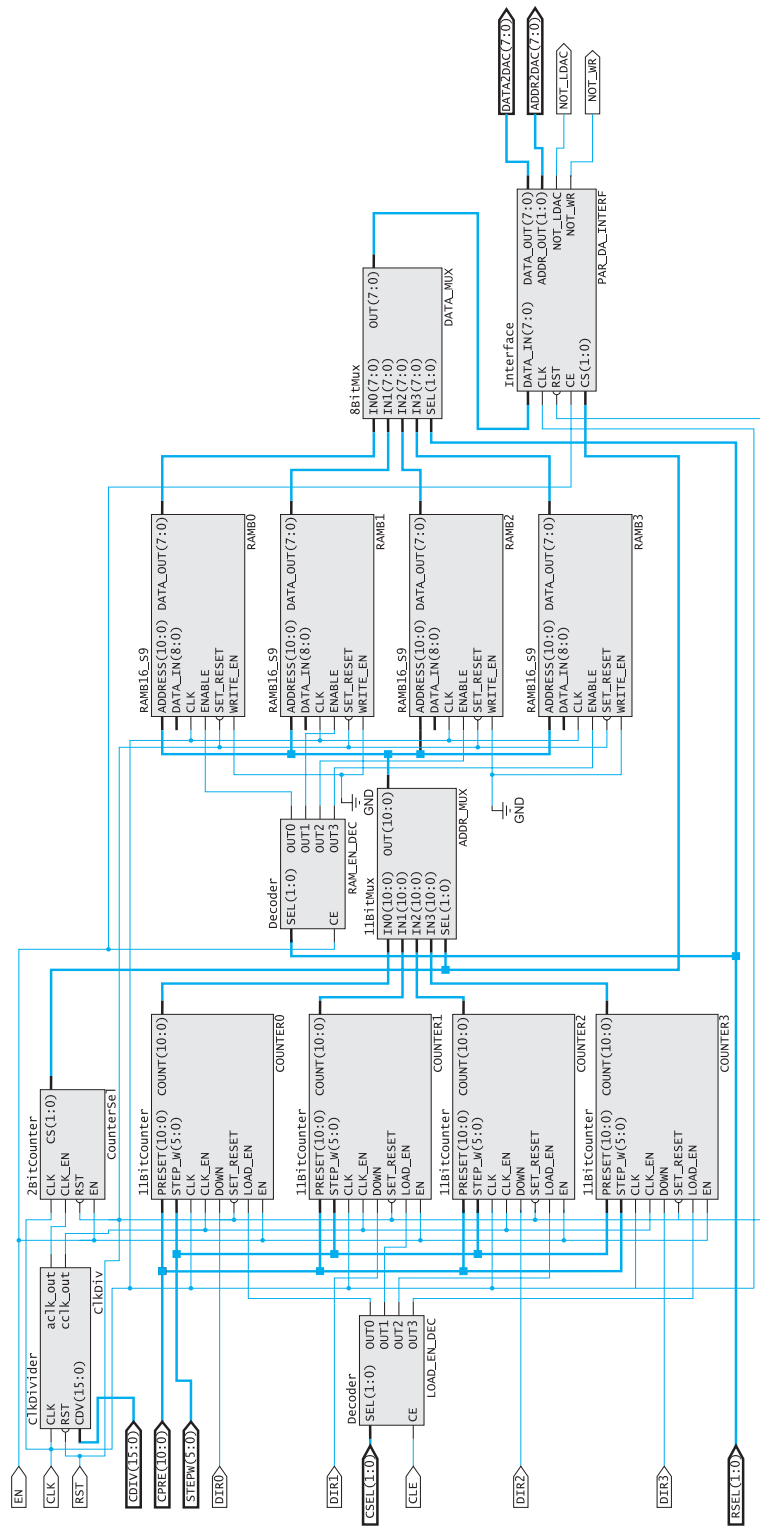
Figure 91: RTL schematic of the waveform generator compatible with the analog power unit designed in VHDL. Each RAM block contains one specific waveform (e.g. *sine* or *force*). Depiction after [14].

D | APPENDIX D

ABSTRACT

This appendix is a rudimentary introduction into the bond graph methodology for modeling of dynamic system based on [121, 29]. It provides a foundation for the understanding of the derivation of state equations for the sensor-tendon complex in chapt. 7.

D.1 BOND GRAPHS

Bond graphs are graphical means for representing the dynamics of energy-exchanging systems. The fact that interacting physical systems must transmit power is used to unify the description of interconnected systems independently of their particular domain. Electrical, mechanical, hydraulic, pneumatic, thermal and other systems can be modeled using one common methodology using a small set of ideal lumped elements. A bond graph consists of a number of subsystems or components connected by bonds which represent two generalized variables *effort* (*e*) and *flow* (*f*).

$$\mathbf{S_1} \quad \overline{\quad \overset{\textit{effort}}{\underset{\textit{flow}}{\rule{3cm}{0.4pt}}} \quad} \quad \mathbf{S_2}$$
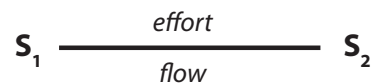
These variables are forced to be identical on the bond and indirectly correspond to energy flow between the interconnected subsystems $\mathbf{S}_1$ and $\mathbf{S_2}$. *Effort* and *flow* are also called *power variables* since their product at a given time is the instantaneous power $P(t)$ flowing between the subsystems

$$P(t) = e(t)f(t).$$

The energy exchanged between the subsystems is the time integral of the power

$$E(t) = \int^t P(t)dt.$$

Since power could flow in either direction between the subsystems, a power convention needs to be established. The bonds are then augmented with half-arrows indicating a time-invariant reference

direction for power flow if the product $e(t)f(t)$ in is positive.[1]

$$\textbf{S}_1 \xrightarrow[\text{flow}]{\text{effort}} \textbf{S}_2$$
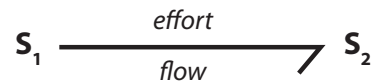
In the above case, positive power flows from $\textbf{S}_1$ to $\textbf{S}_2$. Beside the *power variables*, two other generalized variables are used in the description of dynamic systems – *momentum p* and *displacement q*. In the differential form, these are defined as

$$\frac{dp(t)}{dt} = e(t),$$
$$\frac{dq(t)}{dt} = f(t).$$

For mechanical translational systems, which are of interest here, the *power* and *energy variables* are placeholders for the following physical quantities:

Generalized variables	Mechanical Translation	SI Units
Effort e	Force F	N,
Flow f	Velocity V	m/s,
Momentum p	Momentum P	N-s,
Displacement q	Displacement X	m.

Bonds are used to connect components of which there are four basic generalized types – **S**(ource), **C**(ompliance), **I**(nertia) and **R**(esistance). The meaning of these components depends on the particular physical domain. Sources can be seen as inputs which provide a way of injecting energy into the system.[2] An ideal flow source S_f provides the given flow measure independently of the effort. Similarly, an ideal effort source S_e provides the given effort while the flow may be arbitrary. In case of linear mechanical systems S_f is a velocity and S_e a force source. The other basic components **C**, **I**, **R** are linear spring, mass and linear damper, respectively.
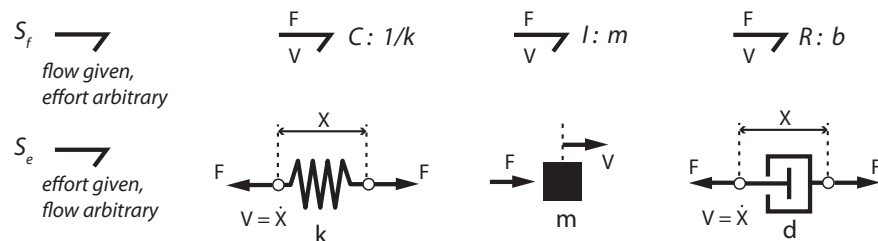
They are also called *1-port elements* since only one bond connects to them. The basic *1-port elements* define how *effort* and *flow* relate to

---

[1]Full arrows are commonly used for the indication of *signal flows* whose influence on the system in terms of power is negligible – e.g. ideal sensors.

[2]Negative "sources" (sinks) draining energy from the system can also be defined.

each other on the corresponding bond. In other words, they define the *constitutive laws* governing the relationship between the *power variables*.[3] For the basic linear components of mechanical translation, these relationships are

$$F = kX, \quad P = mV \text{ and } F = dV,$$

for the spring, mass and damper, respectively.

Beside the *1-port elements* there are also *2-port elements* which include the transformer **TK** and gyrator **GY**.

They are defined by the following *constitutive laws*

$$e_1 = me_2, \quad mf_1 = f_2$$

for the transformer and

$$e_1 = rf_2, \quad rf_1 = e_2$$

for the gyrator.

Thus, both of these ideal elements are power conservative. A mechanical example of a transformer is a rigid lever and of a gyrator, a gyroscope. The factors m and r do not have to be constant - in such case one speaks of a *modulated* transformer or gyrator. However, *2-port elements* are not further considered here.

The last class of bond graph components to be mentioned in this appendix are *3-port junction elements*. They are especially important because they connect other components. One distinguishes between two types of junctions – a 0 or *common effort* junction and a 1 or *common flow* junction. All bonds connected to these junctions have the same *effort* or *flow* variable, respectively. This holds true independent of the sign convention.

common effort junction   common flow junction

However, the sign convention is important to properly add the different *flows* or *efforts* connected to the respective 0 or 1-junction. For the 0-junction it holds true

$$\pm f_1 \pm f_2 \pm f_3 = 0 \text{ and } e_1 = e_2 = e_3,$$

---

[3]The *constitutive laws* can also be defined in terms of *energy variables* or a combination of both types. Also note, that these relationships may in general be not linear but only linear laws are considered here.

while for the 1-junction it has to be

$$\pm e_1 \pm e_2 \pm e_3 = 0 \text{ and } f_1 = f_2 = f_3.$$

Note, that *2-port* junctions are possible and that *n-port* junctions can be represented as a concatenation of the respective *3-port* junction types.

At this point, almost all basic elements required for the derivation of state equations of the sensor-tendon complex have been introduced. But before proceeding to the next section, the issue of causality in bond graphs needs to be explained. Causality defines the cause and effect relationship within a bond graph. Graphically, a perpendicular line is made at one end of a bond. This line is called *causal stroke* and represents the direction in which the effort signal is directed.
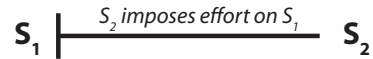
From this definition, the representation of *flow* and *effort* sources can be automatically adjusted.
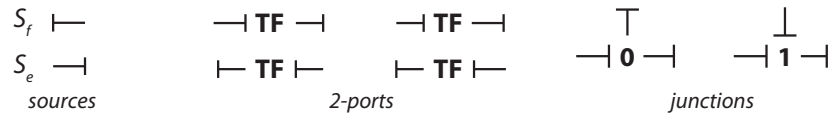
It is also clear, that there can only be one causal stroke at a 0-junction and that all but one bonds have to have causal strokes in case of a 1-junction. In case of the *2-port* elements there are two valid combinations as illustrated above. As soon as an *effort* or a *flow* has been assigned as an input, the assignment at the output is fixed. In case of the other *1-port* elements, there are two possible choices of causalities – the *integral* and the *derivative causality* – depending on the causal formulation of the *constitutive law* as listed below

Element	Causal form	Causal formulation
Resistance	⊣	$e = \Phi_R(f)$
	⊢	$f = \Phi_R^{-1}(e)$
Compliance	⊣	$e = \Phi_C^{-1}\left(\int^t f\,dt\right)$
	⊢	$f = \frac{d}{dt}\Phi_C(e)$
Inertia	⊢	$f = \Phi_I^{-1}\left(\int^t e\,dt\right)$
	⊣	$e = \frac{d}{dt}\Phi_I(f)$

where Φ is a function defining the corresponding law. In the linear case, **R** is indifferent to the causality imposed upon it since the formulations $e = Rf$ or $f = (1/R)e$ differ only in the form of the constant coefficient and do not form a differential equation. However, in case of **C** and **I** the formulation is important because it affects the further processing of a bond graph. A bond graph which is augmented with causal relations – a *causally complete* bond graph – can be used to

automatically derive the dynamic equations of the system which is described by it. In this context, *integral causalities* are preferred since they can be processed more easily.[4]

D.2 STATE EQUATIONS OF THE SENSOR–TENDON COMPLEX

The sensor-tendon model from sect. 7.3 is shown in the schematic illustration below. It consists of a mass and three linear spring elements, whereas the two springs on the right-hand side can be seen as one spring having the effective spring constant $k_{teff} = \frac{k_s k_t}{k_s + k_t}$.
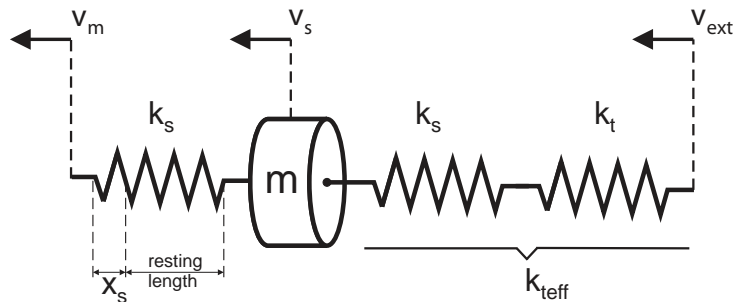
This system is clearly mechanical, translational and linear. The directions for positive velocities (*flows*) are indicated. v_m and v_{ext} are system inputs and v_s is the velocity of the moving mass (the sensor). In order for the power convention to be well-defined, it has to be stated whether the force (*effort*) generating element, i.e. the spring, is positive in tension or compression. In the derivation below, tension is assumed to be positive. The construction procedure for the bond graph is in this case as follows. First, 1-junctions are identified to represent each distinct velocity.

Second, every element which relates to the absolute velocity represented by the particular junction needs to be attached to this junction. v_m and v_{ext} are system velocity inputs and thus are represented by *flow* sources. The mass m is an inertia element moving at the velocity v_s and thus is attached to the corresponding 1-junction.

---

[4]If all components of a bond graph can be defined in the integral causal formulation, a set of ordinary differential equations (ODE) can be derived from the bond graph. If there is a mixture of integral and derivative causalities, the resulting mathematical model is, in general, a differential algebraic equation (DAE).

$$S_f : v_m \;\text{——}\; \mathbf{1}\quad\overset{v_m}{}\qquad\qquad \mathbf{1}\overset{v_s}{}\qquad\qquad \overset{v_{ext}}{}\mathbf{1}\;\text{——}\; S_f : v_{ext}$$
$$\big|$$
$$I : m$$
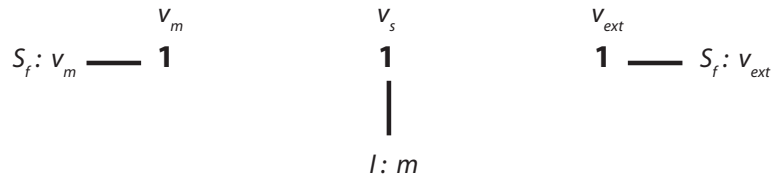
Third, 0-junctions are inserted in order to establish proper relative velocities among the remaining elements. At this point, the half-arrows can be added to the bonds according to the power convention.

$$S_f : v_m \;\rightharpoonup\; \underset{}{\overset{v_m}{\mathbf{1}}}\;\rightharpoonup\; \mathbf{0}\;\rightharpoonup\; \overset{v_s}{\mathbf{1}}\;\rightharpoonup\; \mathbf{0}\;\rightharpoonup\; \overset{v_{ext}}{\mathbf{1}}\;\rightharpoonup\; S_f : v_{ext}$$
$$\qquad\qquad C:k_s \qquad I:m \qquad C:k_{teff}$$
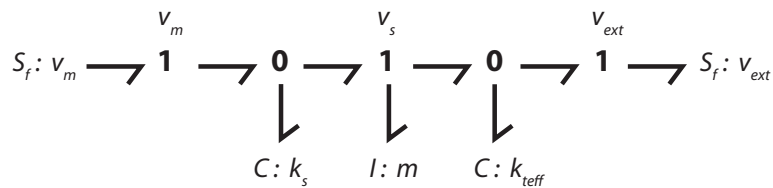
A positive v_m stretches the springs and since the springs are assumed positive in tension the power has to flow from S_f associated with v_m into the system. Similarly, a positive v_{ext} compresses the springs, so according to the power convention the half-arrow shows this time into the *flow* source S_f. The other half-arrows at 0-junctions can be easily deduced by considering the relative velocities across the junctions and their effect on the corresponding spring elements. The half-arrow at the remaining inertia element is directed toward the element since power flows into the element for a positive force acting in the same direction as the positive velocity. The last step consists in augmenting the bond graph with *causal strokes*.

$$S_f : v_m \;\overset{1}{\vdash\!\!\rightharpoonup}\; \overset{v_m}{\mathbf{1}}\;\overset{2}{\vdash\!\!\rightharpoonup}\; \mathbf{0}\;\overset{4}{\longrightarrow}\!\!|\; \overset{v_s}{\mathbf{1}}\;\overset{6}{\vdash\!\!\rightharpoonup}\; \mathbf{0}\;\overset{8}{\longrightarrow}\!\!|\; \overset{v_{ext}}{\mathbf{1}}\;\overset{9}{\longrightarrow}\!\!|\; S_f : v_{ext}$$
$$\qquad\quad 3 \Big\downarrow \qquad 5 \Big\downarrow \qquad 7 \Big\downarrow$$
$$\qquad\quad C:k_s \qquad I:m \qquad C:k_{teff}$$
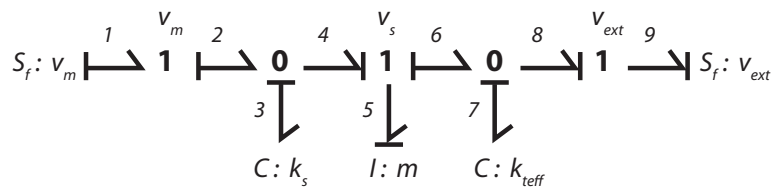
The augmentation with causal relations begins by assigning the required causality to all sources. Then any energy storage element (**C** or **I**) is chosen and assigned the (preferred) *integral causality*. After this step some causal relations may already follow by implication when considering the allowable causal forms of the junctions. In case of the sensor-tendon complex, by assigning the *integral causality* to the mass element **I**, all causal relations become fully defined.

Once a bond graph representation augmented with causal strokes is given, the bonds are labeled with numbers. The derivation of the

dynamic system equations follows now automatically according to three steps:

1. selection of inputs and energy state variables;

2. formulation of the initial set of equations;

3. reduction of these equations to state-space form.

For the above bond graph, the inputs are v_m and v_{ext}. For *integral causalities*, the energy state variables are p-variables on **I**-elements and q-variables on **C**-elements. In case of the sensor-tendon complex the state variables are q_3, p_5 and q_7. The initial set of equations can be found by equating the rate of change of a state variable to an *effort* or *flow*. Accordingly,

$$\dot{q}_3 = f_3 = f_2 - f_4 = v_m - f_5 = v_m - \frac{p_5}{m}.$$

The transition from f_3 to $f_2 - f_4$ is given by the summation of *flows* at the 0-junction. The proper signs are given by the half-arrows. f_2 resolves into the input v_m. f_4 equals f_5 and f_6 but is caused by f_5. f_5 can be resolved into p_5/m according to the corresponding *constitutive law*. Similar procedure holds for the remaining two equations.

$$\dot{p}_5 = e_5 = e_4 - e_6 = e_3 - e_7 = k_s q_3 - k_{teff} q_7$$

and

$$\dot{q}_7 = f_7 = f_6 - f_8 = f_6 - f_9 = f_5 - v_{ext} = \frac{p_5}{m} - v_{ext}.$$

By substituting the physical quantities for mechanical translation against the generalized variables and subscripts against corresponding numbers, a set of ordinary differential equations follows

$$\begin{cases} \dot{x}_s & = -\frac{p_m}{m} + v_m \\ \dot{x}_{teff} & = \frac{p_m}{m} - v_{ext} \\ \dot{p}_m & = k_s x_s - k_{teff} x_{teff} \end{cases}$$

The state-space representation is given by the following state and input matrices

$$\begin{pmatrix} \dot{x}_s \\ \dot{x}_{teff} \\ \dot{p}_m \end{pmatrix} = \begin{pmatrix} 0 & 0 & \frac{-1}{m} \\ 0 & 0 & \frac{1}{m} \\ k_s & -k_{teff} & 0 \end{pmatrix} \begin{pmatrix} x_s \\ x_{teff} \\ p_m \end{pmatrix} + \begin{pmatrix} 1 & 0 \\ 0 & -1 \\ 0 & 0 \end{pmatrix} \begin{pmatrix} v_m \\ v_{ext} \end{pmatrix},$$

and the following output matrix (cf. sect. 7.3)

$$x_f = \begin{pmatrix} 1 & \frac{1}{1+\frac{k_s}{k_t}} & 0 \end{pmatrix} \begin{pmatrix} x_s \\ x_{teff} \\ p_m \end{pmatrix}.$$

x_f is the overall elongation of the force sensor. This relation can be derived in the following way. The elongation of the effective spring

on the right-hand side of the force sensor is x_{teff} and equals $x_s^* + x_t^*$.[5]
But it must also hold true $x_s^* k_s = x_t^* k_t$ and thus $x_{teff} = x_s^* + x_s^* \frac{k_s}{k_t}$.
Accordingly, $x_s^* = \frac{x_{teff}}{(1+k_s/k_t)}$ and $x_f = x_s + x_s^*$.

---

[5]Stars are added to emphasize the fact, that these are components of the effective spring.

LIST OF FIGURES

LIST OF TABLES

BIBLIOGRAPHY

[1] IEEE Standard 176-1987. Standards on Piezoelectric Crystals, 1949. *Proceedings of the Institute of Radio Engineers*, 37(12):1378–1395, 1949.

[2] BC Abbott and DR Wilkie. The relation between velocity of shortening and the tension-length curve of skeletal muscle. *Journal Of Physiology-London*, 120(1-2):214–223, 1953.

[3] Alin Albu-Schaeffer, Christian Ott, and Gerd Hirzinger. A unified passivity-based control framework for position, torque and impedance control of flexible joint robots. *International Journal of Robotics Research*, 26(1):23–39, 2007.

[4] Andrew Gordon Allison. *Aspects of stochastic control and switching: from Parrondos games to electrical circuits*. PhD thesis, The University of Adelaide, 2009.

[5] Salvatore Annunziata, Jan Paskarbeit, and Axel Schneider. Novel bioinspired control approaches to increase the stiffness variability in multi-muscle driven joints. *Bioinspiration & Biomimetics*, 6(4), 2011.

[6] Salvatore Annunziata and Axel Schneider. Physiologically based control laws featuring antagonistic muscle co-activation for stable compliant joint drives. *Applied Bionics and Biomechanics*, 9(3):249–266, 2012.

[7] Panos J Antsaklis and Xenofon D Koutsoukos. Hybrid systems control. *Encyclopedia of Physical Science and Technology,*, 7:445–458, 2002.

[8] Panos J Antsaklis and Anthony N Michel. *Linear systems*. Birkhauser Boston, 1997.

[9] Mustafa Arafa, Osama Aldraihem, and Amr Baz. Modeling and Characterization of a Linear Piezomotor. *Journal Of Intelligent Material Systems And Structures*, 20(16):1913–1921, 2009.

[10] B Armstrong-Helouvry, P Dupont, and CC Dewit. A Survey of Models, Analysis Tools and Compensation Methods for the Control of Machines with Friction. *Automatica*, 30(7):1083–1138, 1994.

[11] Karl Johan Astrom and Carlos Canudas-de wit. Revisiting the LuGre Friction Model Stick-Slip Motion and Rate Dependence. *IEEE Control Systems Magazine*, 28(6):101–114, 2008.

[12] George A Baker Jr. The theory and application of the padé approximant method. Technical report, Los Alamos Scientific Lab., Univ. of California, N. Mex., 1964.

[13] A Ballato. Piezoelectricity: History and new thrusts. *1996 IEEE Ultrasonics Symposium, Proceedings, Vols 1 and 2*

[14] Daniel Basa. A four-phase arbitrary waveform generator for the control of translatory piezo drives. Master's thesis, Bielefeld University, 2010.

[15] Ulrich Bässler et al. *Neural basis of elementary behavior in stick insects.* Springer-Verlag, 1983.

[16] T Baumberger, P Berthoud, and C Caroli. Physical analysis of the state- and rate-dependent friction law. II. Dynamic friction. *Physical Review B*, 60(6):3928–3939, 1999.

[17] Tristan Baumberger and Christiane Caroli. Solid friction from stick-slip down to pinning and aging. *Advances in Physics*, 55(3-4):279–348, 2006.

[18] P Berthoud, T Baumberger, C G'Sell, and JM Hiver. Physical analysis of the state- and rate-dependent friction law: Static friction. *Physical Review B*, 59(22):14313–14327, 1999.

[19] M Bexell and S Johansson. Microassembly of a piezoelectric miniature motor. *Journal Of Electroceramics*, 3(1):73–83, 1999.

[20] AS Bhalla, Ruyan Guo, and Rustum Roy. The perovskite structure–a review of its role in ceramic science and technology. *Material Research Innovations*, 4(1):3–26, 2000.

[21] Giovanni Biancuzzi, Daniel Haller, Thomas Lemke, Martin Wischke, Frank Goldschmidtboeing, and Peter Woias. A dynamic linearization concept for piezoelectric actuators. *Ultrasonics, Ferroelectrics and Frequency Control, IEEE Transactions on*, 58(4):689–697, 2011.

[22] Giovanni Tonietti Antonio Bicchi, S Rizzino, and G Tonietti. Adaptive simultaneous position and stiffness control for a soft robot arm. In *Proc. of IEEE/RSJ International Conference on Intelligent Robots and Systems*, pages 1992–1997, 2001.

[23] AA Biewener. Muscle function in vivo: A comparison of muscles used for elastic energy savings versus muscles used to generate mechanical power. *American Zoologist*, 38(4):703–717, 1998.

[24] Andrew A Biewener. *Animal locomotion*. Oxford University Press, 2003.

[25] Gerd Binnig, Calvin F Quate, and Ch Gerber. Atomic force microscope. *Physical review letters*, 56(9):930, 1986.

[26] P.A. Bliman and M. Sorine. Easy-to-use realistic dry friction models for automatic control. In *Proceedings of 3rd European Control Conference*, 1995.

[27] Till Bockemühl, Nikolaus F Troje, and Volker Dürr. Inter-joint coupling and joint angle synergies of human catching movements. *Human movement science*, 29(1):73–93, 2010.

[28] Manuel Bodirsky, Gustav Nordh, and Timo von Oertzen. Integer programming with 2-variable equations and 1-variable inequalities. *Information Processing Letters*, 109(11):572–575, 2009.

[29] Wolfgang Borutzky. *Bond graphs: A methodology for modelling multidisciplinary dynamic systems*. SCS Publishing House, 2004.

[30] P. Bouchilloux, S. Cagatay, K. Uchino, and B. Koc. Finite element modeling and optimization of tube-shaped ultrasonic motors. *SPIE proceedings series*, 5056:267–276, 2003.

[31] Jean-Pierre Boutrand, editor. *Biocompatibility and performance of medical devices (Woodhead Publishing Series in Biomaterials)*. Woodhead Publishing, 1 edition, 12 2012.

[32] Richard P Brent. *Analysis of the binary Euclidean algorithm*. Department of Computer Science, Carnegie-Mellon University, 1976.

[33] Richard P Brent and Paul Zimmermann. *Modern computer arithmetic*. Number 18. Cambridge University Press, 2010.

[34] Rodney A Brooks. Intelligence without representation. *Artificial intelligence*, 47(1):139–159, 1991.

[35] J. Brufau, M. Puig-Vidal, J. López-Sánchez, J. Samitier, W. Driesen, J.-M. Breguet, N. Snis, U. Simu, S. Johansson, J. Gao, T. Velten, J. Seyfried, R. Estaña, and H. Woern. MICRON: Small Autonomous Robot for Cell Manipulation Applications. In *Proceedings of the 2005 IEEE International Conference on Robotics and Automation*, pages 844–849, 18-22 April, Barcelona, Spain, 2005.

[36] W von Buddenbrock. Der rhythmus der schreitbewegungen der stabheuschrecke dyxippus. *Biologisches Zentralblatt*, 41:41–48, 1921.

[37] T. Buehrmann and E. Di Paolo. Biological actuators are not just springs: Investigating muscle dynamics and control signals. In *Proceedings of the 9th International Conference on Simulation of Adaptive Behavior*, volume 4095, pages 89–100, Rome, Italy, Sep 2006.

[38] TJ Burkholder and RL Lieber. Sarcomere length operating range of vertebrate muscles during movement. *Journal Of Experimental Biology*, 204(9):1529–1536, 2001.

[39] Walter A. Cady. *Piezoelectricity*. Dover Pubns, 12 1978.

[40] C Canudas de Wit and H Olsson. A new model for control of systems with friction. *IEEE Transactions on Automatic Control*, 40(3):419–425, 1995.

[41] Giovanni Cesari. Parallel implementation of schönhage's integer gcd algorithm. In *Algorithmic Number Theory*, pages 64–76. Springer, 1998.

[42] Abdesslam Chrachri and F Clarac. Fictive locomotion in the fourth thoracic ganglion of the crayfish, procambarus clarkii. *The Journal of Neuroscience*, 10(3):707–719, 1990.

[43] Jack G Copeland, Richard G Smith, Francisco A Arabia, Paul E Nolan, Gulshan K Sethi, Pei H Tsau, Douglas McClellan, and Marvin J Slepian. Cardiac replacement with a total artificial heart as a bridge to transplantation. *New England Journal of Medicine*, 351(9):859–867, 2004.

[44] James A Crawford. *Frequency synthesizer design handbook*. Artech House Norwood, MA, 1994.

[45] Holk Cruse. The function of the legs in the free walking stick insect, carausius morosus. *Journal of Comparative Physiology*, 112(2):235–262, 1976.

[46] Holk Cruse. A new model describing the coordination pattern of the legs of a walking stick insect. *Biological Cybernetics*, 32(2):107–113, 1979.

[47] Holk Cruse. What mechanisms coordinate leg movement in walking arthropods? *Trends in neurosciences*, 13(1):15–21, 1990.

[48] Holk Cruse, J Dean, Volker Dürr, Th Kindermann, Josef Schmitz, and M Schumm. A decentralized, biologically based network for autonomous control of (hexapod) walking. *Neurotechnology for biomimetic robots*, pages 383–400, 2002.

[49] Holk Cruse, Thomas Kindermann, Michael Schumm, Jeffrey Dean, and Josef Schmitz. Walknet a biologically inspired network to control six-legged walking. *Neural networks*, 11(7):1435–1447, 1998.

[50] Marie Curie. *Oeuvres de Pierre Curie, publies par les soins de la Socit franaise de physique par Mme Pierre Curie.* 1908.

[51] Dragan Damjanovic. Ferroelectric, dielectric and piezoelectric properties of ferroelectric thin films and ceramics. *Reports on Progress in Physics*, 61(9):1267, 1998.

[52] B Dasgupta and TS Mruthyunjaya. The Stewart platform manipulator: a review. *Mechanism and Machine Theory*, 35(1):15–40, Jan 2000.

[53] David E Dausch. Ferroelectric polarization fatigue in pzt-based rainbows and bulk ceramics. *Journal of the American Ceramic Society*, 80(9):2355–2360, 1997.

[54] JJTH De Best, BHM Bukkems, MJG Van De Molengraft, WPMH Heemels, and M Steinbuch. Robust control of piecewise linear systems: A case study in sheet flow control. *Control Engineering Practice*, 16(8):991–1003, 2008.

[55] Fred Delcomyn. The locomotion of the cockroach periplaneta americana. *Journal of Experimental Biology*, 54(2):443–452, 1971.

[56] Liang Deng and Yonghong Tan. Modeling hysteresis in piezoelectric actuators using NARMAX models. *Sensors And Actuators A-Physical*, 149(1):106–112, 2009.

[57] Alexei Deriglazov. *Classical Mechanics: Hamiltonian and Lagrangian Formalism*. Springer, 2010.

[58] DL DeVoe and AP Pisano. Modeling and optimal design of piezoelectric cantilever microactuators. *Journal Of Microelectromechanical Systems*, 6(3):266–270, 1997.

[59] Aydin Dogan, Kenji Uchino, and Robert E Newnham. Composite piezoelectric transducer with truncated conical endcaps. *Ultrasonics, Ferroelectrics and Frequency Control, IEEE Transactions on*, 44(3):597–605, 1997.

[60] Robert Dunsch and Jean-Marc Breguet. Unified mechanical approach to piezoelectric bender modeling. *Sensors And Actuators A-Physical*, 134(2):436–446, 2007.

[61] Volker Dürr, Josef Schmitz, and Holk Cruse. Behaviour-based modelling of hexapod locomotion: linking biology and technical application. *Arthropod structure & development*, 33(3):237–250, 2004.

[62] Friedrich Eisenbrand and Sören Laue. A faster algorithm for two-variable integer programming. In *Algorithms and Computation*, pages 290–299. Springer, 2003.

[63] Friedrich Eisenbrand and Günter Rote. Fast 2-variable integer programming. In *Integer Programming and Combinatorial Optimization*, pages 78–89. Springer, 2001.

[64] A Endo, N Sasaki, and Y Tomikawa. Linear type ultrasonic motor using two-dimensionally positioned piezoelectric elements. *Ferroelectrics*, 112(1):165–170, 1990.

[65] DC Evans, D Rees, and DL Jones. Design Of Test Signals For Identification Of Linear-Systems With Nonlinear Distortions. *IEEE Transactions On Instrumentation And Measurement*, 41(6):768–774, 1992.

[66] Walter Federle and Thomas Endlein. Locomotion and adhesion: dynamic control of adhesive surface contact in ants. *Arthropod Structure & Development*, 33(1):67–75, 2004.

[67] Anatol G Feldman. Once more on the equilibrium-point hypothesis (lambda model) for motor control. *Journal of motor behavior*, 18(1):17, 1986.

[68] Anatol G Feldman, Valeri Goussev, Archana Sangole, and Mindy F Levin. Threshold position control and the principle of minimal interaction in motor actions. *Progress in Brain Research*, 165:267–281, 2007.

[69] Richard P. Feynman, Robert B. Leighton, and Matthew Sands. *The Feynman Lectures on Physics, Vol. II: The New Millennium Edition: Mainly Electromagnetism and Matter*. Basic Books, first trade paper edition edition, 10 2011.

[70] Richard Phillips Feynman, Robert Benjamin Leighton, and Matthew Linzee Sands. *The Feynman lectures on physics: Mainly mechanics, radiation, and heat*, volume 1. Basic Books, 2011.

[71] Roberto Filippini, Soumen Sen, and Antonio Bicchi. Toward soft robots you can depend on - A study of antagonistic actuation. *IEEE Robotics & Automation Magazine*, 15(3):31–41, 2008.

[72] Jeremy E Frank, Gary H Koopmann, Weicheng Chen, and George A Lesieutre. Design and performance of a high-force piezoelectric inchworm motor. In *1999 Symposium on Smart Structures and Materials*, pages 717–723. International Society for Optics and Photonics, 1999.

[73] Gene F. Franklin, J. David Powell, and A. Emami-Naeini. *Feedback Control of Dynamic Systems*. Pearson Education, 2006.

[74] M Gaefvert. Comparison of two dynamic friction models. In *Proceedings of the IEEE International Conference on Control Applications*, 1997.

[75] Mukesh V Gandhi. *Smart materials and structures*. Springer, 1992.

[76] D Garuckas and J Bareisis. Influence of different factors on the stiffness and strength of multilayer composite elements. *Mechanics of Composite Materials*, 39(2):153–164, 2003.

[77] Ping Ge and Musa Jouaneh. Modeling hysteresis in piezoceramic actuators. *Precision engineering*, 17(3):211–221, 1995.

[78] AK Geim, SV Dubonos IV Grigorieva, KS Novoselov, AA Zhukov, and S Yu Shapoval. Microfabricated adhesive mimicking gecko foot-hair. *Nature materials*, 2(7):461–463, 2003.

[79] H Geyer, A Seyfarth, and R Blickhan. Positive force feedback in bouncing gaits? *Proceedings Of The Royal Society Of London Series B-Biological Sciences*, 270(1529):2173–2183, 2003.

[80] Philip E Gill, Walter Murray, and Margaret H Wright. *Practical optimization*. Academic press, 1981.

[81] D Graham. A behavioural analysis of the temporal organisation of walking movements in the 1st instar and adult stick insect (carausius morosus). *Journal of Comparative Physiology*, 81(1):23–52, 1972.

[82] D Graham. *Pattern and control of walking in insects*. Academic Press, 1985.

[83] Ronald L Graham. *Concrete Mathematics, 2/e*. Pearson Education India, 2008.

[84] Markus Grebenstein and Patrick van der Smagt. Antagonism for a highly anthropomorphic hand-arm system. *Advanced Robotics*, 22(1):39–55, 2008.

[85] Sten Grillner. Control of locomotion in bipeds, tetrapods, and fish. *Comprehensive Physiology*, 1981.

[86] Matthias Gruhn, Géraldine von Uckermann, Sandra Westmark, Anne Wosnitza, Ansgar Büschges, and Anke Borgmann. Control of stepping velocity in the stick insect carausius morosus. *Journal of neurophysiology*, 102(2):1180–1192, 2009.

[87] Matthias Gruhn, Géraldine von Uckermann, Sandra Westmark, Anne Wosnitza, Ansgar Büschges, and Anke Borgmann. Control of stepping velocity in the stick insect carausius morosus. *Journal of neurophysiology*, 102(2):1180–1192, 2009.

[88] Michael Günther and Syn Schmitt. A macroscopic ansatz to deduce the hill relation. *Journal of theoretical biology*, 263(4):407–418, 2010.

[89] SK Ha and YH Kim. Analysis of a piezoelectric multimorph in extensional and flexural motions. *Journal Of Sound And Vibration*, 253(5):1001–1014, 2002.

[90] Gene H Haertling. Rainbow ceramics- a new type of ultra-high-displacement actuator. *American Ceramic Society Bulletin*, 73(1):93–96, 1994.

[91] Gene H Haertling. Ferroelectric ceramics: history and technology. *Journal of the American Ceramic Society*, 82(4):797–818, 1999.

[92] Ulrich Hagn, R. Konietschke, A. Tobergte, M. Nickl, S. Joerg, B. Kuebler, G. Passig, M. Groeger, F. Froehlich, U. Seibold, L. Le-Tien, A. Albu-Schaeffer, A. Nothhelfer, F. Hacker, M. Grebenstein, and G. Hirzinger. DLR MiroSurge: a versatile system for research in endoscopic telesurgery. *International Journal of Computer Assisted Radiology and Surgery*, 5(2):183–193, 2010.

[93] Thomas Little Heath et al. *The thirteen books of Euclid's Elements*, volume 3. DoverPublications.com, 1956.

[94] G Heckmann. Die gittertheorie der festen körper. In *Ergebnisse der exakten naturwissenschaften*, pages 100–153. Springer, 1925.

[95] Thomas Hegewald. *Modellierung des nichtlinearen Verhaltens piezokeramischer Aktoren*. PhD thesis, Universität Erlangen-Nürnberg, 2008.

[96] Tobias Hemsel and Jörg Wallaschek. Survey of the present state of the art of piezoelectric linear motors. *Ultrasonics*, 38(1):37–40, 2000.

[97] Peter Herberts, Christian Almström, Roland Kadefors, and Peter D Lawrence. Hand prosthesis control via myoelectric patterns. *Acta Orthopaedica*, 44(4-5):389–409, 1973.

[98] M Hermann and W Schinköthe. Piezoelectric travelling wave motors generating direct linear motion. In *Conference Proceedings, S*, volume 200, page 203, 1999.

[99] DP Hess and A Soom. Friction at a lubricated line contact operating at oscillating sliding velocities. *Journal of Tribology*, 112(1):147–152, 1990.

[100] Walter Heywang, Karl Lubitz, and Wolfram Wersing, editors. *Piezoelectricity: Evolution and Future of a Technology (Springer Series in Materials Science)*. Springer, softcover reprint of hardcover 1st ed. 2008 edition, 11 2010.

[101] A. V. Hill. *First and Last Experiments in Muscle Mechanics*. Cambridge University Press, 5 1970.

[102] AV Hill. The heat of shortening and the dynamic constants of muscle. *Proceedings of the royal society of london series B-biological sciences*, 126(843):136–195, 1938.

[103] N Hogan. Adaptive-Control Of Mechanical Impedance By Coactivation Of Antagonist Muscles. *IEEE Transactions On Automatic Control*, 29(8):681–690, 1984.

[104] John Hooker. *Integrated methods for optimization*, volume 100. Springer, 2007.

[105] H Hu and R Ben Mrad. On the classical Preisach model for hysteresis in piezoceramic actuators. *Mechatronics*, 13(2):85–94, 2003.

[106] Takuro Ikeda and Takuro Ikeda. *Fundamentals of piezoelectricity*, volume 2. Oxford University Press Oxford, 1990.

[107] Alberto Isidori. *Nonlinear control systems. 2 (1999)*, volume 2. Springer, 1999.

[108] Esmaiel Jabbari. *Handbook of Biomimetics and Bioinspiration: Biologically-Driven Engineering of Materials, Processes, Devices, and Systems*. World Scientific Publishing Company, 2014.

[109] S.C. Jacobsen, H. Ko, E.K. Iversen, and C.C. Davis. Control strategies for tendon-driven manipulators. *IEEE Control Systems Magazine*, 10(2):23–28, 1990.

[110] Bojan Jakimovski. *Biologically Inspired Approaches for Locomotion, Anomaly Detection and Reconfiguration for Walking Robots (Cognitive Systems Monographs)*. Springer, 2011 edition, 2011.

[111] H Janocha and K Kuhnen. Real-time compensation of hysteresis and creep in piezoelectric actuators. *Sensors And Actuators A-Physical*, 79(2):83–89, 2000.

[112] Hartmut Janocha. *Actuators: basics and applications*. Springer Verlag, 2004.

[113] DC Jiles and DL Atherton. Theory of ferromagnetic hysteresis. *Journal of magnetism and magnetic materials*, 61(1):48–60, 1986.

[114] Stefan Johansson, Mats Bexell, and Per Oskar Lithell. Fine walking actuator, Jan. 2002.

[115] CR Johnstun and CC Smith. Modeling And Design Of A Mechanical Tendon Actuation System. *Journal Of Dynamic Systems Measurement And Control-Transactions Of The ASME*, 114(2):253–261, 1992.

[116] Gareth Aneurin Jones and Josephine Mary Jones. *Elementary number theory*. Springer, 1998.

[117] L Juhas, A Vujanic, N Adamovic, L Nagy, and B Borovac. A platform for micropositioning based on piezo legs. *Mechatronics*, 11(7):869–897, 2001.

[118] Laszlo Juhasz, Juergen Maas, and Branislav Borovac. Parameter identification and hysteresis compensation of embedded piezoelectric stack actuators. *Mechatronics*, 21(1):329–338, 2011.

[119] H Jung and DG Gweon. Creep characteristics of piezoelectric actuators. *Review of Scientific Instruments*, 71(4):1896–1900, 2000.

[120] Eric R Kandel, James H Schwartz, Thomas M Jessell, et al. *Principles of neural science*, volume 4. McGraw-Hill New York, 2000.

[121] Dean C Karnopp, Donald L Margolis, and Ronald C Rosenberg. *System Dynamics: Modeling, Simulation, and Control of Mechatronic Systems*. Wiley.com, 2012.

[122] Shaul Katzir. Who knew piezoelectricity? rutherford and langevin on submarine detection and the invention of sonar. *Notes and Records of the Royal Society*, 66(2):141–157, 2012.

[123] Thomas Kindermann. Behavior and adaptability of a six-legged walking system with highly distributed control. *Adaptive Behavior*, 9(1):16–41, 2001.

[124] Donald E. Knuth. *Art of Computer Programming, Volume 2: Seminumerical Algorithms*. Addison-Wesley Professional, 3 edition, 11 1997.

[125] Burhanettin Koc, Serra Cagatay, and Kenji Uchino. A piezoelectric motor using two orthogonal bending modes of a hollow cylinder. *Ultrasonics, Ferroelectrics and Frequency Control, IEEE Transactions on*, 49(4):495–500, 2002.

[126] Andrew J Kurdila, P Panos M Pardalos, and Michael Zabarankin. *Robust optimization-directed design*, volume 81. Springer, 2006.

[127] Minoru Kurosawa, Kentaro Nakamura, Takashi Okamoto, and Sadayuki Ueha. An ultrasonic motor using bending vibrations of a short cylinder. *Ultrasonics, Ferroelectrics and Frequency Control, IEEE Transactions on*, 36(5):517–521, 1989.

[128] Serge Lang. *Introduction to Diophantine approximations*. Springer, 1995.

[129] SY Lee, B Ko, and WS Yang. Theoretical modeling, experiments and optimization of piezoelectric multimorph. *Smart Materials & Structures*, 14(6):1343–1352, 2005.

[130] Daniel Liberzon and A Stephen Morse. Basic problems in stability and design of switched systems. *Control Systems, IEEE*, 19(5):59–70, 1999.

[131] CM Light and PH Chappell. Development of a lightweight and adaptable multiple-axis hand prosthesis. *Medical engineering & physics*, 22(10):679–684, 2000.

[132] Tobias Lilliehorn, Urban Simu, and Stefan Johansson. Multilayer telescopic piezoactuator fabricated by a prototyping process based on milling. *Sensors and Actuators A: Physical*, 107(2):159–168, 2003.

[133] Chih-Jer Lin and Sheng-Ren Yang. Precise positioning of piezo-actuated stages using hysteresis-observer based control. *Mechatronics*, 16(7):417–426, 2006.

[134] Van-Tsai Liu, Chun-Liang Lin, and Home-Young Wing. New realisation of preisach model using adaptive polynomial approximation. *International Journal of Systems Science*, 43(9):1642–1649, 2012.

[135] L. Ljung. *System Identification: Theory for the User*. Prentice-Hall PTR, Upper Saddle River, NJ, 1999.

[136] Niklas Luhmann and Dirk Baecker. *Einführung in die Systemtheorie*, volume 2. Carl-Auer-Systeme-Verlag, 2002.

[137] Matthew M. Lux, Matthew Marshall, Erdal Erturk, and Jean V. Joseph. Ergonomic Evaluation and Guidelines for Use of the daVinci Robot System. *Journal of Endourology*, 24(3):371–375, 2010.

[138] John DW Madden, Nathan A Vandesteeg, Patrick A Anquetil, Peter GA Madden, Arash Takshi, Rachel Z Pytel, Serge R Lafontaine, Paul A Wieringa, and Ian W Hunter. Artificial muscle technology: physical principles and naval prospects. *Oceanic Engineering, IEEE Journal of*, 29(3):706–728, 2004.

[139] Thierry Madiés, Dominique Guellec, and Jean-Claude Prager, editors. *Patent Markets in the Global Knowledge Economy: Theory, Empirics and Public Policy Implications*. Cambridge University Press, 3 2014.

[140] John A Main and Ephrahim Garcia. Piezoelectric stack actuators and control system design: strategies and pitfalls. *Journal of Guidance, Control, and Dynamics*, 20(3):479–485, 1997.

[141] Stephen Mann. A blossoming development of splines. *Synthesis Lectures on Computer Graphics and Animation*, 1(1):1–108, 2006.

[142] H. Marth and R. Gloess. Verstelleantrieb aus Bimorphelementen, Sep. 1993.

[143] William G. May. Piezoelectric electromechanical translation apparatus, 1975.

[144] A Meitzler, HF Tiersten, AW Warner, D Berlincourt, GA Couqin, and FS Welsh III. Ieee standard on piezoelectricity, 1988.

[145] Roel J. E. Merry, Niels C. T. de Kleijn, Marinus J. G. van de Molengraft, and Maarten Steinbuch. Using a Walking Piezo Actuator to Drive and Control a High-Precision Stage. *IEEE-ASME Transactions On Mechatronics*, 14(1):21–31, 2009.

[146] Roel J. E. Merry, Martijn G. J. M. Maassen, Marinus (Rene) J. G. van de Molengraft, Nathan van de Wouw, and Maarten Steinbuch. Modeling and Waveform Optimization of a Nano-motion Piezo Stage. *IEEE-ASME Transactions on Mechatronics*, 16(4):615–626, 2011.

[147] Shane A. Migliore, Edgar A. Brown, and Stephen P. DeWeerth. Novel nonlinear elastic actuators for passively controlling robotic joint compliance. *Journal Of Mechanical Design*, 129(4):406–412, 2007.

[148] Saeed Moaveni. *Finite element analysis: theory and application with ANSYS*. Pearson Education India, 2003.

[149] Ralf Möller. *Das Ameisenpatent*. Elsevier, Spektrum Akad. Verlag, 2006.

[150] William Nash and Merle Potter. *Schaum's Outline of Strength of Materials*. McGraw-Hill, 5 edition, 8 2010.

[151] Z Nawrat and P Kostka. Polish cardio-robot 'Robin Heart'. System description and technical evaluation. *International Journal of Medical Robotics and Computer Assisted Surgery*, 2(1):36–44, 2006.

[152] George L Nemhauser and Laurence A Wolsey. *Integer and combinatorial optimization*, volume 18. Wiley New York, 1988.

[153] C.V. Newcomb and I. Flinn. Improving the linearity of piezoelectric ceramic actuators. *Electronics Letters*, 18(11):442–444, 1982.

[154] RE Newnham, A Dogan, QC Xu, K Onitsuka, J Tressler, and S Yoshikawa. Flextensional moonie actuators. In *Ultrasonics Symposium, 1993. Proceedings., IEEE 1993*, pages 509–513. IEEE, 1993.

[155] D Newton, E Garcia, and GC Horner. A linear piezoelectric motor. *Smart Materials & Structures*, 7(3):295–304, 1998.

[156] Henrik Olsson, Karl J Åström, Carlos Canudas de Wit, Magnus Gäfvert, and Pablo Lischinsky. Friction models and friction compensation. *European journal of control*, 4(3):176–195, 1998.

[157] Zoubeida Ounaies, Karla M Mossi, Ralph C Smith, and Jeffrey D Bernd. Low-field and high-field characterization of thunder actuators. In *SPIE's 8th Annual International Symposium on Smart Structures and Materials*, pages 399–407. International Society for Optics and Photonics, 2001.

[158] Keir Pearson. The control of walking. *Scientific American*, 235:72–86, 1976.

[159] KG Pearson and JF Iles. Discharge patterns of coxal levator and depressor motoneurones of the cockroach, periplaneta americana. *Journal of Experimental Biology*, 52(1):139–165, 1970.

[160] BNJ Persson. Sliding friction. *Surface Science Reports*, 33(3):85–119, 1999.

[161] Njal Bol Pettit and Peter E Wellstead. Analyzing piecewise linear dynamical systems. *Control Systems, IEEE*, 15(5):43–50, 1995.

[162] Rik Pintelon and Johan Schoukens. *System identification: a frequency domain approach*. John Wiley & Sons, 2004.

[163] Bernd Ploss, Wai-Yin Ng, Helen Lai-Wa Chan, Beatrix Ploss, and Chung-Loong Choy. Poling study of pzt/p (vdf–trfe) composites. *Composites science and technology*, 61(7):957–962, 2001.

[164] José Luis Pons Rovira, E Rocon, et al. Scaling of piezoelectric actuators: a comparison with traditional and other new technologies. 2006.

[165] Gill A Pratt and Matthew M Williamson. Series elastic actuators. In *Intelligent Robots and Systems 95.'Human Robot Interaction and Cooperative Robots', Proceedings. 1995 IEEE/RSJ International Conference on*, volume 1, pages 399–406. IEEE, 1995.

[166] Kenneth Price and Rainer Storn. Differential evolution. *Dr Dobbs Journal*, 22(4), 1997.

[167] T Pustelny, P Struk, Z Nawrat, and M Gawlikowski. Numerical and experimental researches of mechanical heart prosthesis. *The European Physical Journal Special Topics*, 154(1):175–181, 2008.

[168] Ernest Rabinowicz. The nature of the static and kinetic coefficients of friction. *Journal of applied physics*, 22(11):1373–1379, 1951.

[169] Micky Rakotondrabe, Mohammad Al Janaideh, Alex Bienaimé, and Qingsong Xu. Introduction: Smart materials as essential base for actuators in micro/nanopositioning. In *Smart Materials-Based Actuators at the Micro/Nano-Scale*, pages 1–14. Springer, 2013.

[170] J Anthony Rossiter. *Model-based predictive control: a practical approach*. CRC press, 2003.

[171] Sylvie Ryckebusch and Gilles Laurent. Rhythmic patterns evoked in locust leg motor neurons by the muscarinic agonist pilocarpine. *Journal of neurophysiology*, 69(5):1583–1595, 1993.

[172] Ahmad Safari and E Koray Akdoğan. *Piezoelectric and acoustic materials for transducer applications*. Springer, 2008.

[173] David Salomon. *Curves and surfaces for computer graphics*. Springer New York, 2006.

[174] T Sashida. Trial construction and operation of an ultrasonic vibration driven motor. *Japan Applied Physics*, 51(6):713–720, 1982.

[175] Ansgar B Schäufele and Karl Heinz Härdtl. Ferroelastic properties of lead zirconate titanate ceramics. *Journal of the American Ceramic Society*, 79(10):2637–2640, 1996.

[176] Malte Schilling, Thierry Hoinville, Josef Schmitz, and Holk Cruse. Walknet, a bio-inspired controller for hexapod walking. *Biological cybernetics*, pages 1–23, 2013.

[177] Malte Schilling, Jan Paskarbeit, Thierry Hoinville, Arne Hüffmeier, Axel Schneider, Josef Schmitz, and Holk Cruse. A hexapod walker using a heterarchical architecture for action selection. *Frontiers in Computational Neuroscience*, 7:126, 2013.

[178] Georg Schitter, Philipp J Thurner, and Paul K Hansma. Design and input-shaping control of a novel scanner for high-speed atomic force microscopy. *Mechatronics*, 18(5):282–288, 2008.

[179] Josef Schmitz. Load-compensating reactions in the proximal leg joints of stick insects during standing and walking. *Journal of experimental biology*, 183(1):15–33, 1993.

[180] J Schmitz and G Hafeld. The treading-on-tarsus reflex in stick insects: phase-dependence and modifications of the motor output during walking. *Journal of experimental biology*, 143(1):373–388, 1989.

[181] Josef Schmitz, Axel Schneider, Malte Schilling, and Holk Cruse. No need for a body model: Positive velocity feedback for the

control of an 18-dof robot walker. *Applied Bionics and Biomechanics*, 5(3):135–147, 2008.

[182] Axel Schneider, Holk Cruse, and Josef Schmitz. Decentralized control of elastic limbs in closed kinematic chains. *The International Journal of Robotics Research*, 25(9):913–930, 2006.

[183] R Shadmehr and MA Arbib. A Mathematical-analysis Of The Force-stiffness Characteristics Of Muscles In Control Of A Single Joint System. *Biological Cybernetics*, 66(6):463–477, 1992.

[184] Wacław Sierpiński. *Teoria liczb*. Instytut Matematyczny Polskiej Akademi Nauk, 1950.

[185] U Simu and S Johansson. Fabrication of monolithic piezoelectric drive units for a miniature robot. *Journal Of Micromechanics And Microengineering*, 12(5):582–589, 2002.

[186] Urban Simu and Stefan Johansson. Analysis of quasi-static and dynamic motion mechanisms for piezoelectric miniature robots. *Sensors And Actuators A-Physical*, 132(2):632–642, 2006.

[187] Jonas Sjöberg, Qinghua Zhang, Lennart Ljung, Albert Benveniste, Bernard Delyon, Pierre-Yves Glorennec, Håkan Hjalmarsson, and Anatoli Juditsky. Nonlinear black-box modeling in system identification: a unified overview. *Automatica*, 31(12):1691–1724, 1995.

[188] Sigurd Skogestad and Ian Postlethwaite. Multivariable feedback control: analysis and design. *New York*, 1996.

[189] Jean-Jacques E Slotine, Weiping Li, et al. *Applied nonlinear control*, volume 199. Prentice hall New Jersey, 1991.

[190] JG Smits and Ballato A. Dynamic Admittance Matrix of Piezoelectric Cantilever Bimorphs. *Journal Of Microelectromechanical Systems*, 3(3):105–112, 1994.

[191] JG Smits, Dalke SI, and TK Cooney. The Constituent Equations of Piezoelectric Bimorphs. *Sensors And Actuators A-Physical*, 28(1):41–61, 1991.

[192] T. Söderström and P. Stoica. *System Identification*. Prentice Hall International, Cambridge, UK, 2001.

[193] Jonathan Sorenson. Two fast gcd algorithms. *Journal of Algorithms*, 16(1):110–144, 1994.

[194] K Spanner. Survey of the various operating principles of ultrasonic piezomotors. In *Proceedings of the 10th International Conference on New Actuators*, 2006.

[195] Martin Špiller and Zdeněk Hurák. Hybrid charge control for stick–slip piezoelectric actuators. *Mechatronics*, 21(1):100–108, 2011.

[196] Damien Stehlé and Paul Zimmermann. A binary recursive gcd algorithm. In *Algorithmic number theory*, pages 411–425. Springer, 2004.

[197] R Storn and K Price. Differential evolution - A simple and efficient heuristic for global optimization over continuous spaces. *Journal of Global Optimization*, 11(4):341–359, 1997.

[198] Gerald Jay Sussman, Jack Wisdom, and Meinhard Edwin Mayer. *Structure and interpretation of classical mechanics*. MIT Press, 2001.

[199] David Sworder. Feedback control of a class of linear systems with jump parameters. *Automatic Control, IEEE Transactions on*, 14(1):9–14, 1969.

[200] Filip Szufnarowski and Axel Schneider. Force control of a piezoelectric actuator based on a statistical system model and dynamic compensation. *Mechanism and Machine Theory*, 46(10):1507–1521, 2011.

[201] Naofumi Takagi. A vlsi algorithm for modular division based on the binary gcd algorithm. *IEICE TRANSACTIONS on Fundamentals of Electronics, Communications and Computer Sciences*, 81(5):724–728, 1998.

[202] S Takahashi. Recent developments in multilayer piezoelectric ceramic actuators and their applications. *Ferroelectrics*, 91(1):293–302, 1989.

[203] Jan Tichý, Jiří Erhart, and Erwin Kittinger. *Fundamentals of Piezoelectric Sensorics: Mechanical, Dielectric, and Thermodynamical Properties of Piezoelectric Materials*. Springer, 2008.

[204] Jan Tichy and Gustav Gautschi. *Piezoelektrische Messtechnik: physikalische Grundlagen, Kraft-, Druck-und Beschleunigungsaufnehmen, Verstärker*. Springer, 1980.

[205] Masahiko Tominaga, Ryuta Kaminaga, James R Friend, Kentaro Nakamura, and Sadayuki Ueha. An ultrasonic linear motor using ridge-mode traveling waves. *Ultrasonics, Ferroelectrics and Frequency Control, IEEE Transactions on*, 52(10):1735–1742, 2005.

[206] Lung-Wen Tsai. Design of tendon-driven manipulators. *Journal of Mechanical Design*, 117:80–86, 1995.

[207] K Uchino. Piezoelectric ultrasonic motors: overview. *SMART MATERIALS & STRUCTURES*, 7(3):273–285, 1998.

[208] K Uchino, editor. *Advanced Piezoelectric Materials: Science and Technology*. CRC Press, 9 2010.

[209] Kenji Uchino. *Piezoelectric Actuators and Ultrasonic Motors*. Springer, 1 edition, 11 1996.

[210] Kenji Uchino and Jayne Giniewicz, editors. *MicroMechatronics (Materials Engineering)*. CRC Press, 4 2003.

[211] Andrew Vardy and Ralf Moller. Biologically plausible visual homing methods based on optical flow techniques. *Connection Science*, 17(1-2):47–89, 2005.

[212] Alfredo Vázquez Carazo et al. *Novel piezoelectric transducers for high voltage measurements*. PhD thesis, Universitat Politècnica de Catalunya, 2000.

[213] Igor Aleksandrovich Viktorov. *Rayleigh and Lamb waves: physical theory and applications*, volume 147. Plenum press New York, 1967.

[214] V. Vishnevsky, L. Gultiaeva, I. Kartaschew, and V. Lavrinenko. Piezoelectric motor, 1976.

[215] A Visioli. Modified anti-windup scheme for PID controllers. *IEEE Proceedings-Control Theory And Applications*, 150(1):49–54, 2003.

[216] Woldemar Voigt. *Lehrbuch der Kristallphysik*, volume 34. BG Teubner, 1910.

[217] Jozef Vörös. Modeling and identification of hysteresis using special forms of the coleman-hodgdon model. *Journal of Electric Engineering*, 60(2):100–105, 2009.

[218] J Wallaschek. Contact mechanics of piezoelectric ultrasonic motors. *Smart Materials & Structures*, 7(3):369–381, 1998.

[219] Tim Walther. Implementation einer schnellen und fehlerfreien datenübertragung für einen fpga-basierten wellenformgenerator. Master's thesis, Bielefeld University, 2010.

[220] SY Wang. A finite element model for the static and dynamic analysis of a piezoelectric bimorph. *International Journal of Solids and Structures*, 41(15):4075–4096, 2004.

[221] Xinmao Wang and Victor Y Pan. Acceleration of euclidean algorithm and rational number reconstruction. *SIAM Journal on Computing*, 32(2):548–556, 2003.

[222] Gernot Wendler. Laufen und stehen der stabheuschrecke carausius morosus: Sinnesborstenfelder in den beingelenken als glieder von regelkreisen. *Zeitschrift für vergleichende Physiologie*, 48(2):198–250, 1964.

[223] Alfred L. W. Williams and J. Walter Brown. Piezoelectric motor, 08 1942.

[224] Jack M. Winters, Savio L-Y. Woo, and Idd Delp, editors. *Multiple Muscle Systems: Biomechanics and Movement Organization*. Springer, softcover reprint of the original 1st ed. 1990 edition, 11 2011.

[225] Anne Wosnitza, Till Bockemühl, Michael Dübbert, Henrike Scholz, and Ansgar Büschges. Inter-leg coordination in the control of walking speed in drosophila. *The Journal of Experimental Biology*, 216(3):480–491, 2013.

[226] Qingsong Xu and Yangmin Li. Dahl Model-Based Hysteresis Compensation and Precise Positioning Control of an XY Parallel Micromanipulator With Piezoelectric Actuation. *Journal of Dynamic Systems Measurement and Control-Transactions of the ASME*, 132(4), 2010.

[227] Y Yamagata, T Higuchi, H Saeki, and H Ishimaru. Ultrahigh vacuum precise positioning device utilizing rapid deformations of piezoelectric elements. *Journal of Vacuum Science & Technology A: Vacuum, Surfaces, and Films*, 8(6):4098–4100, 1990.

[228] Yutaka Yamagata and Toshiro Higuchi. A micropositioning device for precision automatic assembly using impact force of piezoelectric elements. In *Robotics and Automation, 1995. Proceedings., 1995 IEEE International Conference on*, volume 1, pages 666–671. IEEE, 1995.

[229] Jiashi Yang. *An introduction to the theory of piezoelectricity*, volume 9. Springer Verlag, 2005.

[230] J Zakotnik, T Matheson, and V Durr. Co-contraction and passive forces facilitate load compensation of aimed limb movements. *Journal Of Neuroscience*, 26(19):4995–5007, 2006.

[231] Xinliang Zhang and Yonghong Tan. A hybrid model for rate-dependent hysteresis in piezoelectric actuators. *Sensors And Actuators A-Physical*, 157(1):54–60, 2010.

[232] Klaus Zimmermann, Carsten Behn, and Igor Zeidis. *Mechanics of terrestrial locomotion: with a focus on non-pedal motion systems*. Springer, 2009.

[233] C Zollikofer. Stepping patterns in ants-influence of speed and curvature. *Journal of experimental biology*, 192(1):95–106, 1994.